INFORMATION TO USERS

This manuscript has been reproduced from the microfilm master. UMI films the text directly from the original or copy submitted. Thus, some thesis and dissertation copies are in typewriter face, while others may be from any type of computer printer.

The quality of this reproduction is dependent upon the quality of the copy submitted. Broken or indistinct print, colored or poor quality illustrations and photographs, print bleedthrough, substandard margins, and improper alignment can adversely affect reproduction.

In the unlikely event that the author did not send UMI a complete manuscript and there are missing pages, these will be noted. Also, if unauthorized copyright material had to be removed, a note will indicate the deletion.

Oversize materials (e.g., maps, drawings, charts) are reproduced by sectioning the original, beginning at the upper left-hand corner and continuing from left to right in equal sections with small overlaps.

ProQuest Information and Learning
300 North Zeeb Road, Ann Arbor, MI 48106-1346 USA
800-521-0600

COMBINATORIAL STUDIES OF Si-BASED ALLOY NEGATIVES FOR Li-ION BATTERIES

By

Timothy D. Hatchard

SUBMITTED IN PARTIAL FULFILLMENT OF THE REQUIREMENTS
FOR THE DEGREE OF DOCTOR OF PHILOSOPHY

AT

DALHOUSIE UNIVERSITY
HALIFAX, NOVA SCOTIA
August 2004

DALHOUSIE UNIVERSITY

To comply with the Canadian Privacy Act the National Library of Canada has requested that the following pages be removed from this copy of the thesis:

Preliminary Pages

Examiners Signature Page (pii)

Dalhousie Library Copyright Agreement (piii)

Appendices

Copyright Releases (if applicable)

Table of Contents

List of Figures

List of Tables

Abstract

Si-based materials are promising candidates to replace graphite as the negative electrode in Li-ion batteries. Si and Si-based materials are attractive because they can reversibly alloy with large amounts of Li. This leads to batteries with higher energy density when compared to cells made with graphite negative electrodes.

A crucial problem remains to be overcome before Si-based materials can be used in commercial Li-ion cells. Graphite electrodes can withstand up to a thousand or more charge/discharge cycles without losing significant amounts of capacity. The Si-based materials, on the other hand, lose much of their capacity after only a few cycles. This makes them unacceptable for use in rechargeable batteries.

Alloy electrodes that are amorphous tend to have better capacity retention than crystalline materials of similar composition. There are many elements that alloy with Li, so there is a large sample space of possible composite electrode materials that can be tested. A method is needed that can produce libraries with large composition ranges that also contain amorphous material.

Amorphous films can be produced by sputter deposition that would not be amorphous if created by other means such as physical mixing or melt spinning. Sputter deposition also lends itself easily to combinatorial methods. This thesis describes the development of a combinatorial deposition system that can produce ternary films with linear and orthogonal composition variations and large amorphous ranges. Infrastructure to perform combinatorial electrochemical testing has also been developed.

Studies of a-Si and a-Si-based alloys containing Al, Ag, Ge, Sn and Zn have been conducted. Results of combinatorial studies for binary and ternary systems are presented. In-situ XRD studies have been conducted for a-Si and some specific compositions of SiZn. These results are discussed as well as the phases formed during electrochemical cycling of these cells.

List of Abbreviations and Symbols Used

λ	wavelength
μ_{anode}	chemical potential of Li in the anode
$\mu_{cathode}$	chemical potential of Li in the cathode
ρ_n	electron density of atom n
ω	angular velocity
a-Si	amorphous Si
A	absorption correction factor for electron microprobe
A^+	positive ion of element A
B	magnetic field
BCC	body cenetred cubic
c	speed of light
c-Zn	crystalline Zn
d	crystallographic plain spacing
D	grain size
DC	direct current
DEC	diethyl carbonate
DMM	digital multimeter
dQ/dV	differential capacity
e	magnitude of the charge on an electron
e^-	electron
E	electromotive force
E	electric field
EC	ethylene carbonate
EDS	energy dispersive spectroscopy
EMF	electromotive force
F	fluorescence correction factor for electron microprobe
f_n	form factor of atom n
FCC	Federal Communications Commission
F_{hkl}	geometrical structure factor of the (hkl) plane

(hkl)	Miller indices of crystallographic planes
hcp	hexagonal close packed
I	current; scattered x-ray intensity
I_o	incident x-ray intensity
LC	series connected inductor and capacitor
Li-ion	lithium ion
m	mass
M	metal
M_A	molar mass of element A
m_e	electron mass
MMA	multichannel microelectrode analyzer
n	efficiency of electron trapping
Ni-Cad	nickel cadmium
NiMH	nickel metal hydride
PVD	physical vapour deposition
q	scattering vector
Q	total charge transferred
RF	radio frequency
SCCM	standard cubic centimetre per minute
SEM	scanning electron microscopy
T_c	critical temperature
TC_A	theoretical capacity of element A
TEM	transmission electron microscopy
TMO	transition metal oxide
V	potential
w	peak width
WDS	wavelength dispersive spectroscopy
XRD	x-ray diffraction
Z	atomic number

Acknowledgement

There are a lot of people behind the work presented in this thesis. The development of the combinatorial infrastructure was a group effort and the work of many people was required. The contributions of Arman Bonakdarpour, Mike Fleischauer, Simon Trussler and David Stevens, among others, was essential to the combinatorial project.

I would like to thank all of the members of the Dahn Lab (past and present) for helping to make such a wonderful work environment. The ability to turn to knowledgable people to help when you hit a snag is a tremendous advantage.

Without some diversion from work, the work will begin to suffer. There was never any shortage of people to provide recreational opportunities and I would like to thank them. Without Shane, Kev, Robbie, Jody, Mike, Dave, the fine staff at Wendy's, Adam, bacon and other companions my time here at Dalhousie would not have been nearly as prosperous.

Much thanks is due to my supervisor, Dr. Jeff Dahn. I cannot imagine someone providing a better environment for a student to conduct their graduate work.

I would like to thank my parents for their continuous support. Finally, my thanks and love to my wife Kimberley. Your support has been a crutch to me over the past five years, and you will soon give me the greatest gift of all when you present me with my son.

Chapter 1. Introduction

1.1. Motivation

As the world relies more and more on mobile electronic devices such as cell phones and lap top computers, batteries are becoming more and more important. Lithium ion cells are becoming the most popular choice for rechargeable battery packs. This is due to their superior performance when compared to other available battery chemistries.

Although Li-ion batteries have been well researched and developed to become the highest energy batteries, they face ever-increasing performance demands. Electronic devices are becoming smaller and smaller, resulting in less space available for batteries. Also, people are expecting these smaller batteries to last longer between charges. Furthermore, Li-ion batteries have not yet evolved to the point where they can meet their ultimate challenge – battery powered electric vehicles. These factors necessitate the continued improvement of the performance of Li-ion batteries. As current materials being used in Li-ion batteries have already been highly optimized, new and better materials must be found. The purpose of this thesis is to describe a search for advanced negative electrode materials for Li-ion batteries. This entails not only the production, characterization and testing of new materials, but also the development of a combinatorial search technique to speed the process of finding better materials.

1.2. Batteries

An electrochemical cell is an energy storage device that is capable of converting the chemical energy of the materials in its electrodes to electrical energy that can be used to power an external device. A battery is actually a collection of individual units called cells. Each cell typically consists of two electrodes and an electrolyte. At the negative electrode electrons are liberated from the material and can flow through an external circuit. A positive ion is also released from the negative electrode into the electrolyte. At the positive electrode the electrons are recombined with positive ions from the electrolyte, which is an ionic conductor that allows ions to flow between the two electrodes. A schematic of a typical cell is shown in Figure 1.1. In this cell, the negative electrode is made from Li and Sn is serving as the positive electrode.

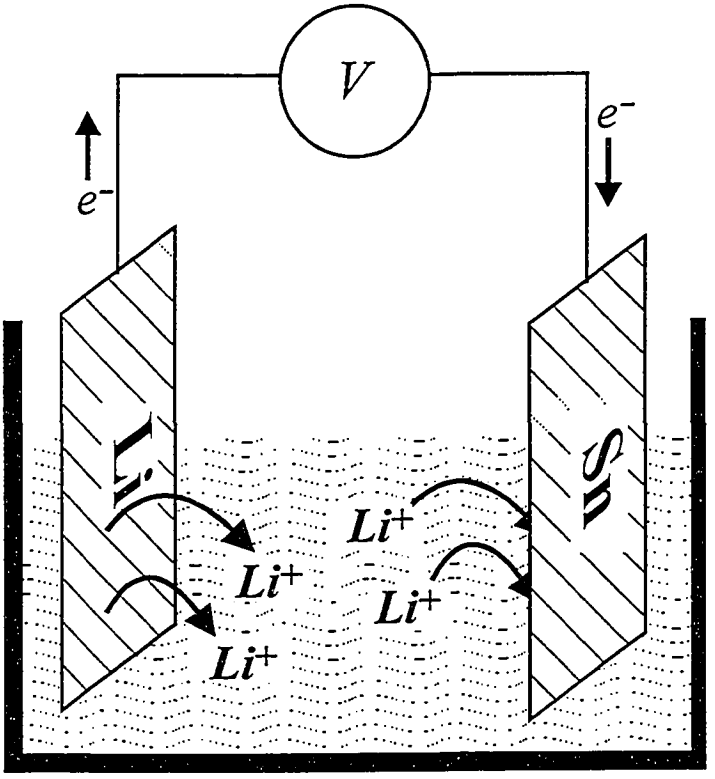

Figure 1.1. A schematic of a Li-Sn cell.

The driving force, or electro-motive force (EMF), of the cell comes from the difference of the chemical potentials of Li atoms in the two electrodes:

$$E = - \frac{\mu_{cathode} - \mu_{anode}}{e}$$

For Li and Li-ion batteries, $\mu_{electrode}$ is the chemical potential of Li atoms in the electrode in question and e is the magnitude of the electronic charge. To be absolutely correct, the electrode called the anode or cathode should be switched for the charge or discharge of the cell. In this thesis, we will call the electrode that gives up electrons during the discharge of the cell the negative electrode, and the electrode that accepts electrons will be called the positive electrode. In this context, it is more energetically favourable for the Li atoms to be in the positive electrode than in the negative electrode and this energy difference is what enables the cell to perform work.

There are several different types of rechargeable batteries available on the market [1]. The most common are the lead-acid battery found in automobiles, nickel-cadmium (Ni-Cad) and nickel-metal-hydride (NiMH) used in many battery operated toys and early cell phones and the lithium ion (Li-ion) battery found in most newer cell phones and laptop computers. Table 1.1 shows a comparison of the properties of some of these batteries and illustrates the superior energy density of the Li-ion battery over other available technologies. This superior energy density is what allows the smaller battery packs on new cell phones and laptop computers to last as long as they do. It also drives the quest to find better and better materials for use in these batteries.

Table 1.1. A comparison of some common rechargeable batteries.

	NiCd	NiMH	Li-ion
Gravimetric Energy Density (Wh/Kg)	48 (Sanyo CP-2400 SCR)	92 (Sanyo HR-3U (2300))	177 (E-One/Moli Energy)
Cycle Life (to 80% of initial capacity)	1000	300 – 500	500 – 1000
Fast Charge Time	1 hr	2 – 4 hr	1 – 2 hr
Overcharge Tolerance	moderate	low	very low
Self-discharge / Month (at room temperature)	20 %	30 %	< 10 %

Figure 1.2 shows the construction of a typical Li-ion cell. It is often referred to as a jellyroll because the electrodes are rolled up in a tube with a micro-porous separator between them. The separator provides electrical isolation of the electrodes while still allowing ions to travel from one to the other in the electrolyte. The jellyroll is inserted in a nickel-plated steel or Aluminum can and electrolyte is added. The can is capped with a pressure sensitive safety vent. The safety vent generally acts as the positive contact and the can itself is the negative contact of the cell.

1.3. Development of Li-ion Batteries

The first Lithium batteries appeared in the 1970's [2 – 9]. These batteries used lithium metal as the anode. Since Li has a very low potential (-3.05 V *vs.* Standard Hydrogen Electrode [10]) and low density it is ideal for high voltage, lightweight batteries. A layered intercalation compound such as MoS_2, TiS_2 or V_2O_5 was used as the positive electrode. In these batteries, lithium atoms could be reversibly inserted between the layers of the positive electrode.

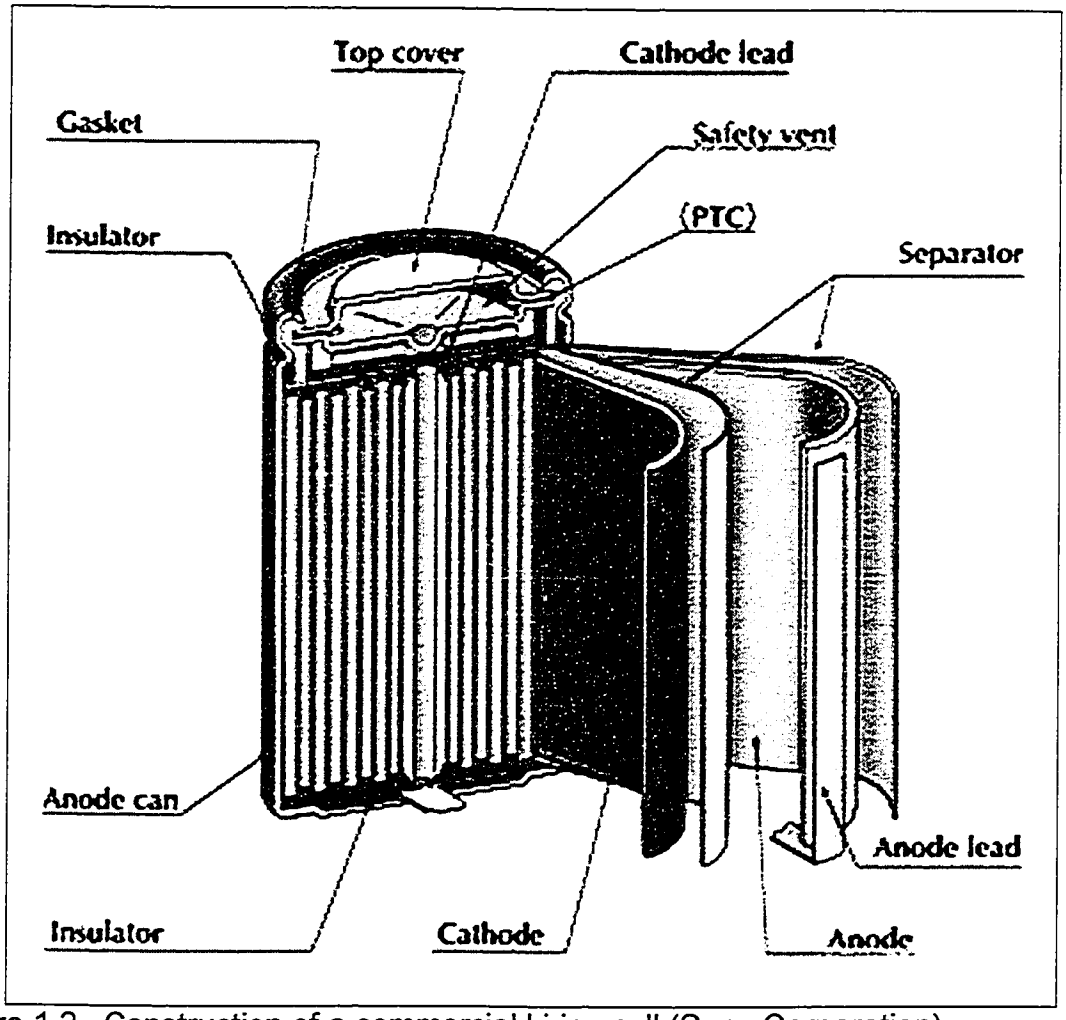

Figure 1.2. Construction of a commercial Li-ion cell (Sony Corporation).

The use of lithium metal in rechargeable cells was soon found to be too unsafe for use in consumer electronics. This lack of safety was found to be from changes in the surface morphology of the lithium that occurred during repeated charge and discharge cycles of the battery [11, 12]. During the removal of lithium from the positive electrode and its electroplating on the metal foil negative electrode, high surface area growths would form. This increased surface area dramatically reduced the thermal stability of the cell. If the cell was subsequently exposed to elevated temperatures, uncontrolled chemical reactions could occur causing the cell to heat to very high temperatures in a very short time. This was

called thermal runaway and included smoke and flame being emitted from the cell's safety vent.

To overcome the safety problems with using lithium metal as the negative electrode, the industry turned instead to graphite electrodes [13-15]. Lithium atoms can be reversibly inserted between and removed from the layers of the graphite (intercalated/de-intercalated). This reaction is highly reversible and the potential difference between Li in graphite and Li metal is only about 0.1 V, so there is not a large loss of cell voltage from switching to graphite negative electrodes. More importantly, graphite negative electrodes have proven to be much more thermally stable over repeated charge/discharge cycles than Li metal.

In most Li-ion batteries produced today, the negative electrode is made from some form of layered or graphitic carbon. The positive electrode is typically made from $LiCoO_2$, a layered transition metal oxide (TMO) or $LiMn_2O_4$ that has a spinel structure. $LiCoO_2$ is the most popular choice. A fully charged cell will have potential of 4.2 V and a standard 18650 cell (a cylindrical cell 18 mm in diameter and 65 mm long) has a capacity of about 2.4 Ah.

1.4. Alloy Negatives

As an alternative to using graphite anodes, many researchers have focused on Li-containing alloys. Li can react reversibly with many different elements to form alloys [13, 16-21]. The basic reaction is:

$$xLi + M \Leftrightarrow Li_xM.$$

Table 1.2 shows a list of some elements that can react with Li. The table includes the number of Li atoms that react with each element and also the theoretical capacity of the element. The theoretical capacity is the amount of charge that can be transferred in a Li-ion cell with the particular element in question being used as the negative electrode. It is typically measured in mAh/g or mAh/cc. These capacities are usually based on the fully lithiated phase of the element found in equilibrium phase diagrams. As will be seen in Chapter 5, this is not always an accurate way of predicting the capacity attainable from an electrochemical cell operating at room temperature.

Table 1.2. Theoretical capacities of some lithium alloys.

Element M	**X in Li_xM**	**Capacity** (mAh/g)
Ca	2	1337
Al	1*	990
Si	4.4*	4200
Ge	4.4	1625
Sn	4.4*	993
Pb	3.75	485
Ag	3*	750
As	3	1073
Sb	3	660
Bi	3	385
Pt	2	275
Au	3.75	510
Zn	1*	423
Hg	3	401
Ba	4	781
C	0.1667	372

* see Chapter 5 for discussion of number of Li that can alloy with these elements

During the 1980's and 1990's, there was a large amount of research directed at lithium alloys for use as negative electrode materials. A major part of this effort was from Huggins et al. [22-27] and Besenhard et al. [13-15, 28, 29]. Although the alloy negatives show great potential due to their very high specific

capacity when compared to graphite, they have not yet found their way into commercial Li-ion cells. The problem is that they do not retain their capacity over a large number of charge/discharge cycles [13,30]. Some will actually fall below 50% of their initial capacity after less than five cycles. To be used in a commercial cell, capacity retention would have to be much better than this.

The capacity loss in these alloy materials can occur for several reasons. In crystalline materials, new inter-metallic phases are formed upon lithium insertion [13,30]. This leads to inhomogeneous volume expansions in the two-phase regions that can cause cracking and pulverization of the material. As a result of this cracking, some of the particles may lose electrical contact with the electrode and capacity is lost.

In amorphous alloys, the capacity loss occurs for a different reason. Beaulieu et al. [31-34] have shown that in amorphous alloys of Si and Sn, the expansion upon lithium insertion is homogeneous and that 10 - 30 micron pieces of thin films expand and contract reversibly without further pulverization. Similar results have been obtained elsewhere for a-Si [35, 36]. It appears that in these amorphous films, the capacity loss occurs because contact is lost to expanding and contracting particles undergoing large volume changes and not because of the pulverization that occurs in crystalline films. Some work by Jung et al. [37] on thin a-Si films has also shown some promise, with the thin film negative electrodes included in a full Li-ion cell with a $LiMn_2O_4$ positive electrode.

In light of the capacity fading problem with alloy negatives, interest faded in favour of carbon materials. However, after Fuji Film showed that amorphous

tin oxide composite materials could be used as negative electrode materials [38], the interest in alloy negatives was revived. The performance of these tin oxide composites was closely studied by Courtney et al. [39-43]. They found that the oxygen in the SnO samples would react irreversibly with Li to form Li_2O, leaving the Sn free to react reversibly with Li. If the voltage over which the cells cycled was carefully controlled they had good capacity retention with capacities rivalling that of graphite. In these materials, however, high Sn concentrations could be detrimental to the cell's performance. If there was too much Sn it would tend to aggregate, forming larger and larger particles on successive cycles. These larger particles would then pulverize in the manner described above causing the cell to lose capacity. Also, the high irreversible capacity due to the oxygen is a problem for commercial cells where the amount of Li is fixed.

Despite the fact that tin oxide composites have not been successfully integrated into commercial Li-ion cells, they did provide an idea of to how overcome the problems of alloy negatives. A possible solution was to surround the active material with an inactive, or less active, matrix that may help buffer the expansion on lithiation and provide structural support [23, 44-48]. This method has shown that it is possible to surround the active material in an inactive matrix without oxygen to cause high irreversible capacities. However, despite the fact that several researchers have studied this type of material, the approach has had only limited success, and the presence of an inactive matrix imposes a significant penalty on specific capacity. Green et al. [49] have tried to take advantage of the fact that small particles seem to expand and contract reversibly by creating

structured silicon negative electrodes. These negative electrodes consist of pillars deposited on silicon substrates. They show some promise, although Coulombic efficiency was less than ideal.

A similar approach is to apply coatings to the active materials. These can be either an inactive material to act as a buffer or a different active material. There has not been much work done on negative electrode materials using this approach. Some studies have focused on coating Si-based negative electrode materials with carbon [50-52]. In this case, the carbon coating was mainly intended to improve conductivity. Another effort focused on creating particles of active material A coated with a second active material B [53]. This had limited success, and the results reported were highly dubious. Some work on coatings has also been done with positive electrode materials. Cho showed that coatings of metal oxides dramatically improved the high voltage performance and thermal stability of $LiCoO_2$ [54], although his explanation of the mechanism involved turned out to be incorrect [55].

Perhaps a better solution is to use an elastomeric binder to hold the particles of the electrode. Elastomers that can be extended 2.5 times have been shown to improve the cycling of amorphous alloys significantly [56]. These binders can accommodate the huge expansions of the alloy negatives. They help hold the expanding particles together and keep them in electrical contact, so that they cannot break away and become isolated, thus reducing capacity.

Table 1.2, shows that there are a large number of elements that can alloy with lithium. Even if candidate elements are limited to those that are cheap, non-

toxic and abundant, there are still a vast number of possible combinations that could be considered for use as negative electrode materials. Indeed, this is clear from the literature where there has been a great deal of effort focused on various alloys of these elements. So far, the results of these studies have generally not been good. The alloys studied still show poor capacity retention during charge/discharge cycling. Much of the recent literature pertaining to alloy electrodes also shows that these materials tend to have very large first cycle irreversible capacity [57-61]. Indeed, Wachtler et al. [58] reported irreversible capacities for Sn/SnSb alloys as high as 65% of first discharge. As was pointed out in the article, these high irreversible capacities may have more to do with structure than the elements used, as the same elements have been used in other studies without such high irreversible capacities.

In light of the results found by Beaulieu et al. [31-34], many researchers have begun studying amorphous silicon and amorphous silicon-containing alloys. Sayama et al. [35] found similar results to those of Beaulieu, in that ~6 μm columns were formed in a-Si thin films during cycling. These columns then cycled reversibly with little capacity loss. Maranchi et al. [36] also found similar results with excellent cycling and high capacities of ~3500 mAh/g in 250 nm thick a-Si films on copper substrates. Netz et al. [57] experimented with several alloys containing silicon. Their materials were promising in terms of charge/discharge cycling, but still suffered from large first-cycle irreversible capacity.

It has been shown that in thin films of $Si_{1-x-y}Al_xSn_y$ the cycling performance is very much better for amorphous samples than for crystalline samples [62].

The transition from amorphous to crystalline samples was marked by a very dramatic decrease in capacity retention. This is illustrated in Figure 1.3. Figure 1.3a shows a non-equilibrium ternary phase diagram for sputtered SiAlSn libraries. The numbers mark the compositions used in electrochemical test cells. Figure 1.3b shows the discharge capacity *versus* cycle number for the cells. It is clear that the best capacity retention is for cells from the amorphous region of the non-equilibrium 'phase diagram'. For amorphous samples it was also found that there was relatively low irreversible capacity (< 20%) and good cycling regardless of the composition of the film. Song et al. found similar results for Mg_2Si films, although their amorphous films were 30 nm thick as compared to their nanocrystalline films, which were 380 nm thick [63].

Since some of the results for alloy negatives have shown such great potential in terms of high capacity, good capacity retention and low irreversible capacity, there is a lot of incentive for further study. However, in light of the huge number of possible alloys to study, it is difficult to perform a thorough search of the candidates using traditional, one at a time synthesis techniques. In the chapters to follow, a combinatorial technique to study large portions of binary and ternary systems will be developed. Also, electrochemical results of many alloy systems will be presented along with an attempt to understand the mechanisms involved when Li is alloyed with amorphous Si and amorphous Si-containing materials.

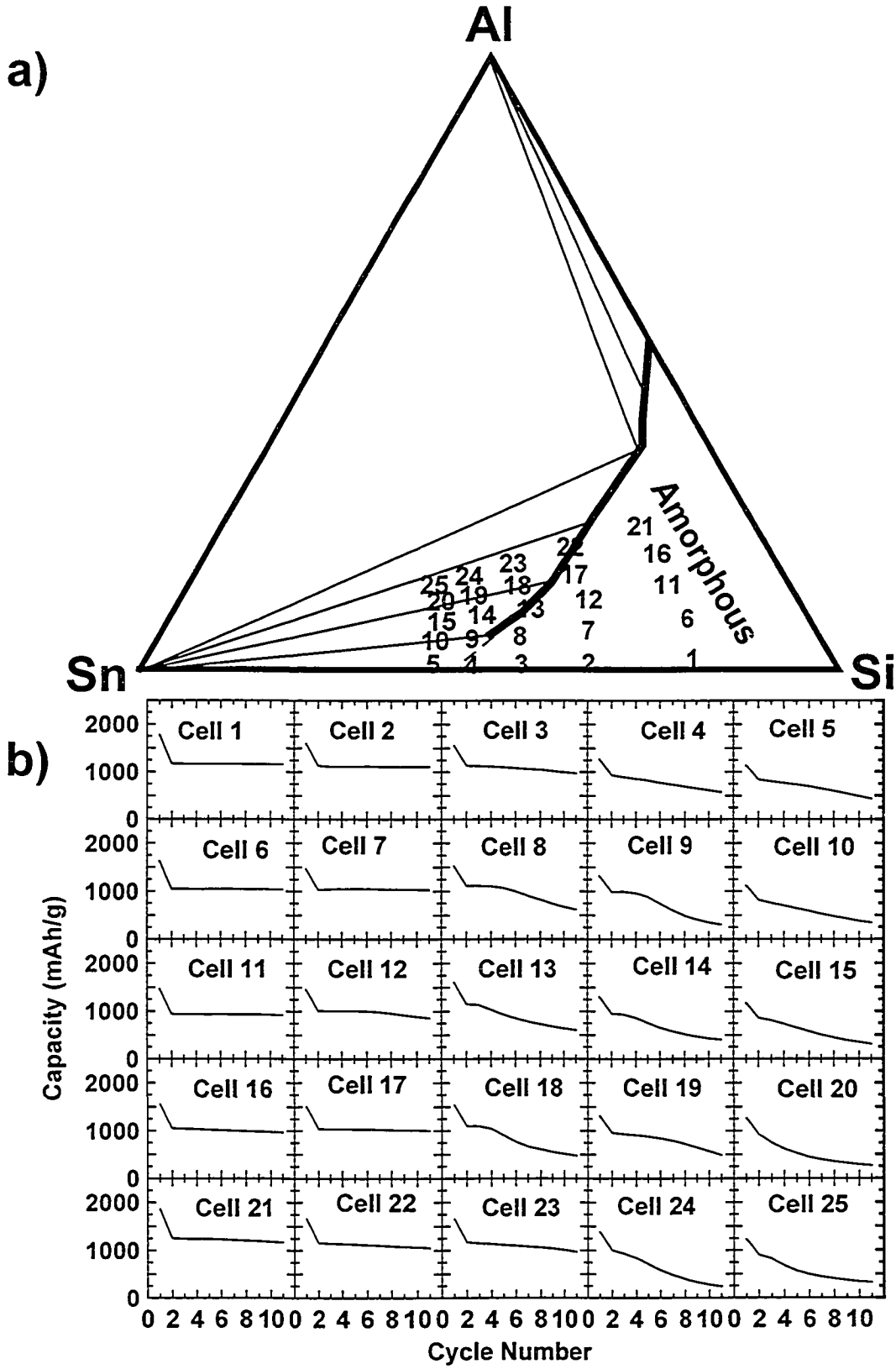

Figure 1.3. a) SiAlSn non-equilibrium phase diagram showing the location of electrochemical test cells. b) capacity *vs.* cycle number for the cells from a) (from reference [62]).

Chapter 2. Combinatorial Materials Science

2.1. The Need for Combinatorial Materials Science

Over time, society has greatly benefited from advances in the knowledge of materials. Throughout history, new discoveries in materials have allowed technology to advance, improving the quality of life for large numbers of people. Figure 2.1 shows one example of how improved materials have improved available technologies. It shows how the maximum cutting speed has advanced over time along with the introduction of new blade materials. This has made the jobs of wood and metal workers much easier and helped to advance the construction industry in general.

Through advances in materials and materials processing techniques, many consumer products continue to evolve. The continued development in the semi-conductor industry has led to rapid advancement in computer technology over the last two decades. As another example, some of today's portable electronics are very small, and without present day advanced battery materials, they could not operate for long without needing to be recharged.

These advances have resulted from the hard work of many scientists over the years. In the search for new materials, a researcher would traditionally produce, characterize and test each candidate material one at a time. This can be a very time consuming process. Consider just the binary compounds, those made from only two elements. If we restrict ourselves to those elements that are non-radioactive and non-toxic, there are about seventy useful elements.

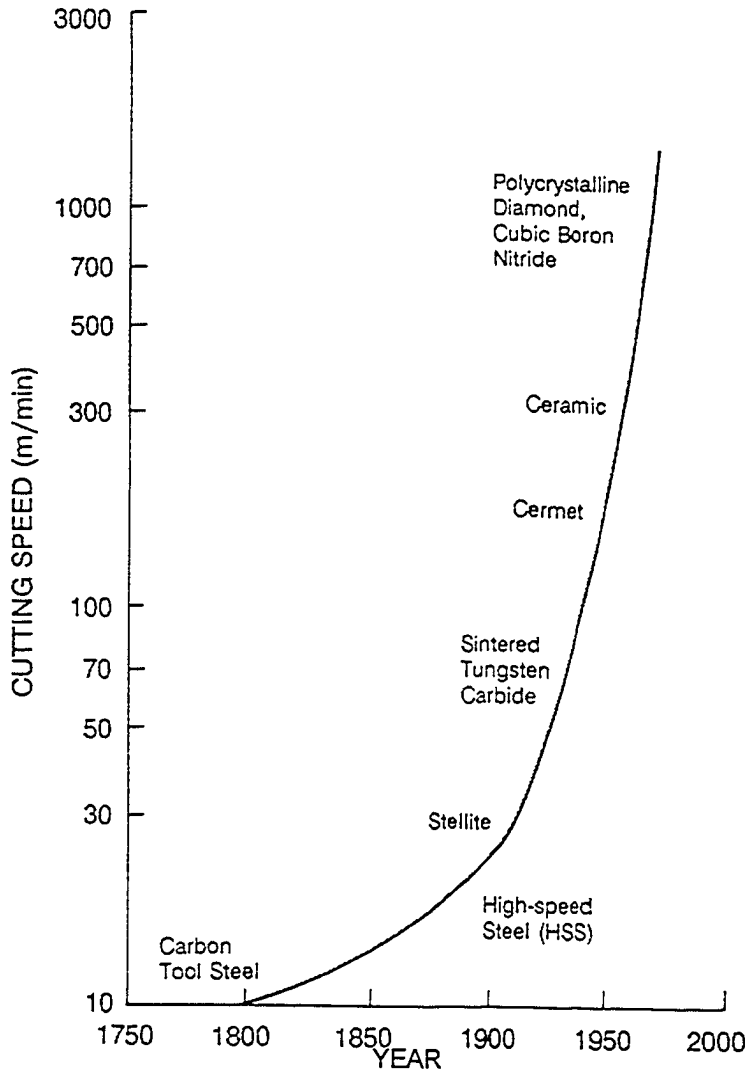

Figure 2.1. Advancement of cutting speeds over time.

Also, we will limit ourselves to ten stoichiometries per binary system. This means that there are 70 X 69 X 10 = 48300 possible binary materials. This is a very large sample space, although it is now nearly entirely known. If we move to ternary and larger systems, the sample space expands exponentially to a point where searching thoroughly using one at a time techniques becomes impossible.

Consider the case of the search for high temperature superconductors. Figure 2.2 shows a plot of maximum critical temperature *versus* the number of

elements that a superconducting material contains. The curve drawn through the data points shows, upon extrapolation, that in order to obtain a room temperature superconductor it should be necessary to include at least eight elements in the material. Probably more than eight would be needed, as the curve drawn seems to be a poor fit. If a straight line is drawn through the data points, then it would show that 12 or 13 elements would be needed. If we again restrict our search to seventy elements, there would be approximately $6X10^{19}$ possible eight-element mixtures to produce and test. If we assume that a scientist can make and analyze five mixtures per day, then 1 million scientists working 300 days per year would take 40 billion years to fully screen the eight element compounds.

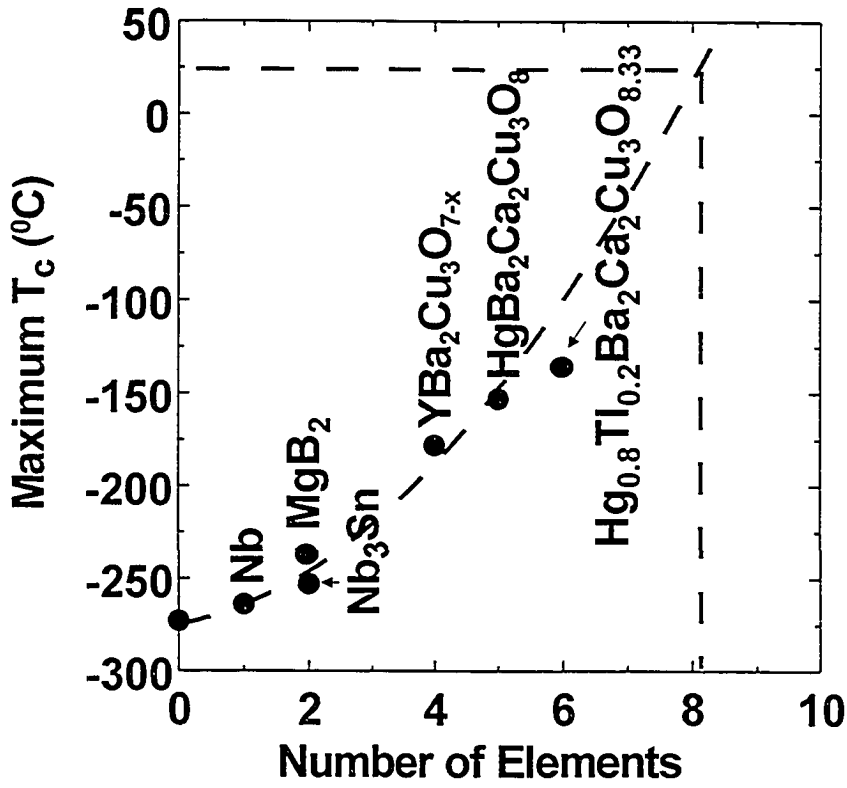

Figure 2.2. Maximum critical temperature for superconductors *versus* number of elements.

Clearly, combinatorial methods are needed to undertake any search for materials of the nature described above. These methods allow the simultaneous production and testing of multiple samples at once. Instead of making and testing materials one at a time, it is possible to make and test hundreds, thousands or even millions of samples in one experiment.

2.2. A Brief History

The area of research that is probably most commonly associated with combinatorial methods is pharmaceuticals. This industry has used combinatorial methods for discovering chemicals for new drugs for two decades. In one of the most common methods compounds are attached to polymer beads. After a reaction, the beads are split into separate containers, and different agents are added. The beads containing the products of these reactions are mixed (or pooled), then split again and reacted with different reagents. The process is repeated a certain number of times. Tags attached to the beads at each step indicate the reagents with which each bead has been treated. This technique is usually called the 'split pool' method. One of the first reports of combinatorial chemistry was from Geyson in 1984 [64]. He showed that 27000 different combinations of tripeptides could be formed by starting with three pools of 30 amino acids. Furthermore, an active combination could be found in less than 100 experiments, far less than would be required to screen all of the combinations one at a time.

Although combinatorial research in materials has received less attention until recently, it has actually been practiced for almost twice as long. In one of

the first reports of combinatorial methods being applied to materials research, Kennedy et al. [65], in 1965, produced isothermal ternary phase diagrams using three evaporation sources opposite the vertexes of a triangular substrate. Some of the best-known early work was performed by Hanak in the late 1960's and early 1970's [66-70]. He showed how a multi-component single vapour source could be used to deposit a spread of compositions on a single substrate [66]. This is illustrated in Figure 2.3.

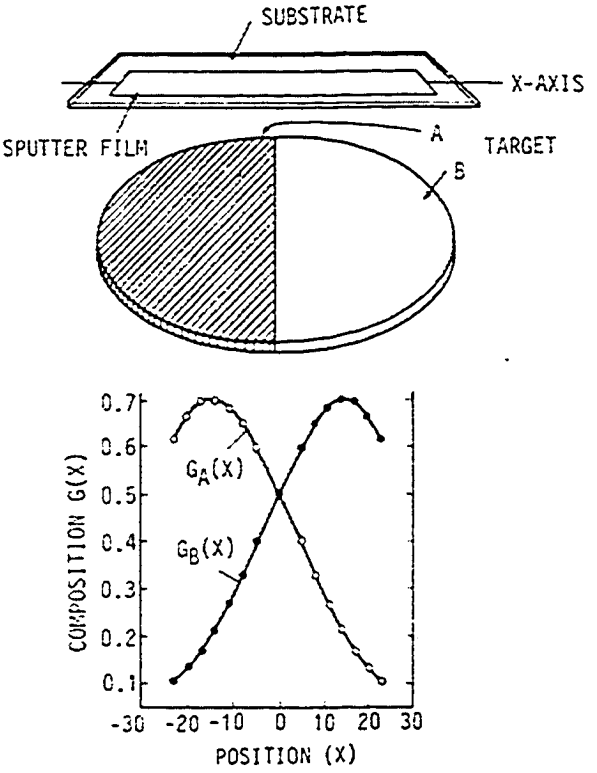

Figure 2.3. A composite target and its deposition profile *vs.* position on the substrate (from reference 66).

After the work by Hanak, the interest in combinatorial materials science faded. One likely reason for this is that at that time the data handling capabilities of computers were not able to keep pace with the production and analysis of new materials using combinatorial techniques. Also, sophisticated equipment is

needed for high throughput testing of combinatorial samples. The infrastructure was just not adequate to take full advantage of combinatorial methods.

In the 1990's, the idea of applying combinatorial methods to the discovery of new materials was revived by Xiang and Schultz at Lawrence Berkeley National Labs [71]. They used a set of computer controlled shadow masks in front of sputtered beams to produce combinatorial libraries of spatially addressable thin solid films. They used a series of oxide precursors to deposit 128-member libraries of possible superconducting materials. The libraries were annealed to crystallize the samples after deposition and then a four-probe technique was used to measure resistance *versus* temperature in order to identify superconducting compounds. An example of one of their libraries is shown in Figure 2.4.

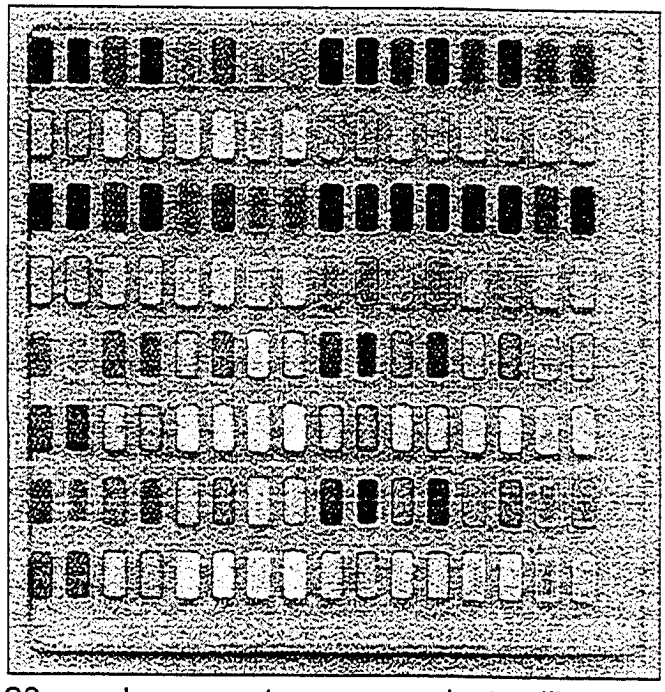

Figure 2.4. A 128-member cuprate superconductor library prior to annealing from Berkley National Labs. Each pixel is about 1 mm × 2 mm (from [71]).

In 1995 a company called Symyx Technologies (Santa Clara, California) was formed by Schultz and Zaffaroni to exploit combinatorial methods for materials research. Symyx is recognized as the world leader in the field. They produce combinatorial libraries using a wide variety of techniques to find materials for a wide variety of applications. One example is shown in Figure 2.5. This library consists of approximately 25000 different compositions on a 3-inch diameter wafer. This library was produced by thin-film electron beam evaporation in a search for new phosphorescent materials. As a result of this work, new red and blue-white phosphors were discovered for use in flat panel displays for portable devices and fluorescent lamps [72, 73].

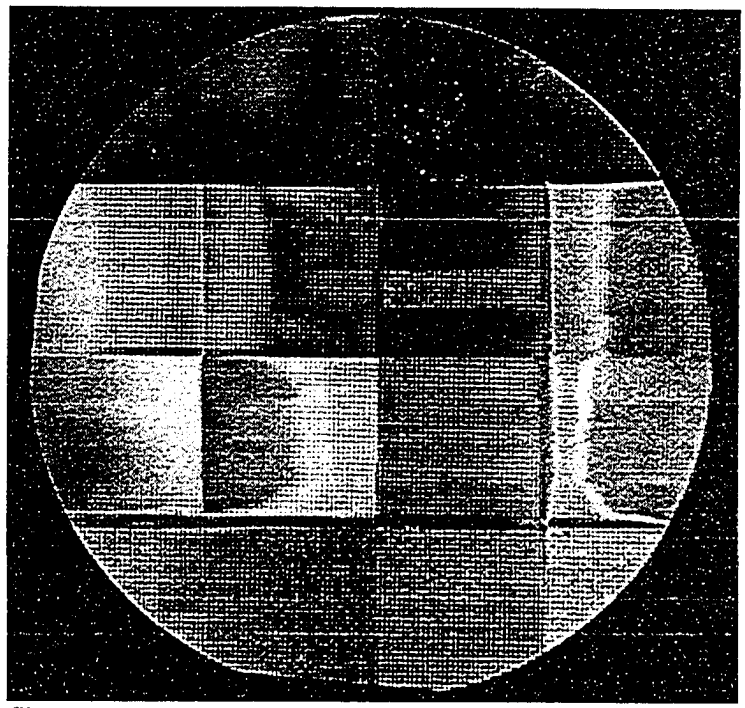

Figure 2.5. Thin film electron-beam deposited library containing ~25000 different regions on a 3" diameter Si wafer.

Besides pharmaceuticals, superconductors and phosphorescent materials, combinatorial methods are being applied in many other areas. Some

examples include fuel cell catalysts, magneto-resistive materials and, more recently, battery electrode materials. There is now enough interest in combinatorial chemistry and materials science that many conferences have symposia dedicated to it and there are even entire conferences dedicated to the subject. Journals are also starting to put together special issues for reporting combinatorial work in materials and there is a journal entitled Journal of Combinatorial Chemistry published by the American Chemical Society dedicated to the subject.

2.3. Producing Combinatorial Libraries

There are two basic methods for producing combinatorial libraries using physical vapour deposition techniques such as sputtering or thermal evaporation. The first method relies on a series of depositions through a set of shadow masks in order to build up libraries of multi-layered films with a different layering at each location. This is the method that Xiang used for his work mentioned above [71]. An example of this method, sometimes referred to as fractional masking, is illustrated in Figure 2.6. Each mask is used in four orientations so that different elements can be deposited on different areas of the substrate. The series of deposit and rotate steps combined with the different mask patterns allows libraries to be built which contain many different layer combinations.

One advantage of the fractional masking technique is that it is very flexible. The masking system to be used can be designed for a wide variety of purposes. The number of elements to be used, how they are to be combined, how large the individual samples are to be and the number of samples in the

library to be created can all be varied as needed to accomplish the goals of the researcher. The way the library will be laid out can be determined in advance to allow detailed planning of characterization and testing techniques to be used. Also, with this technique, each sample in the library has a consistent composition throughout, so a precisely known stoichiometry or structure is tested as opposed to an average across a sample with varied composition.

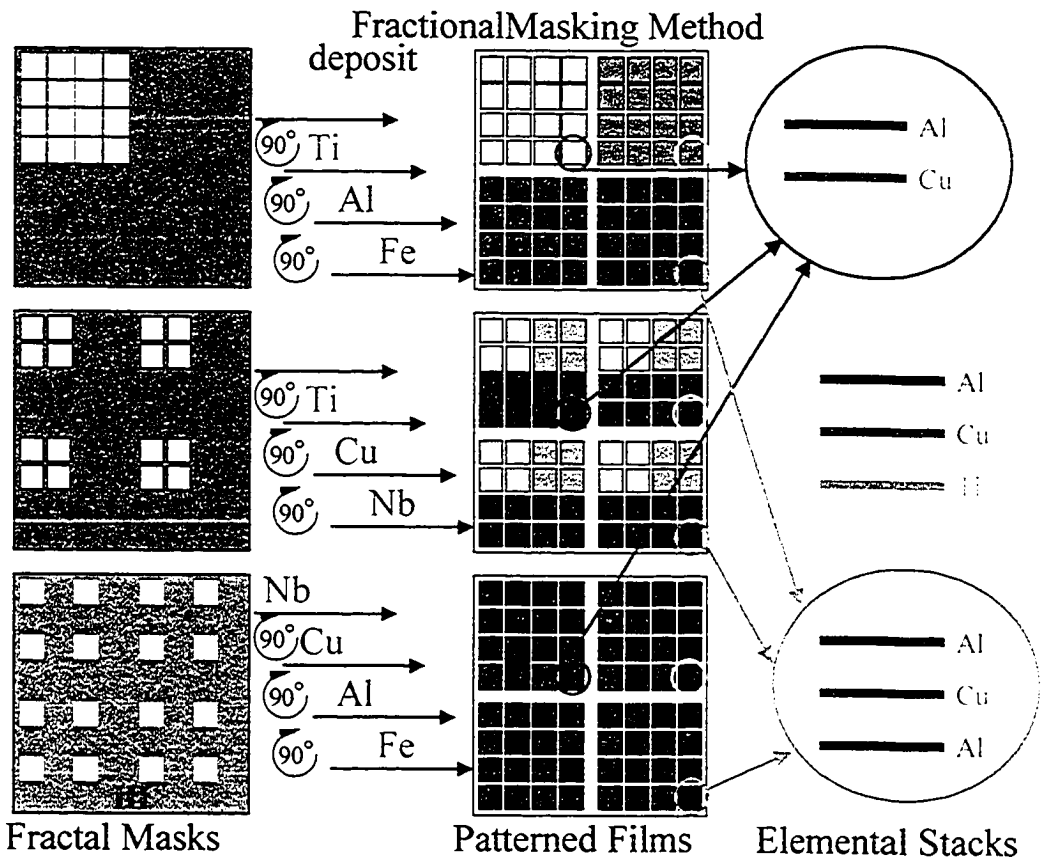

Figure 2.6. An example of the fractional masking technique of producing combinatorial libraries.

A major disadvantage of the fractional masking technique is that if intimate mixing of elements in the samples is desired, the library has to be annealed following deposition of the multi-layered films. This adds an additional step to

library production and can be quite difficult. If high temperatures are required, the choice of substrate for the library can be limited and additional technical difficulties can be encountered. Also, the anneal step can eliminate meta-stable or amorphous phases from the library that may be desirable for some purposes. Another disadvantage of this method is that it needs sophisticated computer-controlled motor-driven mask carousels. These can be expensive and prone to breakdown, especially when incorporated into a vacuum deposition system. Also, most systems for producing this type of library are capable of producing only one sample at a time. If repeatability is to be demonstrated, two or more separate depositions must be done.

The second method for producing combinatorial libraries is called the composition-spread method. This is the method used by the pioneers of combinatorial materials science, Hanak and Kennedy [65, 66]. There are several variations of this technique, but most consist of mixing the flux from several vapour sources in order to produce a film with composition varying with position. These methods generally produce continuous films across the substrate as opposed to individual isolated pixels as is common in the fractional masking technique. Two of the most common ways to accomplish this are illustrated in Figure 2.7. In the off-axis co-deposition technique, vapour sources are arranged in such a way that there will be a large area of overlap in their deposition profiles. This method has been used in many different forms. Hanak started with a single, multi-component target to produce a binary film [66]. The method shown in the figure employs two targets to produce a binary film in much the same manner as

Hanak's. Kennedy et al. [65] produced isothermal ternary phase diagrams using three evaporation sources located at the vertices of a triangular substrate. Van Dover et al. [74] used up to four targets on the corners of a square to produce large portions of quaternary phase diagrams. These methods all share the advantages of being simple to implement with no moving parts or precision motors necessary to drive shutters. Also, the elements in the films are intimately mixed as deposited so an anneal step may not be required. However, the stoichiometry variation in the films produced is non-linear and the composition can vary very quickly over a short distance on the substrate.

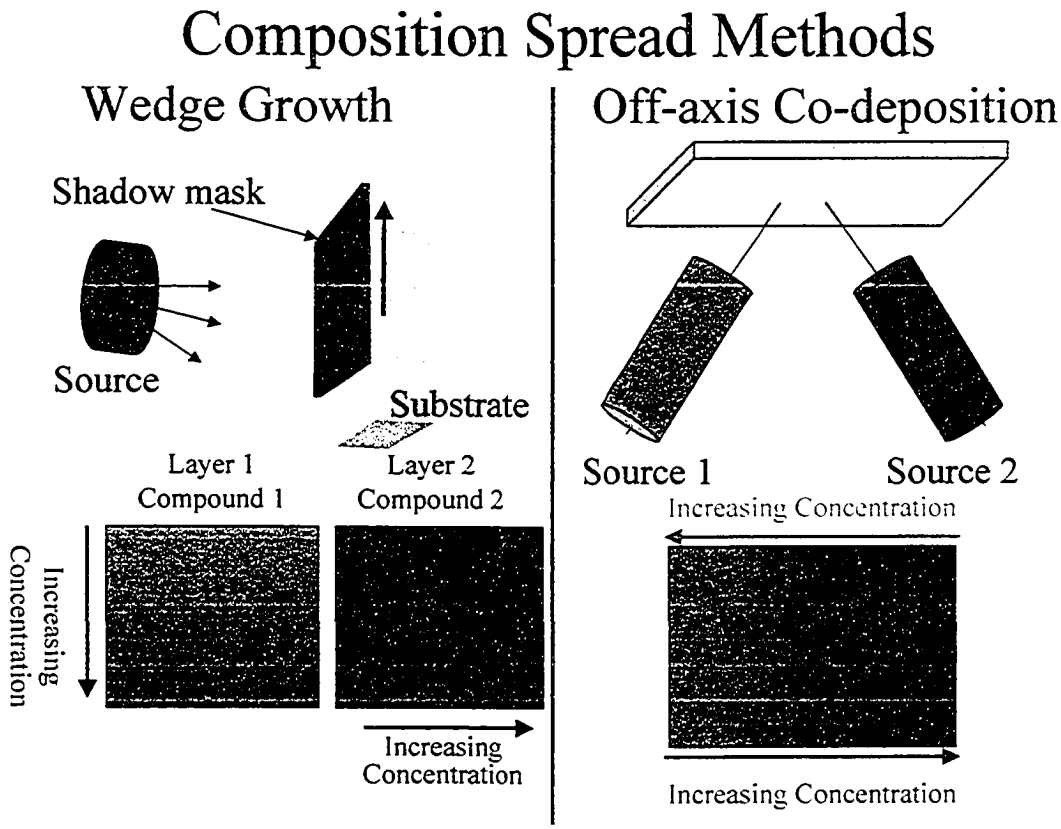

Figure 2.7. Illustrations of two examples of the composition spread method of combinatorial library deposition.

Xiang et al. [75, 76] developed a method, referred to as the wedge growth method in Figure 2.7, in which the composition can be varied linearly with position. In this method, a target is energized and a shutter is moved slowly across the substrate. In this way, a wedge of material is deposited on the substrate that varies linearly in thickness from one side to the other. The substrate is then rotated to prepare for a wedge of another material. The substrate can be rotated by 90° in order to produce a binary film or by 120° in order to produce a ternary. This method produces gradients of composition and thickness. The process can be repeated many times in order to build very complex stoichiometries. This method suffers from the same drawbacks as the fractal masking method in that the libraries must be annealed to cause inter-diffusion of elements to obtain homogeneous phases.

Other researchers have developed methods similar to that of Xiang in order to produce ternary phase diagrams [77]. However, these methods tend to rely on complicated precision masking schemes with computer-controlled motors in the vacuum chamber. While these methods are very elegant and sophisticated, they are also quite complex and expensive to implement. Also, they usually do not overcome the problem of needing to anneal the libraries produced and they also only produce one library at a time. What is needed is a method to produce binary and ternary libraries with linear composition gradients that can produce multiple large libraries at once. Such a method was developed and will be described in the next chapter.

Chapter 3. Film Deposition

3.1. Physical Vapour Deposition

Physical vapour deposition (PVD) is the usual way that combinatorial films are deposited, either for composition spread or fractional masking techniques. It is a collective term that encompasses a broad range of methods all designed to accomplish the common task of depositing a thin solid film on a chosen substrate. With these techniques, atoms are ejected from a target material in vacuum or low-pressure plasma and then adhere to the substrate, forming a film. The atoms can be ejected by evaporation or by bombardment of energetic particles or photons. In evaporation, the atoms are ejected by vaporization due to heating of the target. With techniques using bombardment of particles or photons the target atoms are ejected by momentum transfer.

Sputtering is a very robust form of PVD. With sputtering, a film of nearly any material can be deposited under a wide range of conditions onto nearly any substrate. The target material can be just about any solid material including insulators and materials with very high melting points. The characteristics of the deposited films can also be tuned by adjusting different sputtering characteristics such as the energy of the bombarding particles, pressure of the process gas and the geometry of the system.

3.2. Sputtering

Sputtering is a form of PVD that uses bombardment of energetic ions to eject atoms from a target material in order to deposit a film on a substrate. A simplified schematic of a typical sputtering chamber is shown in Figure 3.1. The

target is kept at a high negative potential by the power supply, forming the cathode of the system. The substrate and the rest of the chamber are kept at ground and are therefore the positive electrode or anode for the system. The substrate can be biased either positively or negatively, heated, cooled and/or rotated as desired. The bombarding ions come from a plasma, which is usually formed from an inert gas (typically Ar). Alternatively, a more reactive gas such as N_2 or O_2 may be used if this element is desired in the film.

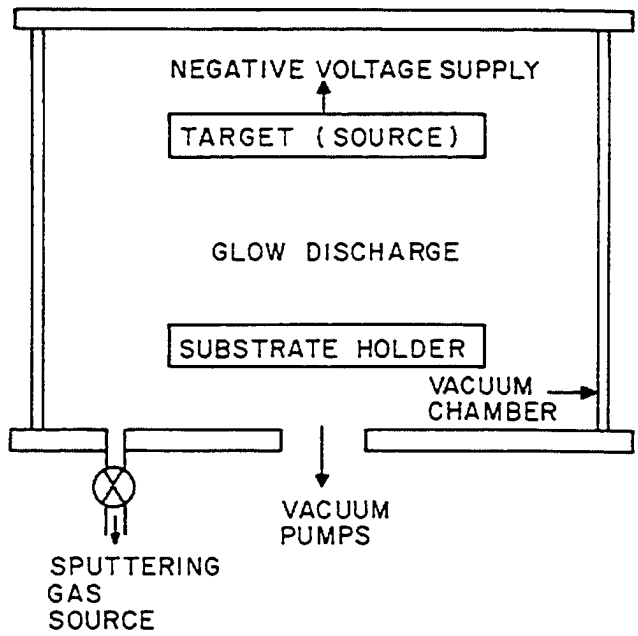

Figure 3.1. A basic schematic of a sputtering chamber (from reference 79).

Within the plasma, positive ions (Ar^+) are accelerated towards the target because of the electric field established when the target is energized. The energetic ions from the plasma strike the target and eject atoms from it. Secondary electrons can also be ejected from the target, which can then strike Ar atoms and create more ions, sustaining the plasma.

Most sputtering systems incorporate magnets in the sputtering source. The purpose of the magnets is to help increase sputtering rates by enhancing the plasma near the sputtering target. The secondary electrons created by collisions of energetic ions with the target will only create new ions during their travel from the target to the anode. The magnetic fields set up near the targets cause the electrons to follow a spiral path, thus increasing their travel time and the likelihood that they will collide with gas atoms and create more ions. Sputter sources equipped with magnets are generally referred to as magnetrons. A diagram is shown in Figure 3.2.

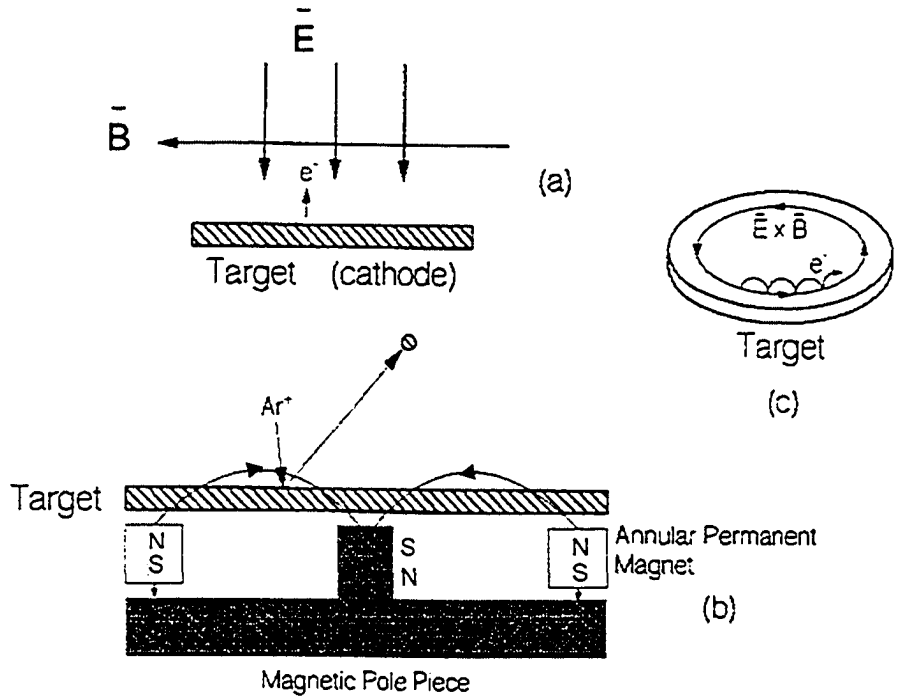

Figure 3.2. The magnetron: (a) in the planar magnetron sputtering arrangement, whether DC or RF, a static magnetic filed is created parallel to the surface of the sputtering target to retain secondary electrons in that region; (b) an annular design, such as the one shown here schematically in exploded cross section, is often employed; (c) the electrons drift in the **E**×**B** direction, actually executing a cycloidal path (adapted from reference 78).

Probably the most critical parameter in the sputtering process is what is known as the sputtering yield. This is the number of target atoms sputtered per bombarding ion. This determines the rate at which the target will be sputtered and also how fast the deposited film grows. It is very important to be aware of this when trying to mix the deposition from multiple targets to form a film with a specific composition or range of compositions. The sputtering yield depends on the incident particle energy and species, the incident angle and the surface binding energy of the target. Much like in the photoelectric effect, there is a threshold energy below which the incident ion cannot eject atoms from the target, regardless of flux. This is related to the target surface binding energy and is typically ~ 20 – 40 eV. Above this threshold energy, yield increases with energy of the incoming ions. The yield reaches a maximum at high energies, usually in excess of 10 keV. At these energies, the incident ions penetrate more deeply into the target and lose energy by stripping away electrons instead of knocking atoms from their lattice sites. Table 3.1 presents a brief summary of sputtering yields for selected elements in various process gases.

Table 3.1. Sputtering Yields by 500 eV Ions.

Ion and amu	Be (9)	Al (27)	Si (28)	Cu (64)	Ag (106)	W (184)	Au (197)
He^+ (4)	0.24	0.16	0.13	0.24	0.2	0.01	0.07
Ne^+ (20)	0.42	0.73	0.48	1.8	1.7	0.28	1.08
Ar^+ (40)	0.51	1.05	0.50	2.35	2.4.-3.1	0.57	2.4
Kr^+ (84)	0.48	0.96	0.50	2.35	3.1	0.9	3.06
Xe^+ (131)	0.35	0.82	0.42	2.05	3.3	1.0	3.01

From reference [80].

The momentum transfer process involved in sputtering can be classified into three categories based on energy. These classes are 1) low energy, single

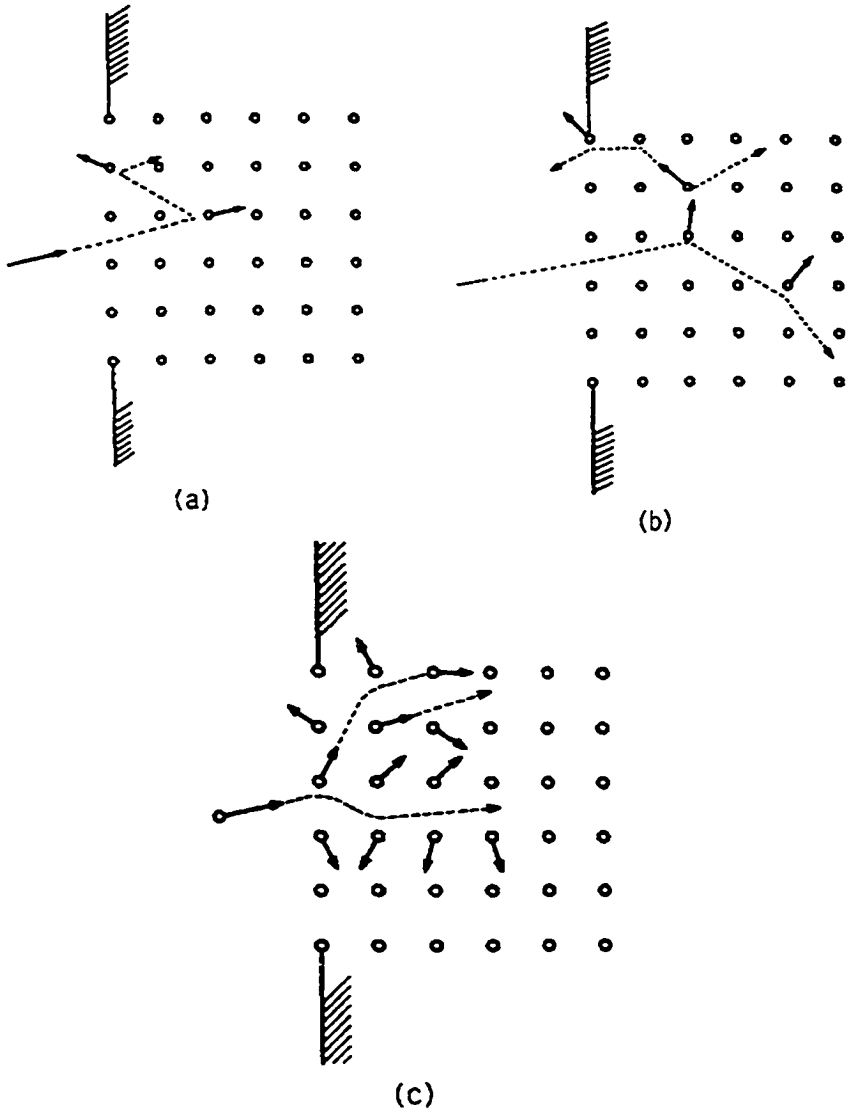

Figure 3.3. Sputtering has three energy regimes: (a) the low-energy, single knockon regime; (b) the linear cascade regime, where "a recoil cascade occurs but collisions between moving atoms are infrequent"; and (c) the spike regime, a high-energy regime where the majority of atoms within the spike volume are in motion (from reference 78).

knock-on, 2) linear cascade and 3) spike [78]. These are illustrated in Figure 3.3. In the low energy regime, the incident ion will generally interact with one stationary target atom. The linear cascade is the common mode for sputtering. In this mode, the incident particle may interact with several target atoms although most collisions still involve one moving and one stationary atom. In this regime,

sputtering yield is proportional to the energy density incident at the surface of the target. In the spike, or non-linear, mode most of the atoms in the cascade region are in motion. In this case, the atoms are similar to a vapour and they are thermally emitted. Yield is no longer linearly related to energy density and can increase very rapidly for a small increase in energy. There is a critical yield to distinguish between the linear and spike regimes, although reported values vary widely from 1 to 20 [78].

3.3. DC and RF Sputtering

3.3.1. DC Sputtering

For sputtering metallic materials (conductors and semi-conductors), high voltage DC power supplies are used. The target, acting as the cathode, is kept at a constant negative potential with respect to the substrate and chamber walls.

Figure 3.4 is a schematic of the applied voltage as a function of current for a typical DC discharge. The relation is divided into six different regions based on the functional form of the voltage/current curve. In the Ohmic Conduction region, there is a small free electron density and very low currents are found. At higher voltages, but still in the low current range, the current reaches a saturation limit and becomes constant. In this region, the applied field removes free electrons as fast as random processes such as photoemission from stray radiation create them. If the applied potential is increased far enough, impact ionization of neutrals begins. This creates additional free electrons and also some ions. This region is known as Townsend Discharge. At still higher potentials, the ions begin to have enough energy to create charged particles by knocking free electrons

from the cathode material. These secondary electrons now create a much larger number of ions. This point is called Breakdown and is when the plasma becomes self-sustaining. Because of the higher number of free electrons, the voltage does not need to be nearly as high to maintain the same current.

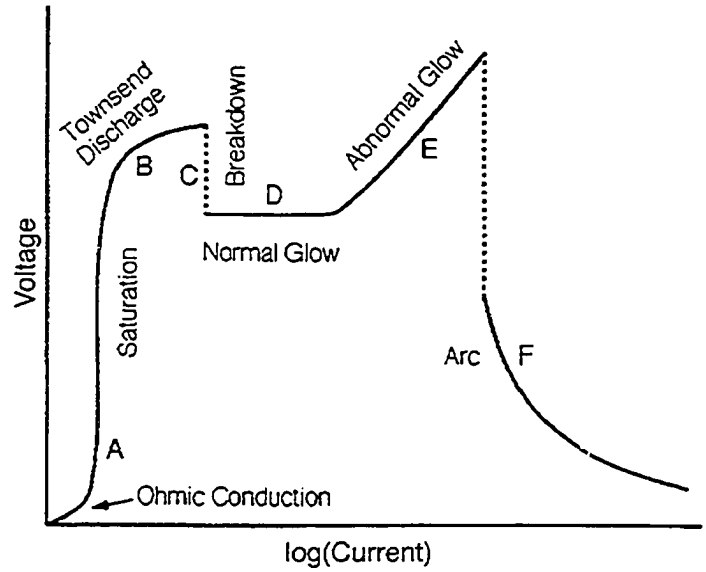

Figure 3.4. Schematic of applied Voltage *versus* current for a DC discharge (from reference 78).

After Breakdown occurs, the Normal Glow region occurs. Here, the potential is nearly constant over a range of currents. Secondary electron production is localized at corners and irregularities of the cathode where the electric field is greatest. The current increases as ion bombardment spreads over the surface of the entire cathode at nearly constant potential. When the entire cathode surface is used, the current can only increase if the potential is also increased. This is called the Abnormal Glow region and is where most sputtering processes actually take place. The current/voltage relation is:

$$I = kV^n$$

where k is a constant and n is a measure of the efficiency of electron trapping near the target. The potential is typically several hundred volts, although it can be in excess of 1000 V. Typical current densities are from 1 to 100 mA/cm^2 with voltages less than 800 V. Increasing the power from the power supply will produce increased voltage and current density. Above this current density range, the target can heat and cause thermal emission of electrons. This leads to an avalanche of ion production in the plasma and an arc discharge occurs.

3.3.2. RF Sputtering

In order to sputter insulating materials an alternating current (AC) power source is used. A diagram of a typical apparatus is shown in Figure 3.5. Typically, a radio frequency of 13.56 MHz is used for RF sputtering. This is an FCC-designated frequency for plasma discharges.

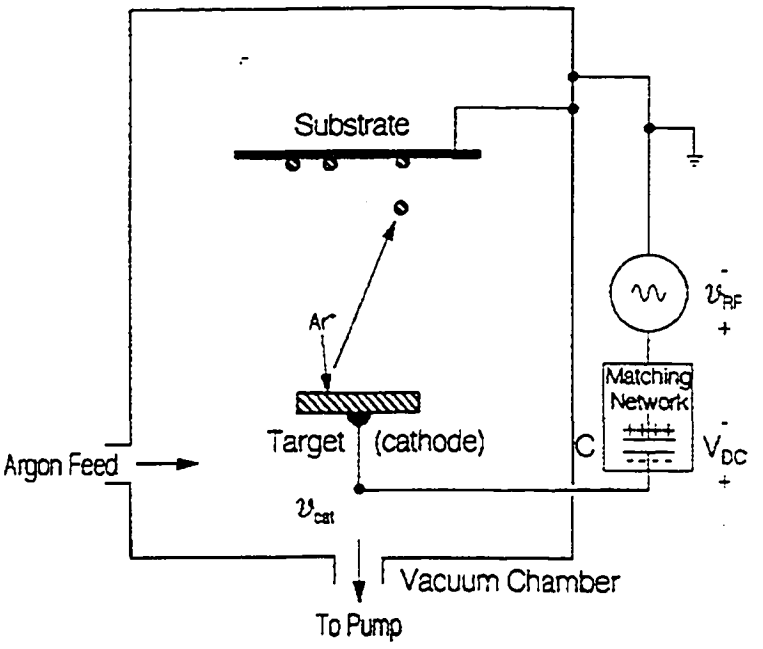

Figure 3.5. A schematic representation of an RF sputtering system. The set-up is similar to that of DC sputtering, however a series capacitor leads to a negative self-bias of the target, and an impedance matching network optimizes the power transfer (from reference 78).

The RF power supply is capacitively coupled to the target by a series capacitor. This capacitor allows the formation of a negative bias for the target. Figure 3.6 shows how the self-bias is established through the difference in mobility of Ar^+ and e^-. During the positive half of a cycle, an initially high electron current flows to the capacitor. On the ensuing negative half of the cycle, the ion current is much smaller due to the lower mobility of the Ar^+ ions in the plasma. Over a few cycles, the target will build up a negative bias. As illustrated in the figure, this leads to zero net current through the capacitor over an entire cycle. At high frequencies, the Ar^+ ions cannot keep up with the RF variations and so will respond only to the negative DC bias of the target. This situation is then very much like DC sputtering as the ions in the plasma are continuously accelerated towards the target.

To optimize power transfer, the RF power source needs to be impedance matched to the plasma. Power supplies are generally made to transfer power to a 50 Ω load. However, the plasma's impedance, which is capacitive, tends to be much higher than this. In order to maximize power transfer, a matching network consisting of a tuneable LC circuit is used to transform the plasma impedance to 50 Ω. The tuning can be done manually or can be computer controlled. The impedance of the plasma will depend on factors such as the pressure in the chamber and therefore the matching network must be able to quickly respond to any changes in order to provide the most efficient power transfer possible.

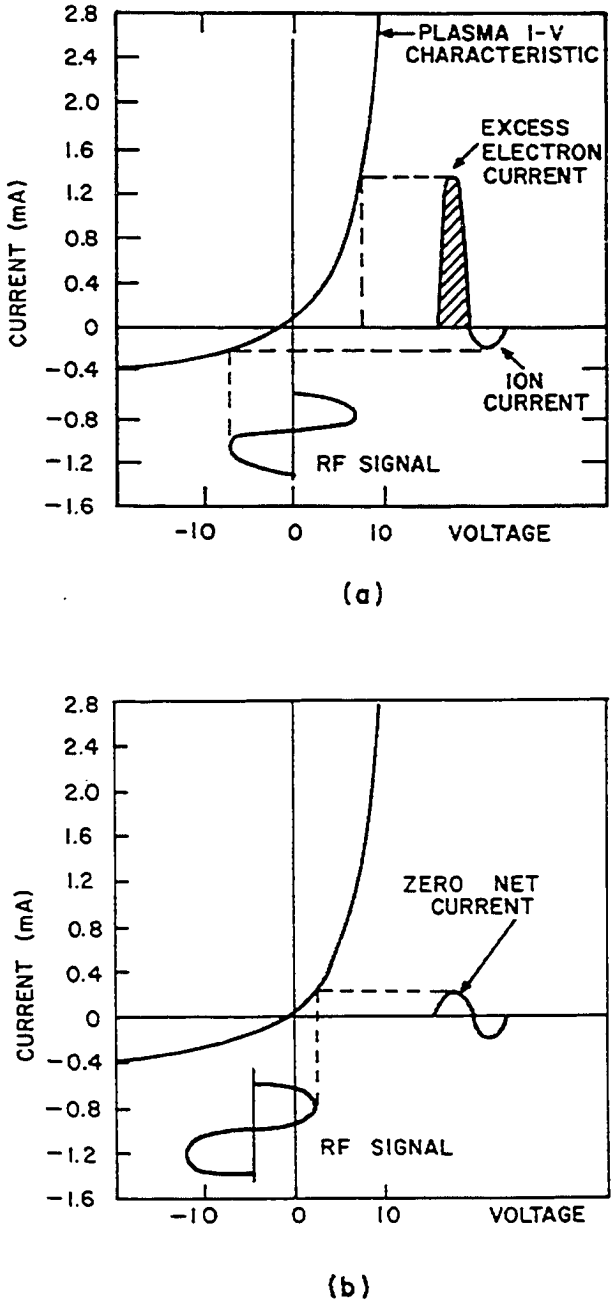

Figure 3.6. The formation of DC self-bias in a capacitively coupled RF discharge (a) During the first cycle, before a DC bias is developed, there is an excess electron current. (b) After a first few cycles, a DC bias is formed so the sum of electron and ion currents would be zero over a full cycle (from reference 79).

3.4. Plasma Characteristics

A plasma is a gas containing mainly neutral atoms along with some ionized atoms and free electrons. In a weakly ionized plasma (~1 mTorr) there

are approximately 10^4 to 10^7 neutral atoms per ion. New ions are created by interactions between neutral atoms and energetic electrons. Besides creating new ions, interactions of neutrals with energetic electrons can lead to the excitation of atoms. The atom then decays to its ground state, emitting a photon. This can cause the plasma to glow, giving rise to the term glow discharge.

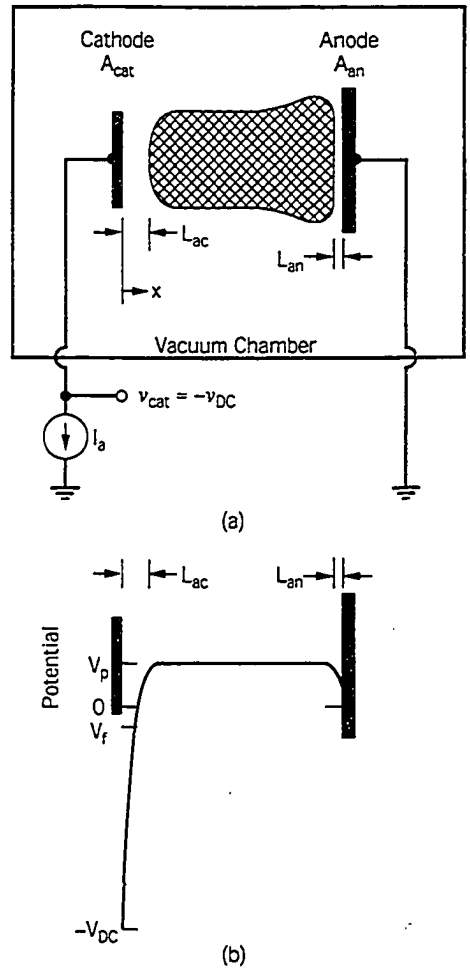

Figure 3.7. Schematic diagram of: (a) DC sputtering discharge, and (b) the potential profile (from reference 78).

Figure 3.7 shows a schematic of a DC sputtering discharge. Also shown is the potential as a function of position in the plasma. At the cathode, the mobile

electrons are quickly swept away from the negative applied potential. The less mobile positive ions are more slowly attracted towards the cathode. This leaves a small region near the cathode with a charge density not equal to zero. This is called the cathode sheath and is an area with a high electric field. The remainder of the plasma, with the exception of a smaller anode sheath, is very close to being equipotential. Because of the lower mobility of the positive ions, the body of the plasma is left at a slightly positive potential compared to the ground anode. This potential is usually quite low, approximately 10 V.

From Figure 3.7b, it is evident that ions will bombard the substrate (anode) as well as the target (cathode). However, the relatively small accelerating voltage means that the ions will have very low energies and very little (if any) sputtering will occur.

The maximum energy of particles bombarding the cathode will be determined by the sum of the applied potential at the cathode plus the potential of the plasma body. The maximum energy will be that of a charged particle accelerated across this potential. However, a process in the plasma can cause the energy of bombarding particles to be less than the maximum. The process is symmetric charge exchange and is illustrated in Figure 3.8. In this process, an energetic ion passing a neutral atom can take an electron from the neutral. This leaves an energetic neutral (with energy proportional to the amount of the sheath that has been crossed before charge exchange) travelling towards the cathode and a cold ion that can now be accelerated towards the cathode. There is little energy or momentum transfer involved with this process. It is evident that not all

of the bombarding particles are ions and they may have energies somewhat less than the maximum available. The sputtering yield is the same for ions and neutrals of the same species, so this does not affect the sputtering rate. However, yield is dependant on energy so this can influence the sputtering rate.

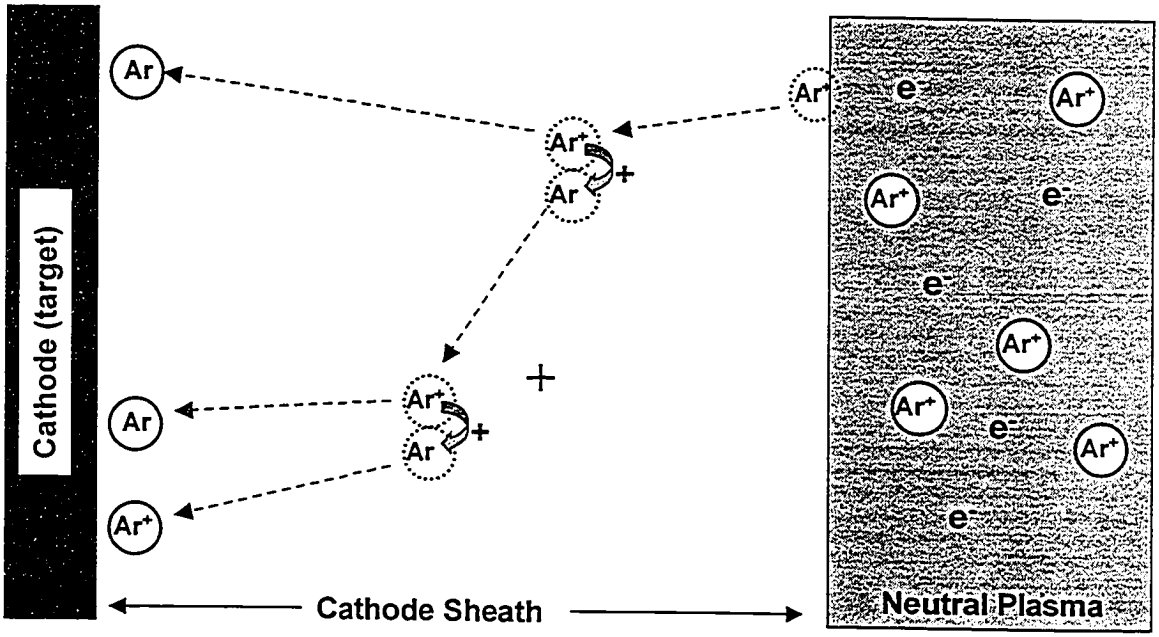

Figure 3.8. The process of symmetric charge exchange within the cathode sheath. When two charge exchange events occur, as shown here, a single ion entering the sheath is converted into two neutrals plus an ion, all of which strike the cathode (from reference 78).

3.5. Description of Equipment Used

The sputtering machine used is a Corona Vacuum Coaters model V-3T multi-target system. A picture of the machine and accompanying electronics is shown in Figure 3.9. The interior of the chamber is shown in Figure 3.10. The system is equipped with five magnetron guns and has three DC and two RF power supplies. The chamber is cylindrical and is approximately 80 cm in diameter and 30 cm deep. The substrate table is water-cooled and can be

rotated by a computer-controlled stepper motor. An external constant temperature water bath provides the cooling for the table.

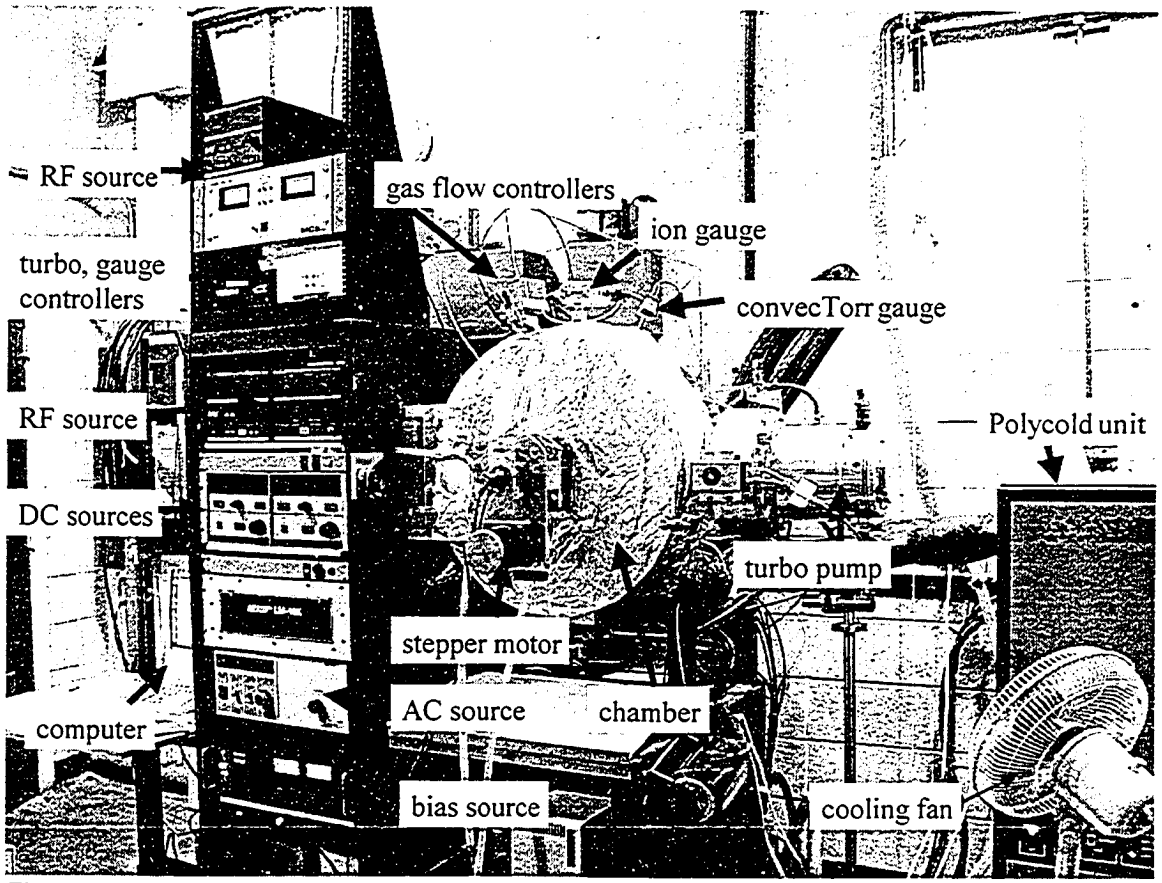

Figure 3.9. A general view of the Corona sputtering system used. Different parts are labelled on the figure (from reference 82).

The system is pumped with a Varian 500 L/s turbo pump backed by a mechanical roughing pump. It also has a R2000 series Polycold fast cycle water vapor cryopump to eliminate water vapor by condensing it on the cold coils inside the chamber. The chamber itself is wrapped with heating tape and covered in aluminum foil to enable baking of the chamber to minimize water vapour. Base pressures of approximately 1 x 10^{-7} Torr can be reached after approximately three to four hours of pumping. The lowest pressure achieved was ~4 x 10^{-8} Torr after two days of continuous pumping. Fore line and chamber pressures are

measured with Varian convector thermal conduction/convection gauges in the range of 1 mTorr to atmospheric pressure. There is also a Bayard-Alpert ionization gauge to measure pressures from ~1 x 10^{-8} to 1 x 10^{-4} Torr.

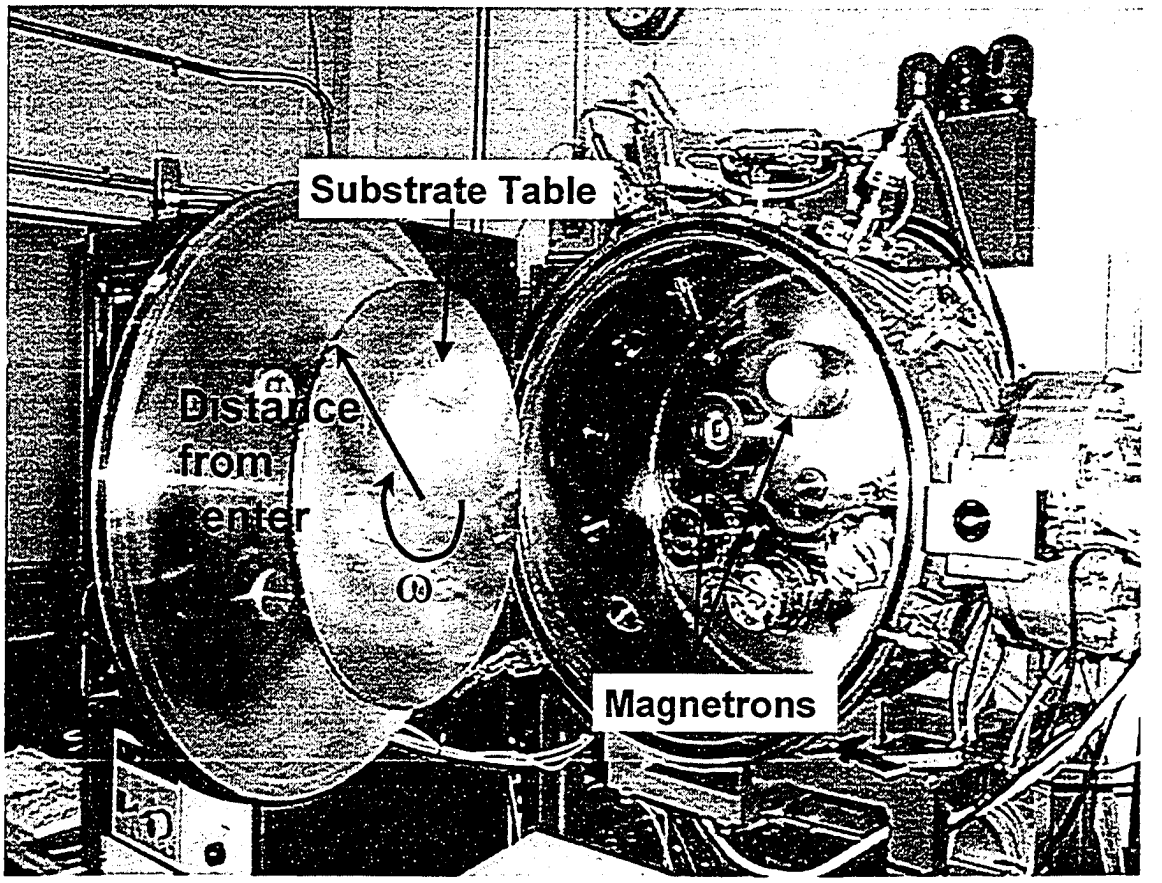

Figure 3.10. The interior of the sputtering chamber. The substrate table and magnetrons are indicated.

The sputtering targets are 5.0 cm in diameter, and the target to substrate distance is 5.0 cm. The magnetrons are placed at 60° increments on the flat back wall of the chamber. The centers of the targets are 13.3 cm from the cylindrical axis of the chamber. The rotating substrate table shares the same cylindrical axis. The magnetrons use rare-earth Nd-Fe-B magnets from Tridus International Inc. (Rancho Dominguez, CA, USA). These magnets have remnant induction (B_r) of 1.26 - 1.32 Tesla, which yields field strength of about 600 Gauss

at the surface of the targets. More information on the magnets used can be found in [104]. The magnetrons are water-cooled to dissipate heat generated by sputtering. The maximum operating temperature of the magnets is only about 80 °C (the Curie point is about 310 °C), so demagnetization is a risk if the magnets are not adequately cooled. The entire magnetron assembly, which is insulated from the chamber wall by an insulating disk, is kept at the applied potential during sputtering. A ground shield cap that exposes only the target to the plasma protects the magnetron body. This prevents sputtering of the magnetron itself. Tunnels are also mounted on the magnetrons to localize deposition to the substrate table. These tunnels are 10 cm in diameter and allow less than 0.5 cm clearance between them and the substrate table. Four of the magnetrons are used for sputtering targets and the fifth is reserved for a specially designed plasma-cleaning electrode. This electrode is energized with a low power to create a low energy plasma near the substrate surface. This helps to clean the substrate in preparation for receiving the sputtered film.

The DC power supplies are Advanced Energy (AE) MDX-1K DC power sources. The RF supplies are AE RFX-600 RF power supplies with a frequency of 13.56 MHz. The RF supplies are equipped with computer controlled matching boxes to tune the input impedance of the plasma to optimize power transfer. Reflected power is generally less than 20 %. The DC supplies can supply up to 1000 W and the RF up to 600 W and are remotely controlled. Powers are generally kept below 200 W. There is also an AE PE-1000 power supply (40

kHz) that can power two targets simultaneously and a Sorenson DC power supply for applying a DC bias to the substrate table.

Gas flow is computer controlled through two MKS type M100B Mass-Flo controllers. One of these is used for the process gas, which is five nines purity Argon. Oxygen and nitrogen can also flow through the other controller. Oxygen is often used in the plasma cleaning process. Gas flow is measured in standard cubic centimeters per minute (SCCM). Typical pressures during sputtering are from ~1.5 – 5 mTorr, requiring 2 – 5 SCCM of Argon.

Computer control of the system components is achieved with Advantech ADAM 4000 data acquisition modules. These modules operate in RS-845 protocol and use EEPROM to store configuration and calibration information. The different controllers used are ADAM-4021 for analog output, ADAM-4017 for analog input, ADAM-4060 for relay output and ADAM-4520 for RS-232/RS-485 conversion allowing the system devices to communicate with a computer. The stepper motor and pressure gauges are interfaced directly via RS-232 ports. The control software is written in Delphi 2.0 and is updated and maintained by Arman Bonakdarpour.

3.6. Modifications to Produce Combinatorial Films

The sputtering machine used is a very open ended and versatile piece of equipment that can be easily modified and upgraded. It was our goal to build a system for composition spread studies of amorphous binary, ternary, and quaternary metal systems. We wanted to ensure intimate mixing of the elements as sputtered, because any heating step to cause inter-diffusion of thick layers

would crystallize the amorphous phases. Film thicknesses of up to 5 μm were desired. Large substrates (75 mm X 75 mm) to maximize the number of patterned electrodes with connecting leads that could ultimately be fabricated for combinatorial electrochemistry were needed. The as-purchased machine would allow this, but we also wanted to ensure linear and orthogonal composition variations so that stoichiometries could be determined simply from the position on the substrate. In order to achieve this goal, some modifications had to be made to the machine.

3.6.1. Calibrations

In order to properly control the flux from the sputtering target, it is first necessary to have knowledge of how much flux there actually is. Also, in order to achieve desired stoichiometries, one must know the relative sputtering rates of the different targets to be used.

To calibrate a sputtering target, the first step is to pre-weigh a series of 1.3 cm diameter Cu or Al disks. These disks are then loaded on the substrate table in sets of five to seven in radial lines with the center of each line located the same distance from the center of the machine as the sputtering target. The target to be calibrated is then activated for a certain amount of time at a certain pressure and power with one set of disks directly under it. After the deposition is complete, the substrate table is rotated to bring the next set of disks in line with the target. The deposition can then be repeated with different powers or pressures as desired. Up to six sets of conditions can be tested with one sputtering run using this method. If the substrate table is to be rotated during the

calibration, only one set of conditions can be tested, but more disks are used to give a better description of the deposition rate as function of position on the substrate table.

Table 3.2. Some sample data from a Ag calibration.

2 SCCM Ar, 15W			
Film Mass (mg)	**Watt*min**	**mol/kWmin (on a 1.3 cm disk)**	**Distance from machine center (cm)**
0.521	250	1.933E-05	16.2
0.689	250	2.555E-05	14.7
0.718	250	2.661E-05	13.3
0.618	250	2.290E-05	11.8
0.439	250	1.629E-05	10.3
2 SCCM Ar, 50W			
Film Mass (mg)	**Watt*min**	**mol/kWmin (on a 1.3 cm disk)**	**Distance from machine center (cm)**
1.220	500	2.262E-05	16.3
1.661	500	3.080E-05	14.8
1.771	500	3.284E-05	13.2
1.472	500	2.730E-05	11.8
1.063	500	1.972E-05	10.3

Table 3.2 shows some data for the calibration of Ag. The units for deposition shown here are mol / kW*min on a 1.3 cm diameter Cu disk. Other units that could be used include mass / disk, mass / area, thickness / time, etc. The units of number / energy are the best for setting powers of different targets to give a desired stoichiometry of the deposited film. Figure 3.11 shows graphs of the amount of Ag deposited *versus* position for six sets of powers and Ar flow rates (higher flow = higher pressure). It is evident from the figure that the sputtering conditions can have a large impact on the deposition rate. It is clear that more material is deposited with the same total energy as the power used is

increased. Also, the sputtering rate at constant power decreases as the pressure is increased. Figure 3.12 shows the deposition rate as a function of power. At low powers, the rate per unit energy increases very rapidly with power, but begins to level off by about 20 W. At higher powers the deposition rate may even become constant with constant energy, with no dependence on the power.

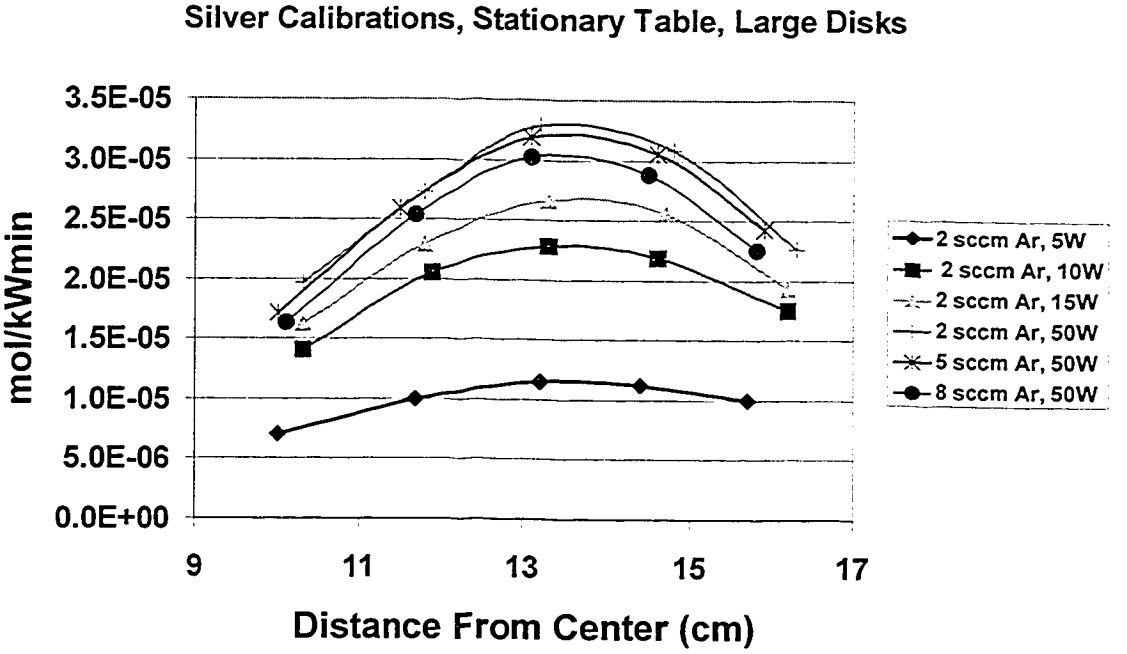

Figure 3.11. Amount deposited on a 1.3 cm disk *versus* position on the substrate table for Ag for different choices of power and Ar flow rate.

The sputtering rate can also be quite different from one element to the next. Figure 3.13 shows calibrations for Ag and Mn done at the same pressure and power. It is clear that Ag sputters much more quickly than Mn. The two curves do, however, have roughly the same shape, with the deposition falling to approximately 70 % of maximum at the same distance from the center of the deposition. This will help in controlling the flux from the targets, as the same procedures should provide similar results from one element to another.

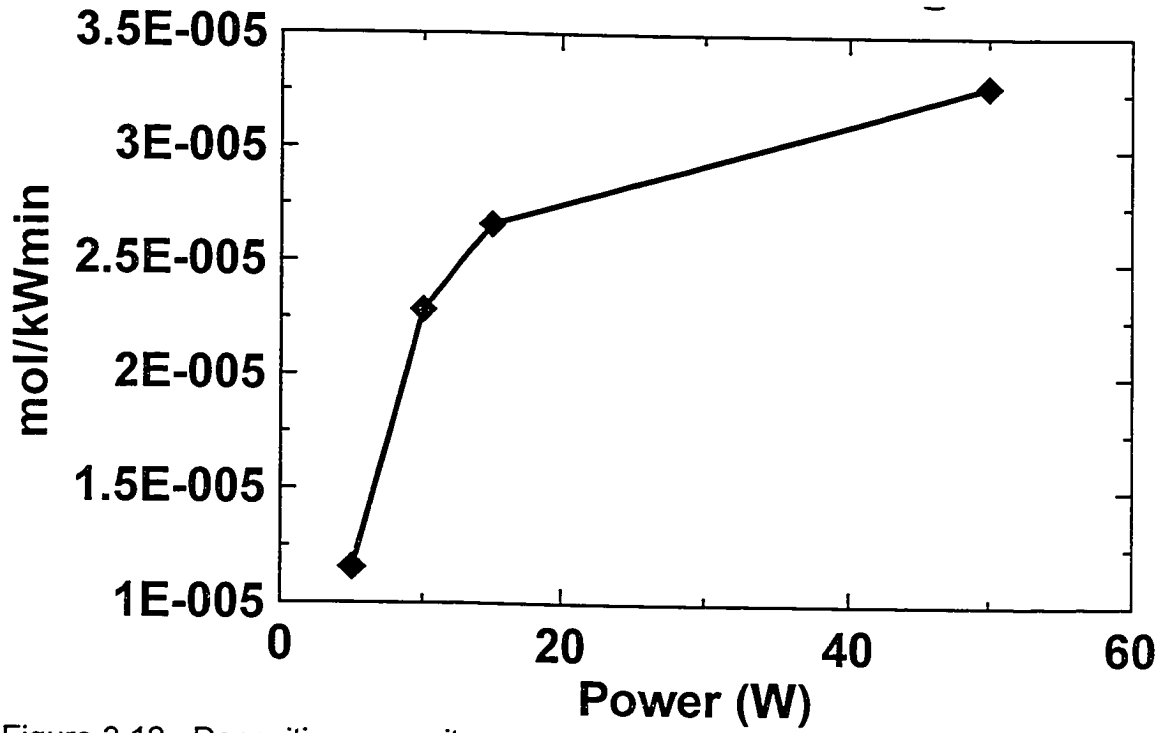

Figure 3.12. Deposition per unit energy *versus* power for Ag at 2 SCCM Ar flow.

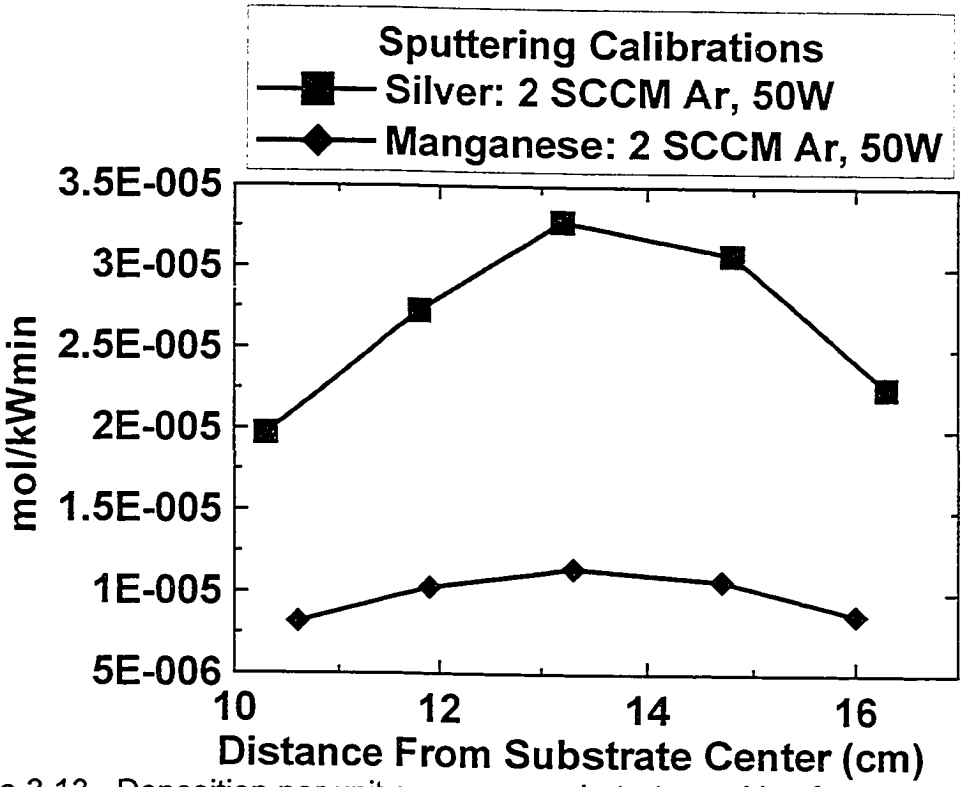

Figure 3.13. Deposition per unit energy *vs.* substrate position for Ag and Mn.

3.6.2. Modifications to Produce Binary Films

If a sputtering target is energized over a rotating substrate table, the resulting deposit will be an annular ring that is thick in the center (directly beneath the center of the target) and decreases in thickness in a non-linear way towards the edges. To create binary films with linear stoichiometry variations, this annular ring must be made in a way that gives it either a constant or linearly varying thickness from one edge to the other.

In order to produce linear stoichiometry variations, one needs to be able to control the flux from the sputtering target. In order to do this, masks have been designed to fit on the tunnels of the sputtering targets. The masks have slots in cut in them that allow only a portion of the flux from the target to pass through and be deposited on the substrate. To design the masks, the calibration data for a target over a stationary substrate is used. The data is fit to a Gaussian function to determine the flux as a function of position over the deposited film. This function is then used to determine the width of the mask slot by combining it with the desired deposition profile and the fact that the flux at a given distance from the center of the machine, r, is being spread over a circle of circumference $2\pi r$ when the substrate table is rotated.

Figure 3.14 shows a picture of the interior of the sputtering machine with two masks in place. One mask is designed to give a constant thickness across the deposition ring and is mounted over a Si target. The other is designed to give a deposit that is thin at the outer edge of the ring and increases linearly in thickness to the inside of the ring. The first mask is referred to as a 'constant'

mask and the second a 'linear-in' mask. 'Linear-out' masks have also been produced. Figure 3.15 shows the composition of the film produced as a function of distance from the center of the machine. As can be seen the desired linear stoichiometry variation has been achieved.

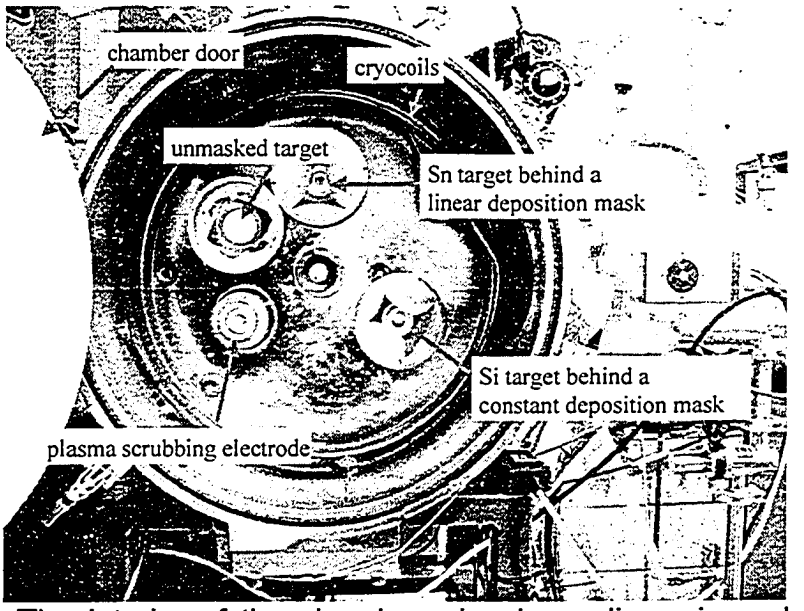

Figure 3.14. The interior of the chamber, showing a linear-in and a constant mask in place on tunnels. The plasma-cleaning electrode is also shown.

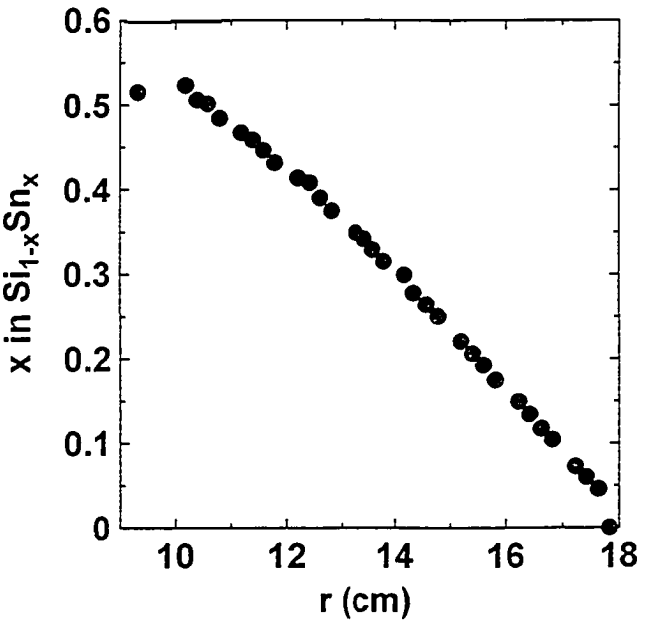

Figure 3.15. Composition *versus* position for the film produced using the masks shown in Figure 3.14.

3.6.3. Modifications to Produce Ternary Films

With the masks described above and a flat, rotating substrate table, stoichiometry variation can only be achieved in one direction. While this is sufficient to produce binary films, we also want to produce ternary films. To produce linear and orthogonal variations of two elements or compounds, the substrate table had to be modified. A table has been constructed that carries five sub-tables. The sub-tables can themselves be rotated by 90° and then returned to their original orientation during the rotation of the main table. The same 'constant', 'linear-in' and 'linear-out' masks are used over the target tunnels. A picture of the modified table is shown in Figure 3.16. Figure 3.17 shows a schematic of the modified substrate table and its operation. The figure shows the substrate table as viewed from the back of the sputtering chamber. Each of the Figures, 3.17a), 3.17b), etc. represents a "snapshot" of **only one** of the sub-tables at a moment of time. We illustrate the operation of the system with a description of the production of $SiSn_xAl_y$ ($0 < x,y < 1$).

Figure 3.17a shows the sub-table positioned opposite the Si target that is covered with the 'constant' mask opening. The arrow on the sub-table is a guide to mark its orientation. As the sub-table passes beneath the Si target a layer of Si that is uniform in thickness is deposited over the 75 mm x 75 mm square sub-table. The main table always rotates continuously and at the moment in time corresponding to Figure 3.17b the sub-table is positioned opposite the Sn target which is covered with a 'linear-out' mask opening. This ensures that a layer of Sn that varies linearly in thickness in the radial direction (**parallel to the arrow**)

is deposited on the 75 mm x 75 mm sub-table. The main table rotates continuously and at the time corresponding to Figure 3.17c, an actuator arm connected to the sub-table strikes a post that is fixed to the chamber. This causes the rotation of the sub-table on its bearing as shown in Figures 3.17c, d and e, until it is in a position where the arrow on the sub-table is pointing tangentially to the edge of the main table (Figure 3.17e).

Figure 3.16. The two-axis combinatorial substrate table with five independently rotating sub-tables.

The main table rotates continuously and at the time corresponding to Figure 3.17f it is located opposite the Al target which is covered with the 'linear-in' mask opening. This ensures that a layer of Al that varies linearly in thickness

in **a direction perpendicular to the arrow** is deposited on the 75 mm x 75 mm sub-table.

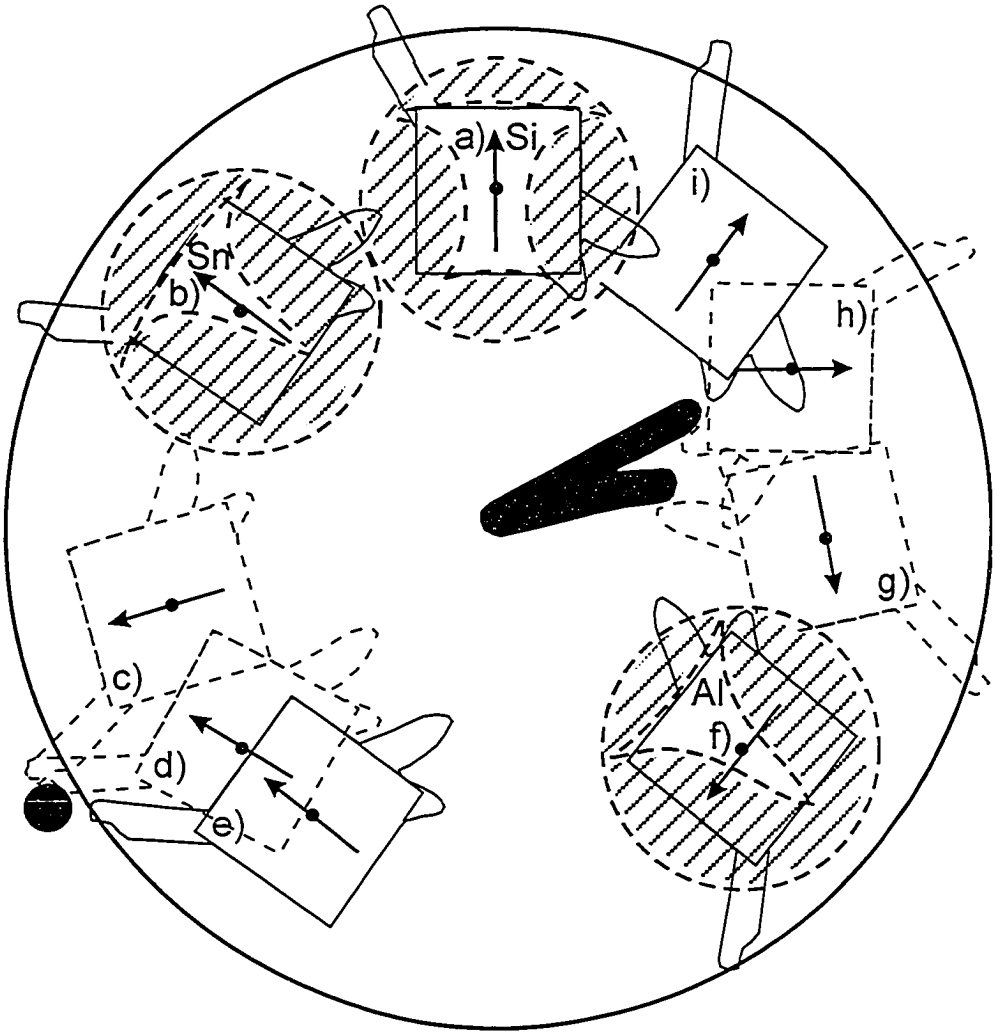

Figure 3.17. A schematic diagram of the rotating table showing "snapshots" of one sub-table at various instants in time. The sequence a - i is described in the text.

The main table rotates continuously and at the time corresponding to Figure 3.17g, a second actuator arm strikes a fixed pair of "fingers" that are rigidly attached to the chamber. This causes the rotation of the sub-table on its bearing as shown in Figures 3.17g, h and i back to its original orientation with respect to the main table, with the arrow pointing in a radial direction. The sub-

table then returns to the position depicted in Figure 3.17a and the process repeats. Typically, the main table is rotated at about 15 revolutions per minute, so each of the five sub-tables passes under each target 15 times per minute. At this rate, the deposition per revolution is on order of a monolayer, and intimate mixing of the elements is achieved. To produce a multi-layered film, the table can be slowed to allow thicker depositions per revolution, or the magnetrons can be programmed to turn off and on at regular intervals to achieve the layer thickness desired.

Figure 3.18 shows the variation in the Al:Si and Sn:Si ratios for a film produced with the method just described. The Si content is constant everywhere on the film. The Al and Sn content do vary linearly and the gradients are orthogonal to each other, as desired.

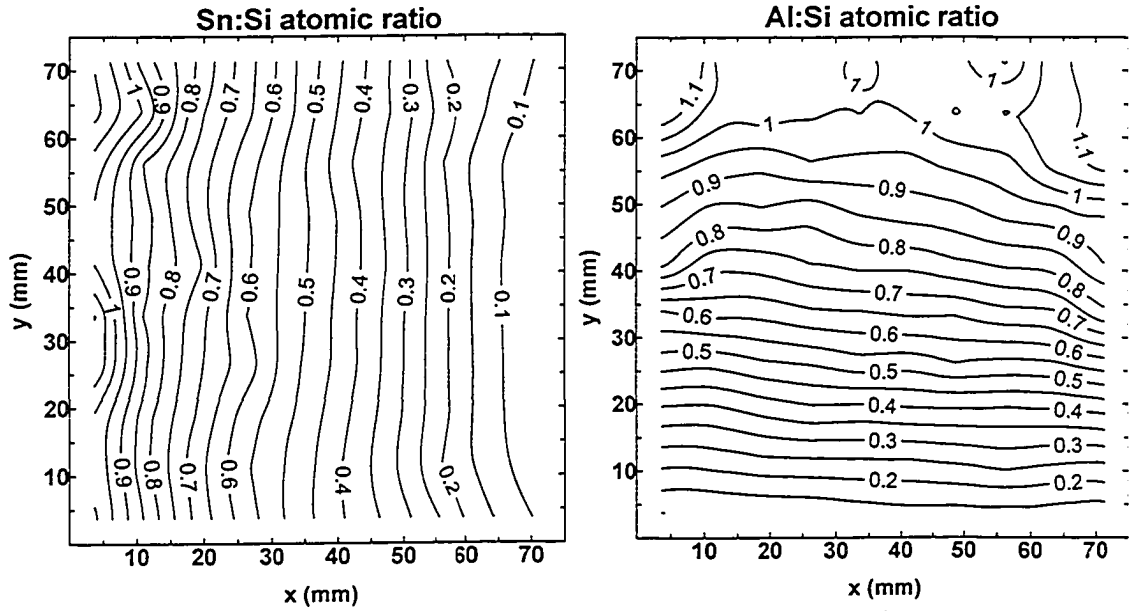

Figure 3.18. Contour maps of the Sn:Si and Al:Si atomic ratios *versus* position on the 75 mm x 75 mm $SiSn_xAl_y$ film. The film was made using the apparatus depicted in Figure 3.17.

Chapter 4. Film Characterization

A film produced using the combinatorial sputtering methods described in the previous chapter must be characterized and tested for its electrochemical behaviour. One sputtering run will typically produce five nominally identical films that are used to discover the composition and structure as a function of position and also to make electrochemical cells. Figure 4.1 is a schematic of the combinatorial substrate table loaded with the substrates typically used in a sputtering run.

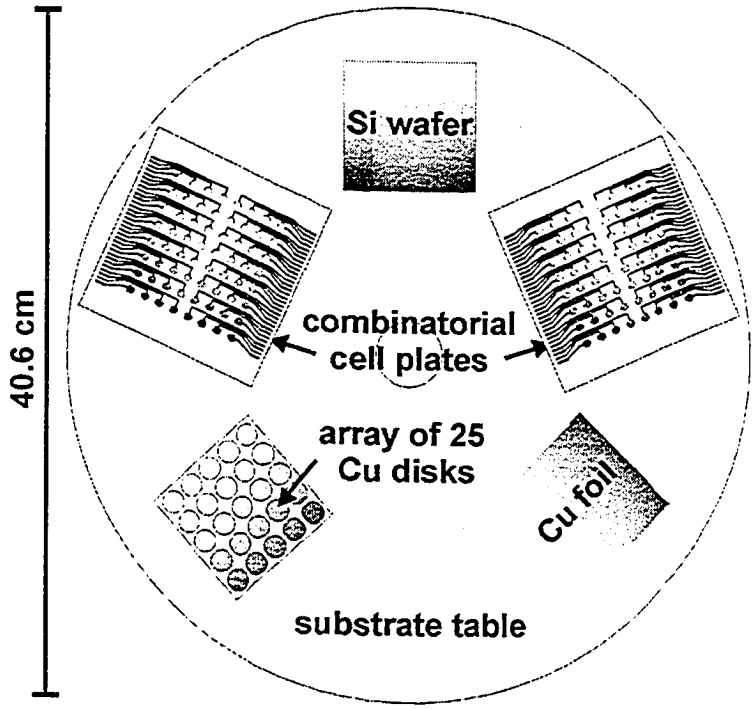

Figure 4.1. A typical arrangement of substrates for a combinatorial sputtering run. The purpose of each substrate is described in the text.

The film sputtered on a Si wafer is used for X-ray diffraction studies to determine the film's structure. The Cu foil is used in electron microprobe experiments to determine the composition of the film as a function of position. The array of 25 Cu disks is weighed both before and after sputtering to determine

the mass deposited per unit area as a function of position. Finally, the combinatorial cell plates are used in electrochemical cells to determine the behaviour of the film when it is alloyed with lithium electrochemically.

4.1. X-Ray Diffraction

4.1.1. Basics of X-Ray Diffraction

X-ray diffraction (XRD) is one of the most common ways to characterize the structure of a crystalline material. In a crystalline material, the atoms are arranged in a regularly repeated pattern forming sets of parallel planes. In an XRD experiment, an X-ray beam illuminates the sample. The incident beam strikes the sample, and is scattered by the electrons within. Since the electrons are associated with the atoms, the electron density will also follow a regular pattern. If the atomic planes of the sample are situated such that the Bragg condition (equation 4.1) is satisfied, then constructive interference of the scattered x-rays occurs. This is shown in Figure 4.2.

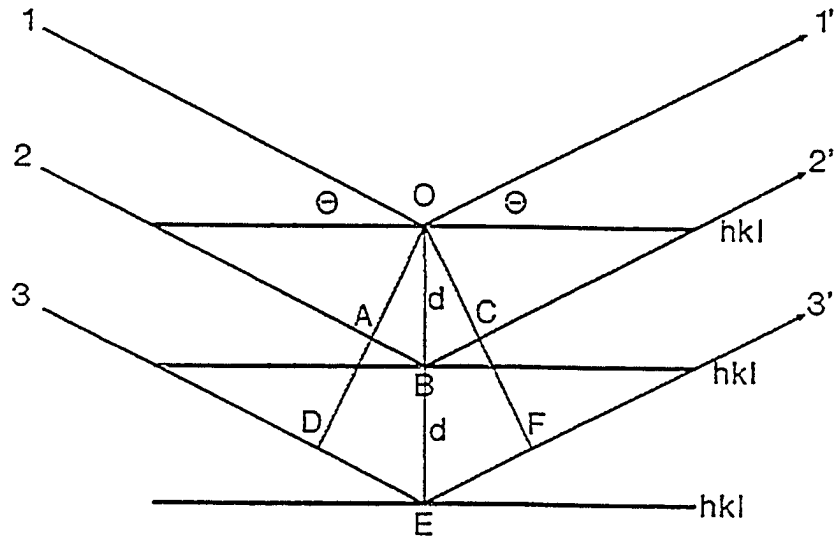

Figure 4.2. Bragg condition is satisfied and constructive interference of scattered waves occurs from the *hkl* planes. The path difference between rays 1/2 and 1/3 are ABC and DEF, respectively, which are integral multiples of the wavelength (from reference 83).

The Bragg condition is satisfied when

$$n\lambda = 2d\sin\theta \qquad 4.1.$$

Here λ is the wavelength of the incident X-ray, d is the atomic plane spacing in the crystal, and θ is the incident angle or Bragg angle. The incident beam, reflected beam and the normal to the diffracting planes are coplanar. The angle between the incident and scattered wave vectors is 2θ, called the scattering angle. Each set of parallel planes will create a strong scattered beam at an appropriate value of the scattering angle, creating a unique x-ray diffraction pattern for each material.

The difference between the reflected and incident beams is called the scattering vector and is usually labeled **q** (as in Figure 4.4 below). An inspection of Figure 4.2 reveals that if the Bragg condition is satisfied then **q** will be perpendicular to the plane from which the beam is reflected. The orientation of the planes is determined by three non-colinear points, one on each of the axes of the unit cell of the crystal structure of the material. The plane is indexed by first finding the intercepts of the plane in terms of the lattice constants of the unit cell. The intercepts are then inverted and reduced to the smallest three integers having the same ratio as the inverted intercepts. The result is used to index the plane and is usually written in the form (*hkl*). The (*hkl*)'s are referred to as the Miller indices of the plane.

From a classical perspective, when the electrons are illuminated with electromagnetic radiation, they begin to oscillate. The oscillating electrons then emit radiation in all directions. The intensity of the scattered X-ray from one

electron at a distance r and angle 2θ from the electron is given by the Thomson equation:

$$I = I_o \frac{e^4}{m_e^2 c^4 r^2}\left(\frac{1+\cos^2(2\theta)}{2}\right) \qquad 4.2.$$

The term in brackets is called the polarization factor, e and m are the charge and mass of the electron and 2θ is the angle between the incident and scattered beam.

Scattering by an individual atom, is equivalent to scattering by a collection of electrons forming a diffuse cloud about the nucleus. To account for the fact that the electrons of the atom do not form a point charge, a form factor has to be added to equation 4.2:

$$f_n = \sum_n \int_0^\infty 4\pi r^2 \rho_n(r) \frac{\sin(kr)}{kr} dr \qquad 4.3.$$

Here, r is the radial distance from the centre of the atom, $\rho_n(r)$ is the atomic electron density, $k = 4\pi\sin(\theta)/\lambda$ and the sum is over all electrons in the atom. The form factor measures the scattering power of the atom. Atoms with more electrons are generally stronger x-ray scatterers.

The atomic positions in a unit cell (the repeating cell in a crystal) are also important in determining the intensity of the scattered radiation. The intensity of scattered radiation from each atom in the unit cell must be summed using the geometric structure factor of the atom:

$$F_{hkl} = \sum_1^N f_n e^{2\pi i(hx_n + ky_n + lz_n)} \qquad 4.4.$$

Here f_n is the scattering factor of n^{th} atom, (*hkl*) are the Miller indices of a given plane, and $(xyz)_n$ are the atomic positions of the n^{th} atom in the unit cell.

In a powder XRD experiment, the grains of the powder are assumed to be randomly oriented. This ensures that for each plane there will be at least some grains situated so that particular plane is parallel to the surface of the sample. This means that for the appropriate incident angle, θ, of the beam the Bragg condition is satisfied and constructive interference occurs, creating a detectable scattered beam. If the sample is a film instead of a powder, then the grains may not be randomly oriented. If there is a preferred orientation, then it is possible that none, or only one, of the planes are appropriately aligned to satisfy the Bragg condition so that an incomplete powder x-ray diffraction pattern is collected.

The size of crystalline grains also has an impact on the diffraction pattern that is obtained. If the grains are large then the peaks in the diffraction pattern are very sharp and well defined. As grain size decreases the peaks become broader and less intense. As an example, the Scherrer formula [83] predicts that the grain size of crystallites that give diffraction peaks having full wiidth at half maximum (in scattering angle) of 2, 4, 6, 8 and 10° are 4.4, 2.2, 1.4, 1.1 and 0.8 nm, respectively. There is clearly a grey area between a nanocrystalline material and an amorphous material. A material having 1 nm grains separated by grain boundaries is hard to distinguish from an amorphous material. For the purposes of this thesis a material will be described as amorphous if the diffraction peaks

are more than about 8 degrees wide in scattering angle (corresponding to 1 nm grains) or if there are no peaks found in the pattern.

4.1.2. XRD Equipment

XRD data was collected using several different machines. First, a Siemens D5000 diffractometer equipped with Cu Kα radiation and a diffracted beam monochromator was used. This diffractometer operates in the θ-θ Bragg-Brentano mode. In this mode, the sample is held fixed and the X-ray source and detector both move on a circle to scan θ. The scattering wave vector is perpendicular to the sample for all Bragg angles so that only planes that are parallel to the substrate diffract X-rays as shown in Figure 4.3.

The second piece of equipment, called the JD 2000, used a PW-1720 Phillips X-ray generator using Cu Kα radiation and a diffracted beam monochromator. A homemade diffractometer was used on this generator. It used a modified version of the Bragg-Brentano geometry in which the source is held fixed and the sample and detector are rotated. Both the D5000 and the JD2000 measure one sample at a time and take several hours to collect the entire diffraction pattern in a series of discrete steps.

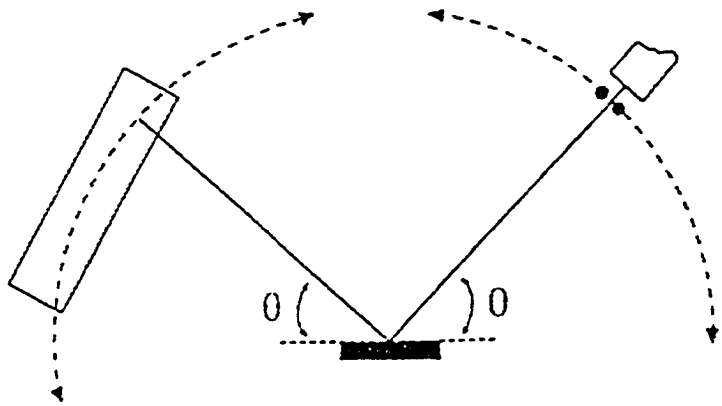

Figure 4.3. The θ-θ Bragg-Brentano geometry (from reference 83).

An INEL CPS120 curved position sensitive detector was also used with the PW-1720 Phillips X-ray generator. The INEL was used for rapid collection of x-ray diffraction patterns for the combinatorial films. This system is equipped with an automated X-Y motion stage, allowing collect and move steps to be sequentially programmed over a 5 cm X 5 cm area. With this system, the sample and incident X-ray beam are stationary. The curved detector then simulates a rotating detector as shown in Figure 4.4. The detector measures the entire diffraction pattern between scattering angles of 6° and 120° at once. Typical collection times are 5 to 10 minutes per pattern. The X-ray beam is incident at about 6° with respect to the sample's horizon, so those atomic planes that would satisfy the Bragg condition at $2\theta = 12°$, will be parallel to the substrate.

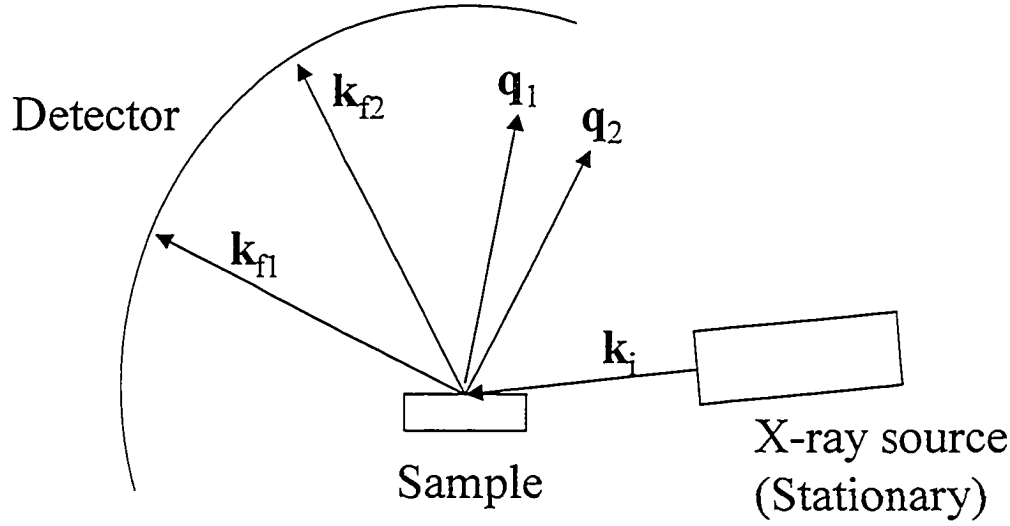

Figure 4.4. A schematic of the INEL diffraction geometry. The sample and the incident beam are stationary and the curved detector resembles a scanning detector, collecting the entire diffraction pattern at once. Consequently the reflected wave vectors (k_{f1}, k_{f2}) and the scattering vectors (q_1, q_2) vary for different points on the detector (from reference 82).

4.2. Electron Microprobe

For compositional analysis, an electron microprobe was used to measure the amount of each element present in the film. Scanning electron microscopy (SEM) studies were performed with a fully automatic JEOL 8200 electron microprobe equipped with five wavelength dispersive spectrometers and a Noran (133 eV resolution) energy dispersive spectrometer. A very brief discussion of the electron microprobe technique will be given here. More detailed descriptions can be found in various sources, including references [84] and [85].

In electron microprobe measurements, a beam of energetic electrons (several keV) is incident on the sample. The incident electrons eject inner shell electrons from the atoms in the sample. When an outer-shell electron fills the vacant inner-shell, a characteristic X-ray with a well-defined wavelength or energy is generated. The energy of the emitted photon is equal to the difference in binding energies of an electron in the outer shell giving up the electron and an electron in the inner shell that is being filled in the transition. The transitions are identified as K, L, M, etc. These correspond to the vacant shells, which will be occupied by outer-shell electrons. The outer shell that gives up the electron to the vacant inner shell is labelled with a Greek letter. As an example, $K_{\alpha 1}$ means the transition of an electron from the first orbital of the L shell to the K shell. Since the electron energies vary from element to element, the emitted x-rays can be used to identify which species are present in the sample.

The detectors compare the intensities of the x-rays produced from the sample to those produced from known standards. Corrections must also be

made for effects related to the atomic number (Z), absorption (A) and fluorescence (F) of the elements in the sample. These corrections, collectively referred to as ZAF, are very mathematically complex and are done by computer. The calculations can be found in reference [86], although we describe the physical origin of each of these corrections below.

Atoms with high atomic number have more electrons and therefore are more likely to interact with the incident electron. More incident electrons are elastically scattered, or back scattered, from elements with high atomic number without expending their energy in the sample. Also, elements with high atomic number will stop incident electrons faster and therefore have a smaller interaction volume. The greater back scattering and stopping power of high atomic number elements needs to be accounted for, and this is the origin of the Z, or atomic number, correction factor. It is especially important when there are elements in the sample with widely varied atomic number.

Since x-rays are generated beneath the surface of the sample, they must travel through the sample to reach the detectors. The sample may absorb some of the x-rays so that they are not detected. The amount of absorption depends on the elements in the sample. This is the origin of the A, or absorption, correction factor.

If one element in the sample has a characteristic x-ray energy that is slightly higher than a characteristic x-ray of another element in the sample, then fluorescence effects are important. The x-ray generated in one element may be absorbed by the other element that then emits its own x-ray. The detector will

then over count the second element at the expense of the first. This is the origin of the F, or fluorescence, correction factor.

Two different methods are used to analyse the x-rays emitted during electron microprobe experiments. In the first method, the energy of the detected photons is measured. This is called Energy Dispersive Spectroscopy (EDS). This method was used to measure the metal content of the sputtered films. The second method measures the wavelength of the detected radiation and is referred to as Wavelength Dispersive Spectroscopy (WDS). WDS is very sensitive and allows trace elements and lighter elements to be detected. WDS was used to measure oxygen content in the sputtered films.

The detectors are calibrated for the appropriate elements before each measurement is made to ensure accurate results. The beam was operated at 15 kV and 20 nA. Count times were typically about 30s. The system's software performs the ZAF calculations and provides the mass and atomic percentage of elements in the sample. The atomic percents reported have an error of about 1 – 2 % according to the Electron Microprobe technical staff.

4.3. Electrochemical Testing

One of the main goals of this thesis is to identify candidate materials to be used as the negative electrodes in Li-ion batteries. Therefore, electrochemical measurements are very important to this study. The electrochemical results not only show how well suited a material is for use in batteries, but can also provide insights into the structure of the materials and the structural changes that occur

during insertion and removal of lithium. The remainder of this chapter will describe the electrochemical testing methods used for this study.

4.3.1. Basic Electrochemistry

Figure 4.5 shows a schematic of a Li metal test cell. In this cell, the material to be tested (sputtered films in this thesis) is used as the positive electrode and a piece of lithium foil is used as the negative electrode. The external circuit is a battery charging system that consists of a current and/or voltage source and monitoring and control equipment. The charging systems and test cell construction will be described in more detail later in this chapter.

The data collected during an electrochemical experiment provides a lot of useful information about the material being tested. On of the most important criteria for a possible electrode material is its reversible specific capacity. For the materials being discussed here, this is a measure of how much lithium can be repeatedly inserted into and removed from the material, which determines how much charge will flow through the external circuit during one half cycle (either a charge or discharge). Specific capacity the charge stored per unit mass with units of mAh/g being the most common. It can be calculated from:

$$\text{specific capacity (mAh/g)} = \frac{Q}{m} \qquad 4.5.$$

In equation 4.5, Q is the total charge transferred during one half cycle (either a charge or discharge) in mAh and m is the active mass of the test material in grams. Volumetric capacity can be found by multiplying the specific capacity (mAh/g) by the density of the test material (g/cc) to obtain the capacity in mAh/cc.

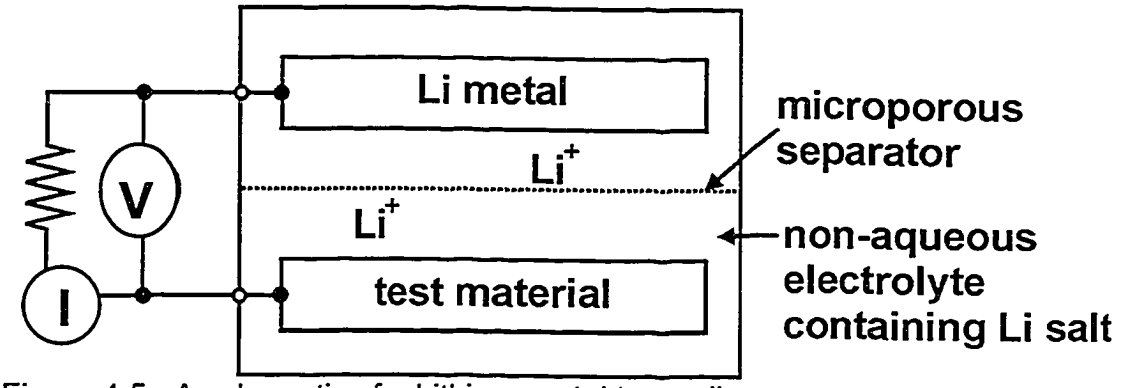

Figure 4.5. A schematic of a Lithium metal test cell.

Other important characteristics of the test material include cycle life and irreversible capacity. Cycle life is a measure of how many charge/discharge cycles the material can undergo before it is no longer useful. Usually this is measured as the number of full cycles achieved before the capacity drops below 80% of the first cycle capacity. Irreversible capacity is a measure of how much capacity is lost during the first cycle. Irreversible capacity occurs when some of the lithium inserted in the test material during the first cycle is used up in irreversible processes instead of being reversibly inserted. This can occur for several reasons. One common cause of irreversible capacity is the formation of a passivating layer on the surface of the test material [58]. Another cause is impurities in the test material that react irreversibly with the lithium during the first insertion. The impurities may be there accidentally, or they may be there intentionally in order to form an inactive matrix around the active material, such as with some of the tin oxide glasses studied by Courtney et al. [39-43].

Besides the capacity, irreversible capacity and cycle life, the electrochemical data (potential *versus* capacity and dQ/dV *versus* potential) can provide information about the structure of the test material. The potentials at

which charge flows can indicate the presence of co-existing phases when lithium is inserted into or removed from a crystalline material. Conversely, an amorphous phase which is having lithium added or removed can also be identified from the relationship between current and potential in an electrochemical experiment. These two cases are illustrated in Figure 4.6.

Figure 4.6a shows graphs of potential *versus* capacity and dQ/dV *versus* potential for the reaction of lithium with a crystalline material, M. In this reaction, when the lithium is added to M, it changes phase to form a new material with a different crystal structure. Since the crystal structures are very ordered, there are specific sites for the lithium to occupy that have specific energies associated with them. This is illustrated in the graph of voltage *versus* capacity shown in Figure 4.6a. At the start of the discharge, the voltage drops but little to no current flows so that the capacity (a measure of charge transferred) does not increase. When the potential reaches a point where it is favourable for the lithium to move into the test material, then charge begins to flow and the capacity increases. Since the energies of the sites available for the lithium are well defined, the voltage does not change until all of the lithium possible is inserted into the test material. When the new phase is completely formed, the voltage drops sharply with added charge. During the charge portion of the cycle, the reverse happens and the lithium is all removed at a single potential. With most of the current flowing at a single potential, plateaux are formed, as shown in the figure, when a two-phase coexistence region is encountered (when an existing crystalline structure is altered to form a new phase).

The middle graph of Figure 4.6a is called a differential capacity plot. It plots dQ/dV, or differential capacity, as a function of voltage. This plot shows at which potentials charge flows during the charge or discharge of the test cell. The sharp peaks in the plot of Figure 4.6a indicate that all of the charge is being transferred at one voltage. The presence of the sharp peaks in the differential capacity plot corresponds to the plateaus in the potential *versus* capacity plot and the peaks appear at the same voltage as the plateaus. The peaks are also indicative of a change of phase occurring in the test material.

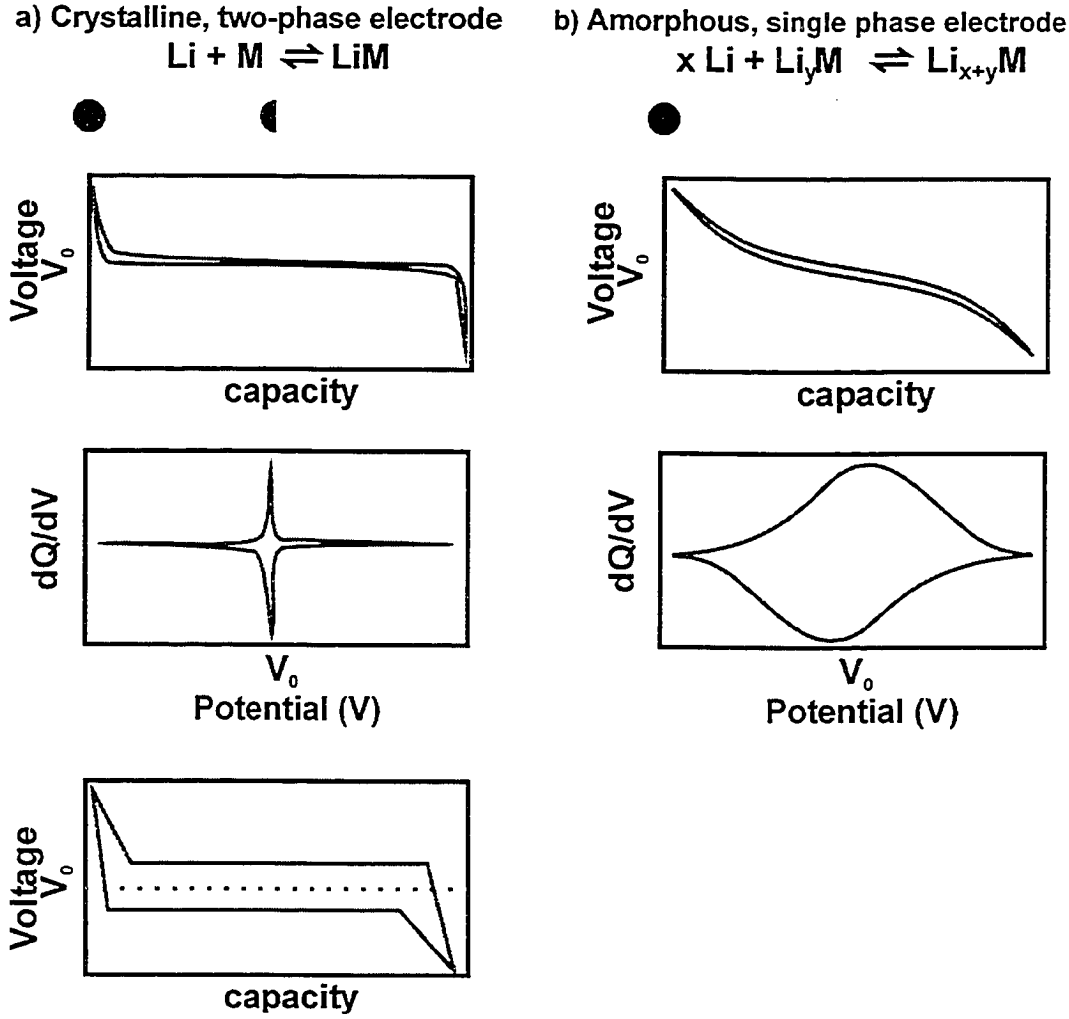

Figure 4.6. Illustrations of potential *versus* capacity and dQ/dV *versus* potential collected from lithium metal test cells for a) a crystalline material, and b) an amorphous material. The two types of plots shown are described in the text.

The first two graphs of Figure 4.6a are for an ideal case in which Li is inserted or removed at equilibrium in the absense of true hysteresis. For real cells the potential at which a plateau occurs is often different between charge and discharge. The phase change that causes the plateau may occur at a potential slightly lower than expected for an equilibrium reaction during the discharge. During the charge, the phase change may occur at a slightly higher potential. This is illustrated for a potential *versus* capacity plot in the bottom graph of Figure 4.6a. The difference between the potentials of the plateaus in the charge and discharge curves is commonly referred to as hysteresis.

The area between the charge and discharge plateaus in the V-Q graph represents energy that is lost during the electrochemical cycling of the cell. The energy is lost when the structure of the material changes from one phase to another when Li is inserted or removed. As Li is inserted into the grains of the material a new phase is formed. The grains will then be made up of two phases having different structures with a boundary in between. As more Li is inserted the new phase grows at the expense of the original phase and the boundary between the two must move through the grains. The movement of the boundary is accompanied by reorganization of the atoms in the material and the bonds between the atoms. This "friction-like" process irreversibly consumes some energy. This is the origin of the hysteresis that occurs in the bottom graph of Figure 4.6a. If the two phases have closely related structures, with almost the same lattice constants, then the magnitude of the hysteresis can be very small.

Figure 4.6b shows graphs of potential *versus* capacity and dQ/dV *versus* potential for the reaction of lithium with an amorphous material, LiM. In this case, the test material has no regularly repeated structure. As lithium is added, the material does not undergo any specific change in structure or phase. Because of the lack of order in the test material, there are no well-defined sites for the lithium atoms with specific energies associated with them. Instead, the lithium can be inserted in random sites with a wide range of energies. As a result, charge can flow over a range of potentials as opposed to one specific potential. This results in a smoothly sloped curve in the potential *versus* capacity plot of Figure 4.6b. Correspondingly, there is not a sharp peak in the dQ/dV *versus* potential plot in Figure 4.6b. Instead, the curve shows broad humps, indicating that charge is being transferred over a wide potential range.

4.3.2. Coin-Type Test Cells

One method of electrochemical testing is to include the test material in a coin-type test cell as the positive electrode and a piece of lithium foil as the negative electrode. It should be noted that even though the materials tested here are positive electrodes in the test cells, in commercial cells they would be used as negative electrode materials. The positive electrode is the one with the largest lithium binding energy. In most commercial Li-ion cells today $LiCoO_2$, which has a larger Li binding energy than the materials under consideration here, is used as the positive electrode.

Figure 4.7 shows a schematic of the construction of a coin-type test cell. The cell is constructed by starting with a stainless steel cell bottom (2325

coin cell hardware – 23 mm outer diameter and 2.5 mm thick) that will act as the positive terminal. The test negative electrode material is placed in the stainless-steel cell bottom. For coin cells, the test material used is one of the pre-weighed Cu disks with the sputtered film on it, or a 1.3 cm diameter disk can be cut with a precision punch from a Cu foil substrate after sputtering. A few drops of electrolyte are added after the test material is placed in the cell bottom. For coin cells, the electrolyte is 1 M $LiPF_6$ dissolved in a 1:2 vol % mixture of ethylene carbonate (EC) and diethyl carbonate (DEC), (Mitsubishi Chemical). A 14 mm-diameter, 125 μm-thick lithium foil disk is placed on top of the separator and centred with respect to the test negative electrode. A stainless steel spacer disc is placed on top of the lithium and a mild-steel spring is added on top of the spacer. When the cell is sealed, the spring is compressed and applies force to the cell bottom and spacer keeping the electrodes under pressure of approximately 200 psi. Finally, a stainless-steel cap with a polypropylene gasket is placed onto the stack. The cap acts as the negative terminal. The cell is then crimped closed to seal it. This assembly procedure is carried out in an argon-filled glove box to exclude water and oxygen from the cell. After the cells are crimped they are removed from the glove box and have metal tabs spot-welded to the positive and negative terminals to allow connection to the chargers with alligator clips.

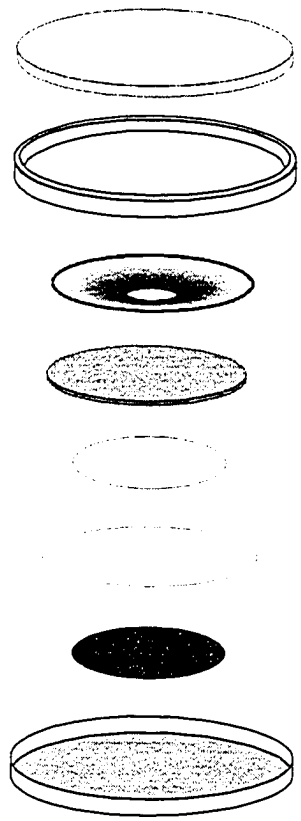

Figure 4.7. A schematic diagram of the parts used to construct a coin type electrochemical test cell.

The cells are kept in temperature-controlled boxes while they are being tested. The charger system used for the coin cells is a high precision system supplied by E-One Moli Energy Corp. The cells are charged/discharged using constant currents between preset voltage limits. Typical voltage limits are 0 to 1.2 V. The Moli system has a current resolution of 1 μA. The currents are usually chosen to give discharges of from 5 to 20 hours (C/5 to C/20) and are estimated based on the mass of active material and theoretical capacities. During cycling, the charger system measures voltage *versus* time with a Keithley 196 digital multi-meter (DMM), which has 6.5-digit precision. Voltage is recorded with 10 μV precision when it changes by more than 5 mV or after a preset time

limit, whichever comes first. The charger system logs potential as a function of time. Capacity is the product of current and time, which is added for each time step to get a cumulative total. Differential capacity (dQ/dV) data can be obtained by differentiating the capacity/potential data.

4.3.3. Combinatorial Electrochemical Cells

There are a number of disadvantages to using coin type test cells to test the electrochemistry of the combinatorial films produced with the methods described in Chapter 3. First, coin cells are time consuming to construct. Each cell takes approximately five minutes to construct, not including preparation time. From a 75 mm X 75 mm substrate, a grid of 25 electrodes, each 1.3 cm in diameter, can be cut. Also, the construction is performed inside a glove box, which adds to the difficulty of cell construction. For each set of cells, approximately three hours is spent working in the glove box. Fatigue and the repetitive nature of the task often leads to poorly constructed cells that do not produce useful data.

The size of the individual electrodes can also be a drawback when using coin cells. Each electrode is quite large, and if a large stoichiometry range is included in the sputtered film, then each electrode can have a large variation in composition instead of being a single composition sample. This means that the data produced is an average for a composition range instead of being representative of a specific composition.

A testing method that used smaller sample sizes, produced more samples per sputtered film and was more convenient to construct was desired. A 64-

channel electrochemical cell was designed to facilitate the testing of the materials produced by combinatorial sputtering.

Figure 4.8 shows a diagram of the combinatorial electrochemical cell plate designed for use with the sputtering system described in Chapter 3. Each electrode consists of an external electrical contact, a circular contact pad (where the material of interest is deposited) and a connecting lead. The contact pads are arranged in an 8 X 8 grid and all fit within one of the 75 mm X 75 mm sub-tables on the two-axis substrate table described in Chapter 3. Each contact pad is 5 mm in diameter, covering a much smaller composition range than the electrodes used in coin cells. The cell plates are loaded on the substrate table as shown in Figure 4.1. The cell plate is masked so that only the contact pads are exposed. The combinatorial film is then sputtered and the mask is removed, revealing 64 discrete samples ready to be included in a test cell.

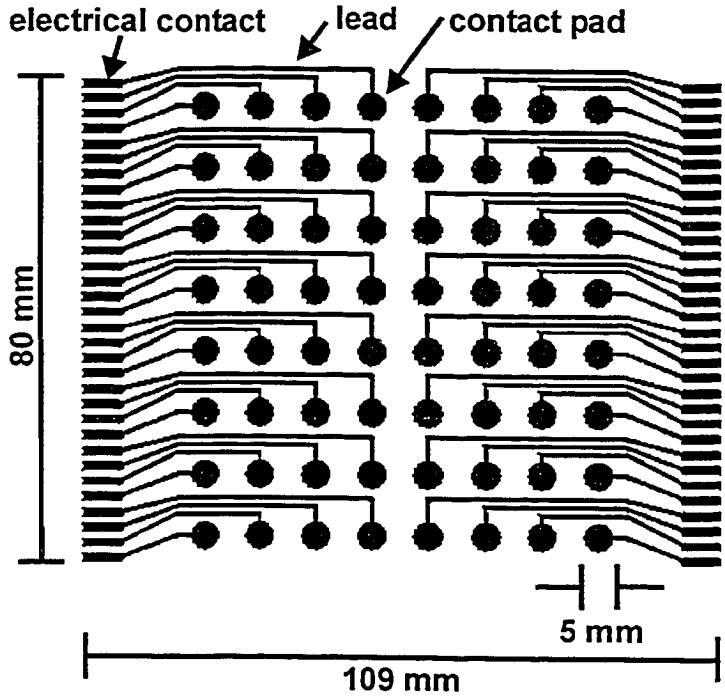

Figure 4.8. A diagram of the combinatorial cell plate (from reference [87]).

The combinatorial cell plates are produced in-house using a simple photolithography process. First, copper is sputtered onto 115 mm X 115 mm frosted glass plates. The copper is approximately 1 to 2 microns thick. The lead pattern shown in Figure 4.8 is etched using the procedure described in [87]. The etching procedure for producing the cell plates was developed by Greg Rockwell. Much of the design work for the cell plates and the design and trouble shooting of the combinatorial cell were performed Simon Trussler, Mike Fleischauer and Jessica Topple.

After the cell plates have received a combinatorial film, they must be included in an electrochemical cell for testing. The combinatorial electrochemical cell is illustrated in Figure 4.9. The cell consists of an aluminum base, onto which the cell plate is placed. The cell plate is then wetted with electrolyte. The electrolyte used is 1 M $LiClO_4$ in a 1:2 vol % mixture of ethylene carbonate (EC) and diethyl carbonate (DEC), (Mitsubishi Chemical). The electrolyte used is different than that used in coin-type test cells. It was found that the $LiPF_6$ electrolyte used in coin-type cells would corrode the silicone o-ring used to seal the cell, making it necessary to switch to $LiClO_4$. A sheet of microporous polypropylene separator (Celgard 2502) is set on the cell plate and more electrolyte is added. A total of 1.5 - 2 mL of electrolyte is used for each 64-channel cell. Lithium foil is laid on top of the separator to act as a common negative electrode for the cell. The cell is then capped with a stainless steel top with an integrated silicone o-ring to seal the cell. The assembly procedure is

performed in an argon-filled glove box, and takes ~ 20 minutes. There is also much less preparation for the combinatorial cell than for a set of 25 coin cells.

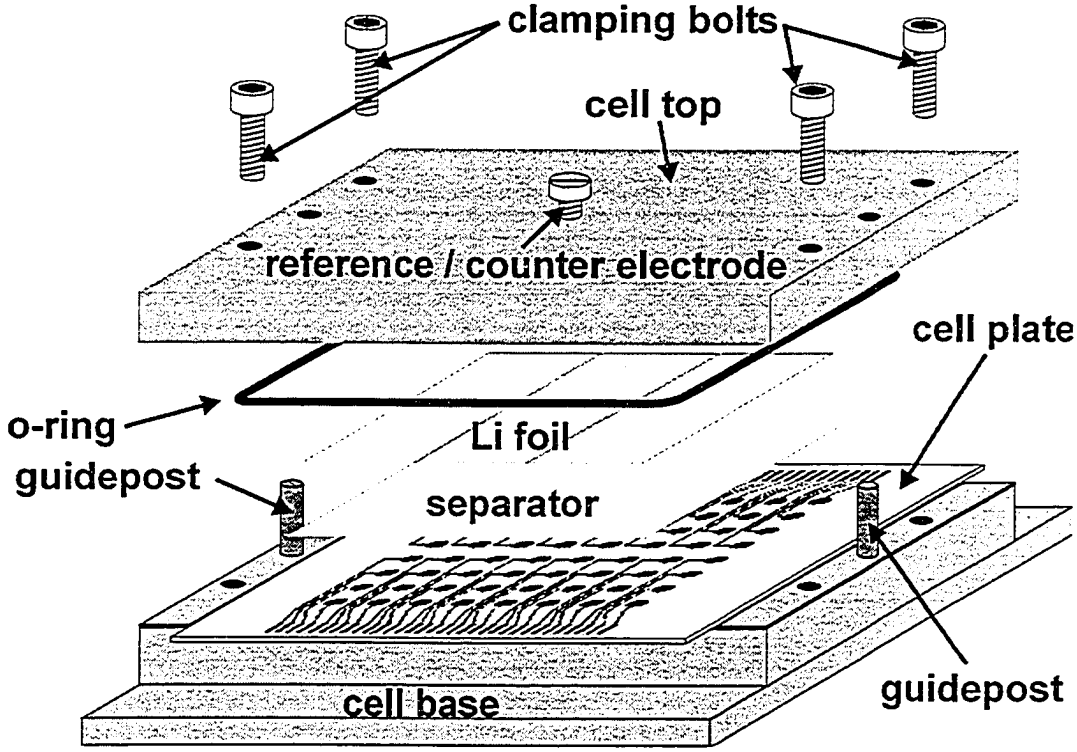

Figure 4.9. Schematic of the construction of a combinatorial electrochemical cell (from reference [87]).

The combinatorial cells are cycled potentiodynamically using two different pieces of equipment. One is a one hundred-channel Scribner model 900B Multichannel Microelectrode Analyzer. It sweeps the potential at a user-defined rate and measures current as a function of time. Since dQ/dV = dQ/dt * dt/dV = I/α (I is current and α is the sweep rate), I is dQ/dV times a constant (sweep rate is constant for the experiments in this thesis). The potential can be held constant for a set period of time if desired. In a typical experiment the Scribner sweeps from 1.2 V to 0 V at a rate of 0.03 mV/s. This is approximately an 11-hour discharge. The potential is then held constant at 0 V for two hours to ensure that

the maximum amount of lithium has been inserted in the test material. The voltage is then returned to 1.2 V at the same sweep rate and held for 30 minutes. The process is repeated for the desired number of cycles. The Scribner records time, potential and current. Capacity can be obtained by integrating the current over a charge or discharge. Differential capacity can be obtained from the current by dividing by the sweep rate and the active mass of the electrode.

The second piece of equipment used for cycling combinatorial cells is an in-house built multichannel pseudopotentiostat called Medusa [88]. Figure 4.10 shows a circuit schematic for an n-channel pseudopotentiostat. Each channel of the combinatorial cell is attached through a resistor R to the positive electrode of a Keithley 213 programmable quad voltage source. As the potential from the quad voltage source is changed, current will flow either to or from the electrode of the combinatorial cell. The current is determined by measuring the potential across the resistor, R, using a Keithley 2750 multimeter equipped with 7708 multiplexer cards. The first work to develop the Medusa was done by Vivien Cumyn. The author performed later updates to the hardware, with software updates by David Stevens and Arman Bonakdarpour.

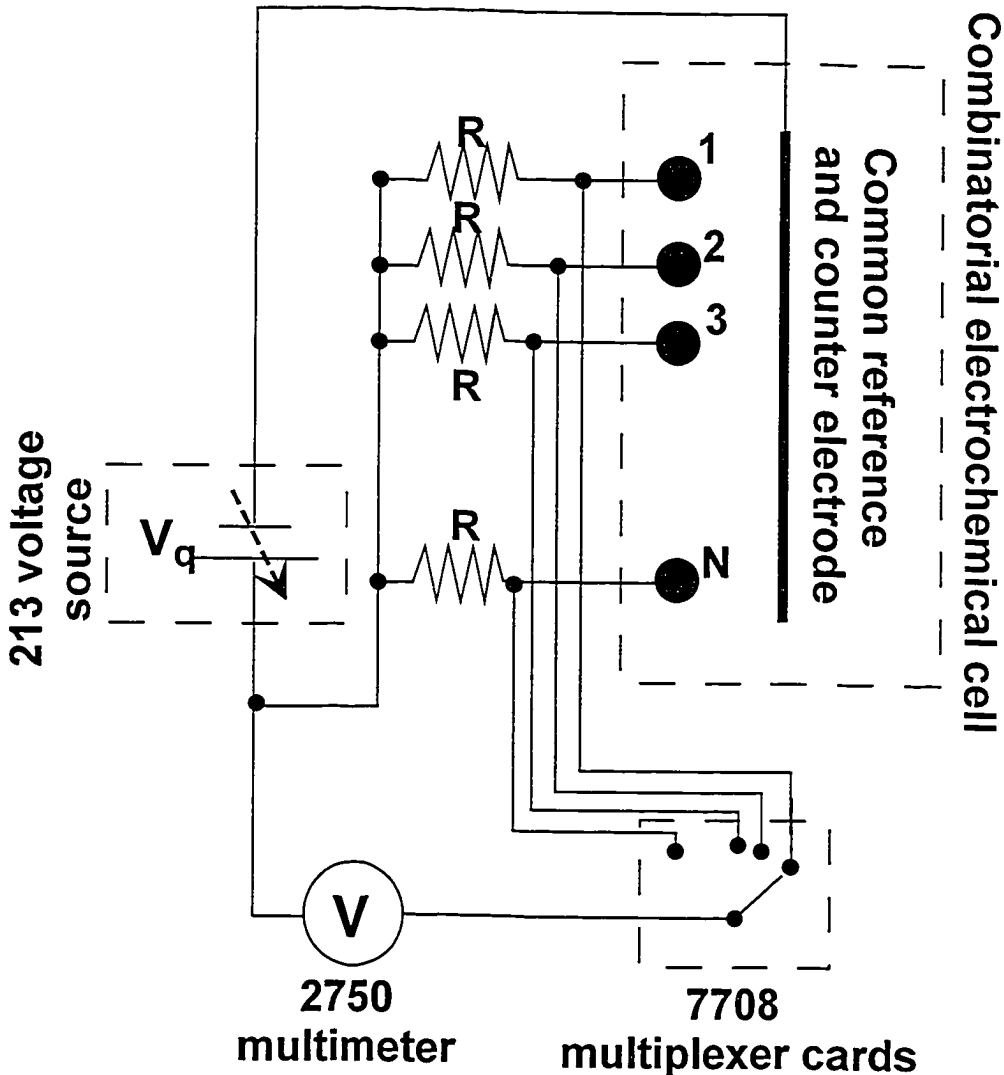

Figure 4.10. Circuit schematic of the multichannel pseudopotentiostat (from reference [88]).

The Medusa is a pseudopotentiostat in that it does not directly control the potential of the electrodes of the combinatorial cell. However, if the resistor, R, is kept suitably small, then the voltage from the quad source will be very close to the potential of the cell. Maximum currents from the individual channels of the combinatorial electrochemical cell are on the order of 0.1 mA. The value of R used is 100 Ω, giving a maximum potential drop of about 10 mV over the resistor R. The Keithley 2750 is a 6.5 digit multimeter and can easily measure a 10 mV

potential drop with high precision. With a maximum potential drop on order of 10 mV, the cell potential closely follows the control potential set by the quad voltage source.

The Medusa sweeps the potential over a set range in a user-defined amount of time. The software then selects a potential step to achieve the desired charge or discharge time. This is essentially the same as the user-defined sweep rate of the Scribner MMA. A typical protocol for the Medusa is to sweep from 1.2 V to 0 V in 12 hours and then hold at 0 V for two hours. The potential is then returned to 1.2 V in 12 hours and held for 30 minutes. The procedure is then repeated for as many cycles as desired.

The Medusa software records time, potential and current (the current is calculated based on the value of the resistor, R). Capacity can again be obtained by integrating the current over a charge or discharge. Differential capacity can be obtained using the current and time data logged by the software.

The data from the Scribner has been found to be as good or better than the data obtained from the coin cells [87]. Also, the Medusa is nearly equivalent to the Scribner [88], and the Medusa can cycle three combinatorial cells simultaneously. The combinatorial cells are much faster and more convenient than coin cells for testing the combinatorial samples produced and give high quality data, so they are a preferable alternative to one at a time testing.

Chapter 5. Single Elements

5.1. The Reaction of Li with a-Si

To take advantage of its high capacity and to overcome its problems with cycling, it is necessary to study Si in detail. This has been an on-going task for some time. Several authors have reported that crystalline silicon becomes amorphous upon alloying with lithium. Limthongkul et al. [89, 90] collected high-resolution electron microscopy and X-ray diffraction data showing the conversion of a crystalline Si electrode into an amorphous Li-Si alloy. They proposed an electrochemically driven solid-state amorphization mechanism similar to thin-film solid-state amorphization. Solid-state amorphization happens when amorphous phases form by reactions in the solid state instead of upon quenching from a melt. Amorphization through diffusive reaction has been known for some time in thin layered films [101].

Testing described in recent reports for a-Si did not obtain the full theoretical capacity expected. From Table 2.1, the theoretical capacity of Si is 4200 mAh/g. This is based on a fully lithiated phase of $Li_{22}Si_5$, or $Li_{4.4}Si$, which is found in the Li-Si equilibrium phase diagram shown in Figure 5.1. One example is from Takamura et al. [91] who report reversible capacities of up to 2200 mAh/g with a first discharge of approximately 3000 mAh/g. In this case, the $Li_{22}Si_5$ phase is apparently not attained. Graetz et al. [92] reported first discharge capacities of up to 3500 mAh/g and reversible capacities of over 2500 mAh/g in 100 nm silicon nanofilms. Also, Maranchi et al. [36] reported similar results with a-Si films from 250 nm to 1000 nm thick. They found reversible capacities of up

to 3500 mAh/g. The work by Jung et al. [37] claimed reversible capacities of 4000 mAh/g for very thin (50 nm) films deposited on glass substrates. The authors, however, did not bother to address the fact that their first several discharges had capacities of up to 6000 mAh/g, well above the theoretical capacity of Si. It seems that for their samples, there is more than the lithiation of silicon occurring and it is not obvious that all of the reversible capacity can be associated with the Si. It is not clear that the Si in Jung's films have been lithiated beyond the 3000 – 3500 mAh/g range that seems to be the limit for the films mentioned above.

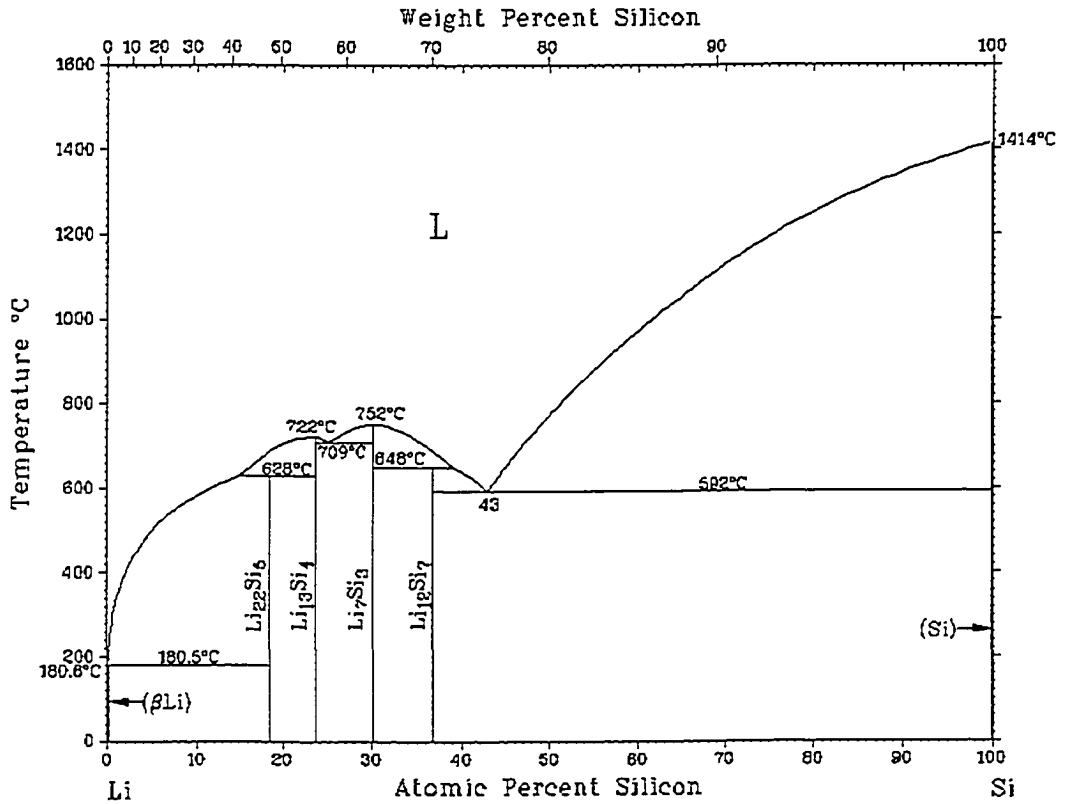

Figure 5.1. The Li-Si equilibrium phase diagram (from reference 93).

Figure 5.2 shows plots of dQ/dV *versus* potential for two sputtered Si electrodes. Figure 5.2a is for a quite thin (~ 0.5 μm thick) film while the graph in

Figure 5.2b is from a much thicker (~ 4.5 μm thick) film. Both were found to be amorphous by x-ray diffraction. These graphs, although for the same material, are very different. In Figure 5.2a, it is evident that there are no sharp peaks in the dQ/dV *versus* potential profile that, as was seen in Chapter 4, indicate two phase regions. In Figure 5.2b, there are several peaks during the discharge but only one during the charge. If the lithiation of these SI electrodes followed the phase diagram of Figure 5.1, we would expect to see several sharp peaks as the electrodes transform from one phase to the next, finally ending in the $Li_{22}Si_5$ phase at the bottom of discharge. During the charge, the same pattern should be witnessed in reverse as the electrodes are converted back to Si. For the electrodes shown in Figure 5.2 it is clear that they do not follow the equilibrium phase diagram during lithiation or delithiation. Also, the two electrodes, which are made of the same material, do not seem to undergo the same reactions or structure changes. The thicker of the two electrodes even follows different reaction paths for charge and discharge. The reasons for the differences between the two graphs in Figure 5.2 and the lower than expected capacity reported for a-Si need to be understood.

In an attempt to understand the behaviour of a-Si electrodes, an *in-situ* x-ray diffraction experiment was performed. This technique employs regular coin type test cells with some modifications made to allow x-ray data to be collected at the same time as the cell is undergoing charge/discharge cycling. For this experiment, the a-Si electrode is sputtered directly onto a Be disk. This disk is incorporated in a coin cell as shown in Figure 5.3. The coin cell is then

constructed normally and the cell is inserted into a specially designed x-ray sample holder. The Be disk acts as a window that allows x-rays to pass through and hit the electrode on the other side. X-ray diffraction data is then repeatedly collected as the cell is very slowly discharged and charged. In this way, changes in the structure of the electrode during cycling can be observed as they happen. This technique is described in detail in reference [94].

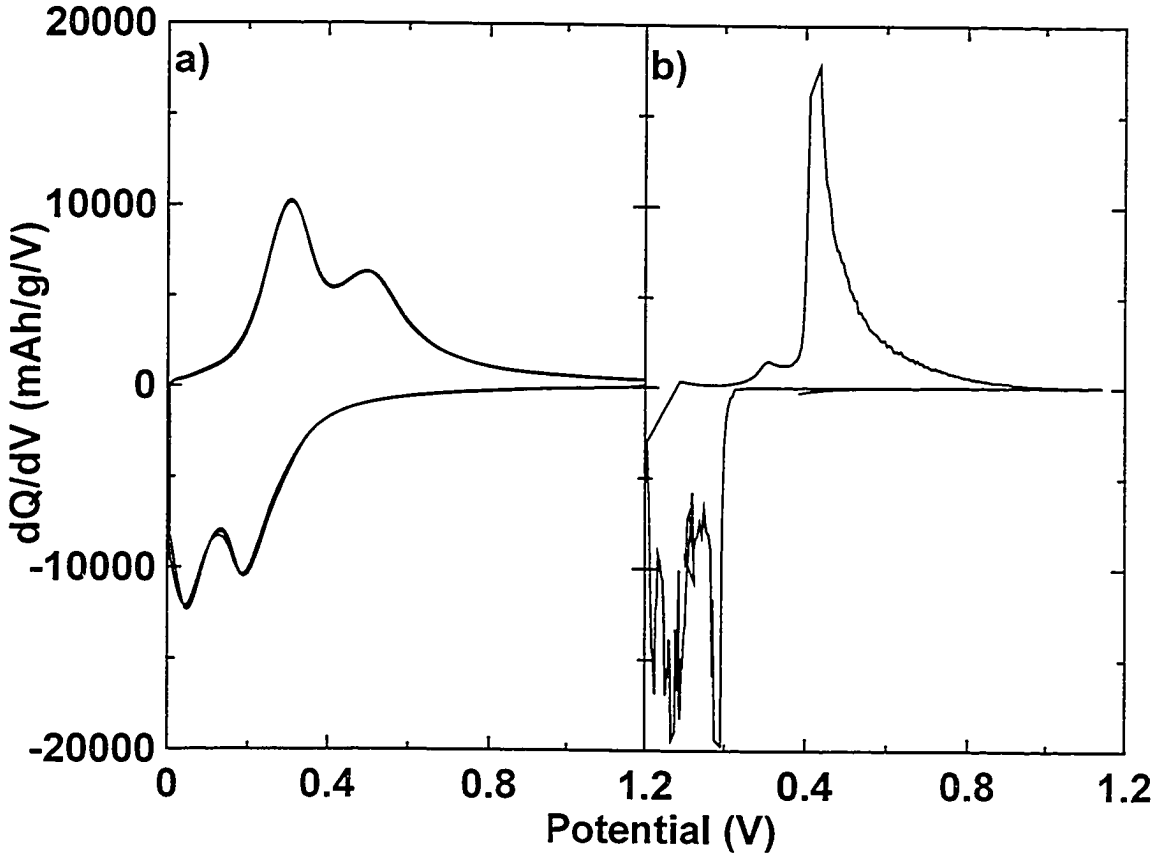

Figure 5.2. Plots of dQ/dV *versus* potential for a) 0.5 μm sputtered a-Si electrode, and b) 4.5 μm sputtered a-Si electrode.

The current was chosen to provide a C/48 rate based on the theoretical capacity of the cell. The in situ cell was discharged using the signature method described in [95]. The current was halved three times with a 30 min. open circuit period between current steps once the lower cut-off potential had been reached.

The first discharge was to 0 V. The cell was then charged to 1.2 V, also using the signature method. The subsequent discharge was limited to 0.1 V. XRD data was collected with a JD2000 diffractometer equipped with a Cu target X-ray tube and a diffracted beam monochromator limiting the beam to Cu Ka radiation. The generator was set for 40 kV and 30 mA. Data was collected between 2θ = 15° and 60° at 0.05° intervals. The count time was 12 s per point, giving total scan times of 3 h. A total of 43 scans were completed over the course of the experiment.

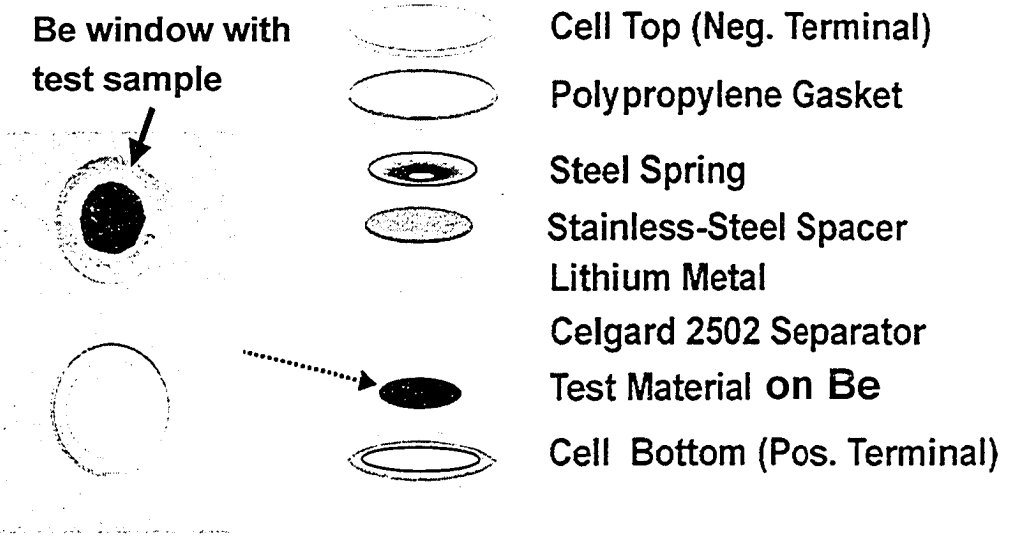

Figure 5.3. Exploded view of the construction of an *in-situ* XRD cell. The cell bottom has a circular hole cut into it to accommodate the Be window containing the test material.

The Si film deposited on a Be window was measured with XRD before the in situ cell was constructed to determine the structure of the film. The result is shown in Figure 5.4. With the exception of peaks from the Be window at approximately 42°, 46°, 52°, and 53°, there are no sharp peaks in the profile. There are two broad humps centred roughly at 29° and 52°. These humps are from the Si film and indicate that it is amorphous, as was desired. Also, from the

mass of Si deposited and using the bulk density for Si, the thickness was estimated to be 12 μm.

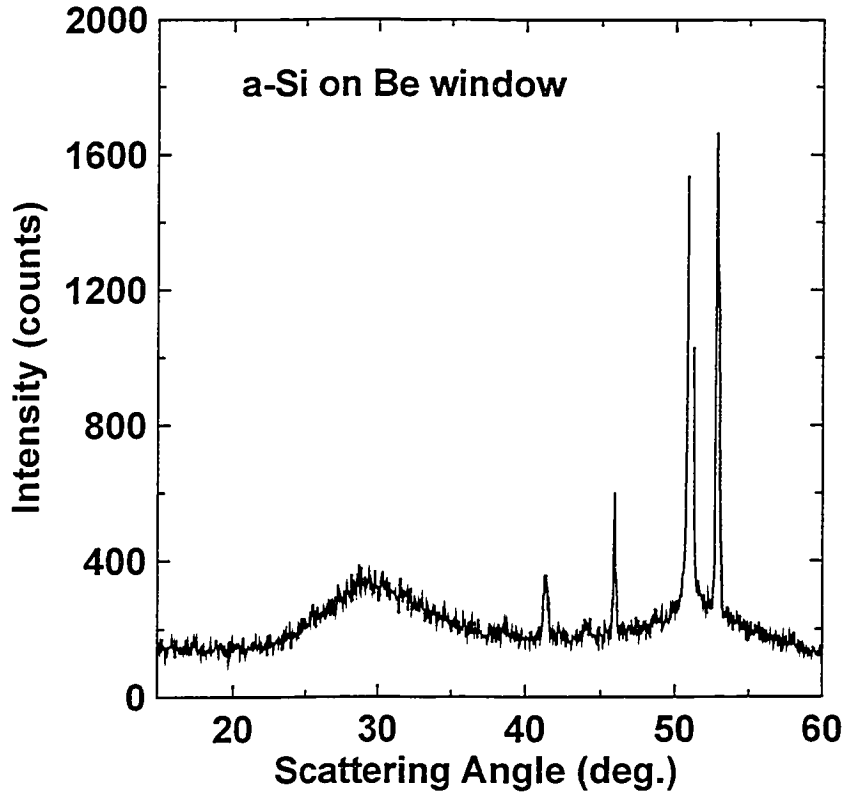

Figure 5.4. XRD pattern of 12 μm a-Si film on a Be window for use in an *in-situ* XRD test cell.

Figure 5.5 shows the potential *vs.* capacity data for the in situ cell constructed from the a-Si film on the Be window. There are two very broad, gently sloping plateaus during the first discharge. One is at approximately 0.2 V and the other at 0.1 V. At the end of the first discharge, the profile shows a change in slope at about 0.03 V, as indicated by the arrow in Figure 5.5. The total first discharge capacity, including signature discharge, is just over 3500 mAh/g. During the first charge, the voltage increases immediately to 0.4 V, where there is a broad plateau. The total first charge capacity is approximately 2500 mAh/g, giving an irreversible capacity of about 1000 mAh/g or nearly 30%

of the first discharge. The second discharge is limited to 0.1 V. There is no obvious plateau in this discharge, just one gentle slope. Also, at the end of the second discharge, there is no obvious change in slope in the voltage-charge (V-Q) relation, and the voltage does not jump as high at the start of the second charge. These features can be explained by the XRD data.

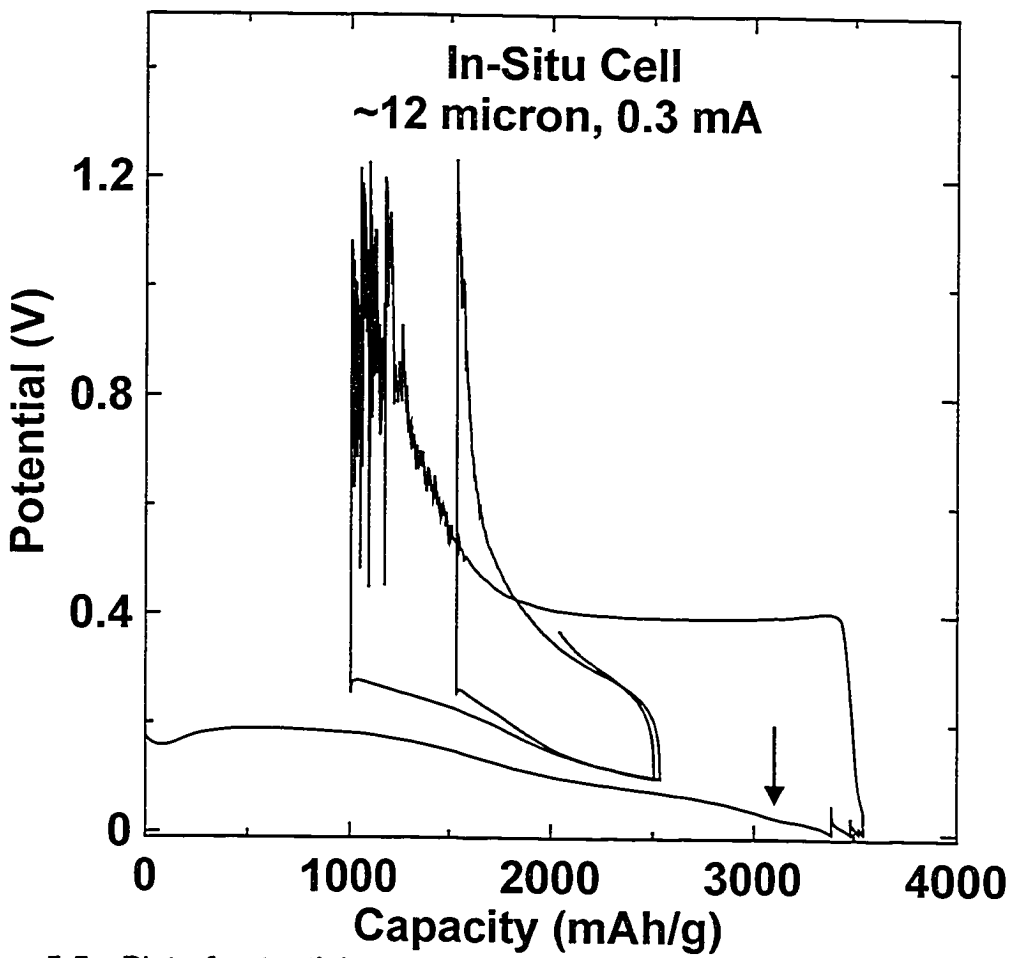

Figure 5.5. Plot of potential *versus* capacity for the *in-situ* XRD cell. The arrow indicates a change in slope near 0.03 V.

Figure 5.6a shows potential *vs.* time for the in situ cell, and Figure 5.6b shows selected XRD patterns taken from the cell. The circled numbers in Figure 5.6a represent the time of the XRD scans, and the numbers to the right of Figure 5.6b indicate scan numbers. To make the changes occurring in the X-ray

patterns more clear, the peaks due to the cell parts have been fitted and then removed by subtraction.

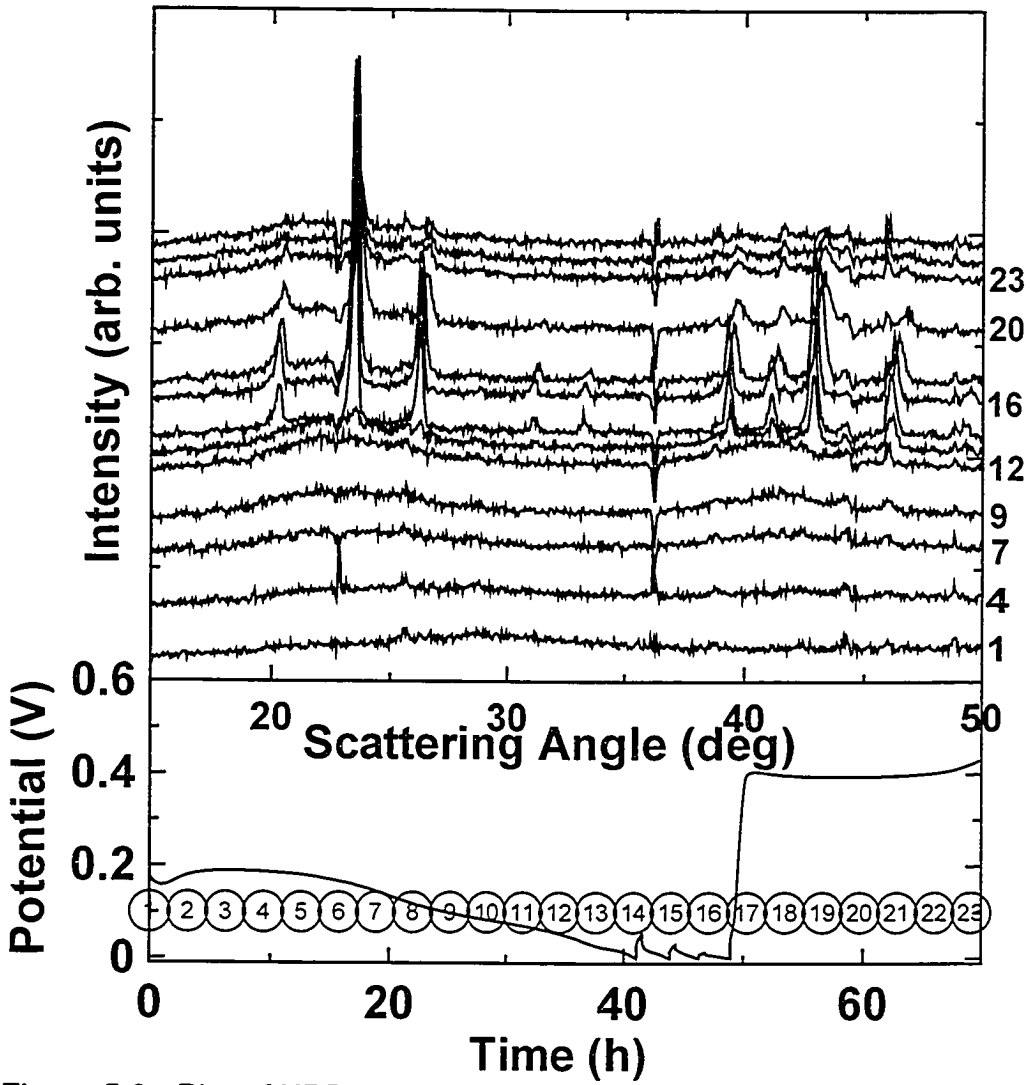

Figure 5.6. Plot of XRD patterns and potential *versus* time for the first discharge and charge of the *in-situ* XRD cell showing a) potential *versus* time and b) selected XRD scans. The circled numbers in 5.6a show the start time of the XRD scans. The numbers to the right of 5.6b show the scan numbers. Diffraction peaks from cell parts have been subtracted.

The first change that occurs in the patterns is that the two humps from the a-Si become a little sharper and shift to a lower angle. This is probably due to the expansion of the Si host matrix as Li atoms are inserted to form a-Li_xSi. The Li_xSi may have a structure similar to Li_4Sn described in [99]. In this structure the

atoms are arranged on an underlying BCC lattice with the Sn in tetrahedra which are not in the positions found in $Li_{22}Sn_5$. This structure produces an XRD pattern with a broad hump near 25° and a sharper peak near 42°, which is similar to what is found in scan 12 of Figure 5.6. This behaviour continues until scan 13. At the start of scan 13, the film is still amorphous, with the lower angle hump shifted to below 25°. During this scan, the potential of the cell begins to change slope at about 0.03 V. Also, a series of new peaks begins to form between 40° and 45°. We also see that at the start of scan 14, there are new peaks forming between 20° and 27°, and that the broad humps from the a-Si have largely disappeared.

Figure 5.7 expands the portion of Figure 5.6 in the range of scans 11 to 15. From this figure, the formation of the new peaks clearly occurs sometime between the start and finish of scan 13. They are not present at the start of the scan but are present at the end. Each scan took approximately 3 h, so the crystallization giving rise to these new peaks must have occurred very rapidly. The crystallization can be associated with the change in slope of the voltage profile that occurs during scan 13.

During scans 16 to 23, the first charge, the new peaks slowly disappear, and the humps from a-Si return in what appears to be a coexisting phase region. This corresponds to the broad plateau that is seen in the capacity *vs.* potential plot of Figure 5.5 during the first charge. Clearly, at the bottom of discharge, the a-Li_xSi crystallizes rapidly to form a new phase. During the subsequent charge, this crystalline phase is converted back to a-Li_xSi, with x approaching zero.

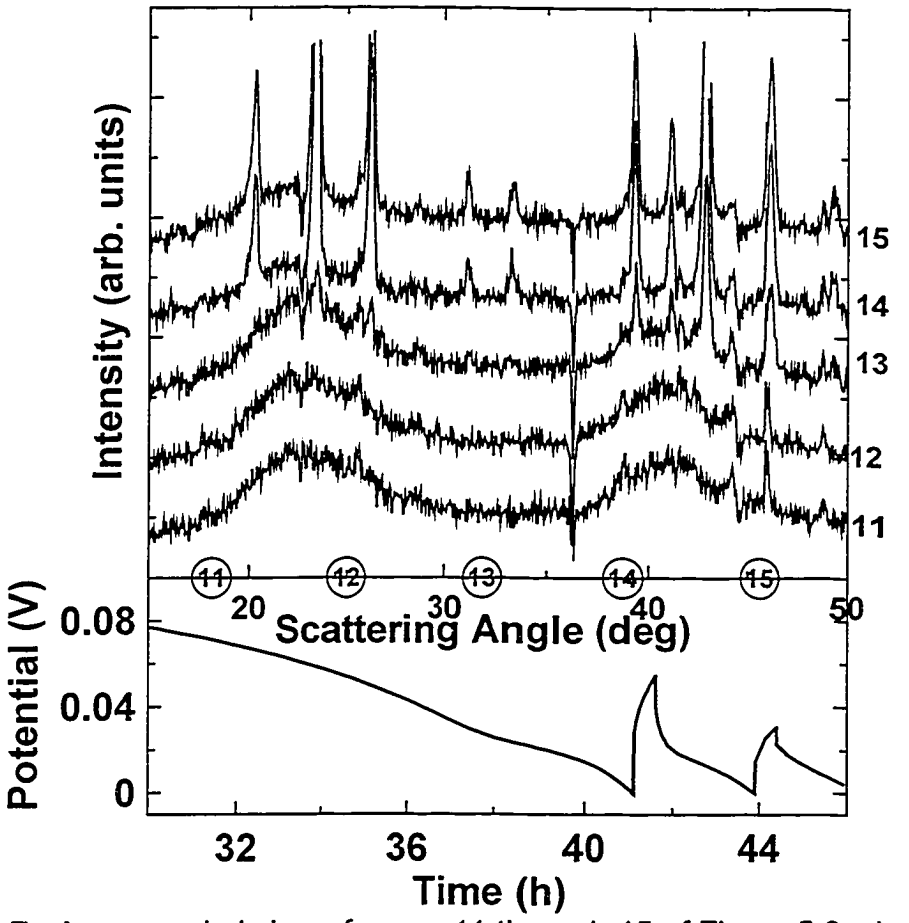

Figure 5.7. An expanded view of scans 11 through 15 of Figure 5.6, showing the bottom of the first discharge. The arrow indicates the change of slope in V-Q corresponding to the crystallization of the film.

Based on the charge transferred and the mass of Si in the cell, the stoichiometry of the crystalline phase can be estimated. From Figure 5.5, the first discharge had a capacity of just over 3500 mAh/g. A composition of $Li_{15}Si_4$ would correspond to about 3580 mAh/g. This phase was first suggested to be the fully lithiated composition of Si attainable in room temperature electrochemical cells by Obrovac and Christensen [96]. Their finding was based on a series of ex-situ XRD experiments in which cells were discharged to certain potentials and then opened for x-ray diffraction. They assumed that $Li_{15}Si_4$ has the same structure type as $Cu_{15}Si_4$ and $Li_{15}Ge_4$.

To help verify that this could be the phase found in the present work, a Rietveld refinement was performed on scan 16 of the in situ cell using Rietica [97]. The cell parts were again removed from the pattern, and the intensities were corrected for absorption by the Be window. The space group of $Li_{15}Si_4$ is I -4 3d (cubic). The lattice constant was found to be 10.777 Å. Si atoms are on the 16c sites (0.462, 0.462, 0.462) with Li on the 48e sites (0.130, 0.177, 0.865) and 12a sites (0.375, 0.0, 0.250). Table 5.1 presents a comparison of the parameters found in this work with those reported by Obrovac and Christensen. The results are close, which is comforting, given that the data for this work was collected through a Be window and included reflections from cell parts.

Table 5.1. Comparison of Rietveld Parameters.

Parameter	This work	Obrovac and Christensen [96]
Lattice constant	10.777 Å	10.685 Å
Si (16c) (x, y, z)	(0.462, 0.462, 0.462)	(0.459, 0.459, 0.459)
Li (48e)	(0.130, 0.177, 0.865)	(0.118, 0.156, 0.961)
Li (12a)	(0.375, 0.0, 0.250)	(0.375, 0.0, 0.250)

Figure 5.8 shows scan 16 and the fit obtained with the parameters just described. The fit has a Bragg R factor [97] of 13, which is fairly good given that the data was taken through a Be window in a coin type test cell. Even though the $Li_{15}Si_4$ phase does not appear in equilibrium phase diagrams for this system, we believe that it is the phase that forms at the bottom of discharge for a-Si.

Figure 5.9 shows the remaining XRD scans taken of the in situ cell. These cover the second discharge/charge cycle of the cell. For this cycle, the discharge was limited to 0.1 V. No peaks of the $Li_{15}Si_4$ phase appear, indicating that no crystallization occurs (the large peak at 26° that appears on scan 29 is a

result of carbon paint added to the cell during scan 28 to improve conductivity between the Be window and the cell case). This is presumably because the potential was not lowered to about 0.03 V, below which the crystallization takes place. The potential *vs.* capacity plot does not contain the slope change that was indicative of crystallization on the first cycle. Also, when the charge begins, the potential does not rise nearly as dramatically as it did during the first charge.

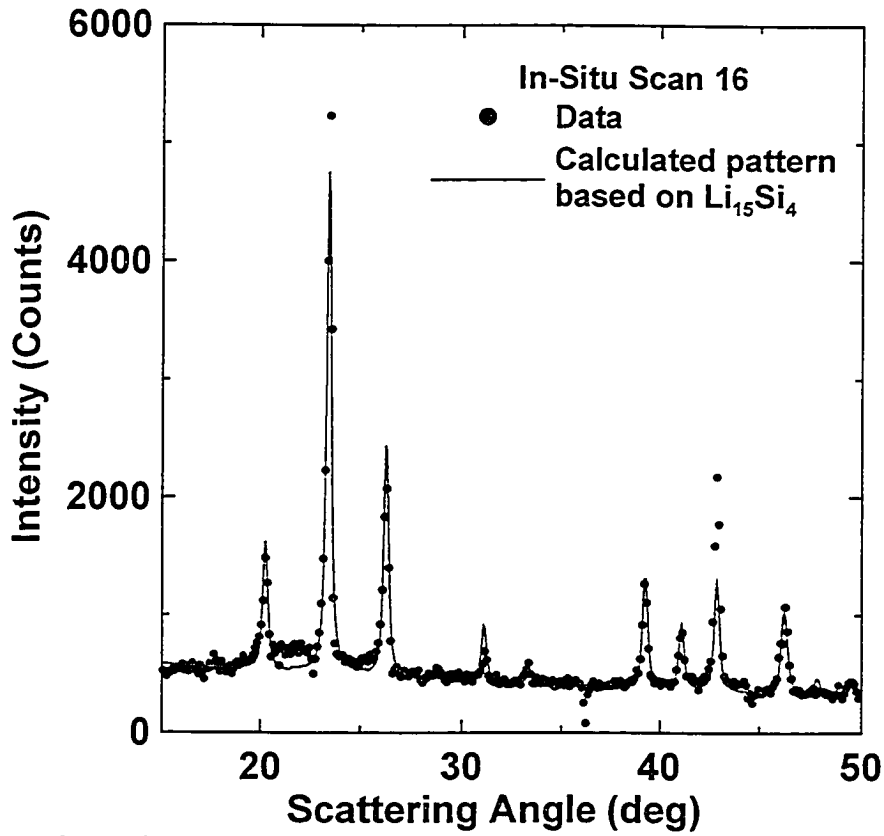

Figure 5.8. Plot of scan 16 (dots) and the Rietveld calculation (line) using the parameters for $Li_{15}Si_4$ described in the text. The data has been corrected for absorption by the Be window.

Using the features in the capacity *vs.* potential plot that are associated with the formation of a crystalline phase in the a-Si films, we can now use electrochemical data to study the structure changes of the films during lithiation/de-lithiation. Figure 5.10 shows a comparison of results from two coin

cells made from a-Si films deposited on Cu foil and one channel of a combinatorial cell plate with pure a-Si. Figures 5.10a and b show the potential *vs.* capacity and dQ/dV *vs.* potential for a 4.5 μm thick film, respectively. Figures 5.10c and d are the corresponding plots for a 2.4 μm thick film, and Figures 5.10e and f are those for a 0.5 μm film.

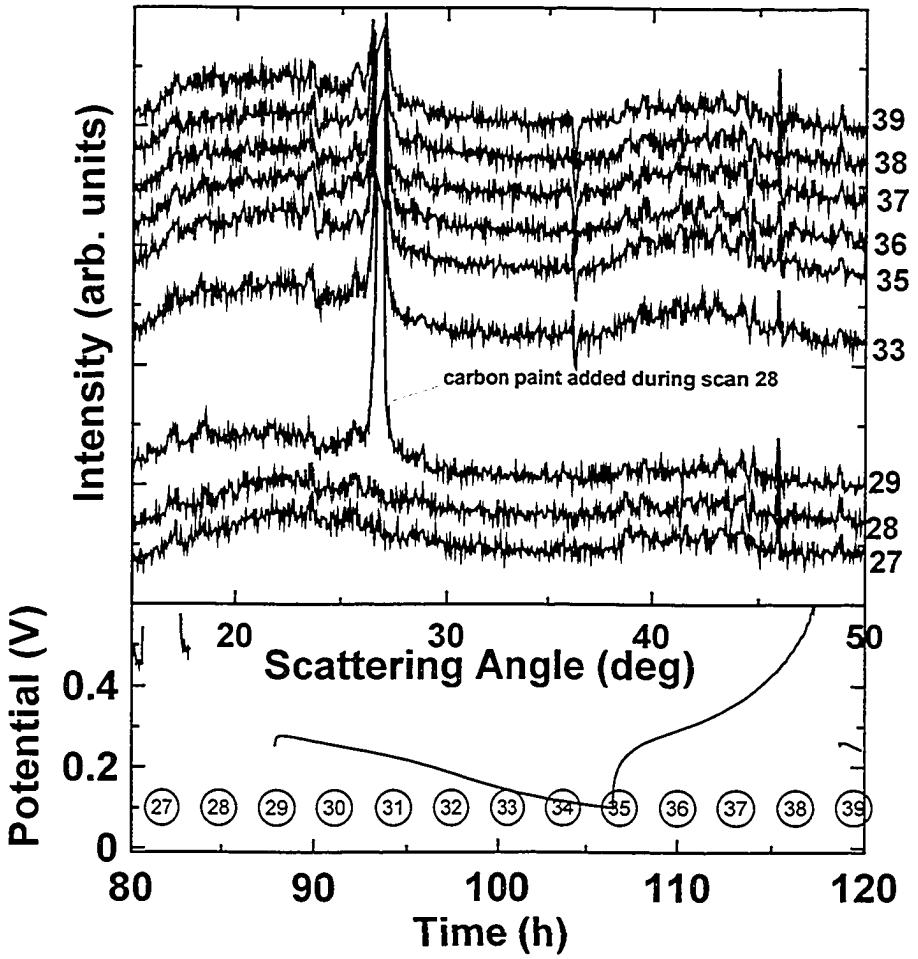

Figure 5.9. Plot of electrochemical and XRD data collected for the second discharge and charge of the *in-situ* XRD cell showing a) potential *versus* time and b) selected XRD scans. The circled numbers in 6a show the start time of the XRD scans. The numbers to the right of 6b show the scan numbers. Diffraction peaks from cell parts have been subtracted.

Figure 5.10a shows the same features in the potential *vs.* capacity plot as the *in-situ* XRD cell. At the bottom of discharge, the slope changes (indicated by

an arrow), indicating the formation of the c-$Li_{15}Si_4$ phase. This is mirrored by the peak in dQ/dV at about 0.03 V indicated by an arrow in Figure 5.10b. Also, at the start of charge, the potential jumps sharply to 0.4 V, where the $Li_{15}Si_4$ phase converts back to a-Li_xSi in a two-phase region. This conversion is accompanied by a sharp peak in the dQ/dV plot of Figure 5.10b at 0.4 V during charge.

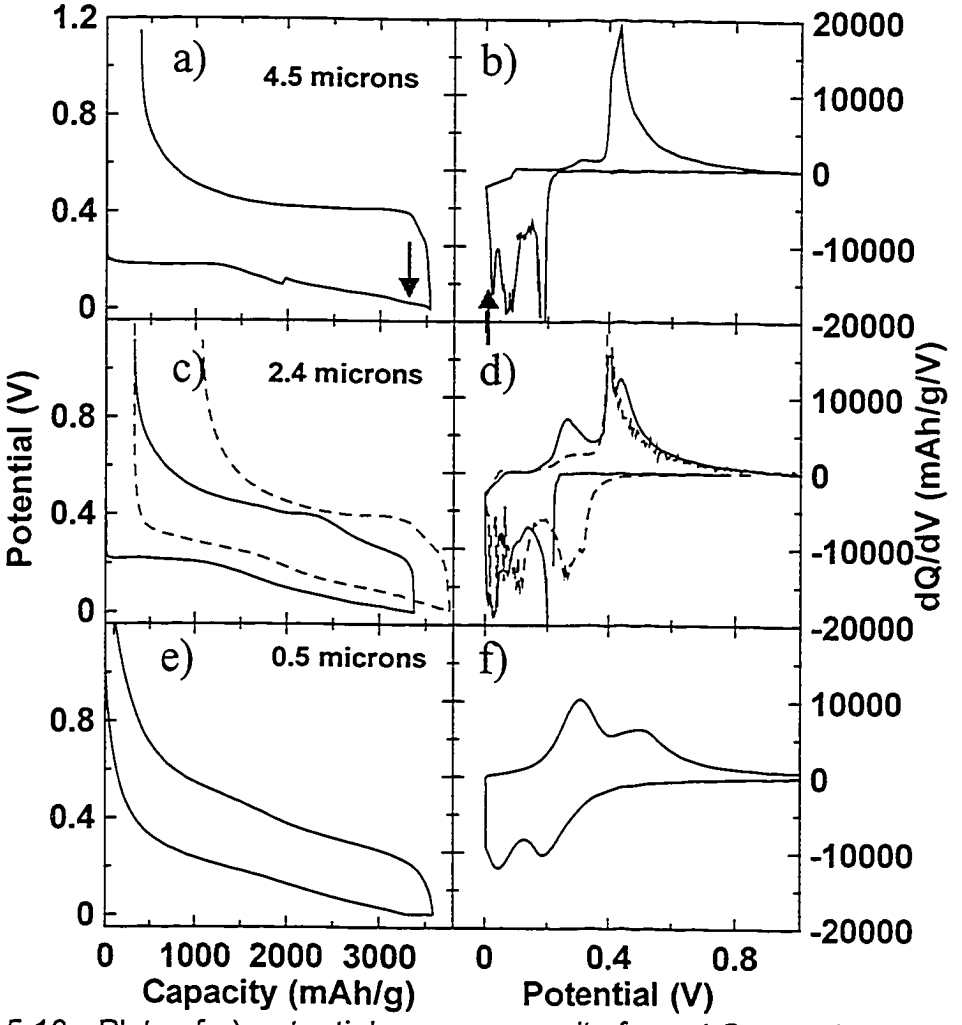

Figure 5.10. Plots of a) potential *versus* capacity for a 4.5 μm thick a-Si film, b) dQ/dV *versus* potential for a 4.5 μm thick a-Si film, c) potential *versus* capacity for a 2.4 μm thick a-Si film (dashed line is second cycle), d) dQ/dV *versus* potential for a 2.4 μm thick a-Si film (dashed line is second cycle), e) potential *versus* capacity for a 0.5 μm thick a-Si film and f) dQ/dV *versus* potential for a 0.5 μm thick a-Si film.

In Figure 5.10c, at the bottom of discharge there is no change of slope in the potential-capacity relation. Also, the cell potential does not go as high at the start of charge. In the dQ/dV *vs.* potential plot for this cell (Figure 5.10d) there are two broad humps, one at 0.3 V and one at 0.5 V during the first charge. During the second discharge (dashed line in the figure) of this cell, there is a slight change of slope in the voltage-capacity curve near 0.03 V, and during the subsequent charge the voltage rises much more quickly to 0.4 V. In the dQ/dV *vs.* potential plot, the two humps during charge have disappeared and are replaced by one sharp peak at 0.4 V.

Figure 5.10f shows the dQ/dV *vs.* potential plot for a 0.5 μm thick a-Si film studied using slow sweep (0.03 mV/s) cyclic voltammetry. This film was cycled 10 times, with no evidence of crystalline phases forming (no sharp peaks in dQ/dV *vs.* potential). At the end of each discharge the electrode's potential was held at 5 mV while the current relaxed (Figure 5.10e). Even this aggressive procedure did not induce the formation of the crystalline $Li_{15}Si_4$ for this thin film. Based on Figure 5.10, it seems that the film thickness is very important in determining if an a-Si film crystallizes during lithiation near 0.03 V. Films of 0.5 μm or thinner never showed evidence of crystallization in our experiments. Films thicker than 5 μm always crystallized upon lithiation. Figures 5.10c and d show that films about 2.5 μm thick sometimes crystallize and sometimes do not. It appears that there is a critical thickness of about 2.5 μm, below which films of a-Si do not crystallize upon lithiation and above which they do crystallize.

It is believed that the thin films do not crystallize because they are more strongly adhered to the substrate and therefore the atoms are more tightly constrained and cannot rearrange themselves to crystallize. This is supported by the work of Beaulieu [31-34] who showed that thin 'towers' of SiSn would grow upwards when Li was inserted but the area of the tower would not change. The adhesion to the substrate constrained the film, allowing it to expand upwards only. In contrast, thicker films would tend to crack and peel up from the substrate, allowing expansion and rearrangement in all directions. The thicker films are more free to rearrange than the thinner ones (the well-adhered films have one boundary "clamped" and the poorly adhered films have all boundaries free). However, many other factors could also play a role in whether or not films crystallize, including, e.g., deposition conditions (conditions were the same for all of the films here, with thicker films sputtered for longer times), morphology, charge/discharge current and temperature.

5.2. The Reaction of Li with Sputtered Al

In the chapters to come, many binary and ternary systems containing Si and one or two other elements will be discussed. In order to fully understand what is happening in these systems, it is necessary to know what each of the individual elements will do when alloyed with Li.

Figure 5.11 shows the LiAl binary phase diagram [93]. There are several equilibrium phases found in this system. The one containing the most Li is the Al_4Li_9 phase which has 2.25 Li per Al. Figure 5.12 shows a plot of dQ/dV *versus* potential for a coin cell made with a sputtered Al electrode. During the discharge

there is a large, sharp peak centred at about 0.2 V. During the charge there is one large sharp peak centred at about 0.5 V and a small broad hump at about 0.35 V. From the phase diagram in Figure 5.11, one might expect three large peaks as the various phases form during lithiation. It seems that in this cell, only the first phase covering a range of $0.01 < x < 0.495$ in $Al_{1-x}Li_x$ is formed.

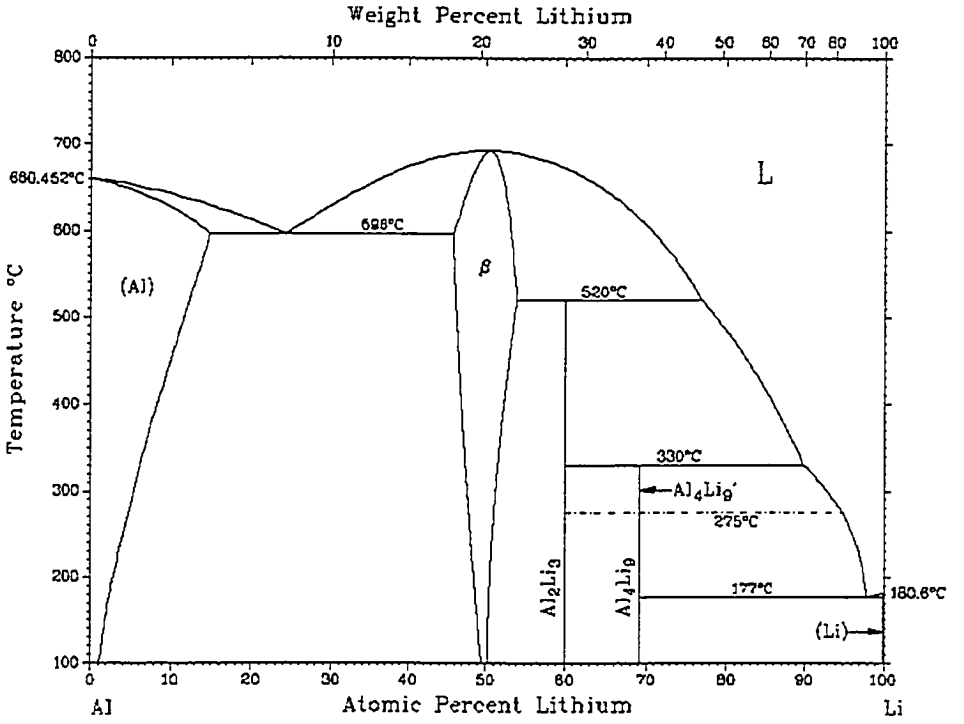

Figure 5.11. The Li-Al binary phase diagram [93].

Figure 5.13 shows the potential *versus* capacity for the first cycle of the same Al cell. The capacity obtained was approximately 1000 mAh/g which corresponds to $x = \sim 1$ in $Al_{1-x}Li_x$. It seems that the limit for Li insertion into sputtered Al in room temperature cells is approximately 1 Li per Al. The phases with higher Li content are not reached in our experiments.

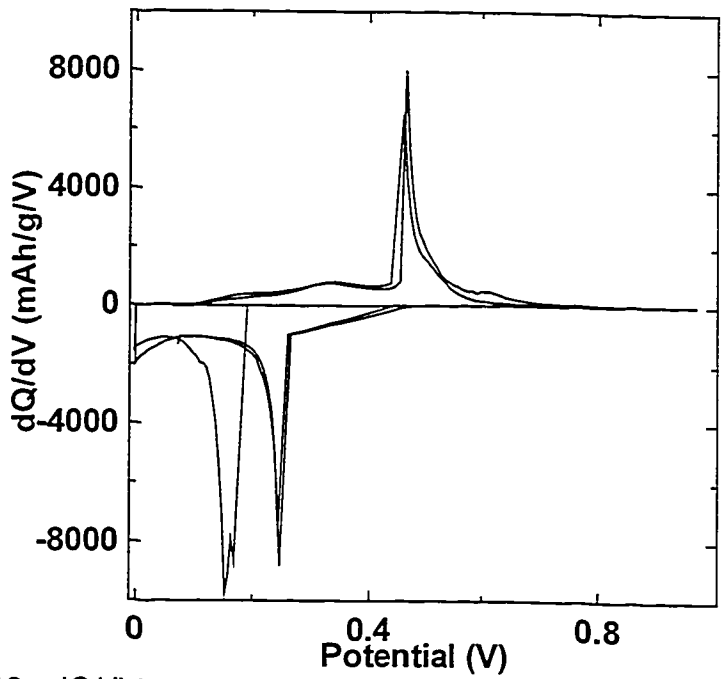

Figure 5.12. dQ/dV *versus* potential for a sputtered Al film cycled between 0 and 1.2 V at a c/12 rate.

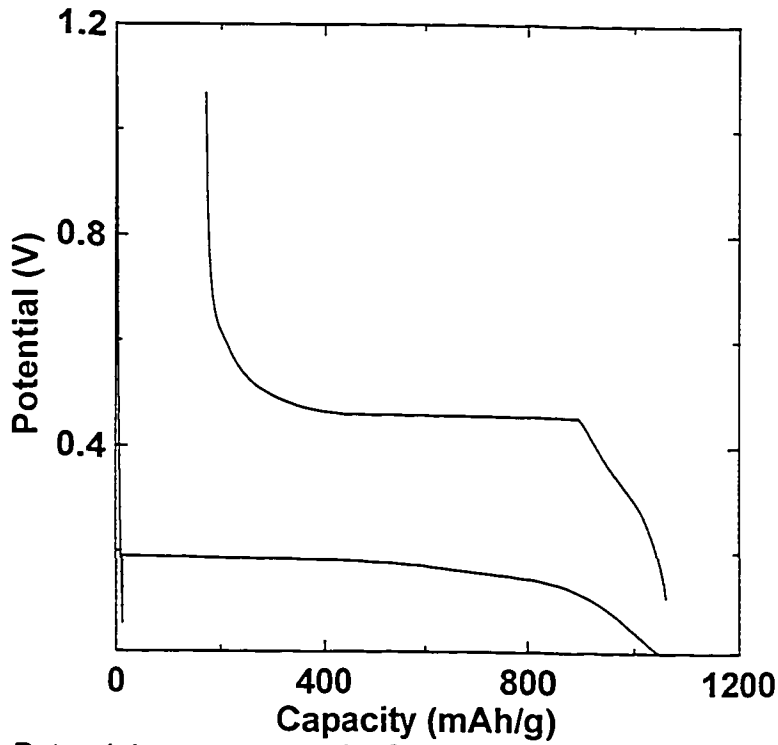

Figure 5.13. Potential *versus* capacity for a sputtered Al film cycled between 0 and 1.2 V at a c/12 rate.

5.3. The Reaction of Li with Sputtered Sn

The reaction of Li with Sn has been extensively studied (for example, reference [43]). For comparison with Sn containing films to be presented in the rest of the thesis, Figure 5.14 shows an example of dQ/dV *versus* potential for a sputtered Sn film. For this film, there are three sharp peaks during both charge and discharge. The sharp peaks during discharge are all above 0.4 V. There is also some activity below 0.2 V. The sharp peaks during charge are all above 0.5 V with a broad hump centred at about 0.45 V.

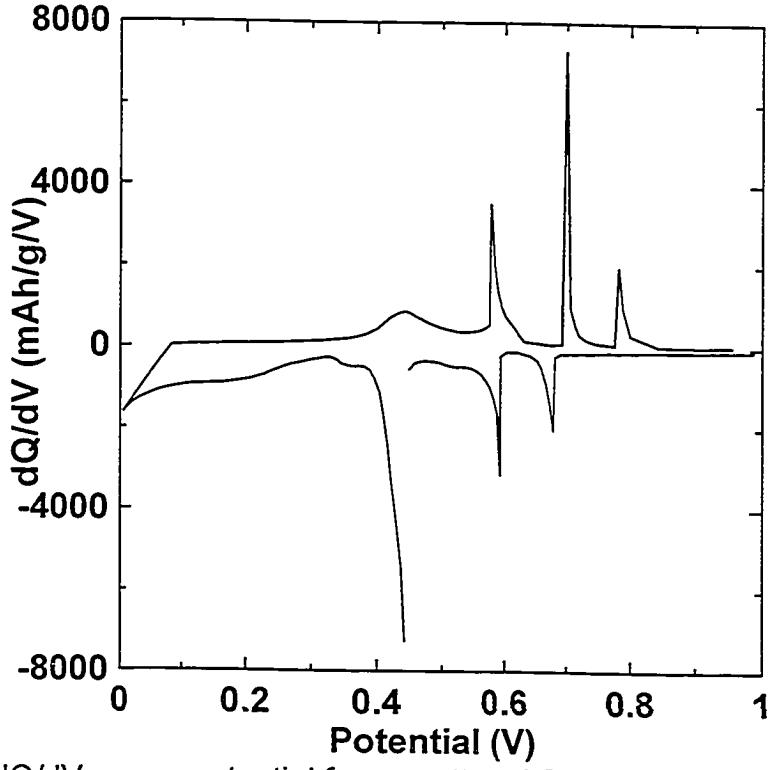

Figure 5.14. dQ/dV *versus* potential for a sputtered Sn film.

Figure 5.15 shows the low temperature portion of the Li-Sn phase diagram [93] and a graph of potential *versus* atomic percent Sn for the first cycle of the sputtered Sn electrode of Figure 5.14. The capacity for this cell was approximately 850 mAh/g, which is less than the theoretical capacity of ~ 990

mAh/g. The final phase reached is not certain. It could be Li_7Sn_2 with an excess of Li or it could be $Li_{22}Sn_5$ with a deficit of Li or a combination of the two phases. Some suggested reactions for the plateaux in the figure are indicated. These plateaux can be matched to the features in the dQ/dV *versus* potential graph in Figure 5.14.

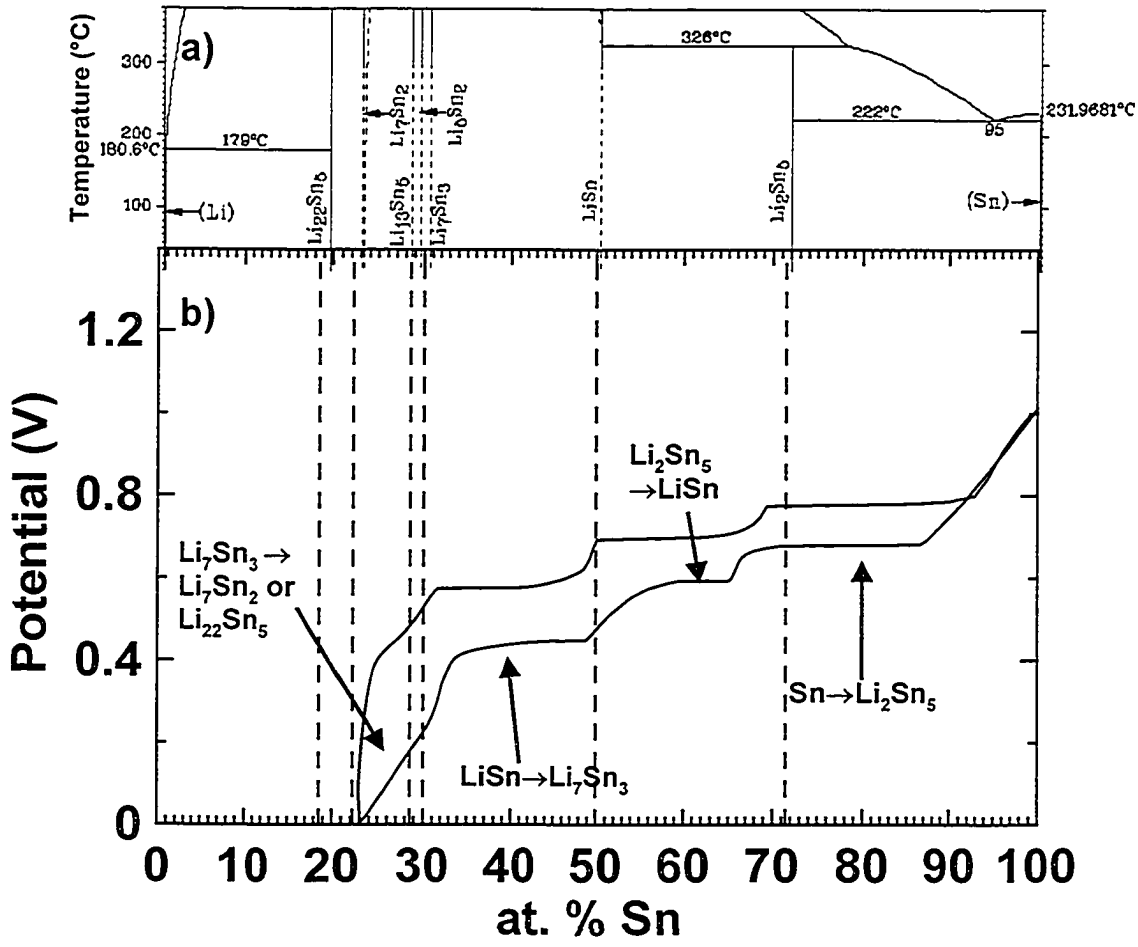

Figure 5.15. a) the LiSn phase diagram and b) potential *versus* atomic percent Sn for the first cycle of the sputtered Sn film of Figure 5.14. Some suggested reactions for each plateau in b) are indicated.

5.4. The Reaction of Li with Sputtered Ag

The phase diagram of the Li-Ag system is shown in Figure 5.16. Again, there are a lot of binary phases in this system. From Figure 5.16 it appears that

a large amount of Li should alloy with Ag and high capacities would be expected. Figure 5.17 shows dQ/dV *versus* potential for a sputtered Ag film. There are three sharp peaks during the discharge indicating that three two phase regions are encountered. There were also three large peaks during charge as well as two smaller ones at higher potential. All of the large peaks occur below 0.2 V. The capacity of this cell was nearly 800 mAh/g, which is equivalent to ~3 Li per Ag. This is near the γ_2 phase in Figure 5.16. It is not clear that the equilibrium phase diagram is followed for the sputtered film as there are more than three phases between pure Ag and the γ_2 phase. Calculations of the theoretical capacity of Ag will assume three Li per Ag in this thesis.

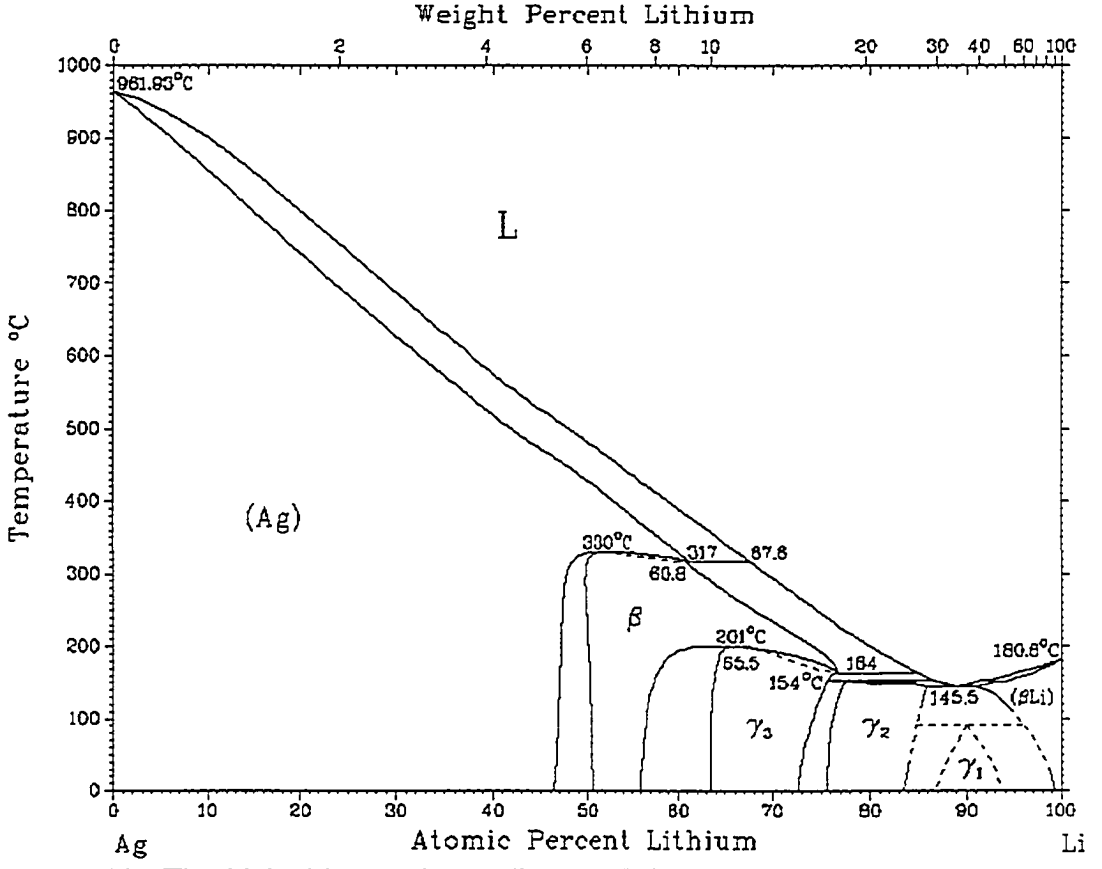

Figure 5.16. The Li-Ag binary phase diagram [93].

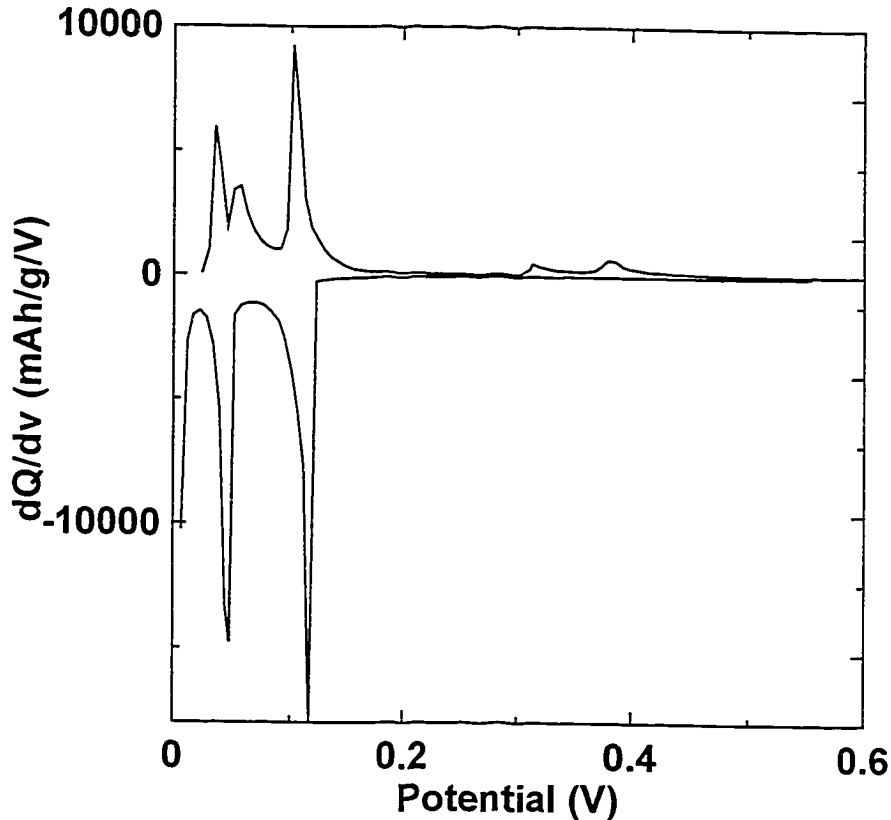

Figure 5.17. dQ/dV *versus* potential for a sputtered Ag film.

Figure 5.18 shows the low temperature portion of the Li-Ag phase diagram [93] and a graph of potential *versus* atomic percent Li for the first cycle of the sputtered Ag electrode of Figure 5.17. The locations of the plateaux in this figure do not match the phase diagram as well as for the Sn film discussed above. Some suggeested reactions for the plateaux are indicated in Figure 5.18. The limit for Li insertion for our experiments in room temperature electrochemical cells seems to be the edge of the γ_2 phase, which corresponds to three Li per Ag.

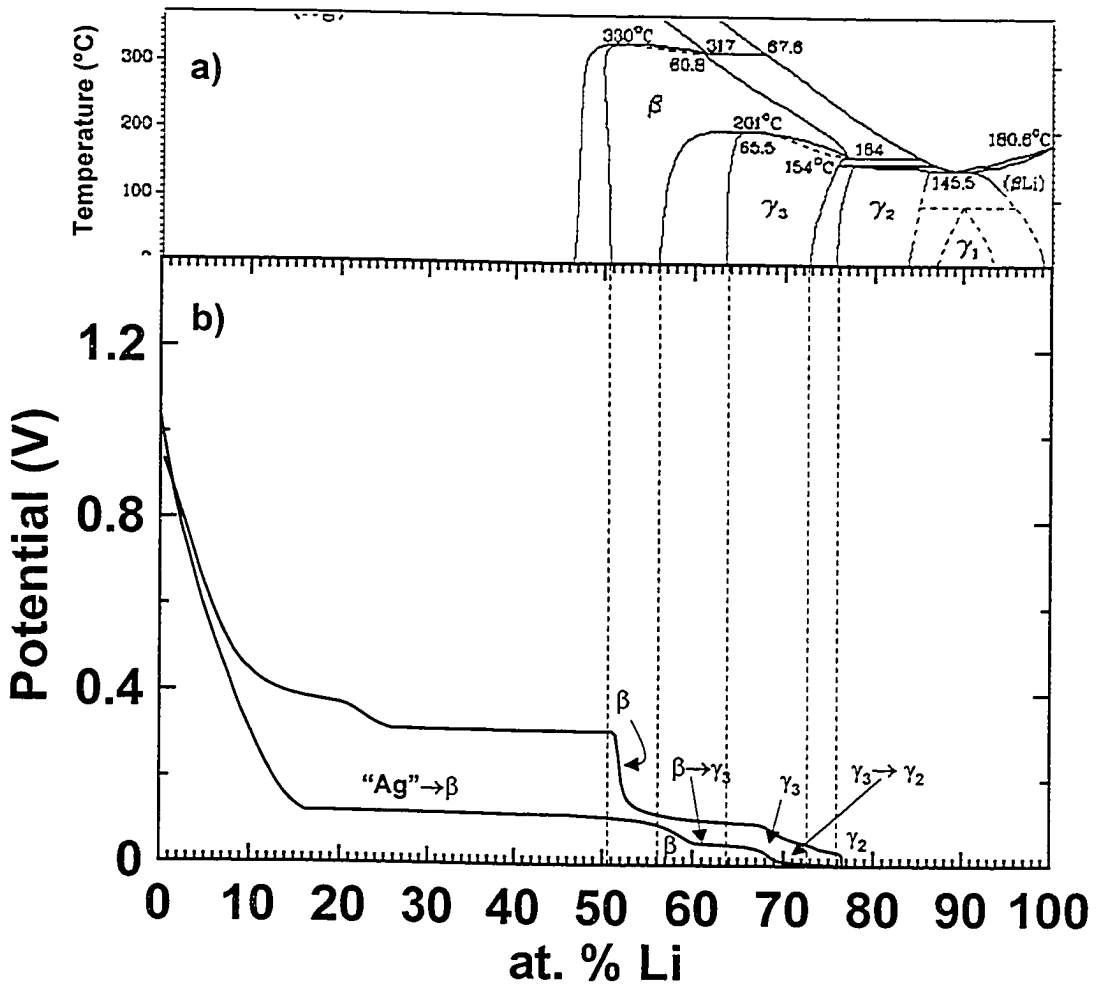

Figure 5.18. a) the LiAg phase diagram and b) potential *versus* atomic percent Li for the first cycle of the sputtered Ag film of Figure 5.17.

5.5. The Reaction of Li with Sputtered Zn

Figure 5.19 shows the phase diagram for the Li-Zn binary system. There are many phases in this system, with most of them occurring for compositions with less than 50 at. % Li. From this figure, one would expect to see several sharp peaks in the dQ/dV *versus* potential graph for a Zn electrode, which is shown in Figure 5.20.

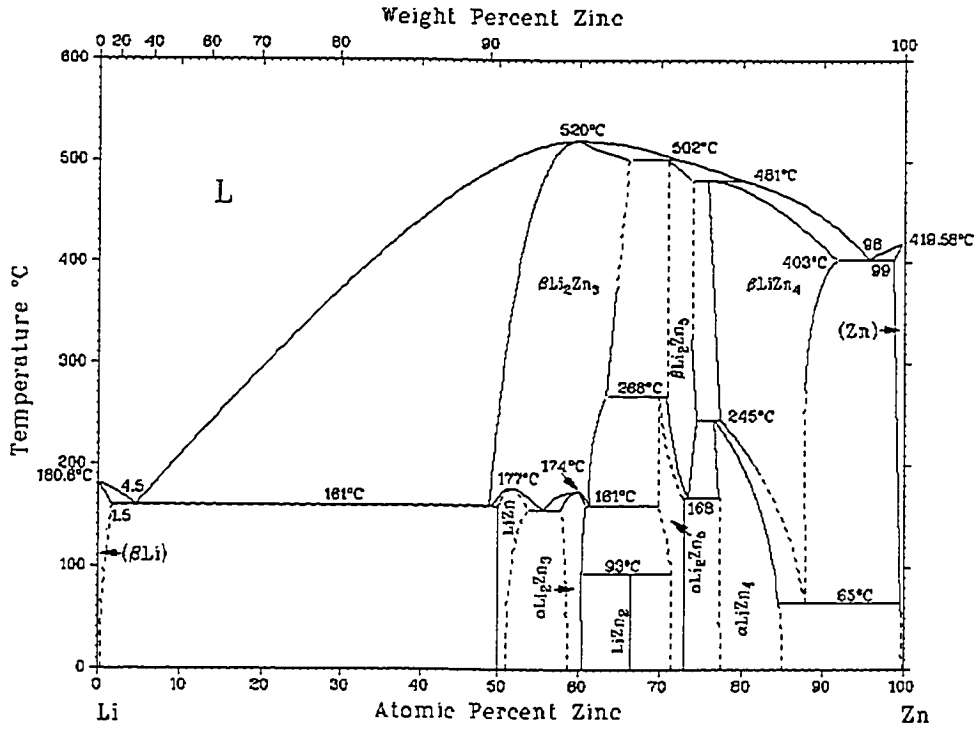

Figure 5.19. The Li-Zn binary phase diagram [93].

During the discharge in Figure 5.20, there are five sharp peaks in the dQ/dV *versus* potential plot. These peaks represent the transitions between phases in Figure 5.19. Figure 5.21 shows a portion of the LiZn phase diagram from Figure 5.19 and potential *versus* atomic percent Zn for the first cycle of the sputtered Zn film from Figure 5.20. The first long plateau at about 0.2 V corresponds roughly to the formation of the $\alpha LiZn_4$ phase. The long sloping region after the 0.2 V plateau covers several phases including αLi_2Zn_5, $LiZn_2$ and αLi_2Zn_3. It is unclear if all (or any) of these phases form or perhaps just the last. These plateaux correspond to the two large peaks near 0.2 V during discharge in Figure 5.20. The last region of the discharge would correspond to the formation of LiZn at just above 0 V. In Figure 5.20, this final region has two peaks in the dQ/dV *versus* potential graph. It seems that the transition from αLi_2Zn_3 to LiZn is

a two-stage process, but what these stages are is not clear. An *in-situ* XRD experiment could shed some light on the matter. The capacity achieved for this cell is just under 400 mAh/g. A capacity of 410 mAh/g would correspond to the LiZn phase being fully formed during the insertion of Li.

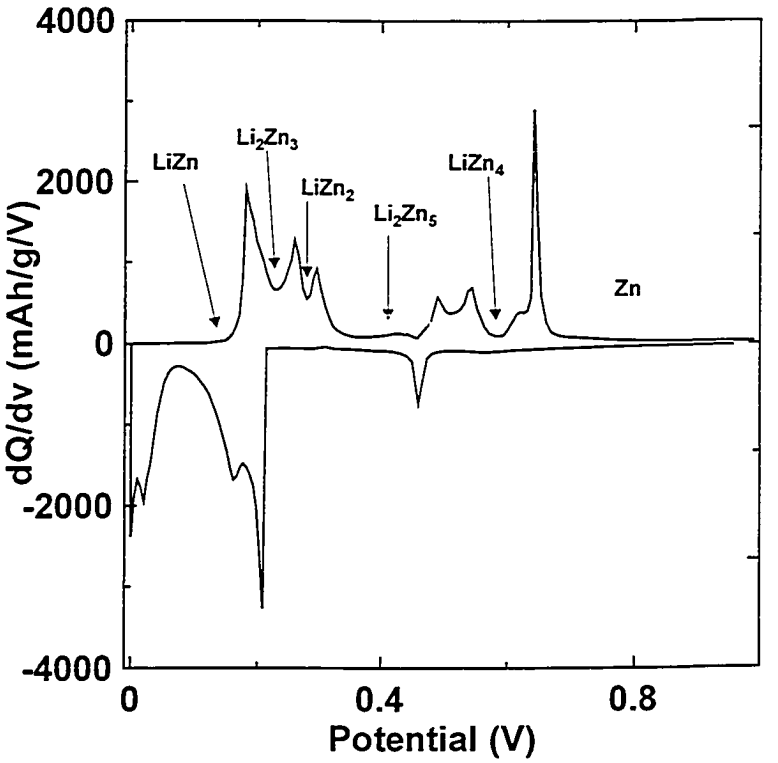

Figure 5.20. dQ/dV *versus* potential for a sputtered Zn film.

During the charge portion of the cycle, there are eight separate peaks in the dQ/dV *versus* potential relationship. It seems that during removal of Li, the electrode passes through each phase on the diagram from LiZn to pure Zn. Some phases have been labelled for the charge in Figure 5.20. In Figure 5.21, the charge portion of the graph of potential *versus* atomic percent Zn follows the phase diagram more closely than for the discharge. This means that the process of Li removal follows a different path than Li insertion. It should not be very surprising that lithium insertion or removal does not closely follow the equilibrium

phase diagram or that a different path is taken during charge and discharge. One would expect the phase diagram to be followed closely only for an equilibrium process, and the electrochemical insertion or removal of Li at room temperature and finite rates is certainly not an equilibrium process.

It is interesting that the $LiZn_9$ phase that appears in [102] is not on this phase diagram. The $LiZn_9$ phase does appear in an *in-situ* XRD cell to be described below. This phase could cause the first peak during charge in Figure 5.20 (first plateau during discharge in Figure 5.21).

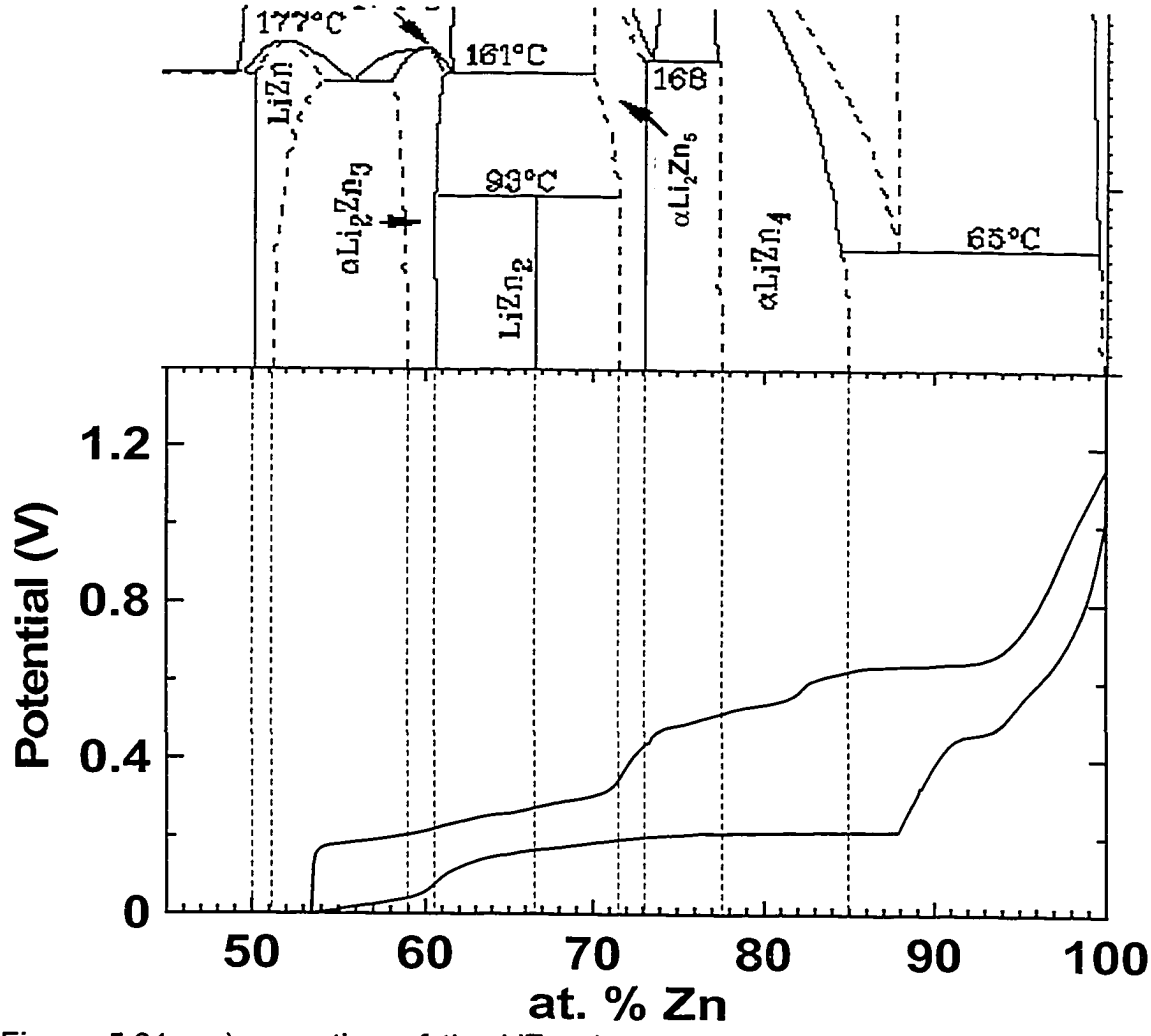

Figure 5.21. a) a portion of the LiZn phase diagram and b) potential *versus* atomic percent Zn for the first cycle of the sputtered Zn film of Figure 5.20.

Chapter 6. Si-M Binaries

6.1. SiSn

6.1.1. $Si_{1-x}Sn_x$ Binary Results

The first Si-M binary system to be studied was the SiSn system. Both Si and Sn can react with a large amount of Li so it is hoped that these alloys will have good capacity retention and low irreversible capacity. The SiSn phase diagram in Figure 6.1 indicates no SiSn phases or significant solid solubility of Si and Sn. It has been shown that sputtering can produce a large amorphous region in this binary system.

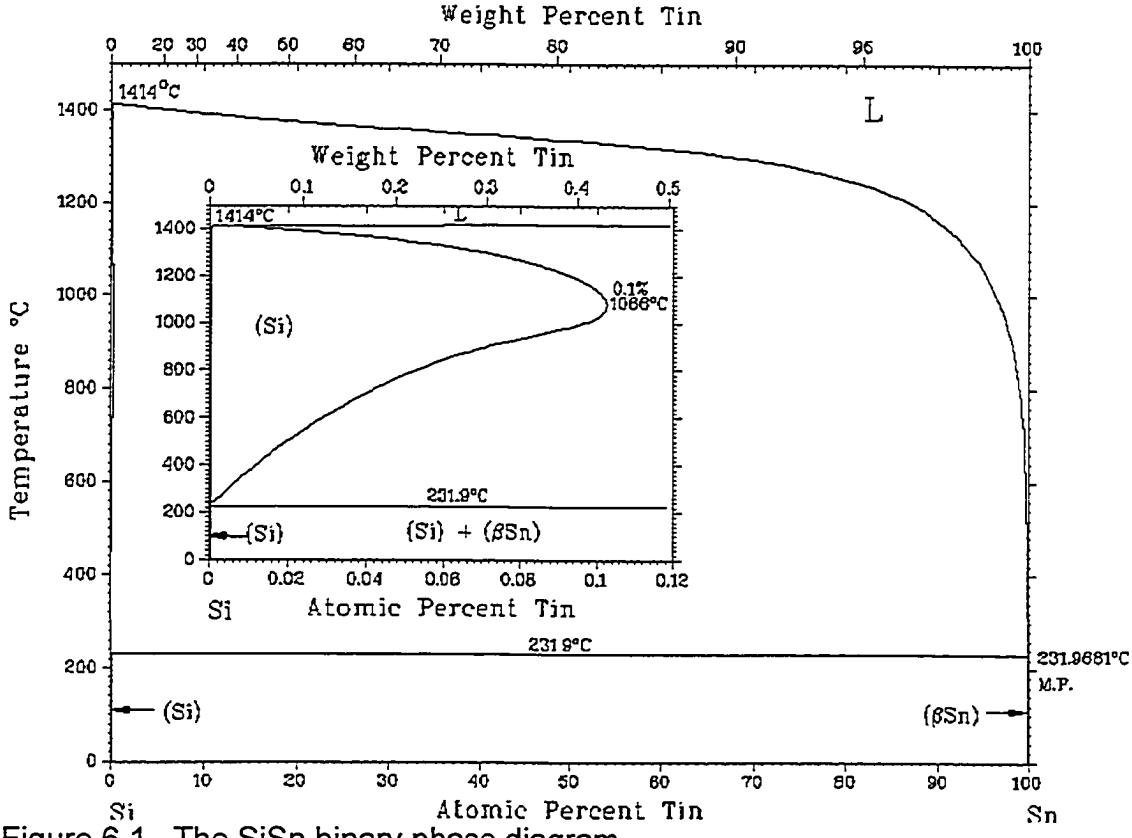

Figure 6.1. The SiSn binary phase diagram.

SiSn binary libraries were prepared using the sputtering system described in Chapter 3. The stoichiometry range of $0 < x < 0.5$ in $Si_{1-x}Sn_x$ was desired

because it has been shown [62, 98] that this is the amorphous range attainable in sputtered SiSn libraries. As was described in Chapter 1, amorphous electrodes tend to perform better than their crystalline counterparts. Figure 6.2 shows the electron microprobe data collected from the library sputtered on a 76 mm x 76 mm copper foil. It shows that a linear variation in the atomic percent of Sn was achieved as desired. From the figure it is seen that the range of stoichiometries covered in this library was approximately $0 < x < 0.45$ in $Si_{1-x}Sn_x$. The copper foil was placed so that a line through its center was along the radius of the substrate table. The microprobe data points that were closest to this line were used to derive composition as a function of the distance from the center of the machine. This function could then be used to determine the composition of each individual electrode of the combinatorial cell. When this is combined with the mass per unit area as a function of position, which was determined from the pre-weighed copper disks included in the run, the theoretical capacity for each of the 64 cells can be determined.

The composition range shown in Figure 6.2 is entirely within the amorphous range for Si-Sn libraries produced by sputtering, so we would not expect to see any evidence of crystalline material. Figure 6.3 shows the x-ray map for this library, produced using the Si (111) wafer that was included in the sputtering run. The angular range displayed is from 20° to 50°, and the direction of increasing Sn content is marked with an arrow. As can be seen the library is amorphous at every data point.

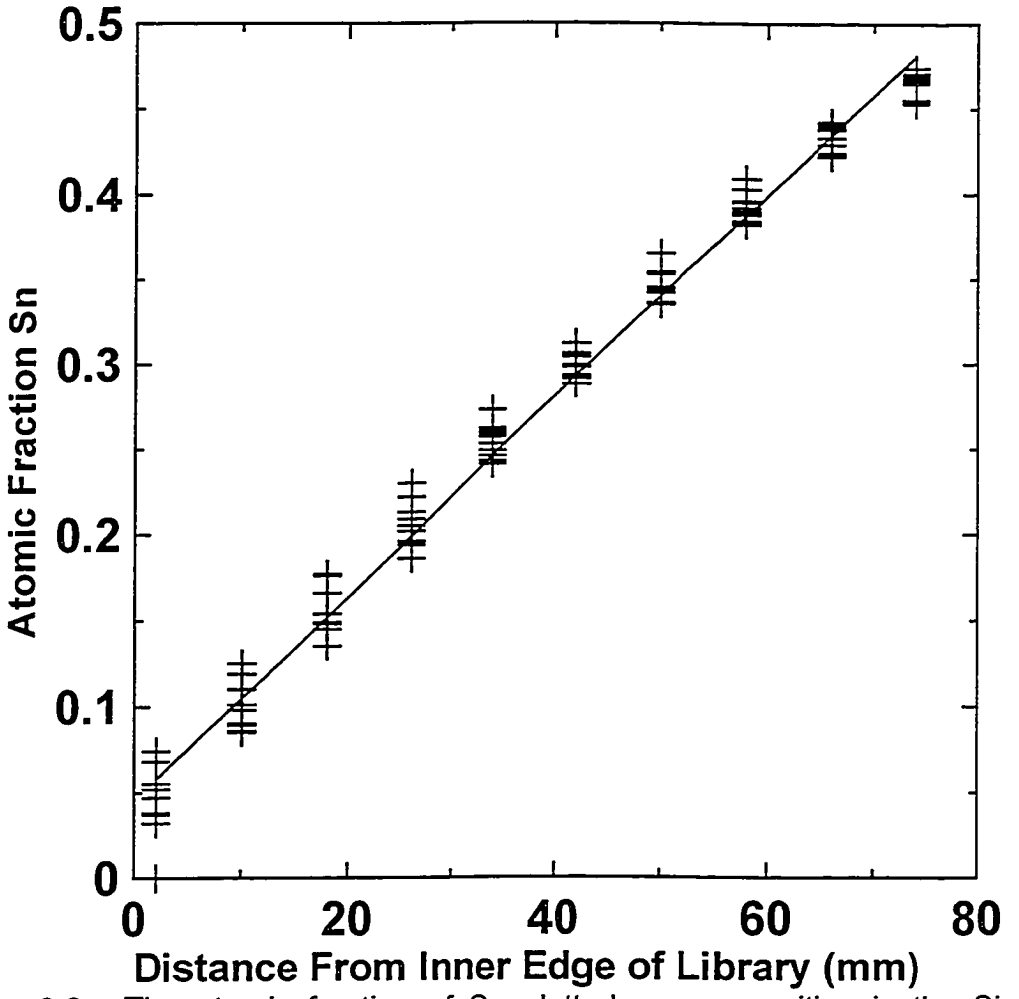

Figure 6.2. The atomic fraction of Sn plotted *versus* position in the $Si_{1-x}Sn_x$ binary library as determined by electron microprobe.

Figure 6.4 shows the graph of current *versus* potential for each of the 64 individual cells that make up the combinatorial electrochemical cell. These are analogous to differential capacity *versus* potential plots. The direction of increasing tin content is marked with an arrow. The voltage range shown is between 0 and 1.2 V and the current varies between -5×10^{-5} A and 5×10^{-5} A. The voltage sweep rate was 0.03 mV/s. By examining the columns of plots it can be seen that the shape of the graphs changes slightly as Sn is added to the film.

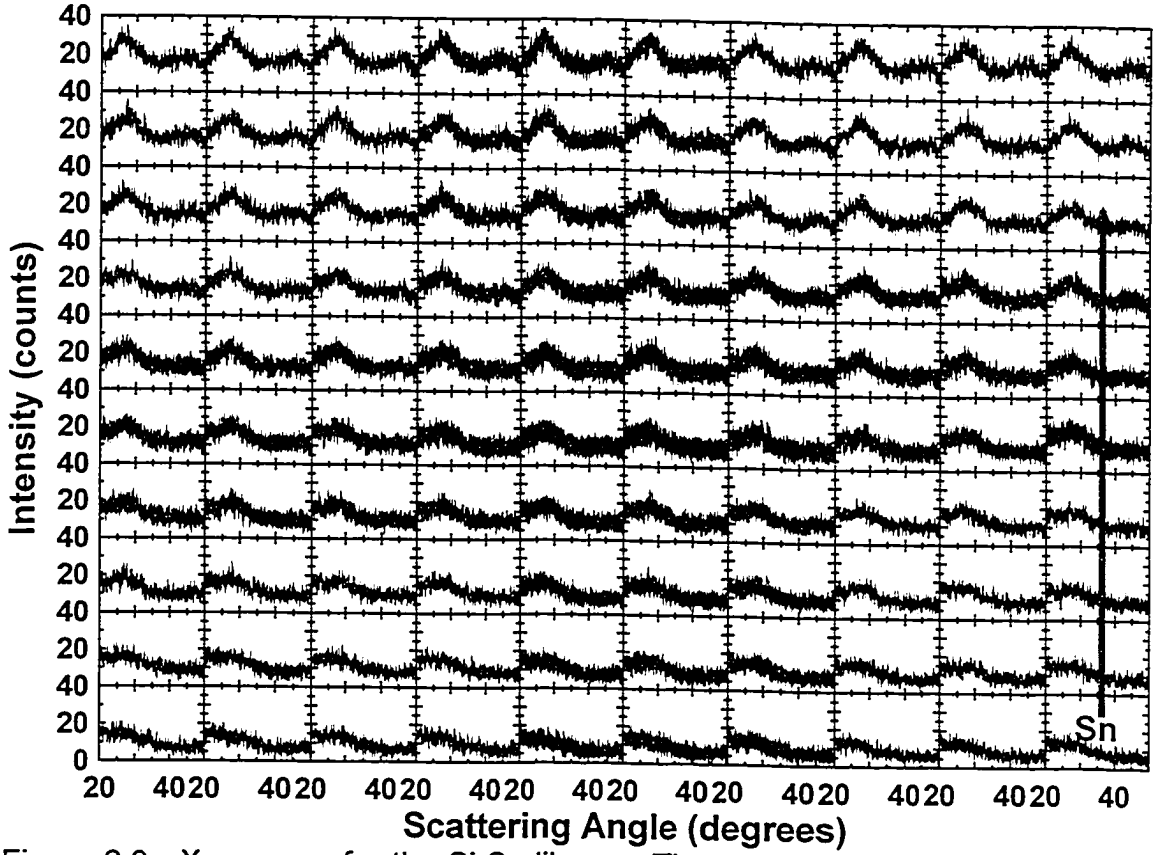

Figure 6.3. X-ray map for the Si-Sn library. The scattering angle range is from 20 to 50 degrees for each panel. The y-axis for each panel runs from 0 to 100 and is the number of counts in 300 seconds. The direction of increasing Sn is marked with an arrow.

Figure 6.5 shows the current *versus* potential plots for one column of cells (33 – 40) on the same axis so that the details may be more easily observed. Only one charge/discharge cycle (the 2nd) is shown to make the graph easier to view. No significant changes occur to the shape of the plots after the 2nd cycle. The approximate composition of each cell is indicated. The shape of the curve changes as tin is added to the film. In particular, the lower voltage of the two humps in the profile remains relatively unchanged as tin content increases (both during charge and discharge), while the higher potential hump grows in size. Also, the lower voltage hump sharpens when only a little Sn is present. Near

maximum Sn content, the higher voltage peak shifts to higher potential during charge and to lower potential during discharge. This behaviour may be related to the fact that the amorphous limit of tin concentration is being approached.

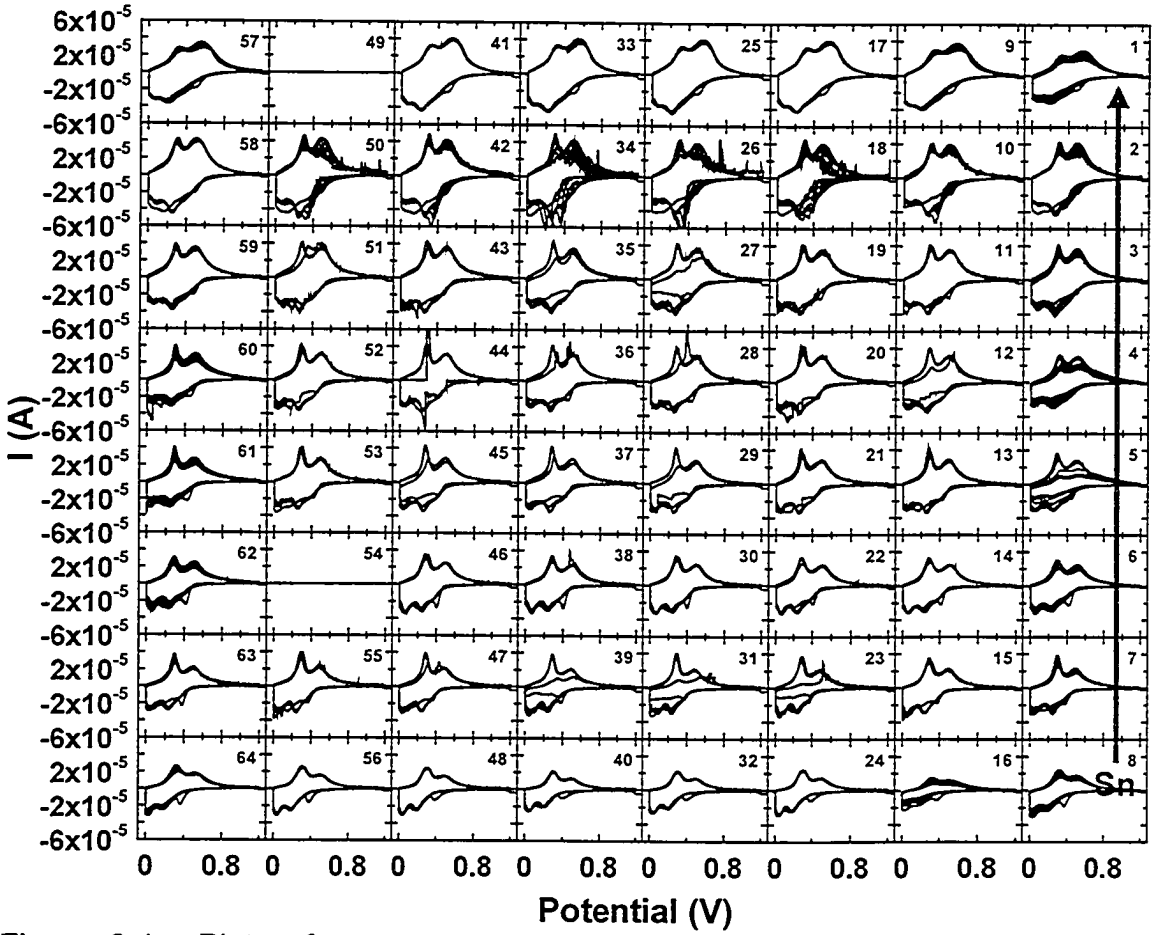

Figure 6.4. Plots of current *versus* potential for cells made from the Si-Sn combinatorial library. The potential limits are 0 to 1.0 V and the current limits are -6 x 10^{-5} to 6 x 10^{-5} A. The sweep rate was 0.03 mV/s. The direction of increasing Sn is marked with an arrow. Ten charge/discharge cycles are shown.

Many of the channels of the combinatorial cell (examples are channels 23, 28, 31 and others) show quite different behaviour between the first cycle and subsequent cycles. For many of these channels there seems to be very high impedance that goes away after the first cycle. This could be caused either by problems with cell construction (improperly wetted separator, heavily passivated

lithium metal, argon bubbles between separator and cell plate) or by the material itself. This type of anomalous first cycle, or formation cycle, has been experienced by others as well (ex. [49, 58]). The reasons for this behaviour are not fully understood, but for the affected channels of the combinatorial cell the subsequent cycling does not seem to suffer and the irreversible capacity for these channels is not nearly as large as that found for other alloy materials.

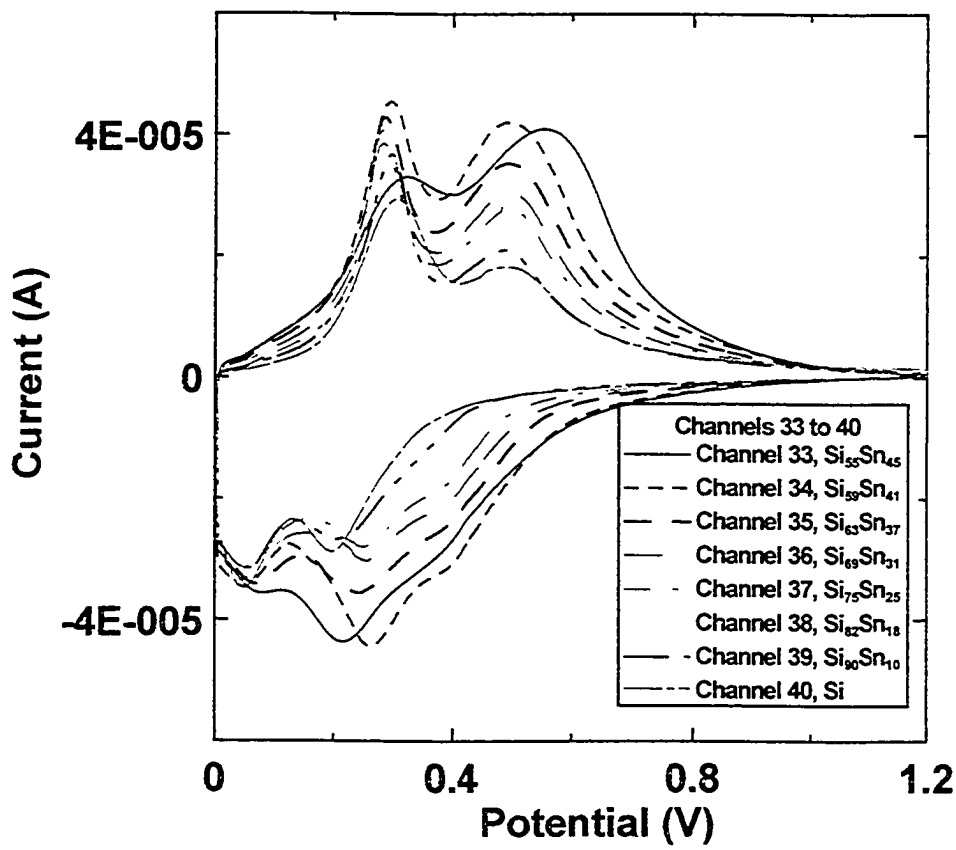

Figure 6.5. Plots of current *versus* potential for the second cycle of a representative column of cells from Figure 6.4 (cells 33 to 40). The approximate composition of each cell is indicated in the figure.

Figure 6.6 shows plots of capacity *versus* potential for each of the 64 channels on the cell plate. In this graph, voltage ranges from 0 to 1.2 V and capacity ranges from 0 to 0.228 mAh. The direction of increasing Sn content is again shown with an arrow. These graphs each have two gently sloping plateaus

during charge and discharge corresponding to the broad humps seen in Figure 6.4. It is evident that the capacity increases as Sn is added to the constant amount of Si in the film (not specific capacity, as this data is not scaled for mass). It should be noted that some of the data around the edge of the cell does not appear to be very good. In particular, some of the graphs (e.g. channels 2, 3, 4, 5, 6, 7) "walk" to the right. The most likely reason for this is a small leak around the o-ring of the combinatorial cell. Small amounts of air (and therefore water) could be leaking into the cell. Oxygen or water would react with lithium in the electrode. During discharge, this causes the current to be higher than it would be in the absence of the leak, so the capacity measured is too high. During charge, the current is lower than it should be (normal current – current from Li reacting with water/oxygen) so the capacity measured is too low. This causes the capacity *versus* potential plot to move a little to the right each cycle.

Figures 6.4 and 6.6 show that the cells in the Si-Sn library generally cycle quite well, regardless of composition. Some cells around the edges of the cell plate show some problems, but this could be because of the combinatorial cell itself, and not the material. Also, the second row of cells from the top shows some poor performance. This row is made up of cells that have approximately 40 atomic percent Sn. There may be something about this particular composition that causes it to cycle poorly. However, a major benefit of the combinatorial approach used here is that we have obtained eight sets of data for each stoichiometry in one experiment. Two of the channels in the second row cycle quite well, so the material must be capable of performing at least that well.

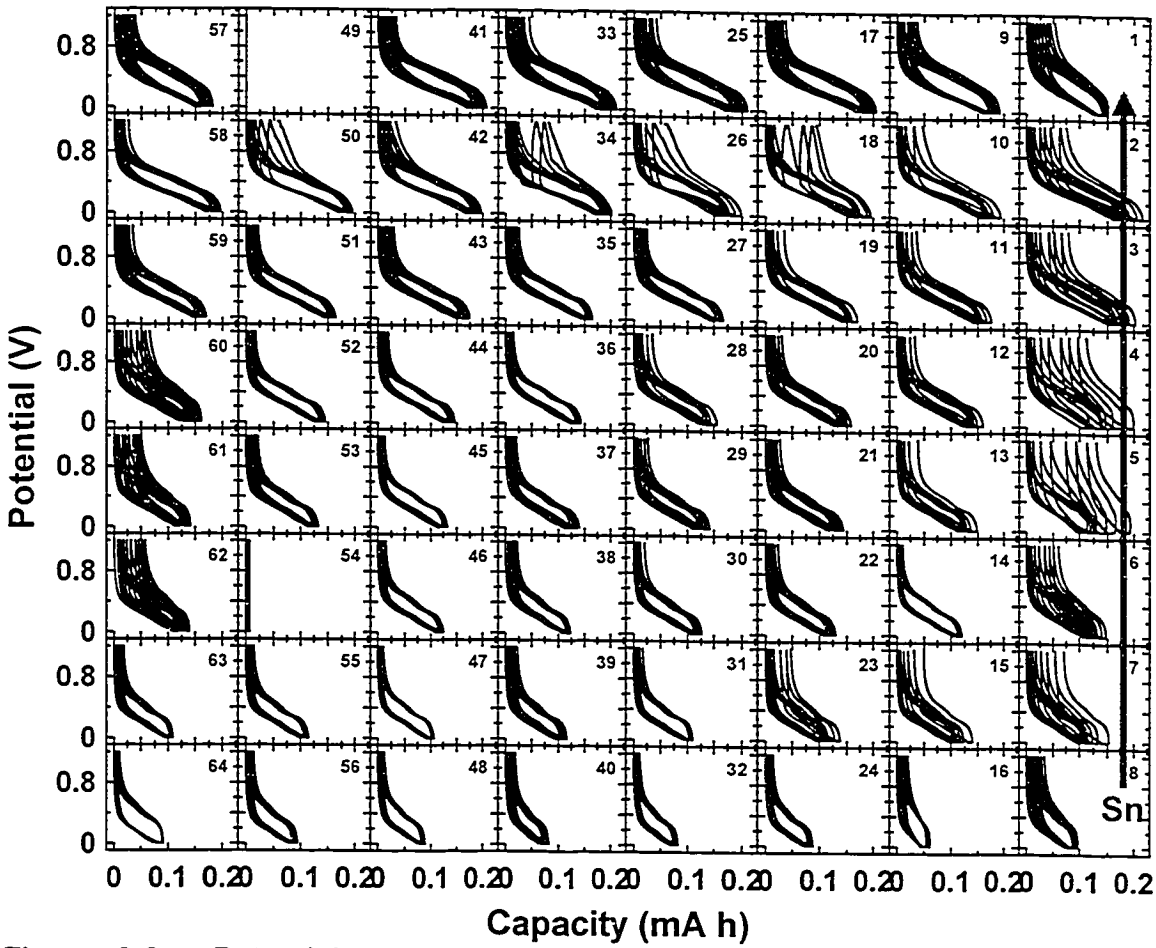

Figure 6.6. Potential *versus* capacity for the cells made from the Si-Sn combinatorial library. The voltage limits are 0 to 1.2 V and the capacity limits are 0 to 0.228 mAh. The direction of increasing Sn is marked with an arrow. Ten charge/discharge cycles are shown.

Figure 6.7 presents graphs of discharge (+) and charge (◊) capacity *versus* cycle number for all 64 cells. This figure shows that the capacity is very stable for at least two cells of all compositions. Capacities of 3500 mAh/g were attained for cells with the highest Si content, dropping to just under 2000 mAh/g for the highest Sn content.

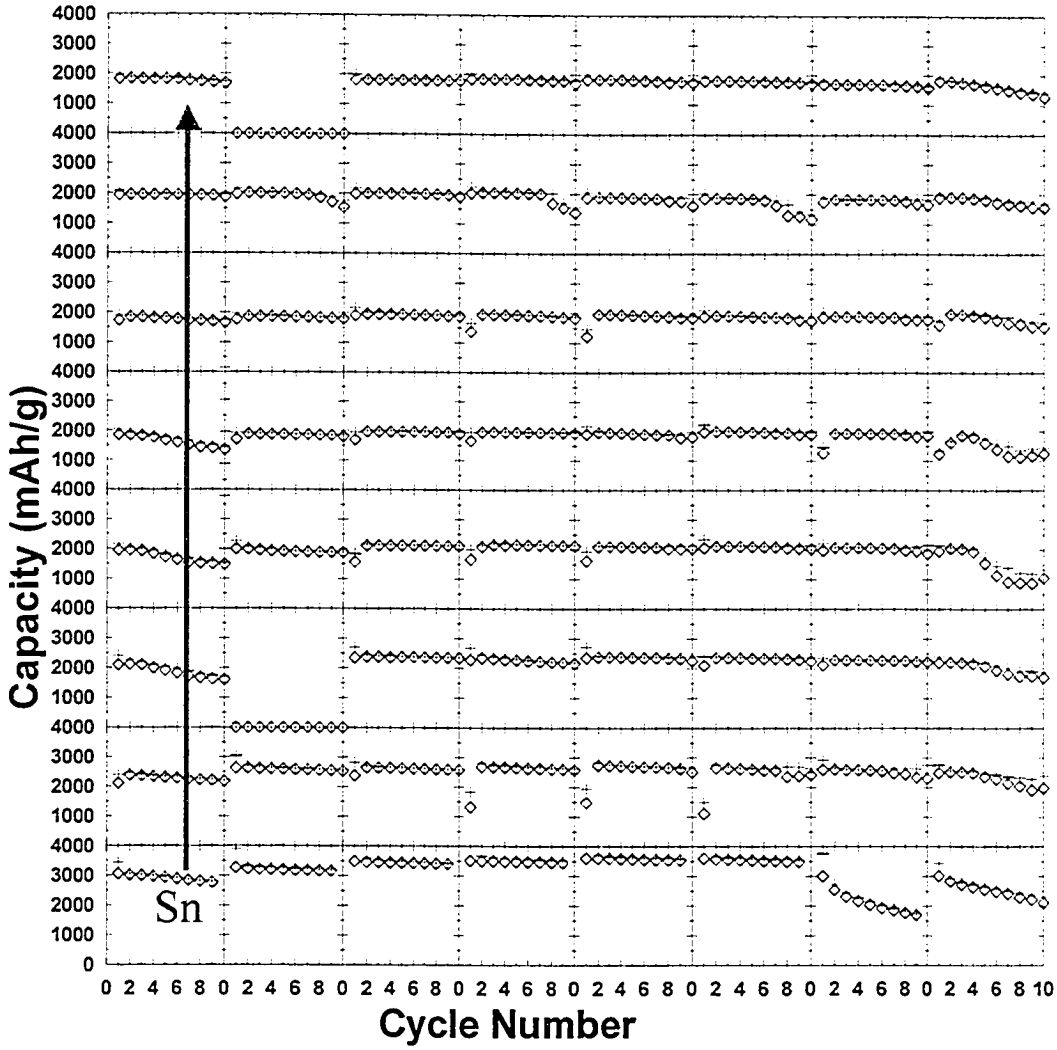

Figure 6.7. Specific capacity *versus* cycle number for the cells made from the Si-Sn combinatorial library. + - discharge; ◊ - charge.

The irreversible capacity (taken as [1 - (first charge capacity)/(first discharge capacity)]) for these cells is plotted *versus* Sn content in Figure 6.8. The irreversible capacity is generally below 15% of first discharge, with a few exceptions. The highest irreversible capacity was less than 30% and occurred in 3 cells with approximately 12 atomic percent Sn (Channels 31, 39 and 47 in Figure 6.6) that showed large first cycle impedance. Other cells with almost the same composition, that did not have this large first cycle impedance, did not

show such large irreversible capacity, so we believe it is an artifact of the high first cycle impedance. The remaining data shows that there appears to be a weak dependence on composition, with the irreversible capacity dropping to below 10% for cells with more than 30 atomic percent Sn.

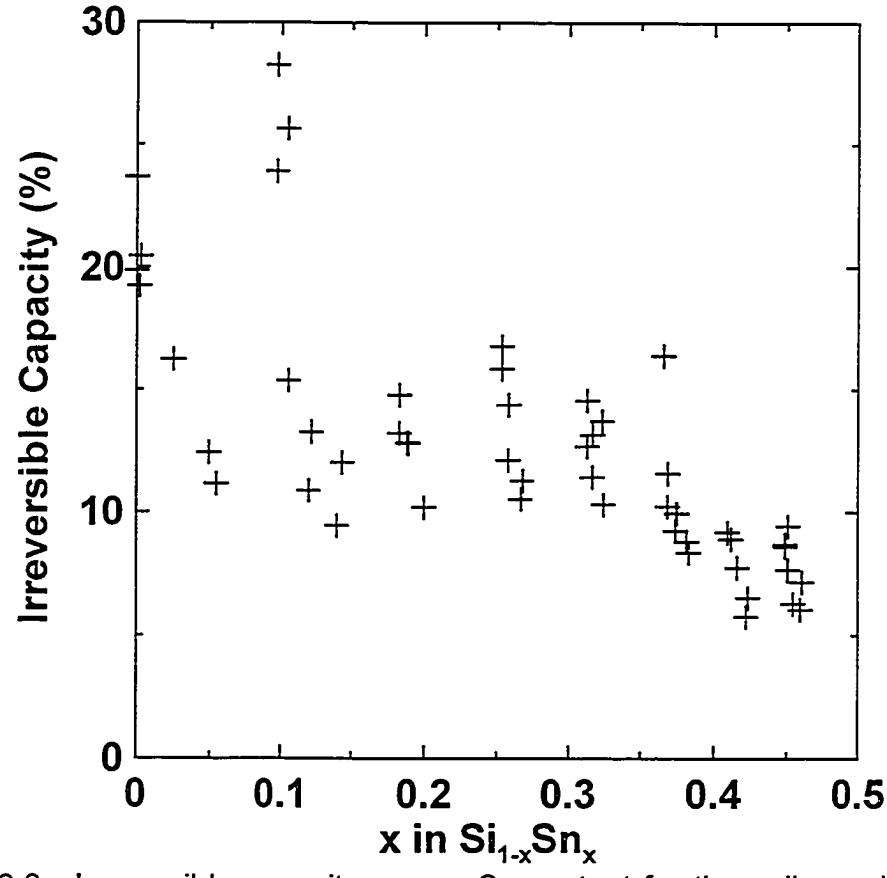

Figure 6.8. Irreversible capacity *versus* Sn content for the cells made from the Si-Sn combinatorial library.

The theoretical capacities of the channels of the SiSn combinatorial library, plotted in Figure 6.9, were calculated based on the following equation:

$$\text{Theoretical Cap.} = \frac{(M_{Si}) * (TC_{Si}) * (1 - x) + (M_{Sn}) * (TC_{Sn}) * (x)}{(M_{Si}) * (1 - x) + (M_{Sn}) * (x)} \qquad 6.1.$$

In equation 6.1, M_A is the molar mass of element A and TC_A is the theoretical capacity of element A. The theoretical capacity of Si is assumed to be 4199 mAh/g, based on the fully lithiated phase of $Li_{4.4}Si$ ($Li_{22}Si_5$) from the equilibrium phase diagram for the SiSn system. The theoretical capacity of Sn is 990 mAh/g, based on a fully lithiated phase of $Li_{4.4}Sn$. The molar mass of Si is 28.1 g/mol and for Sn it is 118.7 g/mol.

Figure 6.9 shows graphs of theoretical capacity (+), second discharge capacity (◊) and tenth discharge capacity (Δ) *versus* x in $Si_{1-x}Sn_x$. From this figure, it can be seen that for those compositions highest in Si content, the full theoretical capacity is not achieved. Those compositions that are more Sn rich, however do achieve nearly 100 % of their theoretical capacity. This figure also shows the generally small amount of capacity loss on cycling. The second and tenth discharges are generally very close to each other, if not directly on top of each other. The capacity fade as a function of Sn content is plotted in Figure 6.10. Capacity fade is generally between 0 and 2% per cycle, with most being below 1% per cycle. There may be a very weak correlation present between composition and capacity fade rate from this data. The best materials, from a fade rate perspective, appear to have a composition near x = 0.3. By comparing fade rates of similar composition within a single combinatorial cell, it was found that the uncertainty in fade rates was about ± 0.2% per cycle. This can be used as an estimate of the error in fade rates within a cell plate. From one cell plate to another, the uncertainty is somewhat higher and is about ± 0.7% per cycle. These errors are consistent for all systems studied, not just the SiSn binary.

As was discussed in Chapter 5, it seems that the fully lithiated phase of Si in room temperature electrochemical cells is $Li_{3.75}Si$ ($Li_{15}Si_4$). Figure 6.11 presents the theoretical capacities and 2nd discharge capacities for the SiSn library with the theoretical capacities calculated assuming only 3.75 Li per Si, which gives a theoretical capacity of 3580 mAh/g instead of 4199 mAh/g.

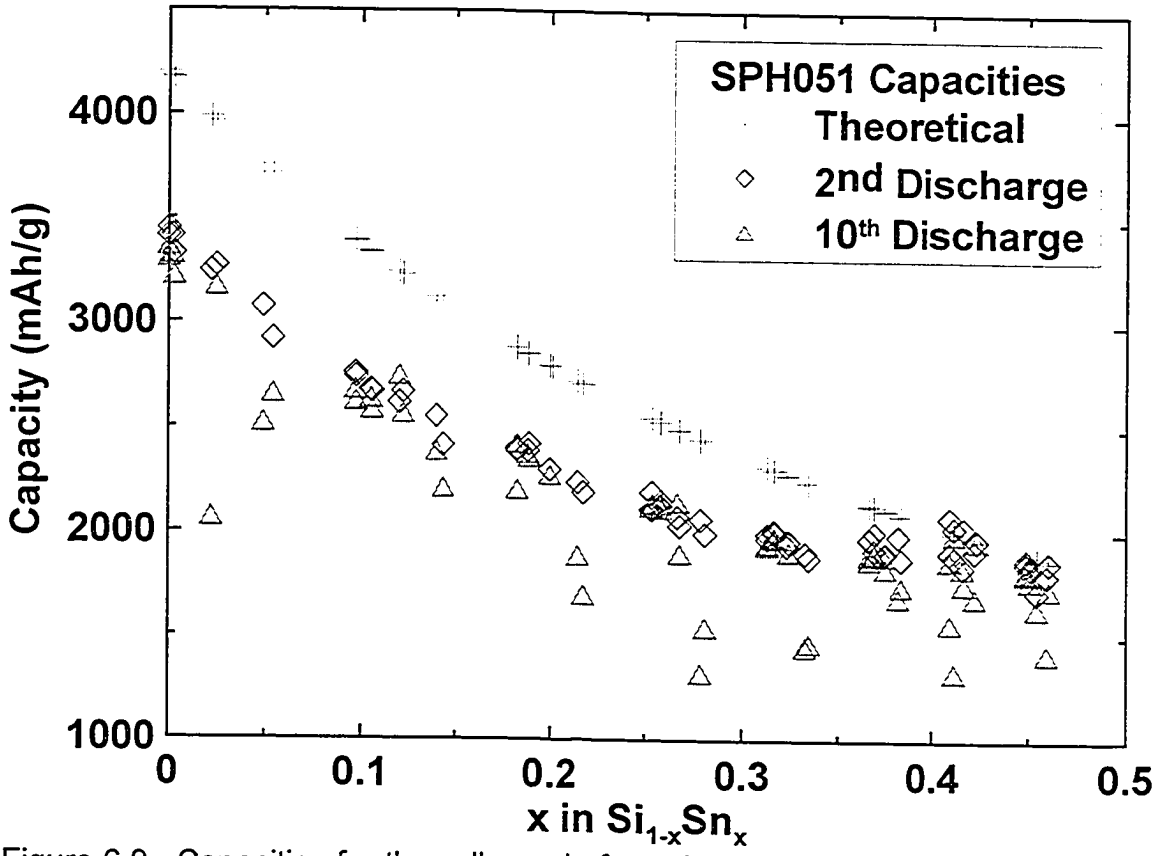

Figure 6.9. Capacities for the cells made from the Si-Sn combinatorial library: + - theoretical capacity; ◊ - 2nd discharge capacity; Δ - 10th discharge capacity.

For low Sn content, the discharge capacities observed now match the theoretical capacities very well (less by a few percent). It would appear that $Li_{15}Si_4$ is the fully lithiated composition for these electrodes, although they do not crystallize like the thicker ones discussed in Chapter 5.

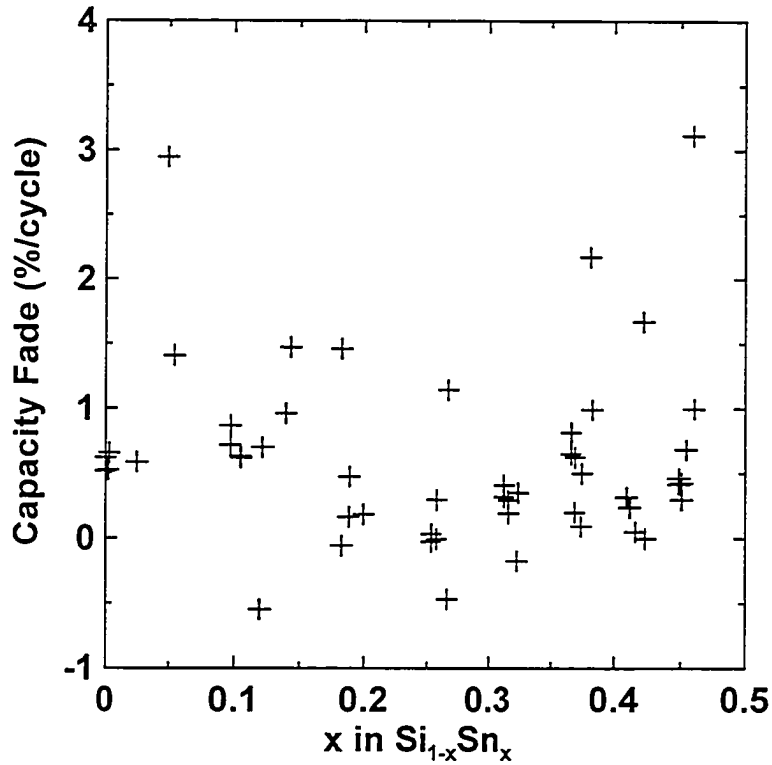

Figure 6.10. Detailed view of the capacity fade in percent per cycle *versus* Sn content for the cells made from the Si-Sn combinatorial library.

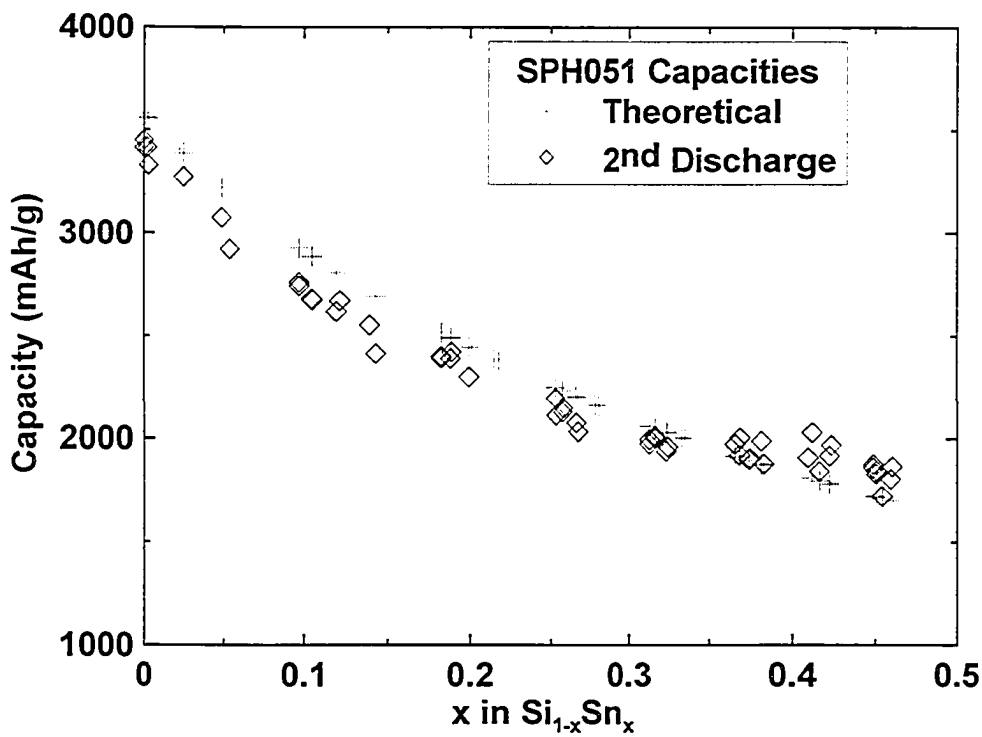

Figure 6.11. Theoretical capacities (+) and second discharge capacities (◊) for the cells made from the Si-Sn combinatorial library.

It should be noted that these results do not preclude the existence of $Li_{22}Si_5$. The $Li_{22}Si_5$ phase is an equilibrium phase, while the electrochemical alloying of Li with Si at room temperature and finite rates is not an equilibrium process. $Li_{15}Si_4$ seems to be the fully lithiated phase attainable in electrochemical test cells at room temperature. It is interesting that for high Sn content the discharge capacities exceed the theoretical capacity calculated assuming the final $Li_{15}Si_4$ state. The transition occurs somewhere above 30 atomic percent Sn, which is also where the irreversible capacity starts to drop to nearly 5%. It would seem that the presence of an adequate amount of Sn allows the material to reversibly reach the final $Li_{22}[Si_{1-x}Sn_x]_5$ phase (as indicated by the achieved capacity equaling the theoretical capacity for channels with high Sn content on the right of Figure 6.9), thus allowing the full theoretical capacity to be reached and also reducing the irreversible capacity.

6.1.2. Conclusions for SiSn

The Si-Sn binary system has been explored by use of combinatorial methods for the range $0 < x < 0.45$ in $Si_{1-x}Sn_x$. Capacities as high as 3500 mAh/g were attained for these materials. The irreversible capacity of all compositions in this range was found to be much smaller than for many other alloy systems reported in the literature, with a maximum of less than 30% and most below 15% with a minimum of ~6 %. Also, the cycling was generally very good, with no strong correlation with composition. Reversible capacities of nearly 3500 mAh/g can be achieved for thin films of Si-Sn with high Si content.

As was seen, the basic shape of the cyclic voltammograms and the capacity *versus* potential plots for all cells were essentially the same, with two broad humps during both charge and discharge. The humps in the voltammograms and the plateaus in the capacity *versus* potential plots all occurred at the same voltage, except for those samples highest in Sn content. All that changed was the relative size of the humps or plateaus. Changes in behaviour do not begin to occur until the amorphous limit of Sn content is approached. Figure 6.12 is a repeat of Figure 6.5 with an additional graph added. The new graph is the current *versus* potential relationship for a coin cell that had a composition of $Si_{42}Sn_{58}$. This is outside of the amorphous range for SiSn. The shape of the graph has changed significantly now, with sharp peaks appearing during both charge and discharge. These peaks are from the crystalline Sn in the cell (see Figure 5.14).

In all of the channels of the combinatorial cell, there was never any evidence found of any crystalline material, either in the as sputtered film by XRD or through analysis of the electrochemical data. Given the behaviour of a-Si films discussed in Chapter 5, one might expect to see some crystallization of the $Li_{15}Si_4$ phase, although the SiSn library studied here was quite thin. The lack of crystallization of the $Li_{15}Si_4$ phase and the fact that adequate Sn content seems to allow the $Li_{22}M_5$ phase to be reached could be viewed as evidence that Sn suppresses the formation of the $Li_{15}Si_4$ phase in electrochemically lithiated a-Si.

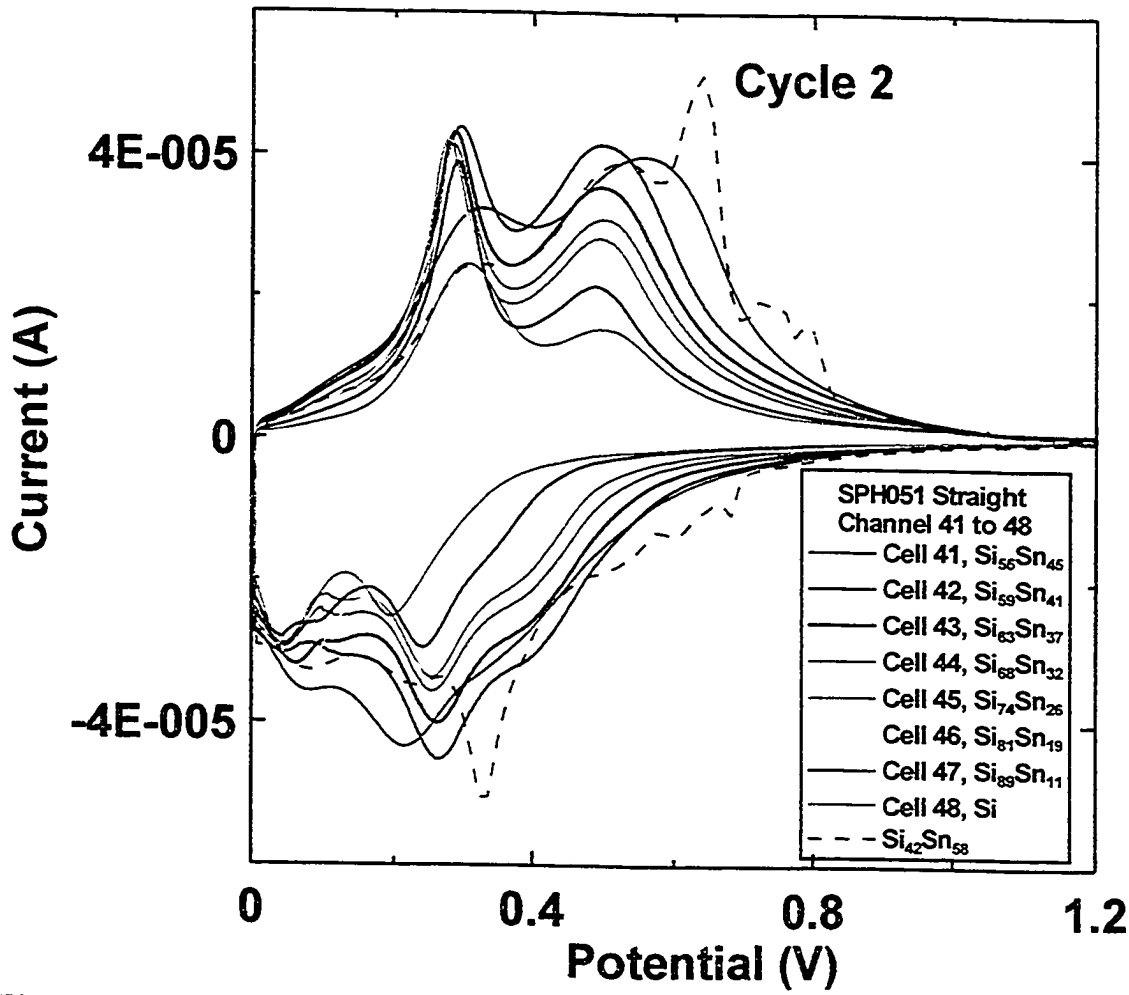

Figure 6.12. Plots of current *versus* potential for the second cycle of a representative column of cells from Figure 6.4 (cells 33 to 40) and a coin cell with higher Sn content. The approximate composition of each cell is indicated in the figure.

6.2. SiAg

6.2.1. $Si_{1-x}Ag_x$ Binary Results

The second Si-M binary system studied was the SiAg system. Ag can also react with a large amount of Li. As with the SiSn system, there are no SiAg phases in the phase diagram shown in Figure 6.13. It is hoped that a large amorphous range will be found for this system.

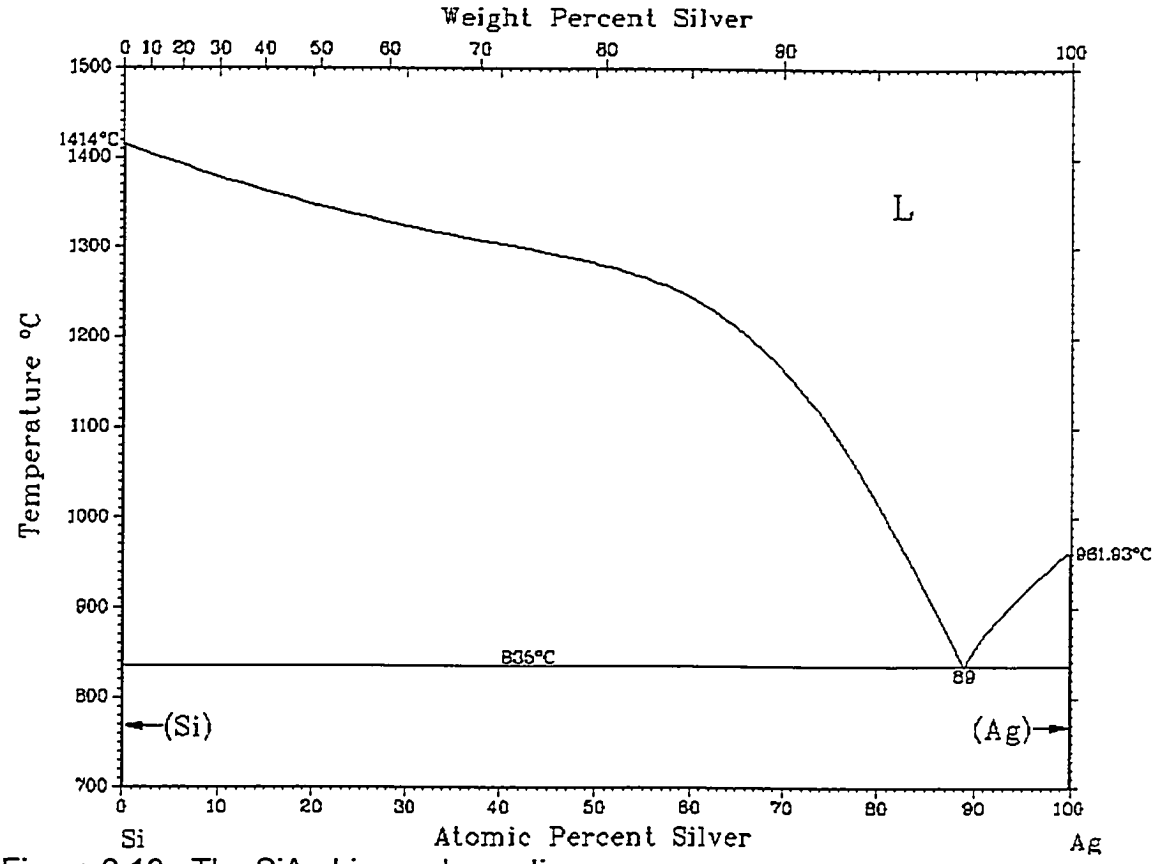

Figure 6.13. The SiAg binary phase diagram.

SiAg binary libraries were prepared using the sputtering system described in Chapter 3. Figure 6.14 shows a plot of the Ag:Si ratio as a function of distance from the center of the substrate table as determined by electron microprobe. The ratio runs from a minimum of about 0.12 to a maximum of about 1.2. This corresponds to approximately $0.12 < x < 0.55$ in $Si_{1-x}Ag_x$. Figure 6.15 shows the XRD patterns collected for a SiAg binary library. The graph shows intensity on the left y-axis and an estimate of position on the library on the right y-axis that can be used to determine the approximate composition for each scan. The thickness of the library ranges between approximately 0.5 to 2 μm.

Only the areas of the library with less than about 20 at. % Ag are amorphous, with the rest showing evidence of nanocrystalline Ag. The (111) peak of Ag at approximately $2\theta = 38°$ is present in most of the library. From the XRD data, it is expected that there should be evidence of crystalline material in the electrochemical data for the SiAg library.

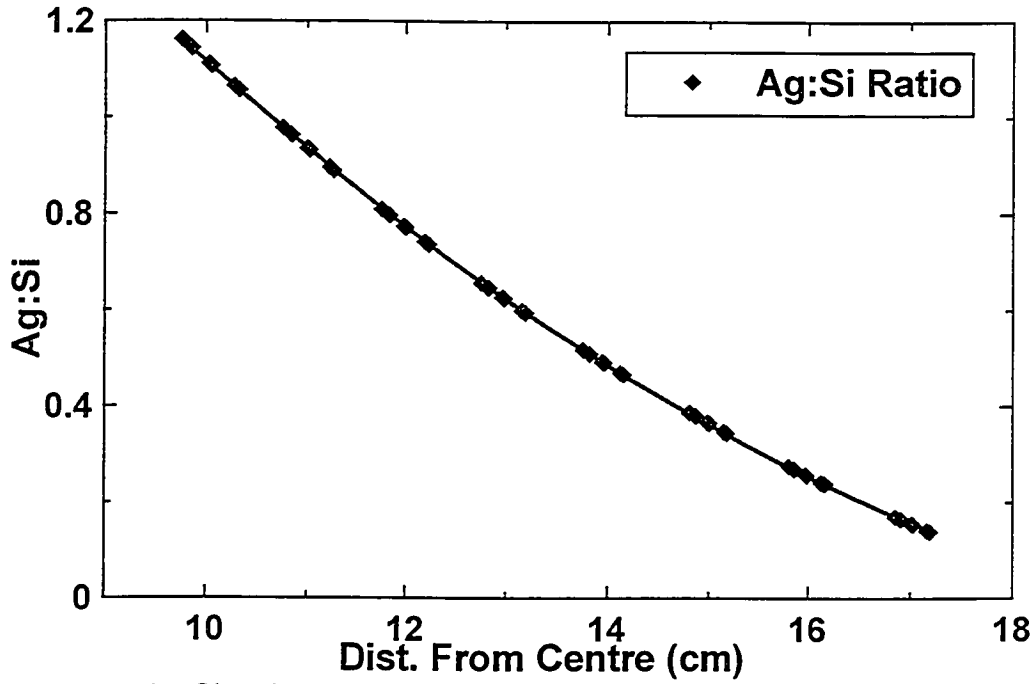

Figure 6.14. Ag:Si ratio as a function of position for the SiAg binary library as determined by electron microprobe.

Combinatorial cell plates were again used for the electrochemistry experiments on the SiAg libraries. As was the case with the SiSn library, eight sets of nearly identical data were obtained from the cell plates. One column, which is representative of the entire combinatorial cell, will be discussed. The column selected is made up of channels 25 to 32, a column from the center of the cell. The dQ/dV *versus* potential plots for these channels are shown in Figure 6.16. There is much more noticeable change in the shape of the graphs

in Figure 6.16 as Ag is added to the a-Si than was the case for SiSn. With the SiAg, however, some channels also show dramatic changes in shape of the dQ/dV *versus* potential plots with cycle number.

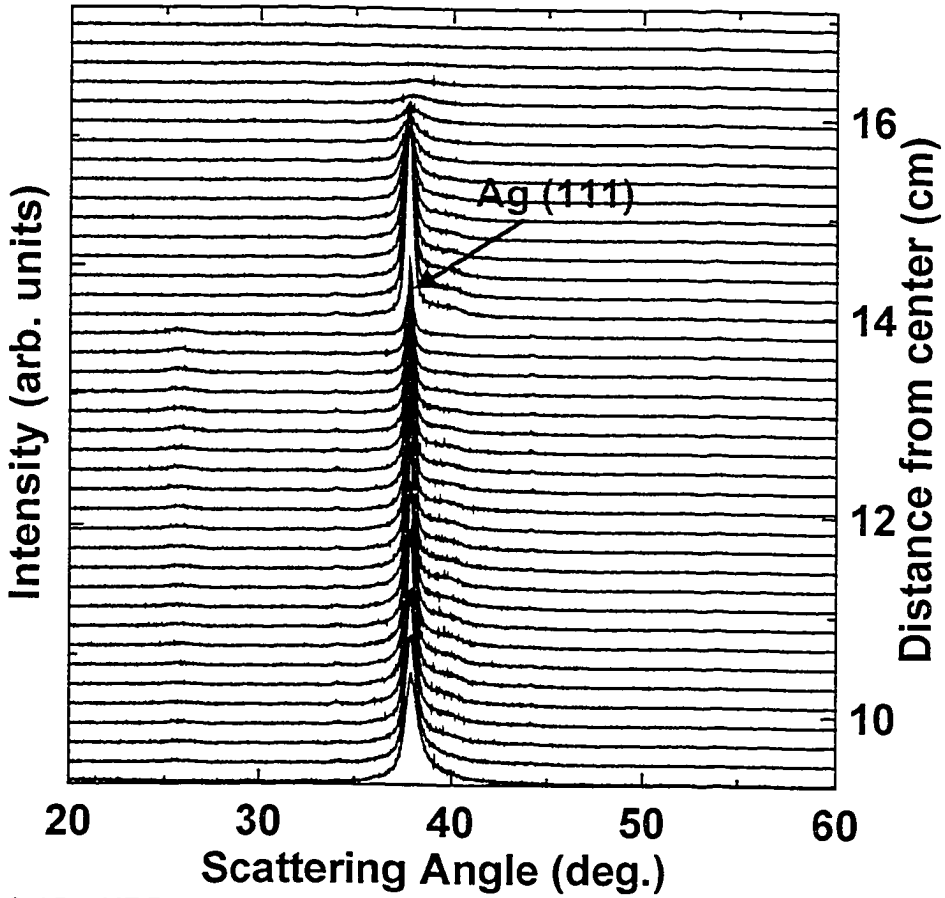

Figure 6.15. XRD patterns as a function of position for the SiAg binary library. The angular range shown is from 20 to 60°.

Figure 6.17 shows the first five cycles of channel 25. The composition of this channel is approximately $Si_{85}Ag_{15}$. A comparison with channels 38 and 39 of Figure 6.5 shows that the effect of adding a small amount of Ag to a-Si is very different than adding a small amount of Sn. A small amount of Sn does not change the overall shape of the dQ/dV *versus* V relation obtained for thin a-Si shown in Figure 5.2a, only strengthens the broad peak at about 0.5 V during charge. Ag, however, changes the shape of the graph very much. The lower

potential peak (around 0.3 V) has completely disappeared, leaving only the broad peak at 0.5 V.

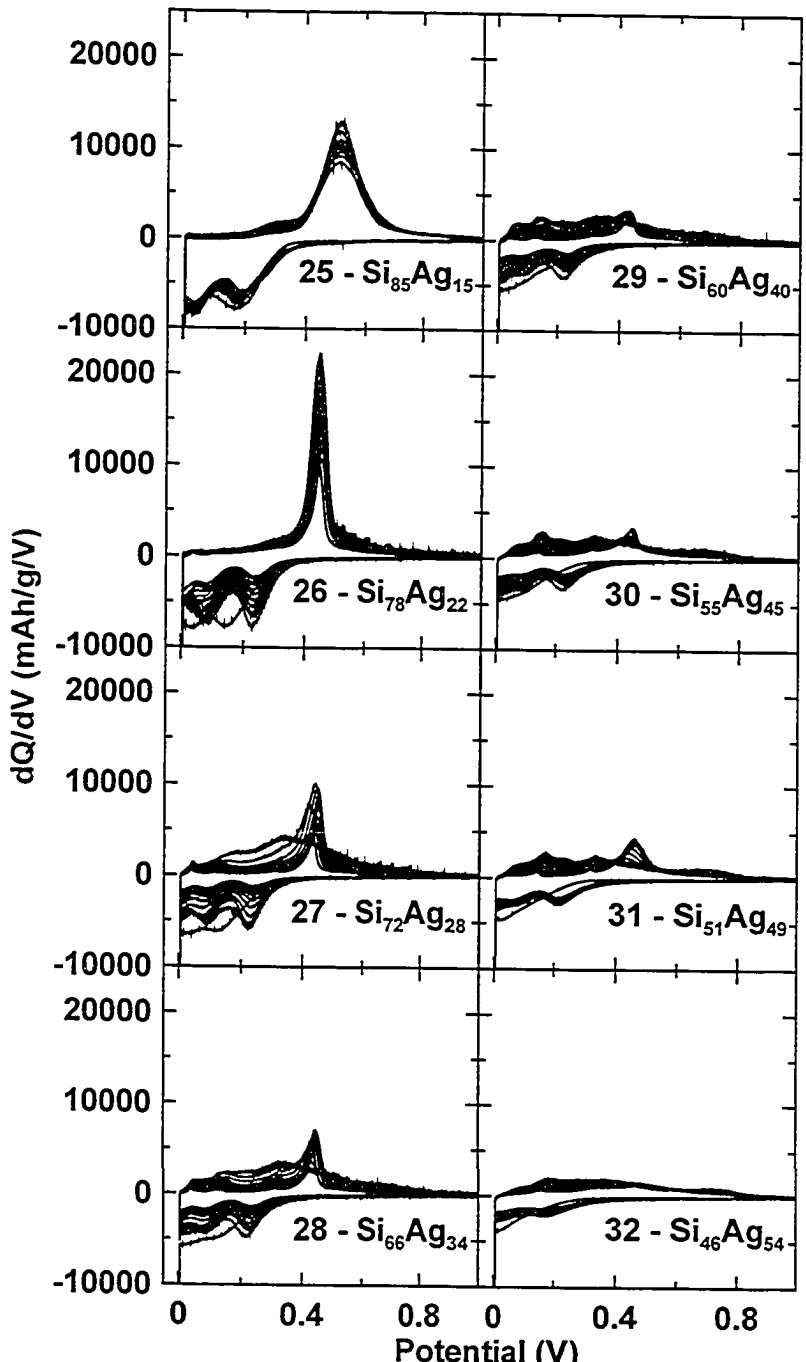

Figure 6.16. Graphs of dQ/dV *versus* potential for the first 12 cycles of one column of channels from a SiAg binary combinatorial cell plate. Approximate composition for each channel is indicated.

The graph in Figure 6.17 looks more like the graph in Figure 5.10b for a 4.5 μm thick a-Si film in which the film crystallizes to $Li_{15}Si_4$ below 30 mV. It is not clear if the $Li_{15}Si_4$ phase has formed for the film shown in Figure 6.17 because the peak during charge is quite broad and there is no obvious peak near the end of the first discharge that was found to be indicative of crystallization in Chapter 5. The inset in the figure shows an expanded view of the boxed area in the main figure. There is a very small peak during charge at low voltage that appears only during the first cycle. This is the only evidence of crystalline Ag for this film. The Ag may be incorporated in the $Li_{15}Si_4$ phase $\{Li_{15}(SiAg_x)_4\}$ and cause the broadening of the 0.4 V peak during the charge.

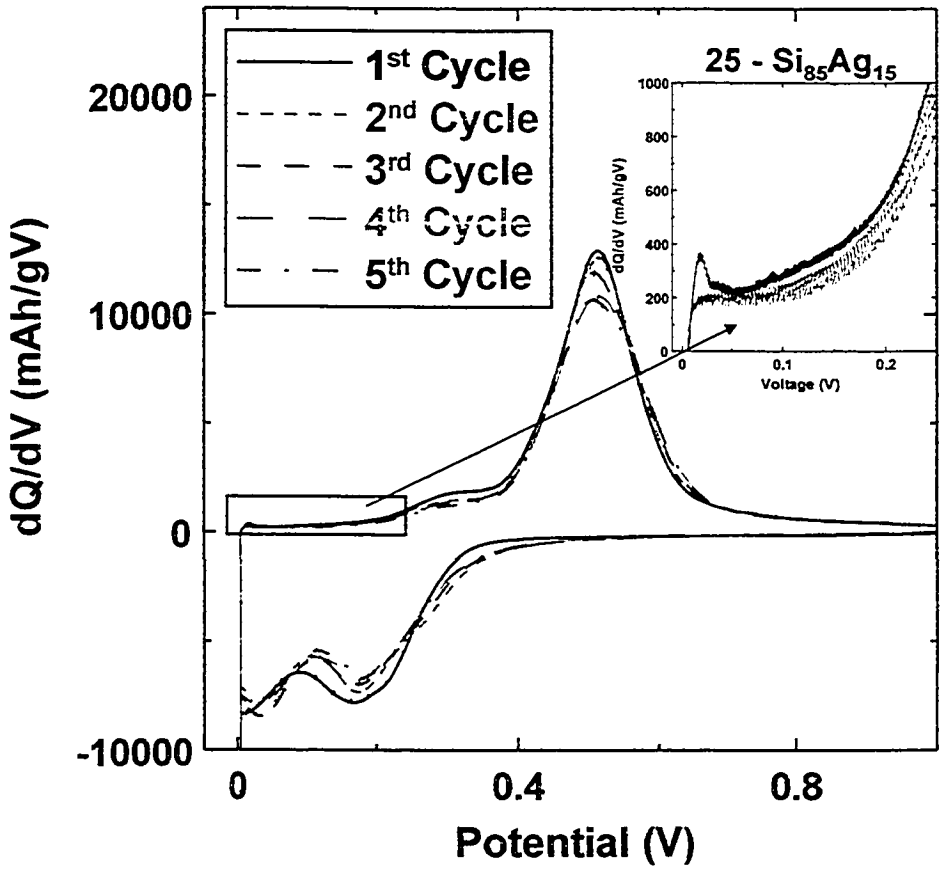

Figure 6.17. Plot of dQ/dV *versus* V for the first five cycles of channel 25 of the SiAg combinatorial cell plate. The inset shows an expanded view of the boxed area in the main figure.

Figure 6.18 shows the first five cycles of channel 26. The composition of this channel is approximately $Si_{78}Ag_{22}$. This graph is somewhat different than the graph for channel 25. The peak during charge is very much sharper for channel 26 and has also moved closer to 0.4 V, where the peak from the $Li_{15}Si_4$ is expected to be. It seems very likely that the $Li_{15}Si_4$ phase has formed for this channel, although it is below the thickness limit for crystallization found in Chapter 5 for a-Si. The inset in Figure 6.18 blows up the boxed region n the main figure. In this inset, the low voltage peaks of Ag are obviously present for the first few cycles. In this cell, it seems that the Ag is not incorporated in the $Li_{15}Si_4$ phase (no broadening of the 0.4 V peak during charge), but instead forms small particles of crystalline Ag that then react with Li normally.

There are no significant changes in the shapes of the graphs in Figures 6.17 or 6.18 with cycle number, indicating that the mechanisms occurring during each discharge and charge are the same.

Figure 6.19 shows the first five cycles of channel 27. The composition of this channel is approximately $Si_{72}Ag_{28}$. Note that the vertical scale on this graph has been changed from Figures 6.17 and 6.18 to make features easier to see. This graph is significantly different than the previous two.

During the first cycle, there is no evidence of the $Li_{15}Si_4$ phase forming for channel 27. There is no sharp peak either during discharge or charge. This graph actually looks more like a-Si than the previous two during the first cycle, even though there is more Ag for this channel. There is a small, broad hump near 0.7 or 0.8 V during charge. It is not clear what causes this hump as neither

a-Si nor Ag have a peak during charge at this potential. The shape of the graph in Figure 6.19 changes dramatically during the second cycle.

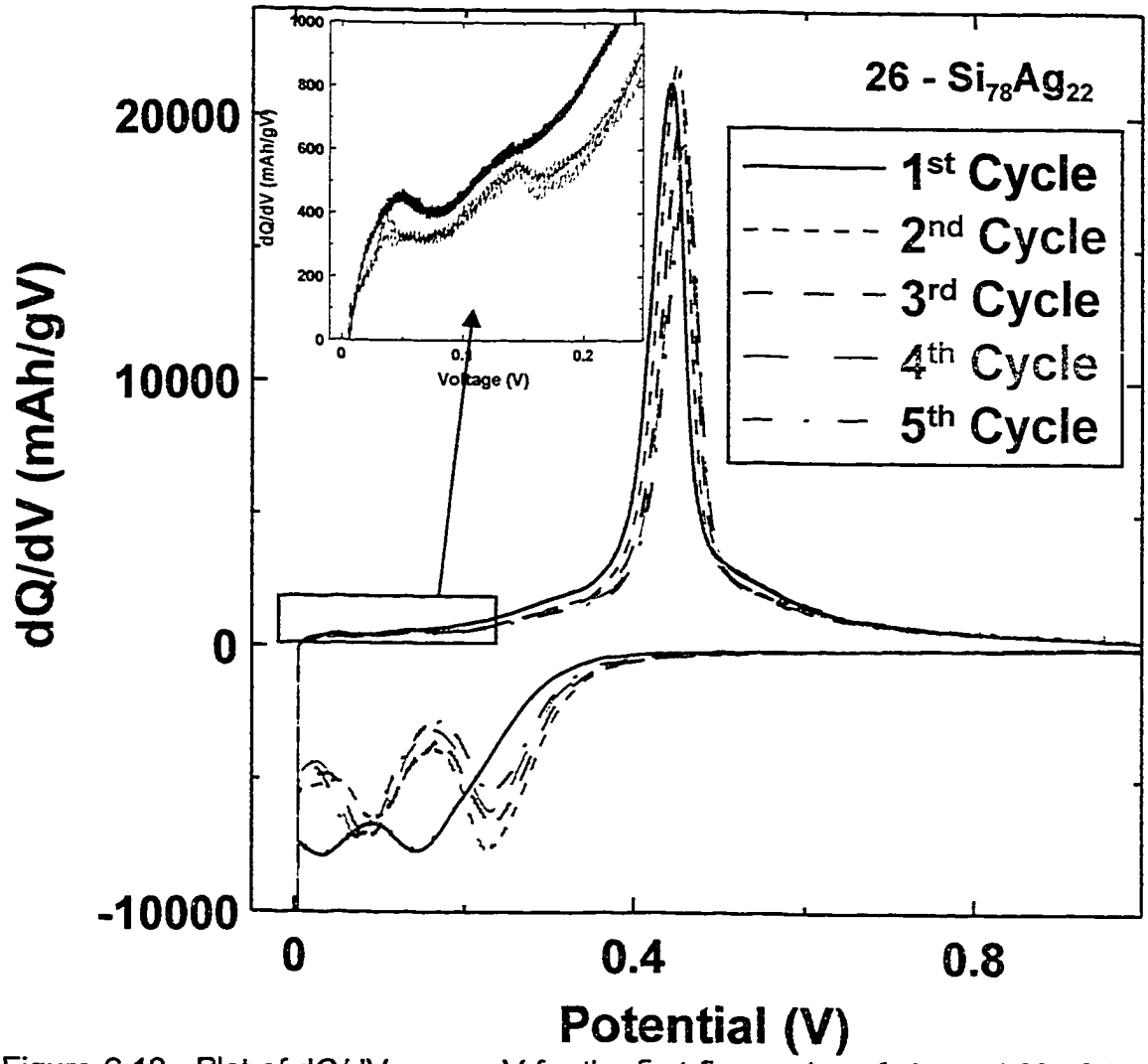

Figure 6.18. Plot of dQ/dV *versus* V for the first five cycles of channel 26 of the SiAg combinatorial cell plate. The inset shows an expanded view of the boxed area in the main figure.

During the second and later charges, a sharp peak develops at 0.4 V. Also, the lower voltage peak at around 0.3 V disappears. Two new small peaks also appear at low potentials during the charges. One is near 0.05 V and the other is near 0.15 V. These peaks are likely from the Ag in the film. As the cycle number increases for channel 27, it appears that the Si in the film begins to

crystallize to form $Li_{15}Si_4$. As more Si crystallizes, we see the single sharp peak at 0.4 V replace the two broad humps during charge. Also, the smaller peaks associated with the Ag become more evident as the humps from the a-Si are reduced. In the inset for this channel, the evidence of the Ag in the film becomes much clearer for the second cycle than for the first. The Ag which is originally widely dispersed throughout the film may be aggregating to form larger particles, simultaneously creating larger areas of a-Si that can crystallize to form $Li_{15}Si_4$.

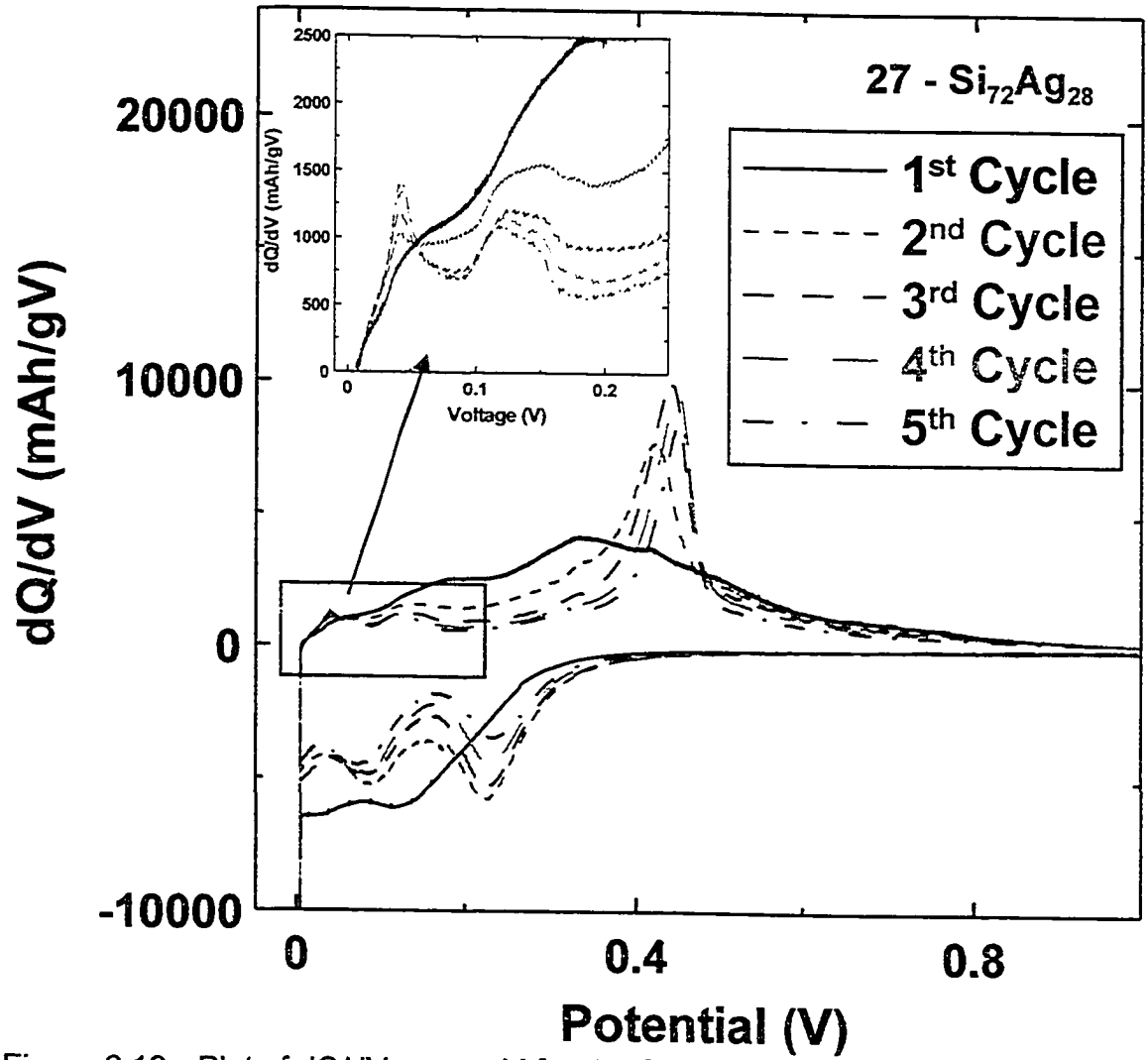

Figure 6.19. Plot of dQ/dV *versus* V for the first five cycles of channel 27 of the SiAg combinatorial cell plate. The inset shows an expanded view of the boxed region in the main figure.

The dQ/dV *versus* V profile for channel 28 ($Si_{66}Ag_{34}$) is very much like channel 27. It starts with no peaks during the first charge, but the peak at 0.4 V quickly develops at the expense of the features normally associated with a-Si. The low potential peaks associated with Ag are also becoming sharper. Channel 29 ($Si_{60}Ag_{40}$) is the next one shown in Figure 6.20. The vertical scale has been reduced even more in this graph. During charge, the Ag peaks are now much stronger and are visible during the first cycle. There is also a new peak emerging at about 0.35 V that was previously overwhelmed by the 0.4 V peak, which is much weaker. The unexplained peak at 0.7 V is also much stronger. There is also a change in the shape of the discharges in this graph. In previous SiAg graphs, there were two broad peaks during discharge of about equal size. In Figure 6.20 these peaks remain, but there is now a new peak at even lower potential. This is due to the higher Ag content for this channel.

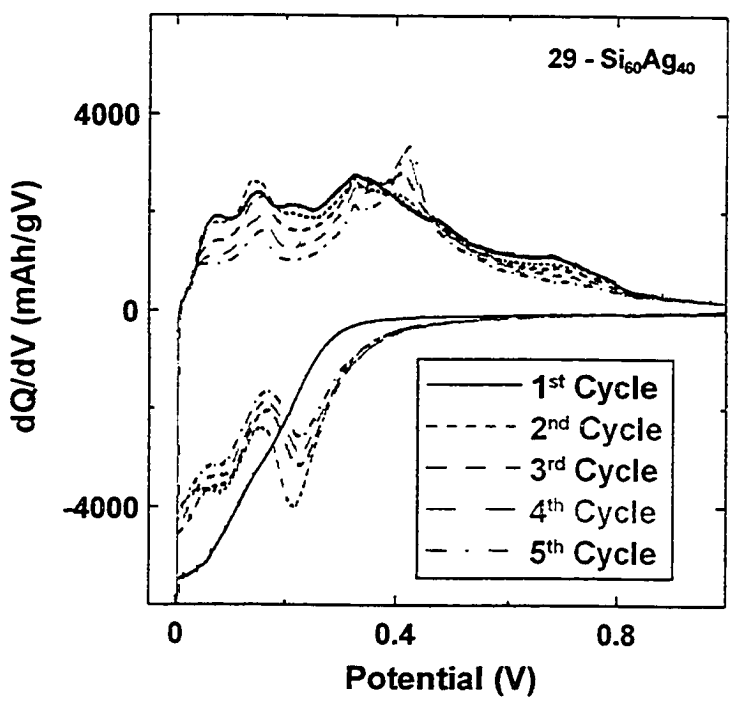

Figure 6.20. Plot of dQ/dV *versus* V for the first five cycles of channel 29 of the SiAg combinatorial cell plate.

Figure 6.21 shows the plot of dQ/dV *versus* potential for channel 30 of the SiAg binary library. This channel has an approximate composition of $Si_{55}Ag_{45}$, so nearly 50 at.% Ag content has been reached. It would appear that the $Li_{15}Si_4$ phase is not able to form for this channel. However, if more cycles are inspected, as shown in Figure 6.22, it can be seen that over a larger number of cycles the $Li_{15}Si_4$ phase does form. Also in Figure 6.22 the Ag peaks are shrinking. This indicates that the capacity from the Ag in the film is fading away.

The pattern of channel 30 is repeated for channel 31 ($Si_{51}Ag_{49}$), with a strong peak at 0.4 V during charge not developing until after the fifth cycle. The only channel that showed no evidence of the $Li_{15}Si_4$ phase was channel 32 with a composition of $Si_{46}Ag_{54}$. This channel showed no evidence of the $Li_{15}Si_4$ phase even after 13 charge/discharge cycles.

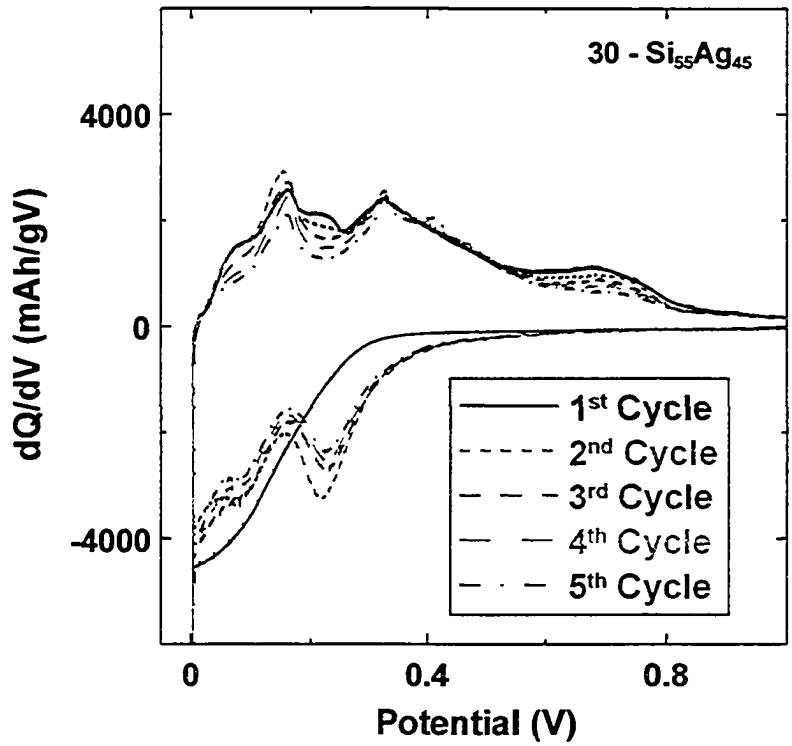

Figure 6.21. Plot of dQ/dV *versus* V for the first five cycles of channel 30 of the SiAg combinatorial cell plate.

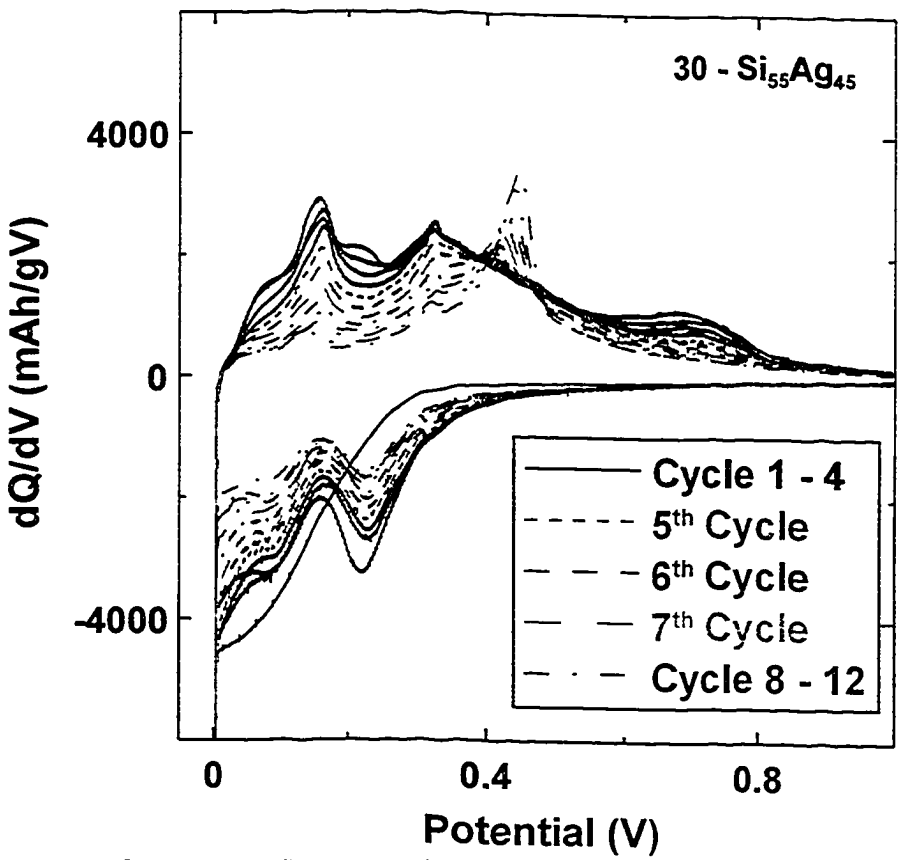

Figure 6.22. Plot of dQ/dV *versus* V for all 12 cycles of channel 30 of the SiAg combinatorial cell plate, showing the growth of the peak at 0.4 V during charge.

From the series of graphs shown above for SiAg, it is evident that the behaviour of a-Si in electrochemical cells is very different when Ag is added than when Sn is added. With Ag in the film there is crystallization of the a-Si as long as the Ag content is not too high, while there is no evidence of crystallization when Sn is added. It is interesting to see if the different behaviour of the SiAg films leads to different capacity retention. Figure 6.23 presents graphs of discharge (+) and charge (◊) capacity *versus* cycle number for all 64 cells in the SiAg combinatorial cell. The capacity retention for the SiAg cells is not nearly as good as for the SiSn cells. This supports the discussion from Chapter 1 in which the superior performance of amorphous materials was described. The SiSn films

do not crystallize during lithiation and therefore perform better than the SiAg films that are crystalline as deposited except for very low Ag content.

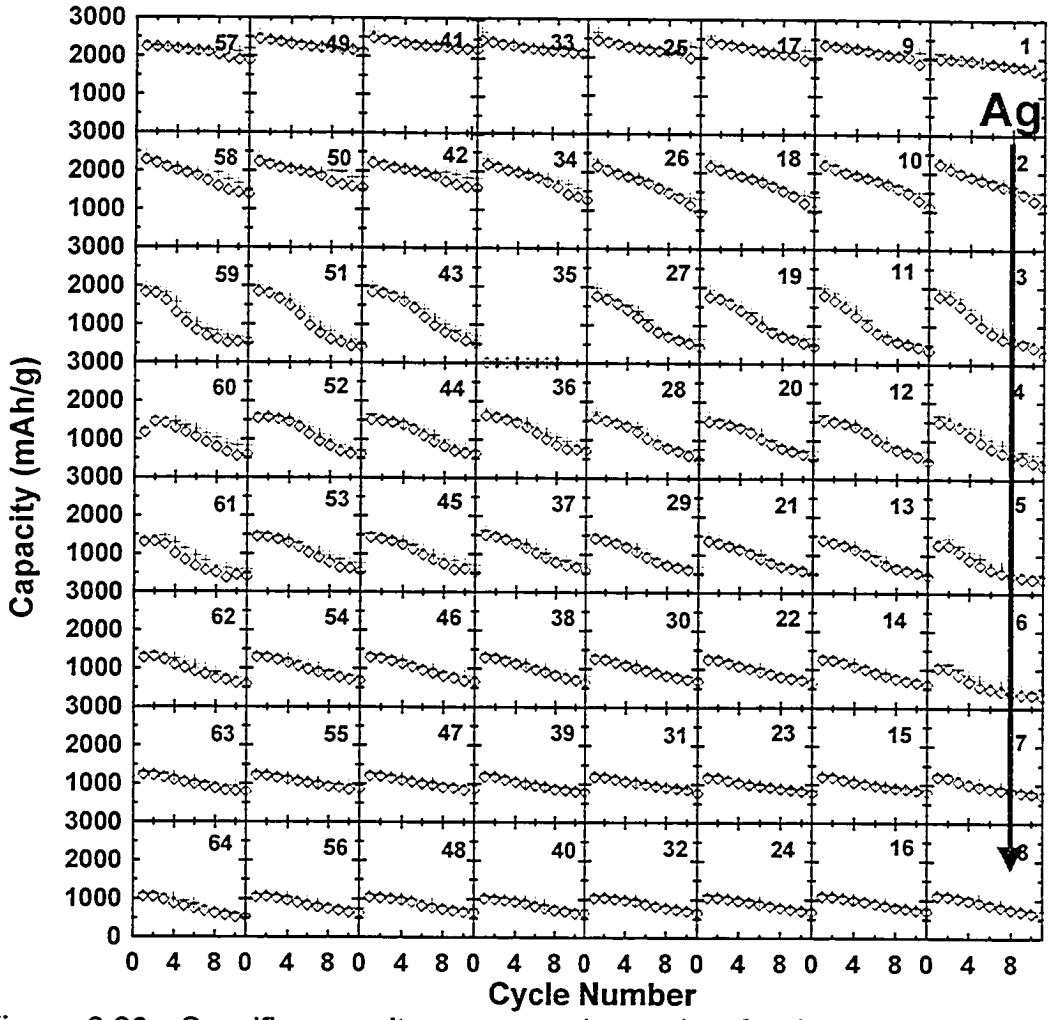

Figure 6.23. Specific capacity *versus* cycle number for the cells made from the Si-Ag combinatorial library. + - discharge; ◊ - charge.

Figure 6.24 is a plot of capacity fade in percent of the first discharge per cycle and irreversible capacity as a percent of the first discharge *versus* Ag content. This figure shows that the fade rate is very much worse for SiAg than for SiSn. Fade rates for SiSn were generally below 1 %/cycle while for SiAg they are generally over 3 %/cycle and as high as 8 %/cycle. The irreversible capacity, on the other hand, is comparable to SiSn in the range of 6 – 10 %.

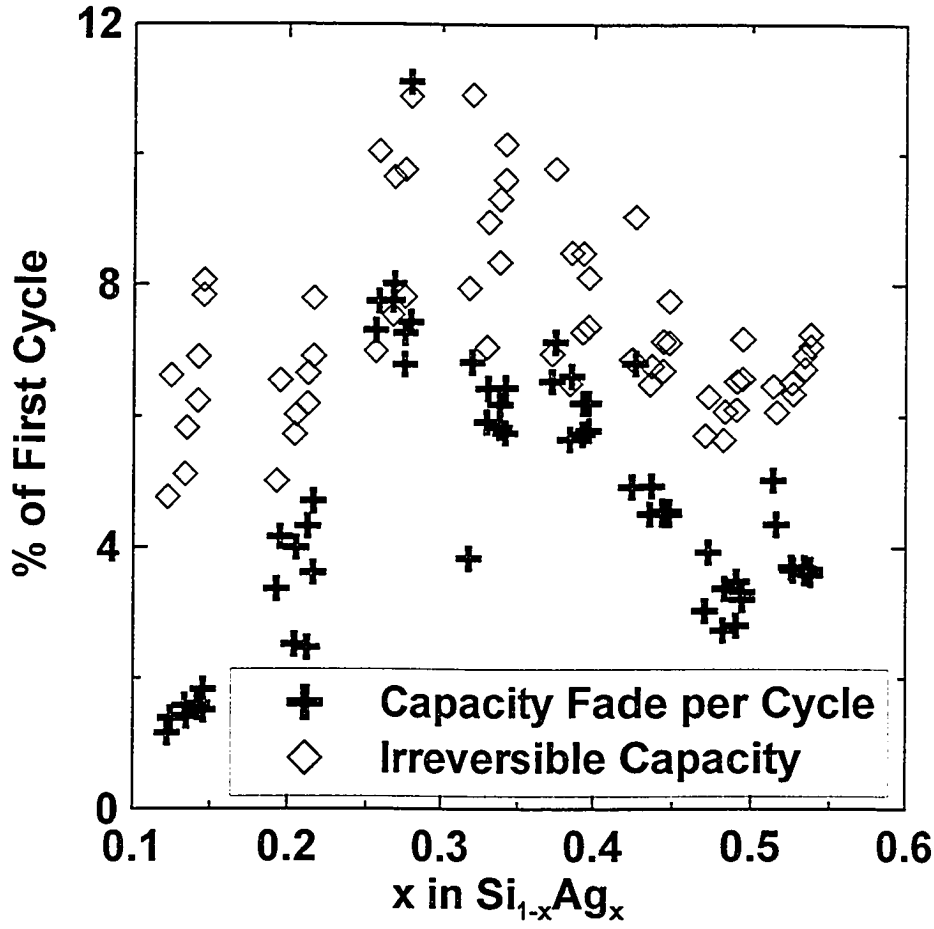

Figure 6.24. Irreversible capacity and capacity fade per cycle *versus* Ag content for the cells made from the Si-Ag combinatorial library.

6.2.2. Conclusions for SiAg

While the irreversible capacity for SiAg was generally better than for SiSn, the electrochemical cycling was much worse. Capacity fade rates were several times greater for SiAg than for SiSn. This could be due to the presence of crystalline material in the SiAg library where the SiSn library stayed amorphous.

The addition of Ag to a-Si did not effect the number of Li that could alloy with Si in room temperature electrochemical cells. The effect of Sn illustrated in Figures 6.9 and 6.11 did not occur for Ag. The addition of adequate Ag did not allow the $Li_{22}M_5$ phase to be reached, as shown in Figure 6.25. The difference

between theoretical capacity (assuming 4.4 Li per Si and 3 Li per Ag) and achieved capacity had no apparent dependence on x in $Si_{1-x}Ag_x$. The capacities achieved appear to be limited to that allowed by the fully lithiated state of $Li_{15}Si_4$.

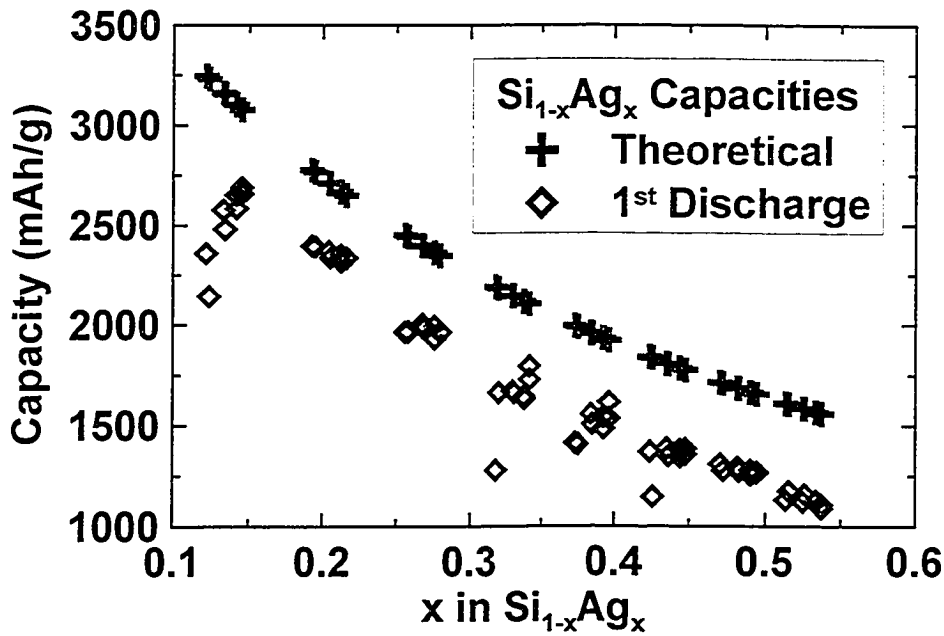

Figure 6.25. Capacities for the cells made from the Si-Ag combinatorial library: + - theoretical capacity; ◊ - 1st discharge capacity.

The shape of the dQ/dV *versus* potential relations changed with cycle number for the SiAg library. Also, the addition of Ag to a-Si, unlike Sn, does not suppress the formation of the $Li_{15}Si_4$ phase. In contrast, the SiAg cells tended to develop crystalline $Li_{15}Si_4$ over a few cycles for channels with moderate Ag content even if it did not appear after the first discharge. A proposed explanation is illustrated in Figure 6.26 and explained below.

When Si is sputtered onto Cu substrates it forms an amorphous film with the atoms randomly oriented and possessing no long-range order. These films will crystallize below 30 mV, as was shown in Chapter 5, forming a $Li_{15}Si_4$ phase.

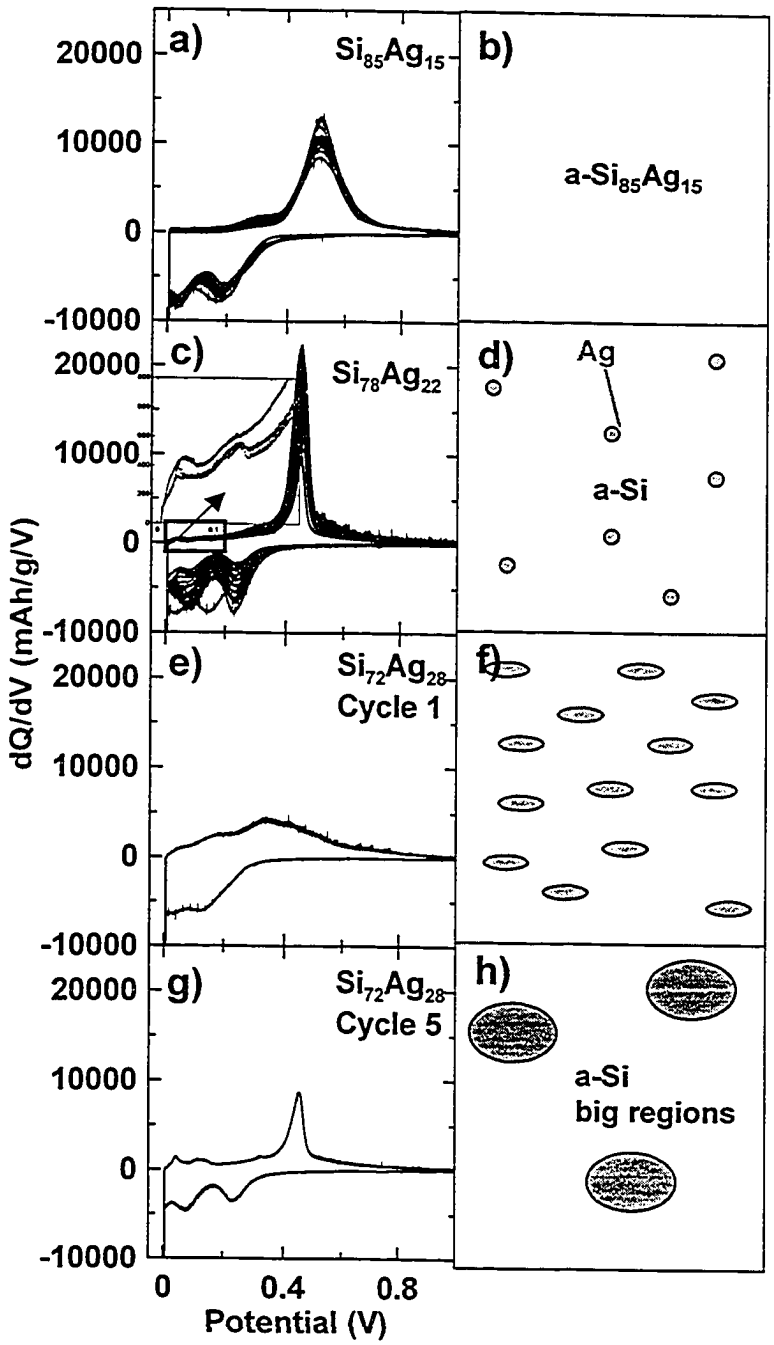

Figure 6.26. Plots of dQ/dV *versus* potential for some SiAg compositions along with diagrams of possible structures of the films. The sequence a – h is described in the text.

The addition of a small amount of Ag can be accommodated in the a-Si matrix without disrupting the formation of the $Li_{15}Si_4$ phase. The dQ/dV *versus* potential plot for this situation is shown in Figure 6.26a. The peak is wider than

expected and shifted to a slightly higher potential. This could be because, as shown in Figure 6.26b, the Ag is likely incorporated into the a-Si (see XRD scans just under 17 cm from center in Figure 6.15) and the $Li_{15}Si_4$ phase [$Li_{15}(SiAg_x)_4$].

With a little more Ag, small particles are formed in the a-Si matrix, as shown in Figure 6.26d. This leaves large regions of a-Si able to form $Li_{15}Si_4$ and the more characteristic dQ/dV *versus* potential plot is obtained, as shown in Figure 6.26c. Also, the inset in Figure 6.26c shows some evidence of crystalline Ag in the film during the charge portion of the cycle.

With even larger Ag particles, there is too much disruption for the Si and it cannot form the $Li_{15}Si_4$ phase during the first discharge. This is illustrated in Figure 6.26f and the more amorphous-like dQ/dV *versus* potential plot is obtained for the first cycle, as shown in Figure 6.26e. However, as seen in Figure 6.19 and 6.26g with 28 at. % Ag, $Li_{15}Si_4$ does form during later cycles. In Figure 6.26g, the Ag peaks are clearly present at low voltage during charge.

It is speculated that during the insertion and removal of Li, the Ag in the film aggregates into larger particles thus leaving larger regions of Si with no disruptions, as shown in Figure 6.26h. These regions are then free to form the $Li_{15}Si_4$ phase during later discharges. The higher the Ag content, the more cycles it takes to achieve adequate aggregation to allow $Li_{15}Si_4$ to form. This type of aggregation or clustering has been proposed elsewhere for Sn in SnO composite films [39-43]. Transmission Electron Microscopy (TEM) studies on SiAg films after various amounts of electrochemical cycling could reveal if Ag grains are growing with cycle number in the manner suggested.

Finally, if the film is made up of more Ag than Si, regions of Si large enough to form the $Li_{15}Si_4$ phase are no longer possible and the peak in the dQ/dV *versus* potential plots at 0.4 V no longer appears even after 12 cycles.

The precise amount of Ag (or size of Ag grains) needed to disrupt formation of $Li_{15}Si_4$ has not been determined. As a compliment to the size of Ag grains needed, it would also be interesting to determine how large a volume of uninterrupted Si is needed to have $Li_{15}Si_4$ form during lithiation. These questions could perhaps be answered by a series of TEM experiments in future work.

6.3. SiZn

6.3.1. $Si_{1-x}Zn_x$ Binary Results

The final binary system to be studied was the SiZn system. The phase diagram for this system is shown in Figure 6.27. There are again no binary phases found in this system.

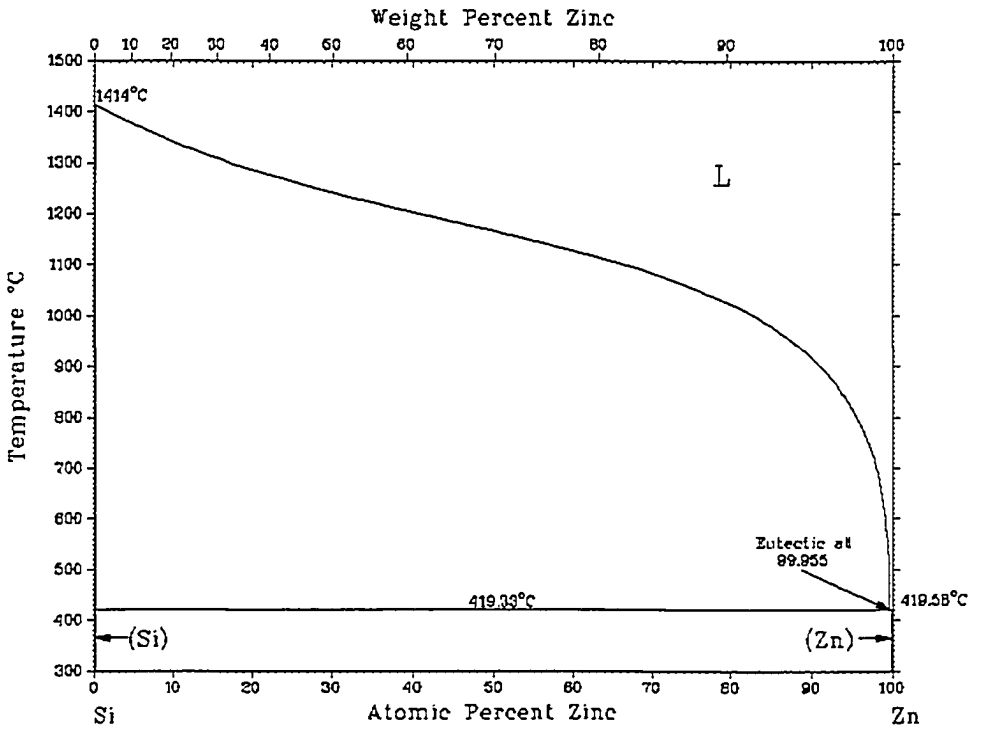

Figure 6.27. The SiZn binary phase diagram.

SiZn binary libraries were prepared using the sputtering system described in Chapter 3. Figure 6.28 shows a plot of the Zn:Si ratio as a function of distance from the center of the substrate table as determined by electron microprobe. The ratio runs from a minimum of about 0.10 to a maximum of about 1.6. This corresponds to approximately $0.10 < x < 0.60$ in $Si_{1-x}Zn_x$. The composition variation is not linear in this case, but a polynomial fit provides an adequate estimate of composition as a function of position on the library. The non-linearity of the Zn:Si ratio is puzzling, but the mass deposited as a function of position is consistent with Figure 6.28 so the microprobe data is assumed to be accurate.

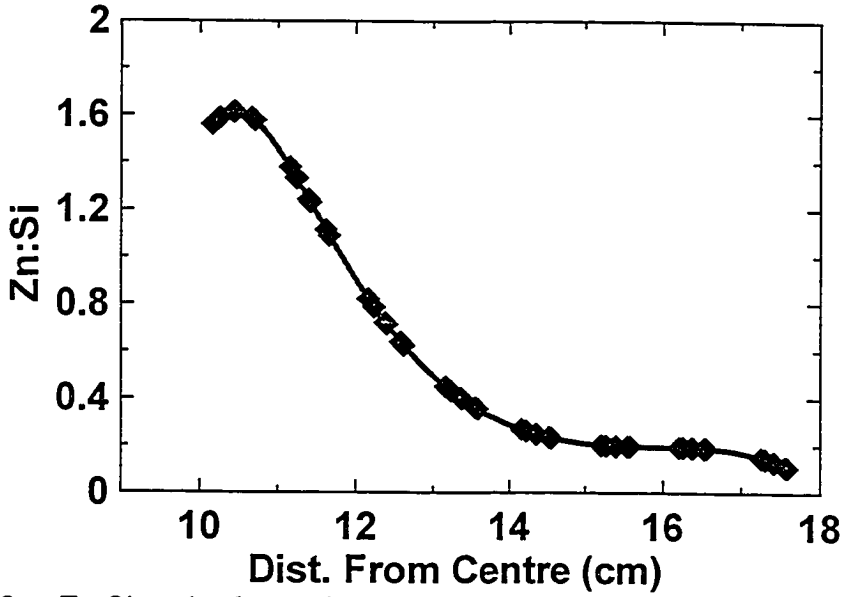

Figure 6.28. Zn:Si ratio for a SiZn binary library as determined by electron microprobe.

The XRD patterns collected for this library are shown in Figure 6.29. Figure 6.29 shows that much of the library is amorphous, with peaks appearing only near the Zn-rich end. The graph shows intensity on the left y-axis and an estimate of position on the library on the right y-axis that can be used with Figure 6.28 to determine the approximate composition for each scan. The thickness of

the library is approximately 0.5 to 2 μm. From Figure 6.29 it is difficult to identify the individual XRD patterns present. Figure 6.30 presents an expanded view of the patterns near the Zn rich end with the individual peaks labeled. All of the peaks are from Zn, with no SiZn or Si phases present.

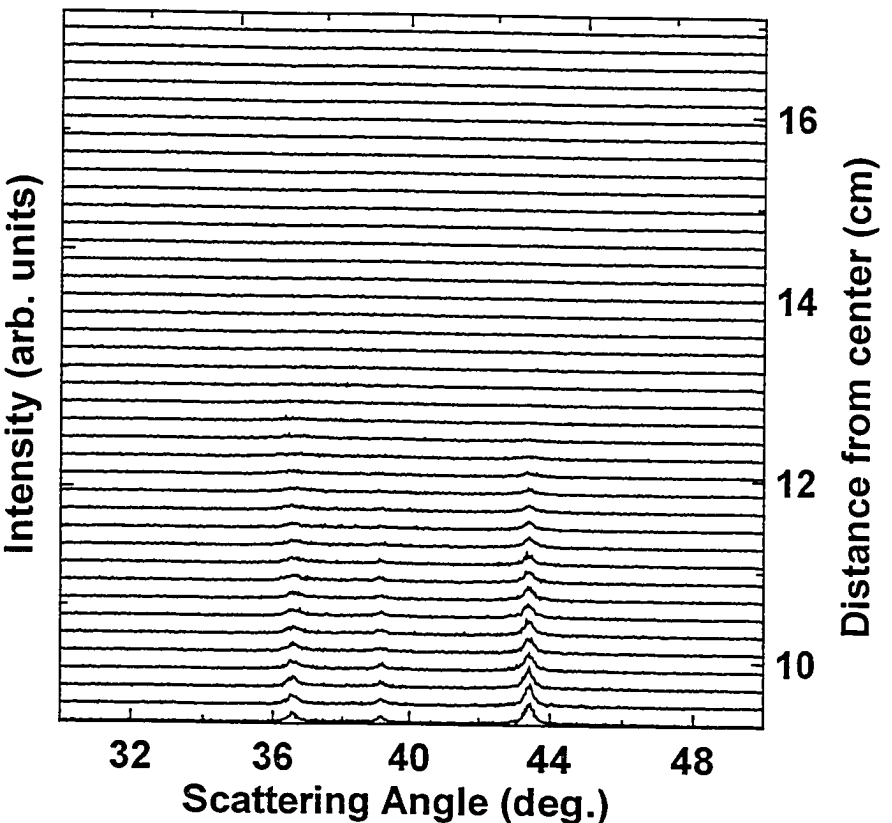

Figure 6.29. XRD patterns as a function of position for a SiZn binary library. The angular range shown is from 30 to 50 °.

This library stays amorphous until the Zn content reaches approximately 50 at.%. When there is more Zn than this, the XRD patterns begin to show several peaks associated with crystalline Zn, as shown in Figure 6.30. This amorphous range is comparable to that of Sn and much larger than Ag.

As was the case for SiAg, a representative column of data from a combinatorial electrochemical cell will be discussed. The column selected is made up of channels 41 to 48, and the dQ/dV *versus* potential plots for these

channels are shown in Figure 6.31. There is shape change with composition and with cycle number in these graphs as well, although not as much as with the SiAg cell.

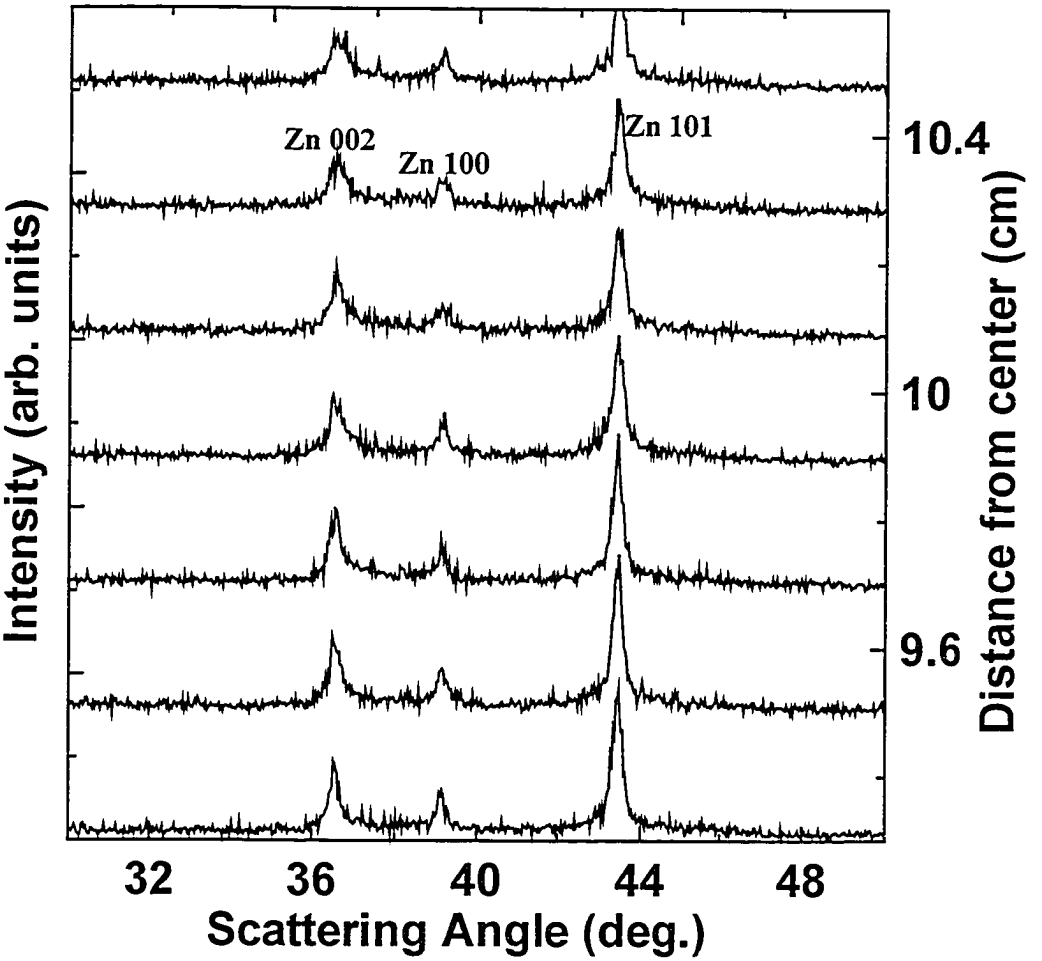

Figure 6.30. Expanded view of XRD patterns from the Zn rich end of the SiZn binary film library of Figure 6.29. The angular range shown is from 30 to 50°.

Figure 6.32 shows the first five cycles of dQ/dV *versus* potential for channel 41. The composition of this channel is approximately $Si_{88}Zn_{12}$. This graph is very similar to the graph of channel 25 of the SiAg cell shown in Figure 6.17. The peak at about 0.5 V during the charge is somewhat sharper for the SiZn cell than the SiAg cell, but otherwise they are nearly identical except that the peak height seems to diminish faster for SiAg than for SiZn.

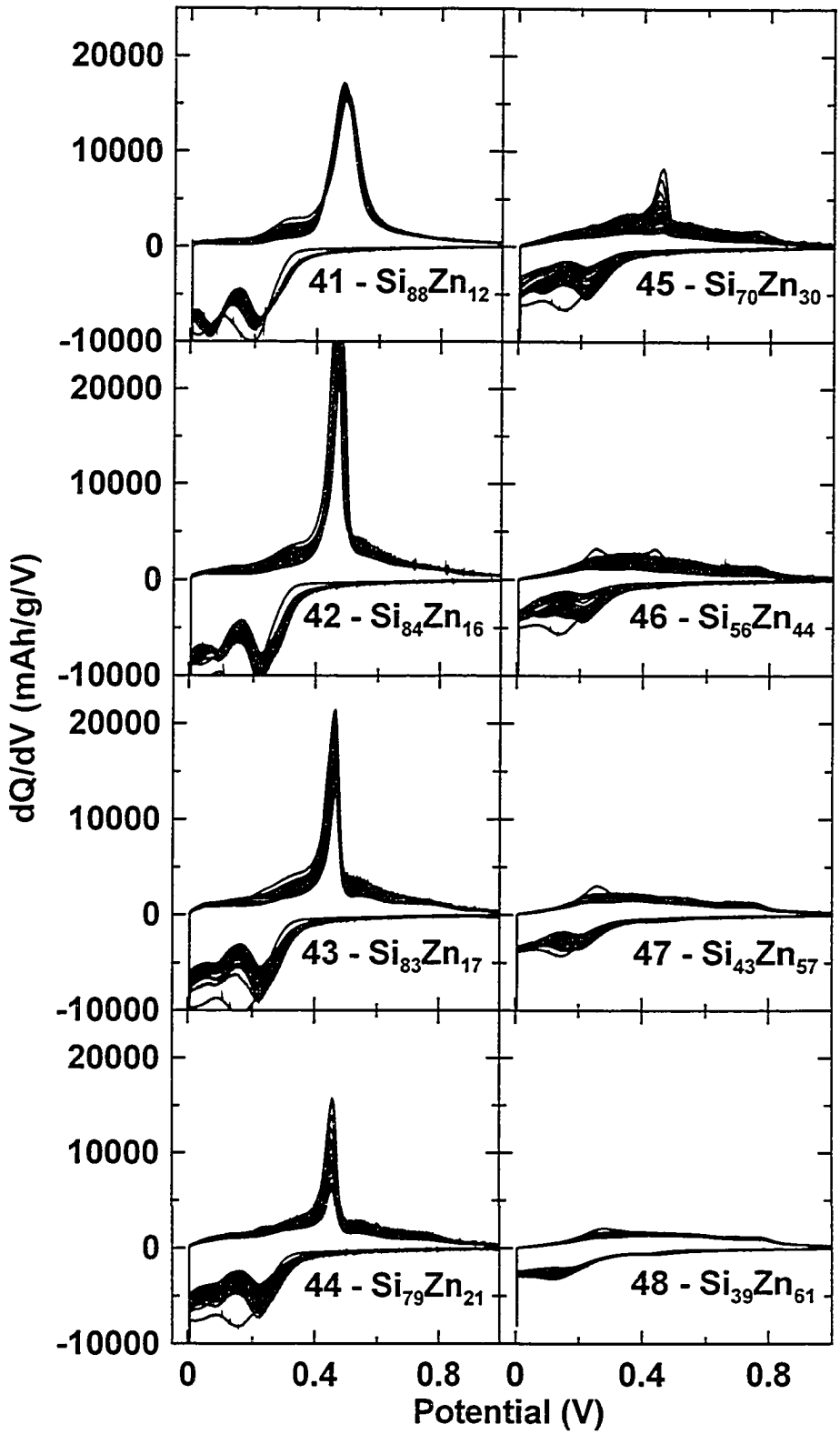

Figure 6.31. Graphs of dQ/dV *versus* V for one column of channels from a SiZn binary combinatorial cell plate. Approximate composition for each channel is indicated.

Figure 6.33 shows the graph of dQ/dV *versus* potential for channel 42 of the SiZn combinatorial cell plate with a composition of approximately $Si_{84}Zn_{16}$. This channel follows a similar pattern to SiAg. The peak during charge becomes much sharper with the addition of more Zn. It also shifts to lower voltage somewhat, although not as far as was the case for SiAg.

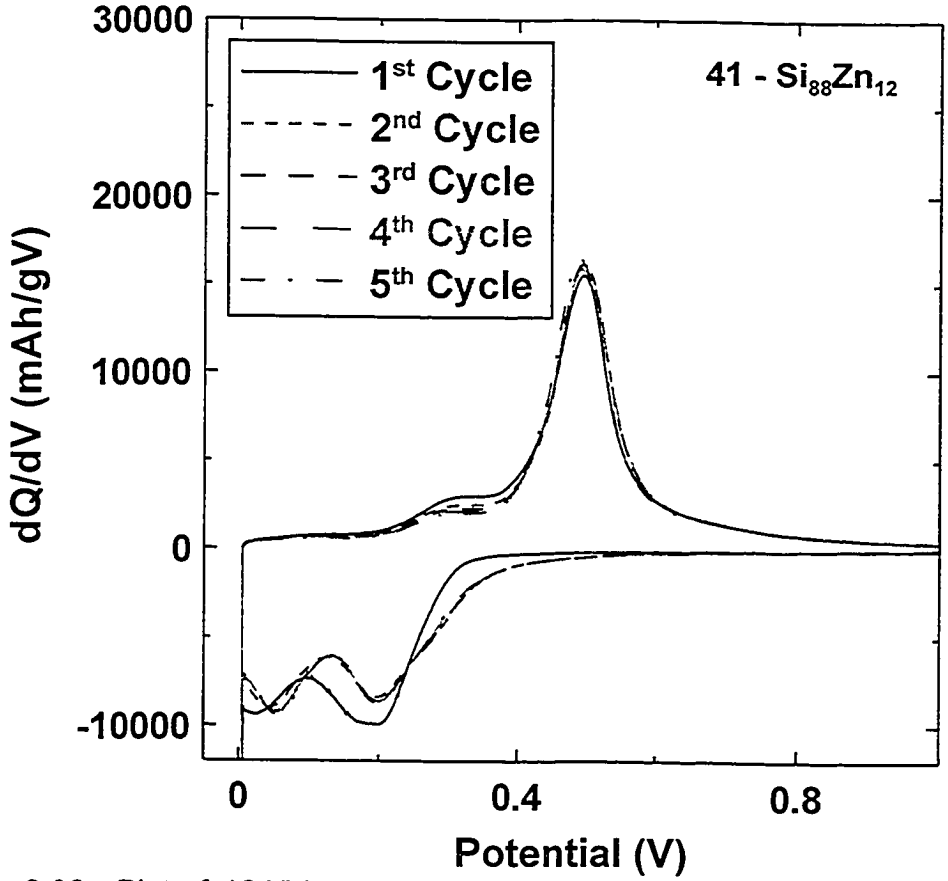

Figure 6.32. Plot of dQ/dV *versus* V for the first five cycles of channel 41 of the SiZn combinatorial cell plate.

The composition for channel 43 is almost the same as channel 42. As a result, the behaviour of these two channels is the same. The composition has changed a little more by channel 44, and the dQ/dV *versus* potential relation has also changed from that of the preceding channels. The graph of dQ/dV *versus* potential for channel 44 is shown in Figure 6.34. The vertical scale has been

changed relative to the previous SiZn graphs for Figure 6.34 to make features easier to identify. During the discharges for channel 44, the two broad peaks are no longer the same as each other like they were for Channle 41. For channel 41, they were about the same, with the lower potential one being a little higher. For channel 44, the higher potential peak is higher in dQ/dV while the lower potential peak has separated into two separate peaks after the first discharge. During the charge, additional broad peaks appear at about 0.55 V and 0.75 V. These are

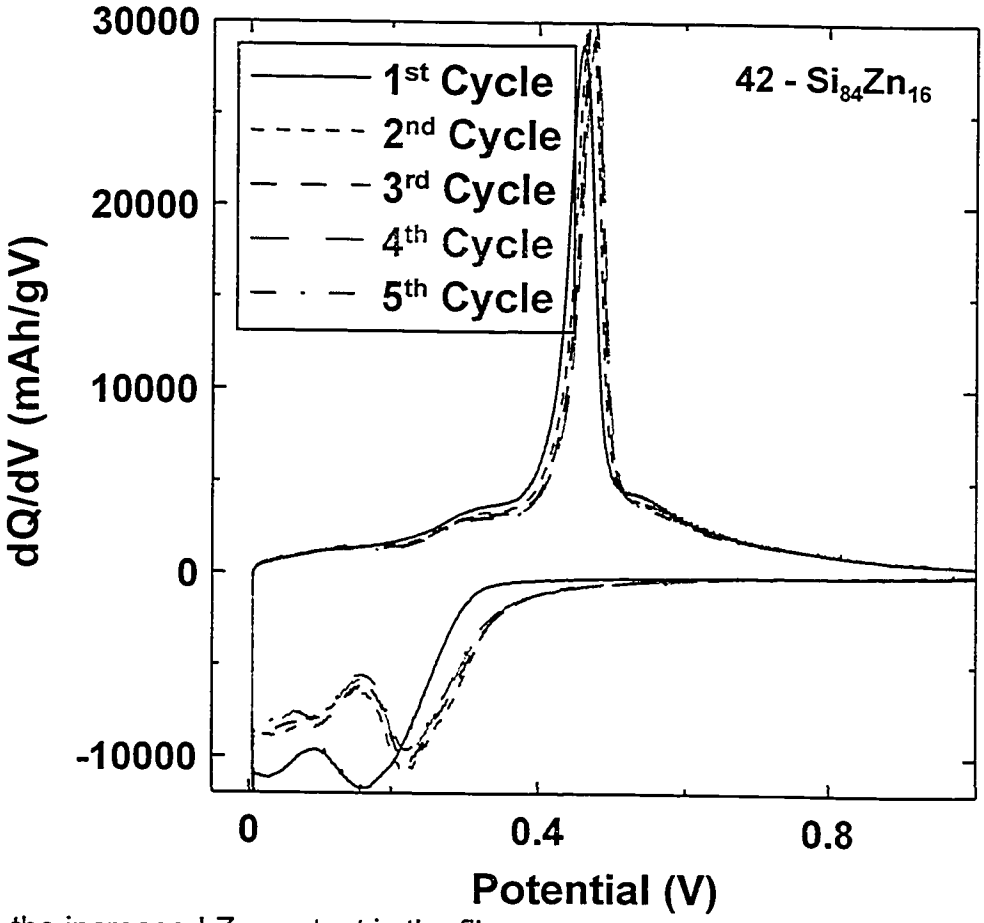

from the increased Zn content in the film.

Figure 6.33. Plot of dQ/dV *versus* V for the first five cycles of channel 42 of the SiZn combinatorial cell plate.

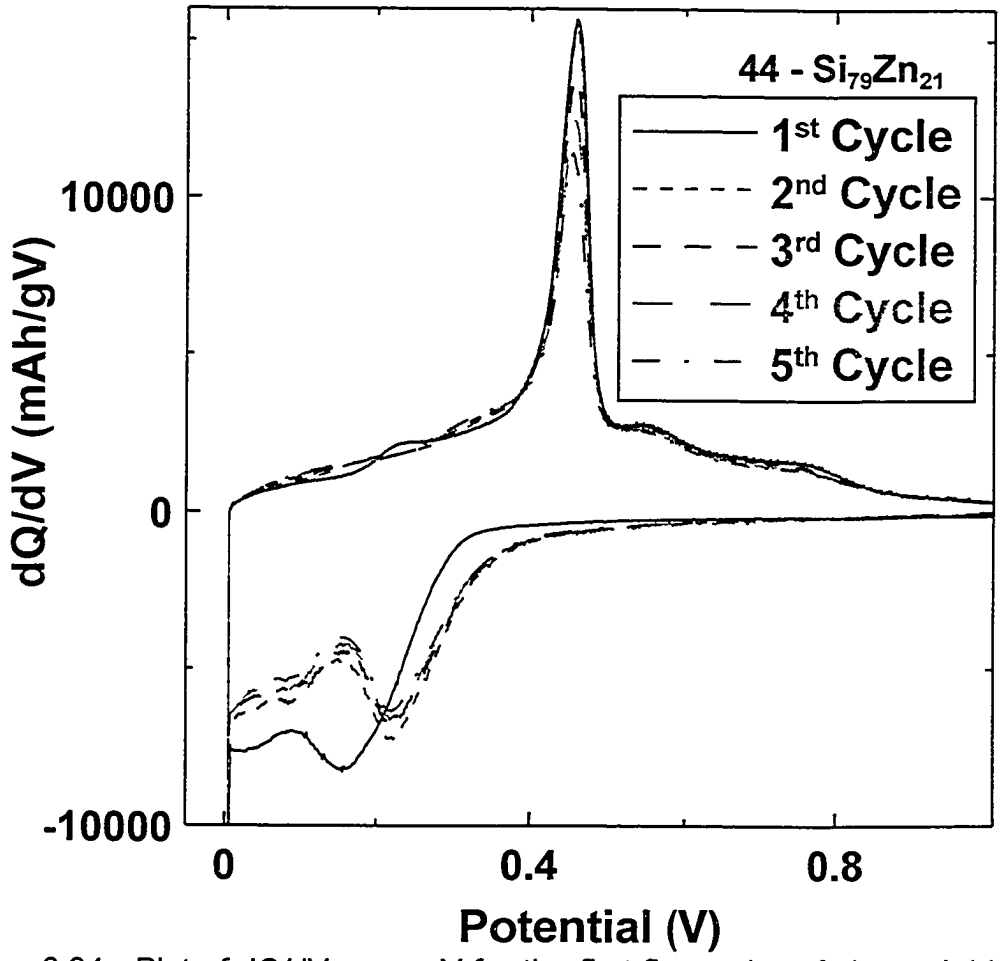

Figure 6.34. Plot of dQ/dV *versus* V for the first five cycles of channel 44 of the SiZn combinatorial cell plate.

Going from channel 44 to channel 45 represents a relatively large change in composition. Channel 45 has an approximate composition of $Si_{70}Zn_{30}$. The graph of dQ/dV *versus* potential for channel 45 is shown in Figure 6.35. This graph is quite different from the other SiZn compositions presented so far. While the first discharge looks very much like those of the other channels, the first charge exhibits a new broad peak at approximately 0.2 V. The sharp peak at 0.45 V is still present although it is reduced somewhat, and the higher potential peaks are more pronounced. Up to this point, the shape of the dQ/dV *versus* potential relationships has not been changing with cycle number for the SiZn cell.

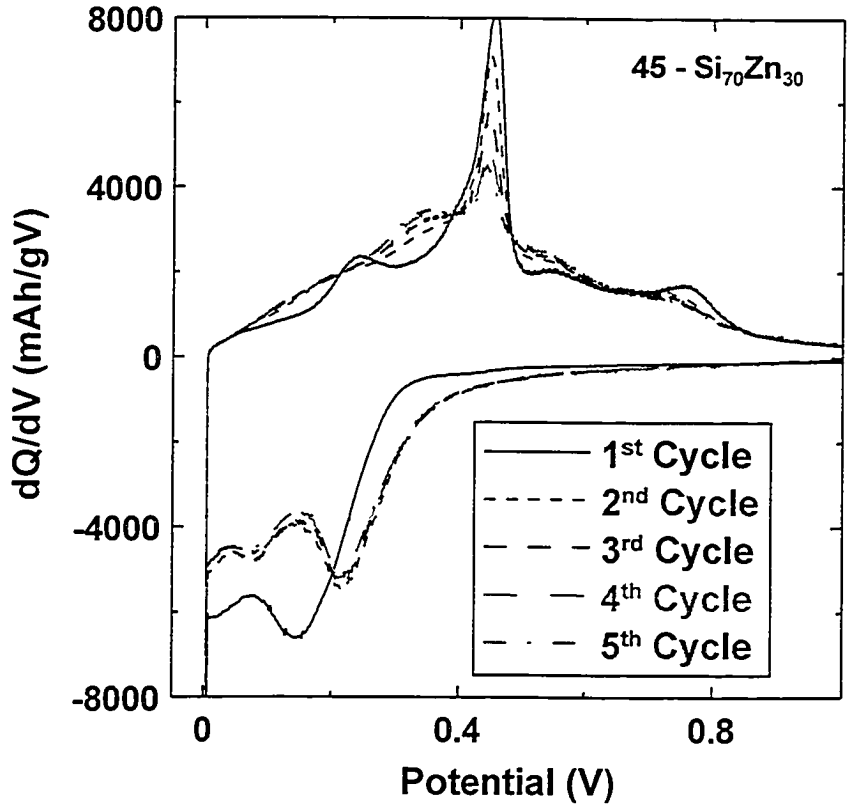

Figure 6.35. Plot of dQ/dV *versus* V for the first five cycles of channel 45 of the SiZn combinatorial cell plate.

For channel 45, the shape of the charge portion of the graph in Figure 6.35 changes with cycle number. The small broad peaks disappear after the first charge. The small broad peaks are also evident in channels 41 to 44, but they do not disappear as rapidly for these channels. It is speculated that these humps are from nanocrystalline Zn in these channels. For channels 41 to 44, the $Li_{15}Si_4$ phase forms during each discharge and the Zn reacts with Li independently. During the following charges the humps appear in the locations of the Zn peaks from Figure 5.18. The peaks are broader for these channels, possibly indicating nanocrystalline Zn. For channel 45, as the peak for $Li_{15}Si_4$ disappears, the broad Zn humps also disappear. This indicates that the Si and Zn are now forming a ternary Li-Si-Zn phase (determined to be Li_2SiZn as described in the next two

sections on *in-situ* XRD). This is significant because it seems that after several cycles the film becomes entirely amorphous or nanocrystalline. This could be beneficial for the long term cycling performance of the material. This behaviour is opposite of that seen for SiAg films of about the same composition, which have Ag grains that increase in size with cycle number.

The shape of the discharge for channel 45 in Figure 6.35 does not change after the first cycle even though the charge portion is changing significantly. At the start, the film making up this channel contains a-Si and crystalline Zn with relatively large particle sizes. During the first discharge, the $Li_{15}Si_4$ phase is formed at low potential. During the charge the peak at 0.4 V from $Li_{15}Si_4$ is prominent and also there are some features from Zn. By the top of the first charge, there is now a mix of a-Si and Zn, but unlike the starting material it is speculated that the Zn grains are much smaller or that it is nano-crystalline. During subsequent discharges, a new phase forms incorporating both Si and Zn. Smaller amounts of $Li_{15}Si_4$ are formed during the hold at low potential. The new phase formed accounts for the different shape of the curve for the second discharge. From this point on, the material at the top of charge is probably a mix of a-Si and nanocrystalline Zn. The new phase is formed during each discharge, so the dQ/dV *versus* potential graph always has the same shape. The different amount of $Li_{15}Si_4$ formed does not change the shape of the curve because it occurs during the hold period at the bottom of discharge. The new phase that forms will be investigated with *in-situ* XRD.

Figure 6.36 shows the graph of dQ/dV *versus* potential for channel 46 of the SiZn combinatorial cell. This channel has a composition of approximately $Si_{56}Zn_{44}$. The first discharge for this channel looks the same as those discussed above, but the first charge now has two fairly sharp peaks, one just above 0.2 V and the other just above 0.4 V. At higher potentials during the first charge, the features seen in the previous channel have become somewhat smoothed out. For the second and later cycles, the peaks of the graph during both discharge and charge are becoming less well defined. The two sharp peaks present for the first charge have completely disappeared. It appears that for this composition the film is either amorphous or contains a nanocrystalline phase beyond the first cycle. Channel 47, with a composition of $Si_{43}Zn_{57}$, is very much like channel 46, except that during the first charge only the lower voltage of the two peaks is present. After the first cycle for channel 47, the graph of dQ/dV *versus* potential becomes very featureless, just like channel 46. Even though the films that make up channels 46 and 47 start with crystalline Zn present, after the first discharge/charge cycle, there is no evidence of crystalline material in the plots of dQ/dV *versus* potential.

Figure 6.37 shows the graph of dQ/dV *versus* potential for the final channel in the column, channel 48. It has an approximate composition of $Si_{39}Zn_{61}$. This graph has almost no features except for one broad peak at about 0.2 V during the first charge that is no longer present during the second charge. This channel, even with its high Zn content, also appears to stay entirely

amorphous beyond the first cycle. There is no evidence of the $Li_{15}Si_4$ phase (the broad peak at 0.4 V) even during the first charge.

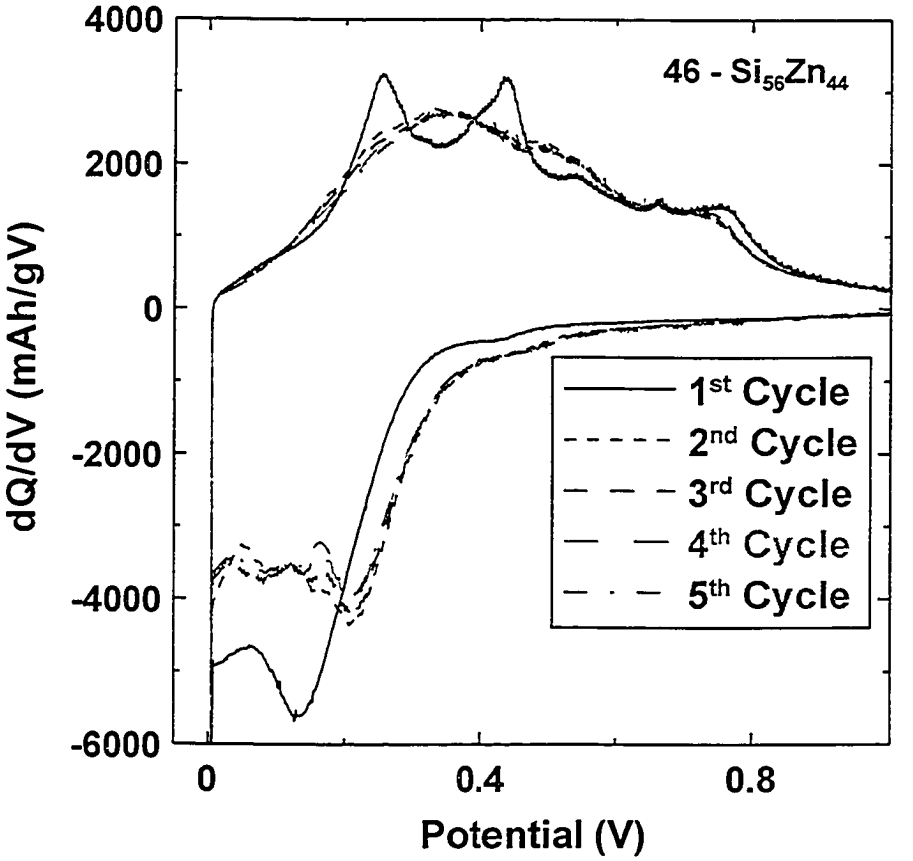

Figure 6.36. Plot of dQ/dV *versus* V for the first five cycles of channel 46 of the SiZn combinatorial cell plate.

It has been shown in the above discussion that the behaviour of SiZn films during electrochemical alloying with Li is very different than that of SiAg films. In SiZn films, the presence of adequate amounts of Zn tended to suppress the formation of the $Li_{15}Si_4$ phase, where Ag did not. Also, with enough Zn in the film, it was found that the film would apparently become completely amorphous or nanocrystalline after a small number of discharge/charge cycles (one cycle for many) while for Ag, there continued to be some evidence of crystalline Ag even if no $Li_{15}Si_4$ phase was present.

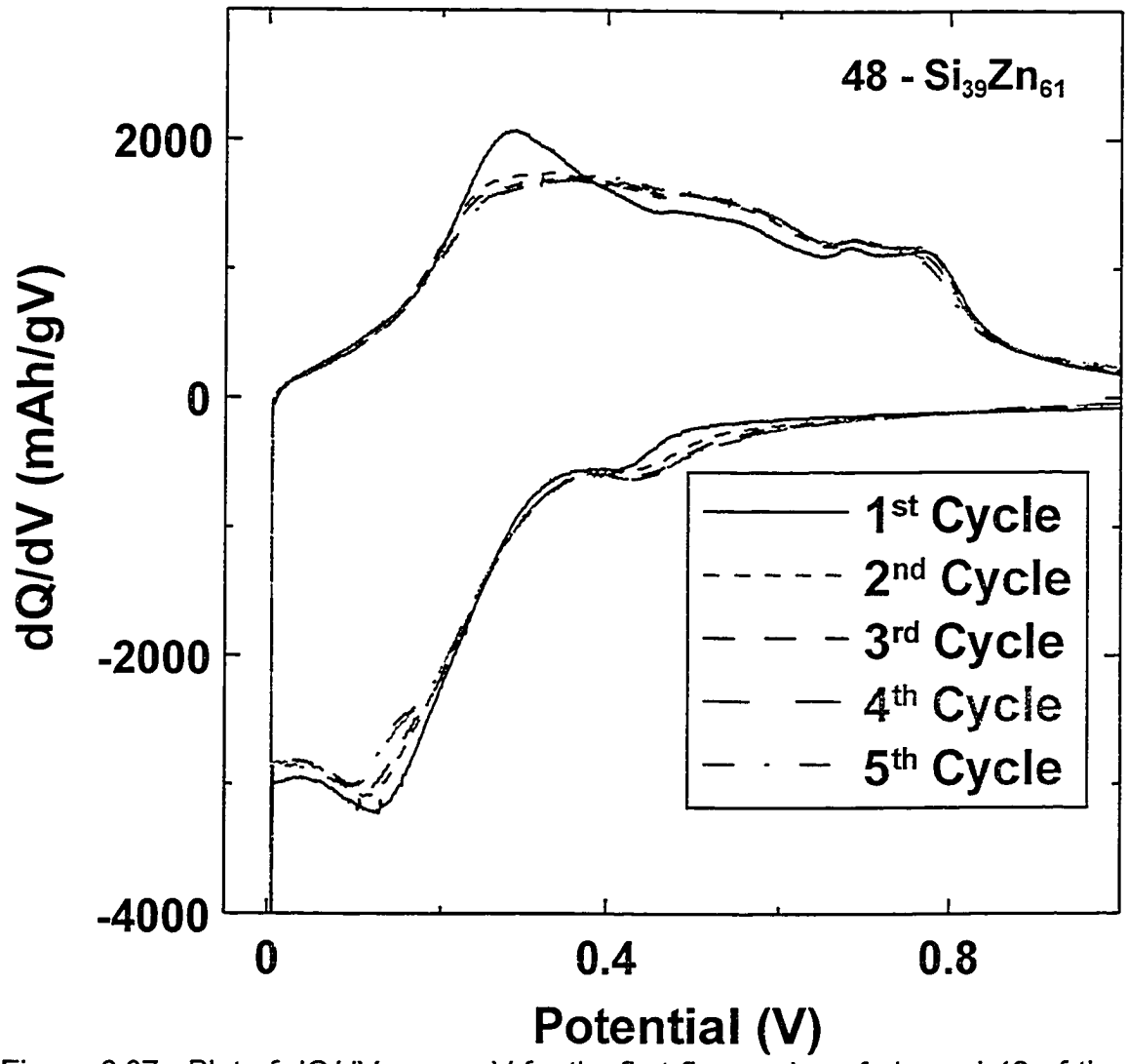

Figure 6.37. Plot of dQ/dV *versus* V for the first five cycles of channel 48 of the SiZn combinatorial cell plate.

The apparent amorphization of the SiZn films should have an impact on their cycle life. Figure 6.38 shows graphs of discharge (+) and charge (◊) capacity *versus* cycle number for all 64 cells in the SiZn combinatorial cell. The capacity retention for the SiZn cells, while not as good as the SiSn cells, is much better than that of SiAg for some areas of the library.

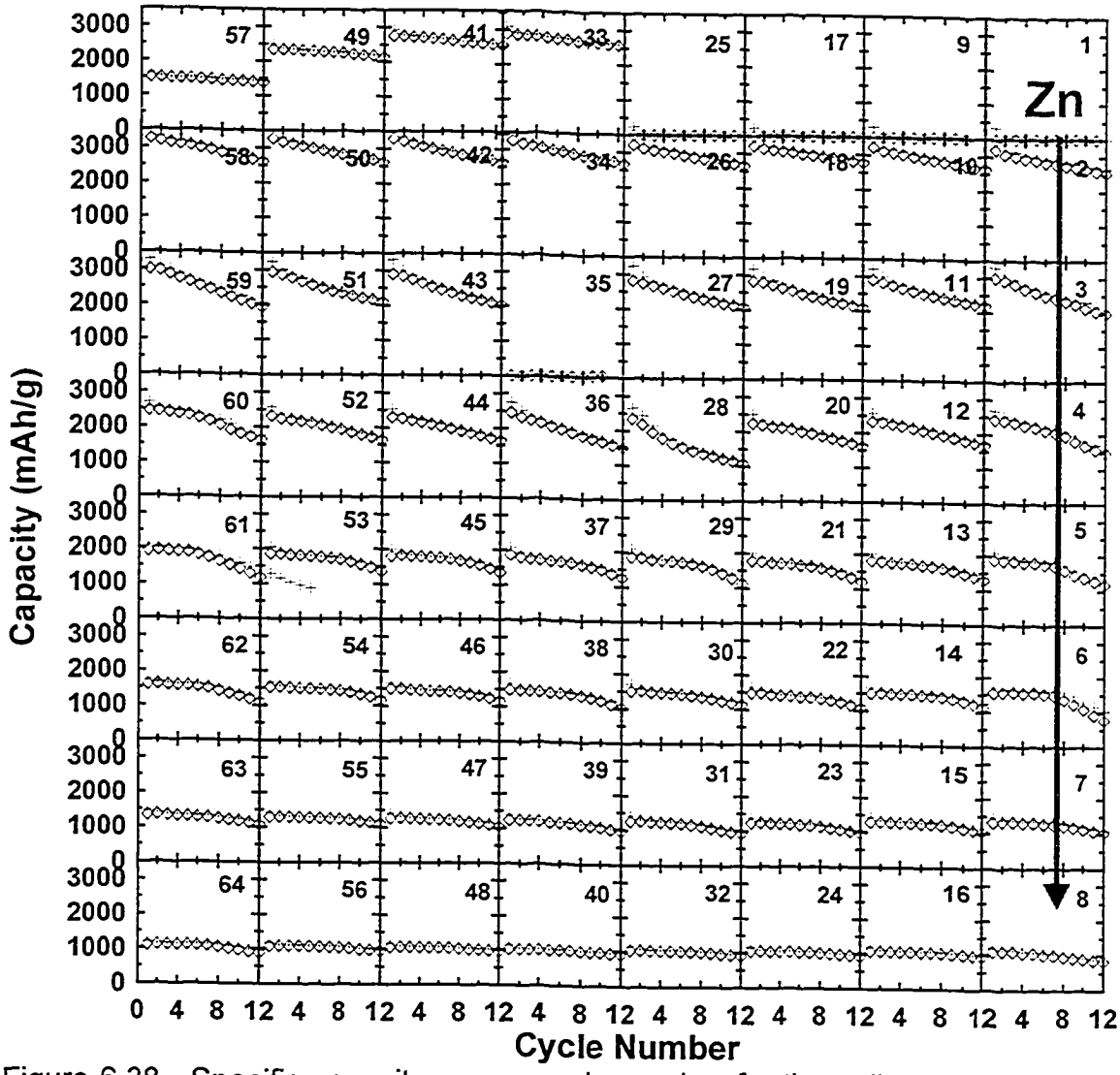

Figure 6.38. Specific capacity *versus* cycle number for the cells made from the Si-Zn combinatorial library. + - discharge; ◊ - charge.

It is interesting that the channels with the highest Zn content tend to cycle the best. The bottom two rows of graphs in Figure 6.38 show the least capacity fade even though these are the cells that start with the most crystalline material. The apparent *in-situ* amorphization of the film during the first cycle allows these cells to benefit from the improved performance of amorphous materials. The cells with less Zn retain crystalline material during charge/discharge cycling and

therefore lose their capacity more quickly. Figure 6.39 plots capacity fade in percent per cycle and irreversible capacity as a percent of the first discharge *versus* Zn content. The fade rates, while not quite as good as those of the SiSn binary library, are much better than for the SiAg library. The fades are mostly below 4 %/cycle with many below 2 %/cycle. The improved cycling with Zn content is evident from the graph. Irreversible capacities are generally in the range of 6 to 12 %. While this is good in comparison to many results reported in the literature, it is not quite as good as for the SiAg library.

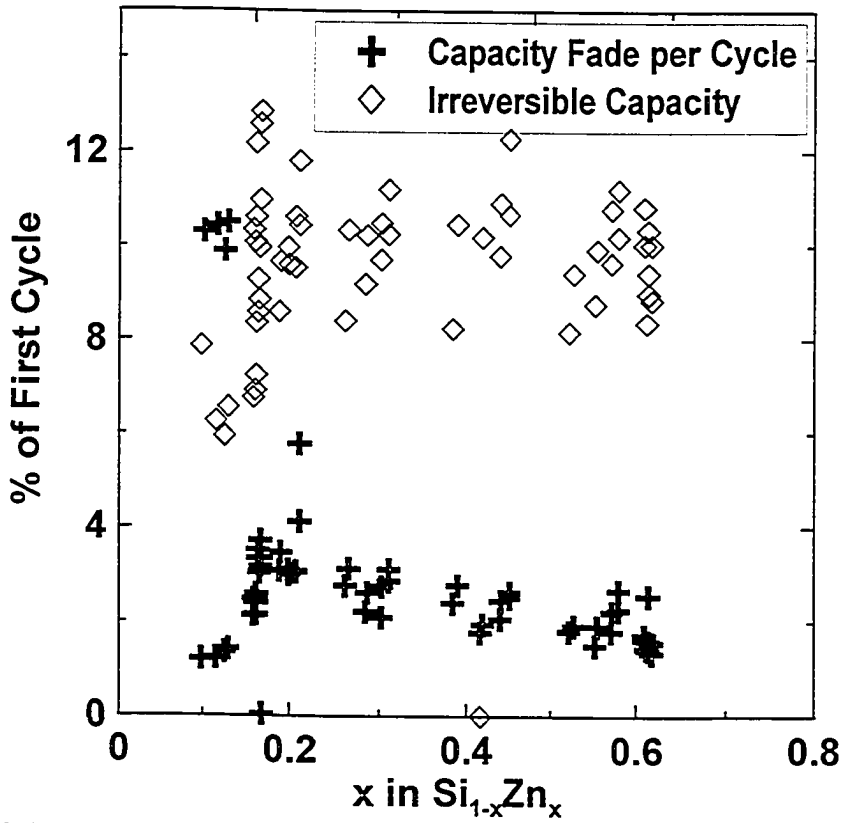

Figure 6.39. Irreversible capacity and capacity fade per cycle *versus* Zn content for the cells made from the Si-Zn combinatorial library.

While it has been seen that an adequate amount of Zn in the SiZn library suppresses the crystallization of the $Li_{15}Si_4$ phase and that the films quickly become amorphous or nanocrystalline during charge/discharge cycling, the

behaviour is not fully understood. In an effort to learn why these films behave as they do, *in-situ* XRD experiments were performed.

6.3.2. SiZn *In-situ* XRD Results

In order to help understand the behaviour witnessed for the SiZn binary system, two *in-situ* XRD experiments were performed. These will now be described.

6.3.2.1. $Si_{62}Zn_{38}$

The target composition for the first SiZn *in-situ* XRD was $Si_{60}Zn_{40}$, which was well into the range that showed crystalline Zn present by XRD from the SiZn binary library. The goals of this experiment were to discover if the Zn actually did become amorphous after the first discharge/charge cycle and to understand the features in the dQ/dV *versus* potential relationship. The stoichiometry achieved was $Si_{62}Zn_{38}$, as determined by electron microprobe. This is between the compositions of channels 45 and 46 from the combinatorial cell plate, shown in Figures 6.35 and 6.36. In order to obtain a strong reflected beam through the Be window of the *in-situ* cell, the film for this experiment needed to be much thicker than the combinatorial cell. The film for this experiment was about 10 μm thick compared to ~ 1μm thick for a similar composition on the combinatorial cell plate.

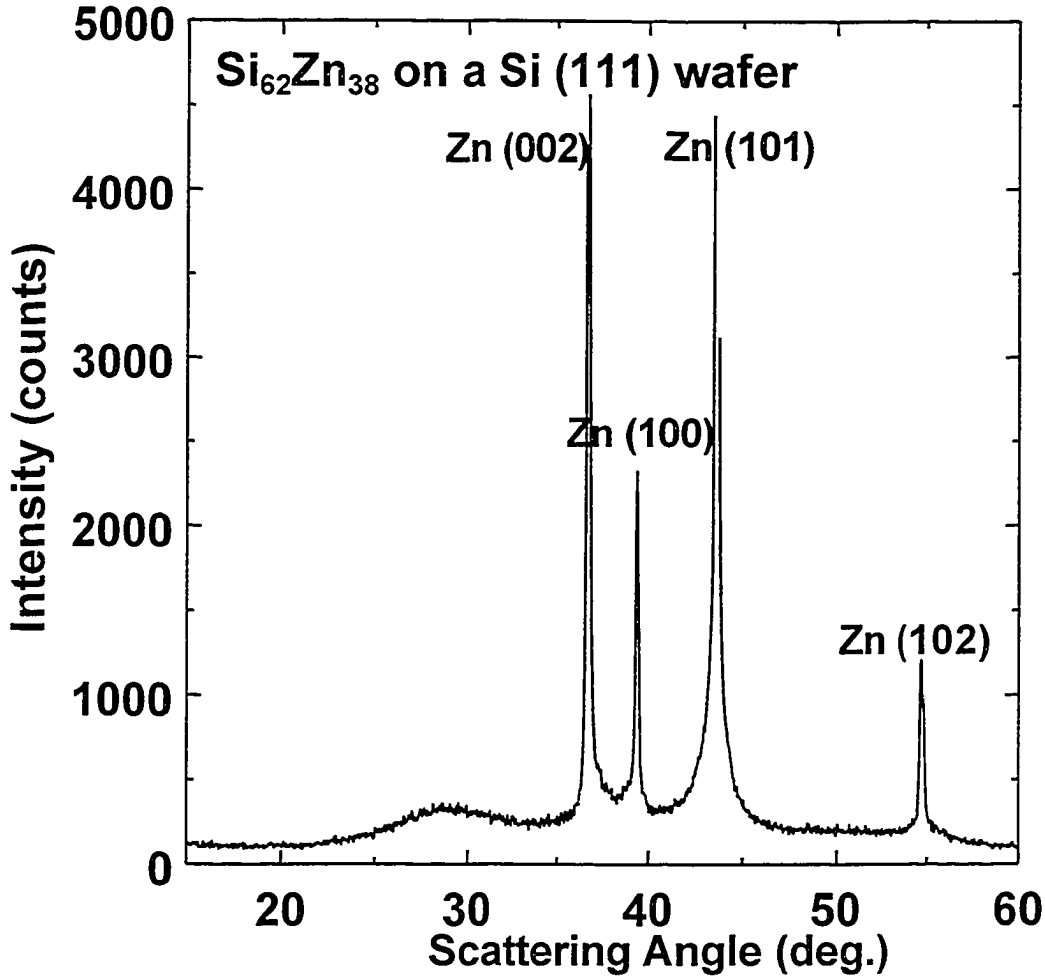

Figure 6.40. XRD pattern of 10 μm $Si_{62}Zn_{38}$ film on a Si (111) wafer.

A piece of a (111) Si wafer was included in the sputtering run that produced the film for the *in-situ* XRD experiment. This was measured with XRD before the *in-situ* cell was constructed to determine the structure of the film. The result is shown in Figure 6.40. The peaks present are from the crystalline Zn in the as deposited film. These peaks are indexed on the figure. There is a broad hump centered roughly at 29°. This is from the a-Si in the film. The tails of the Zn peaks may be obscuring the other, less intense, characteristic hump of a-Si at about 52°. The film sputtered on a Be window was included in an *in-situ* XRD cell as described in Chapter 5.

The dQ/dV *versus* potential graph for the *in-situ* cell is shown in Figure 6.41. The graph is most like that of channel 46 from the combinatorial cell, although the two peaks during the first charge are somewhat broader than for combinatorial cell. Like channel 46, after the first cycle the *in-situ* cell shows no evidence of crystalline material in the dQ/dV *versus* potential relationship.

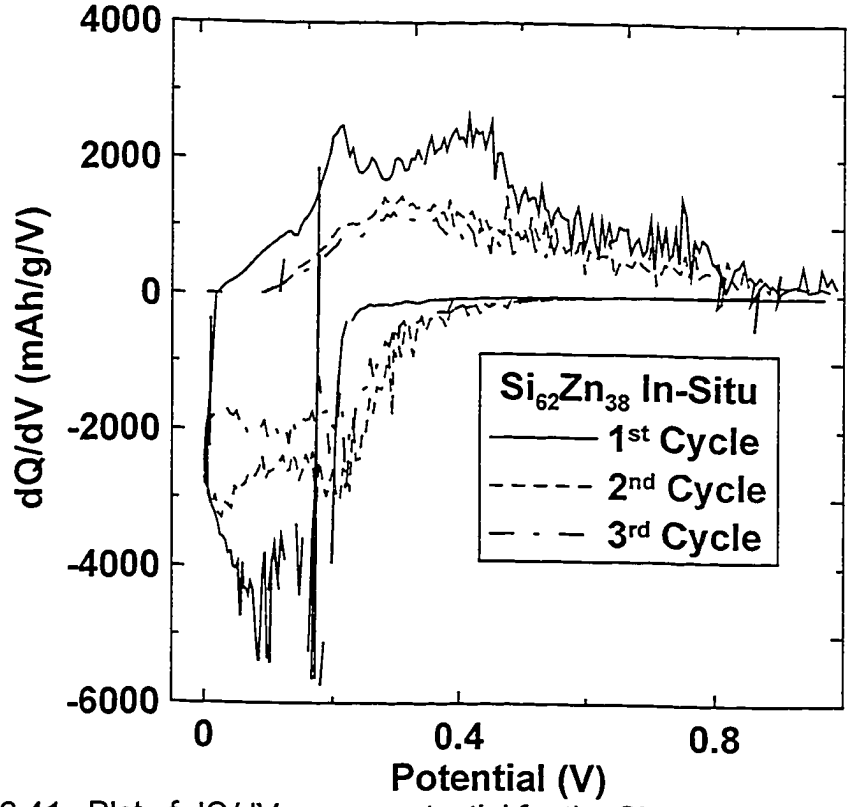

Figure 6.41. Plot of dQ/dV *versus* potential for the $Si_{62}Zn_{38}$ *in-situ* XRD cell.

The first discharge of the *in-situ* cell took a total of 85 hours. The *in-situ* cell was discharged using the signature method described in [95]. The current was halved three times with a 30 min. open circuit period between current steps. The first discharge was to 0 V. The cell was then charged to 1.2 V, also using the signature method. The subsequent discharge was also to 0 V, but the current was doubled. XRD data was collected with the Siemens D5000

described in Chapter 4. The generator was set for 40 kV and 30 mA. Data was collected between 2θ = 15° and 60° at 0.05° intervals. The count time was 12 s per point, giving total scan times of 3 h. A total of 73 scans were completed over the course of the experiment, with 29 of these during the first discharge.

Figure 6.42a shows potential *vs.* time for the first discharge of the *in-situ* cell, and Figure 6.42b shows selected XRD patterns taken from the cell. The angular range shown is from 15 to 50°. The numbers placed across Figure 6.42a at the height of 0.25 V represent the time of the XRD scans. In Figure 6.42b the scans are colour coded to make it easier to track the scan number. The colours used are black, red, blue, green and yellow. They are repeated in that order so, for example, the red scans are 2, 7, 12, etc. To make the changes occurring in the X-ray patterns more clear, the peaks due to the cell parts have been fitted and then removed by subtraction.

In scan 1, the only peaks present are those from the crystalline Zn in the as deposited film. These are quite strong, even through the Be window. The Zn peaks quickly begin to disappear as Li is added to the film. The first new peak that appears is at about 43° and is from $LiZn_9$ (circled in black in Figure 6.42b). This peak is not seen for very long. The next peaks are at about 24° and 42° and are from Li_2SiZn (circled in orange in Figure 6.42b). As the peaks from Li_2SiZn disappear, new peaks form at 24° and 41.5° (circled in mauve in Figure 6.42b). These peaks are from LiZn. These are the last peaks that form during the first discharge. There is no evidence of the $Li_{15}Si_4$ phase forming in this cell.

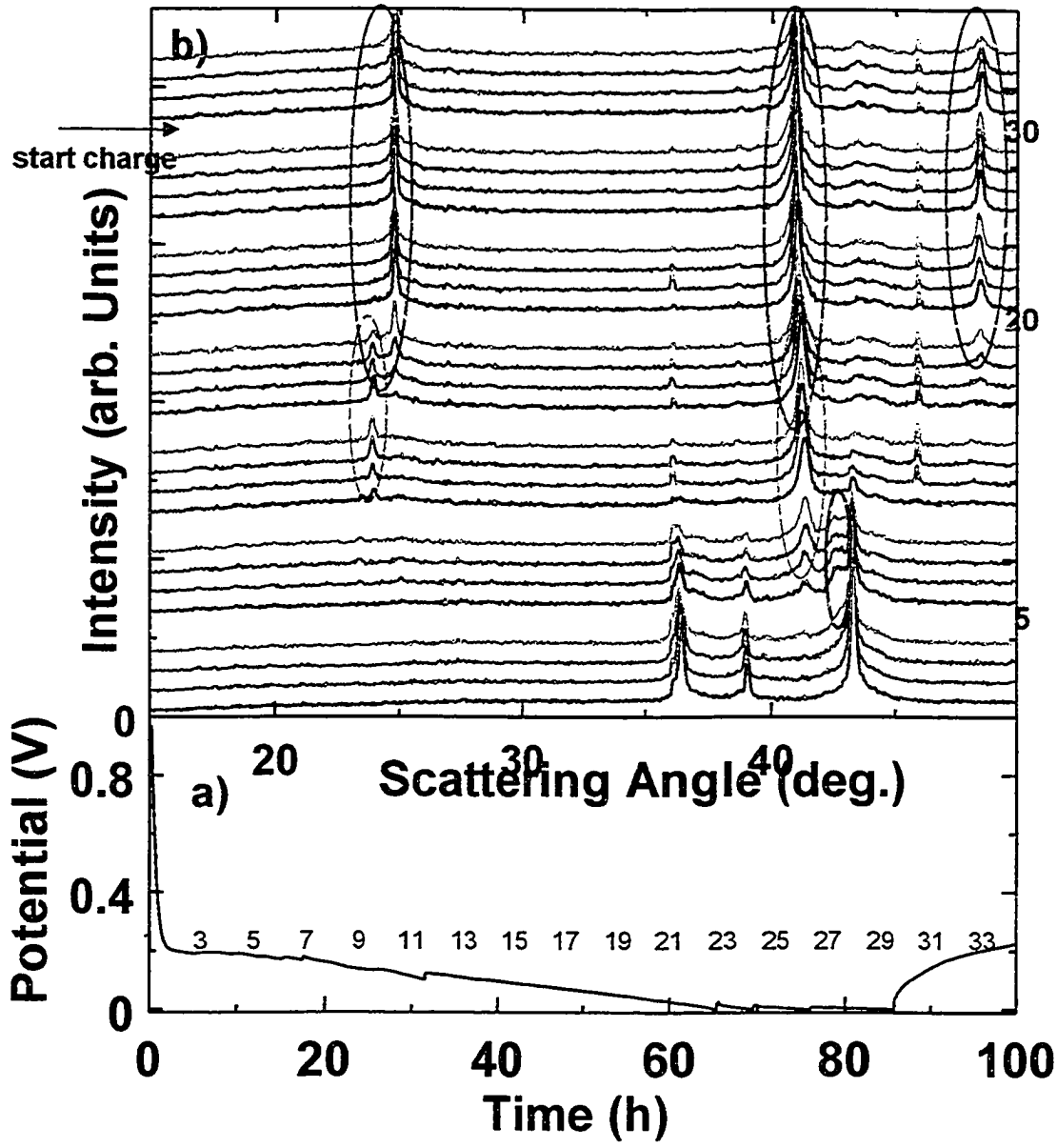

Figure 6.42. Plot of data collected for the first discharge of the $Si_{62}Zn_{38}$ *in-situ* XRD cell showing a) potential *versus* time and b) selected XRD scans. The numbers in 6.42a show the start time of the XRD scans. The colour code in 6.42b is described in the text. Some scans are numbered to the right of 6.42b.

Figure 6.43 shows the potential *versus* time and XRD scans for the rest of the *in-situ* experiment. The first yellow scan in this figure is scan 30. Only every fourth scan number has been shown in Figure 6.43a for clarity.

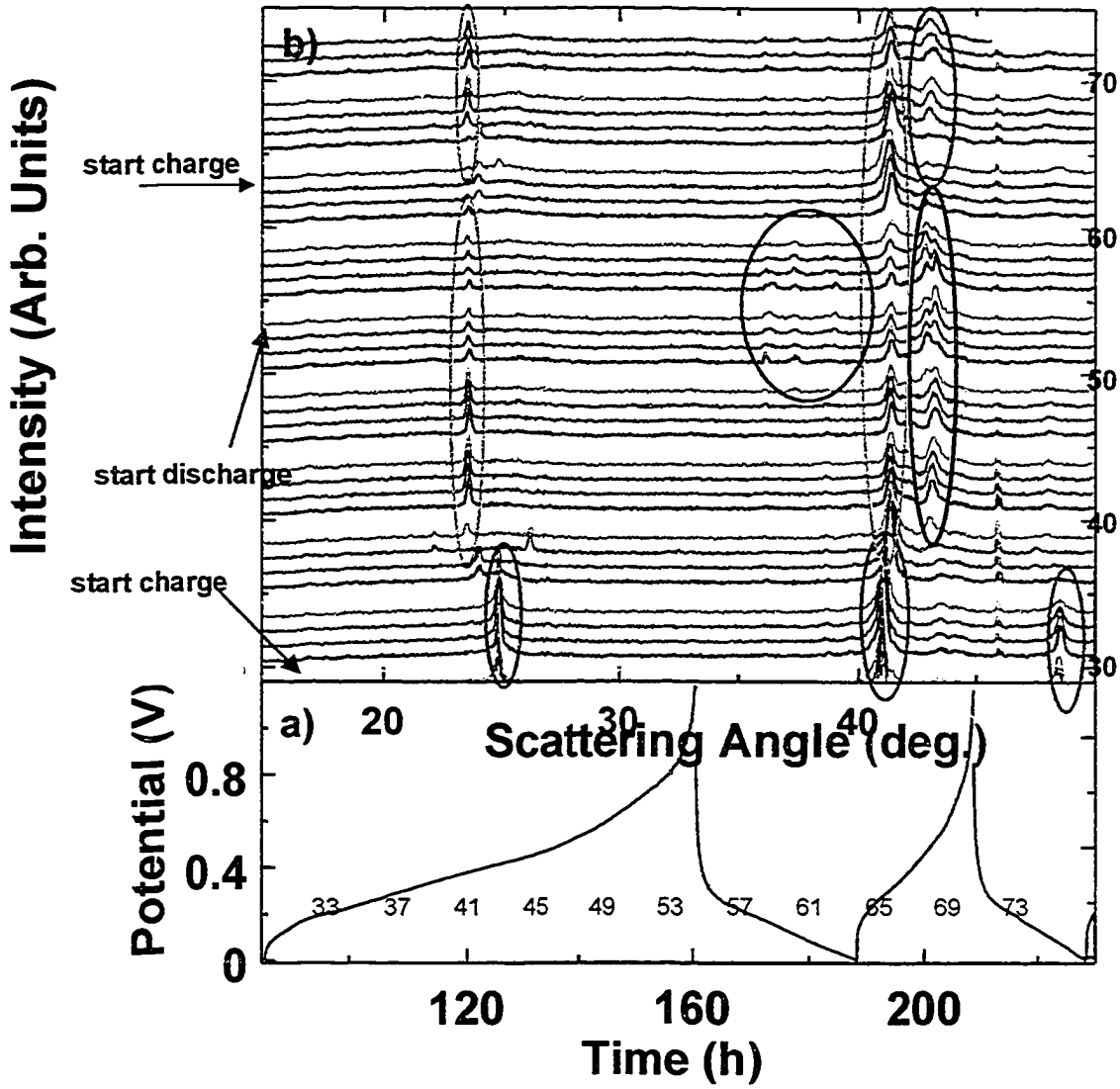

Figure 6.43. Plot of data collected for the first charge to the third discharge of the $Si_{62}Zn_{38}$ *in-situ* XRD cell showing a) potential *versus* time and b) selected XRD scans. The numbers in 6.43a show the start time of the XRD scans. The colour code in 6.43b is described in the text. Some scans are numbered to the right of 6.43b.

During the first charge the LiZn peaks, circled in mauve in Figure 6.43b, disappear. The Li_2SiZn peaks, circled in orange, reform but do not completely disappear by the end of the charge. Circled in black in Figure 6.43b are the 43° peak of Zn and also the $LiZn_9$ peak just to the right of the Zn peak. The Zn peak does not come back as strongly as at the start of the experiment. The $LiZn_9$

peak appears in scan 50 near the end of the first charge. It remains until scan 60, early in the second discharge. This peak does not reappear again. There is also some evidence of the remaining Zn peaks between 35 and 40° that appear near the end of the charge. These are circled in blue in Figure 6.43b.

The second discharge starts at scan 54 in Figure 6.43b (green). The Zn peaks disappear and the Li_2SiZn peaks reform. The LiZn phase does not seem to reform. The second charge starts at scan 64. The Li_2SiZn peaks fade somewhat and the 43° peak (circled in red in Figure 6.43b) of Zn again reforms but is very broad and weak.

It seems that after the first cycle, the cell is going from a mix of a-Si and a-Zn or nanocrystalline Zn at the top of charge to nanocrystalline Li_2SiZn at the bottom of discharge. The lack of sharpness in the XRD peaks indicates that any crystalline material in the film has very small grains or is nanocrystalline – nearly amorphous. This could explain the shape of the dQ/dV *versus* potential plot for the second and third cycles seen in Figure 6.41, which has no sharp peaks at all.

6.3.2.2. $Si_{78}Zn_{22}$

The target composition for the second SiZn *in-situ* XRD was $Si_{80}Zn_{20}$, which was well into the amorphous range with no crystalline Zn present from the SiZn binary library. The goals of this experiment were to see if the $Li_{15}Si_4$ phase did form during the first discharge and then disappear over the next few cycles. The stoichiometry achieved was $Si_{78}Zn_{22}$, as determined by electron microprobe. This is between channels 44 and 45 from the combinatorial cell plate, shown in Figures 6.34 and 6.35.

A piece of a (111) Si wafer was again included in the sputtering run that produced the film for the *in-situ* run. This was measured with XRD before the *in-situ* cell was constructed to determine the structure of the film. The result is shown in Figure 6.44. The broad a-Si humps are again present centered approximately at 29° and 52°. There is a broad peak centered at about 39° that corresponds to the Zn (100) peak and also a broad Zn (101) peak is beginning to form. The Zn (002) peak does not appear at 37°. The Zn (101) is supposed to be the most intense reflection. This combined with the width of the peaks indicates only nanocrystalline Zn with very small particles. The coherence length can be estimated using the Scherrer equation:

$$w = \frac{0.9\lambda}{D\cos\theta} \qquad 6.2.$$

Here, w is the full width at half maximum of an XRD peak measured in radians in the scattering angle, λ is the wavelength of the incident radiation (0.154 nm for Cu kα), D is the coherence length and θ is the Bragg angle. Applying this formula to the Zn (100) peak in Figure 6.44 gives a particle size of about 50 Å in the (100) direction. From the mass and composition of the film deposited and using the bulk density for Si and Zn, the thickness was estimated to be 8.5 μm.

The dQ/dV *versus* potential graph for the *in-situ* cell is shown in Figure 6.45. The graph is most like those of channels 44 and 45 from the combinatorial cell with one sharp peak during the first charge that disappears in later cycles. The peak during charge for the *in-situ* cell is actually gone by the second charge whereas for channel 44 of the combinatorial cell it does not completely disappear and for channel 45 it takes several cycles.

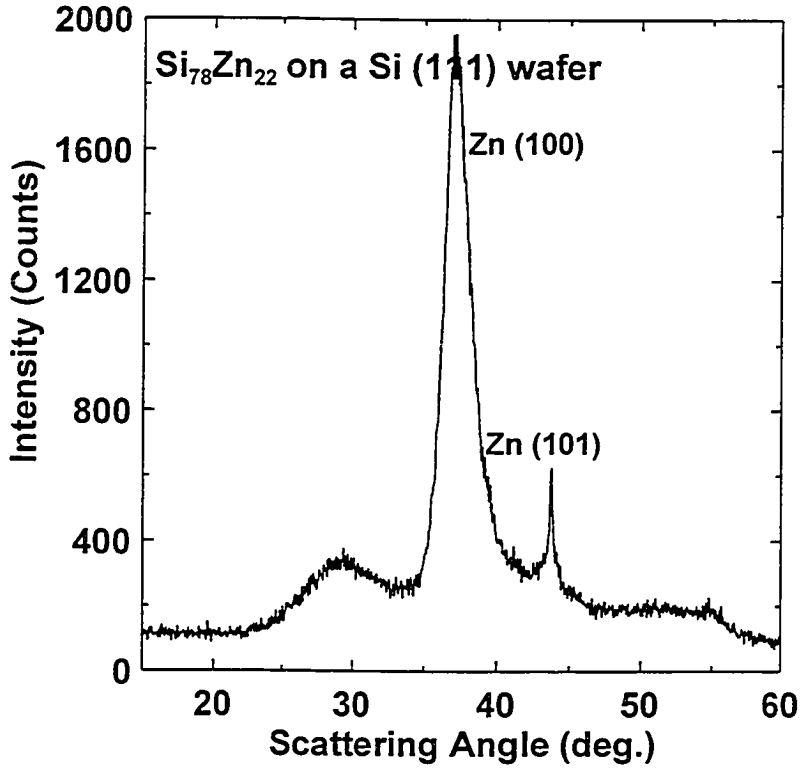

Figure 6.44. XRD pattern of 8.5 μm $Si_{78}Zn_{22}$ film on a Si (111) wafer.

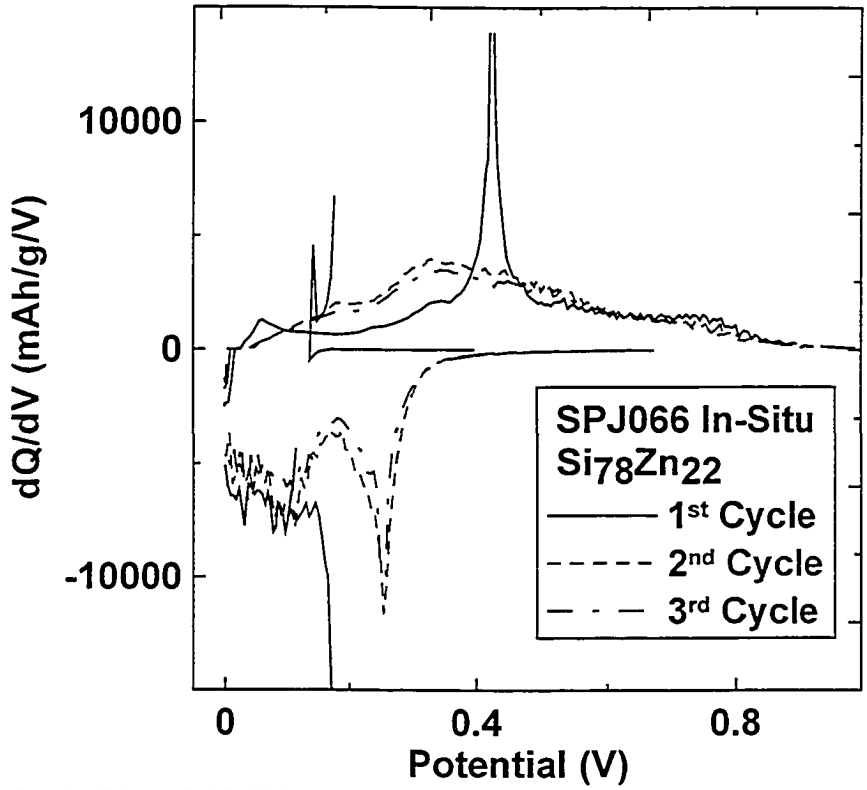

Figure 6.45. Plot of dQ/dV *versus* potential for the $Si_{78}Zn_{22}$ *in-situ* XRD cell.

The first discharge of the *in-situ* cell took a total of 70 hours. It was discharged using the signature method described in [95]. The current was halved three times with a 30 min. open circuit period between current steps. The first discharge was to 0 V. The cell was then charged to 1.2 V, also using the signature method. The subsequent discharge was also to 0 V, but the current was doubled. XRD data was collected with the Siemens D5000 described in Chapter 4. The generator was set for 40 kV and 30 mA. Data was collected between 2θ = 15° and 60° at 0.05° intervals. The count time was 12 s per point, giving total scan times of 3 h. A total of 70 scans were completed over the course of the experiment, with 23 of these during the first discharge.

Figure 6.46a shows potential *vs.* time for the first discharge and some of the first charge of the *in-situ* cell, and Figure 6.46b shows selected XRD patterns taken from the cell. The angular range shown is from 15 to 50°. The numbers placed across Figure 6.46a at the height of 0.25 V represent the time of the XRD scans. In Figure 6.46b the scans are colour coded to make it easier to track the scan number. The colours used are black, red, blue, green and yellow. They are repeated in that order so, for example, the red scans are 2, 7, 12, etc. To make the changes occurring in the X-ray patterns more clear, the peaks due to the cell parts have been fitted and then removed by subtraction.

In scan 1, the only peaks present are the broad Zn (100) peak and a peak from Li at about 36°. The Zn peak quickly disappears as Li is added to the film. The $LiZn_9$ peak at 43° does not appear for this cell. The first new peaks that appear are the Li_2SiZn peaks at about 24° and 42° (circled in black in Figure

6.46b). As the peaks from Li_2SiZn disappear, new peaks form at 24°, 26°, 40° and 44° (circled in mauve in Figure 6.46b). These peaks are from the $Li_{15}Si_4$ phase. These are the last new peaks seen for this cell during the first discharge.

At the start of the first charge, the peaks from the $Li_{15}Si_4$ phase begin to disappear. By scan 35, which corresponds to the end of the plateau during the first charge in Figure 6.46a, the peaks are gone. The Li_2SiZn peaks have not reformed at this point.

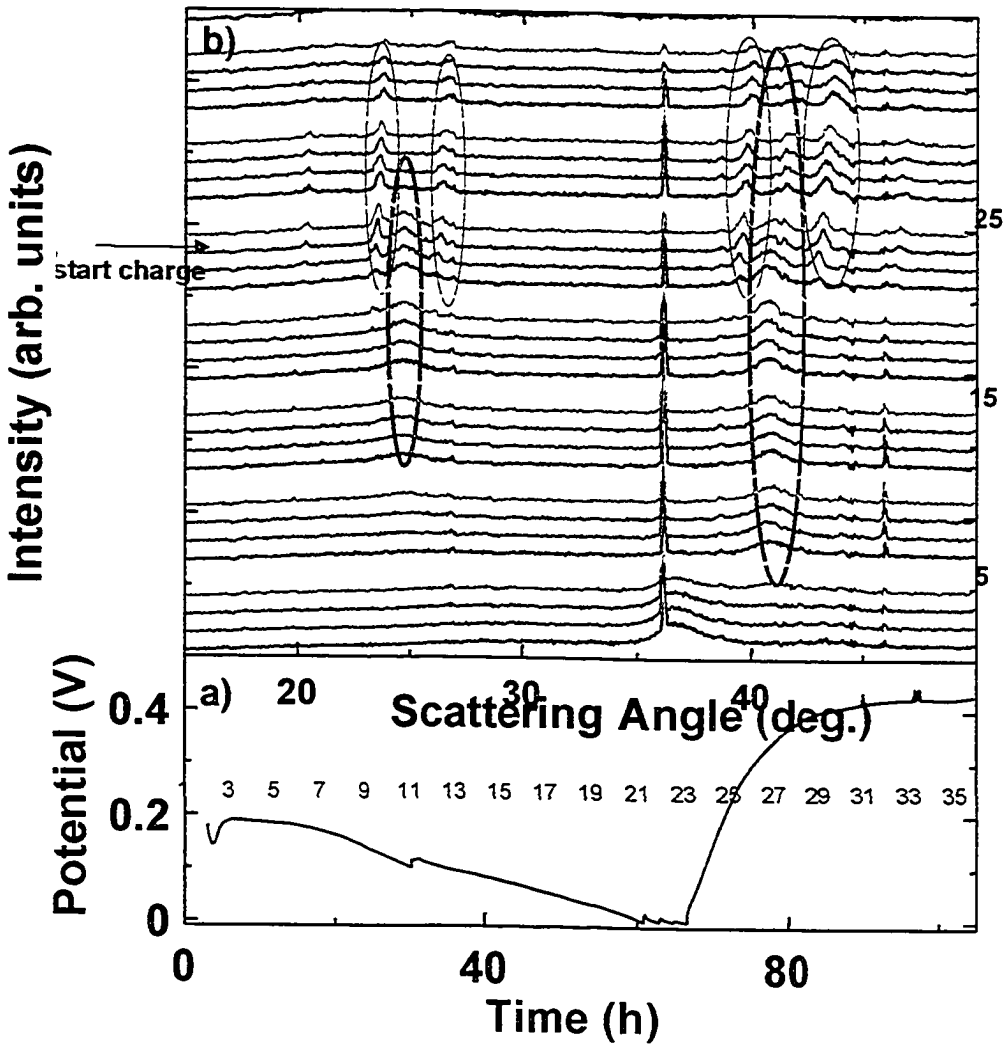

Figure 6.46. Plot of data collected for the first discharge and part of the first charge of the $Si_{78}Zn_{22}$ *in-situ* XRD cell showing a) potential *versus* time and b) selected XRD scans. The numbers in 6.46a show the start time of the XRD scans. The colour code in 6.46b is described in the text. Some scans are numbered to the right of 6.46b.

Figure 6.47 displays the data for the rest of the first charge, the second discharge and the beginning of the second charge. The Li_2SiZn peaks do not reappear, either during the first charge or the second discharge. No Zn peaks reform, and no $Li_{15}Si_4$ peaks reform at any time. Near the end of the second discharge a new peak appears at about 41° (circled in black in Figure 6.47b). This peak at 41° has not been seen before for either *in-situ* XRD experiment.

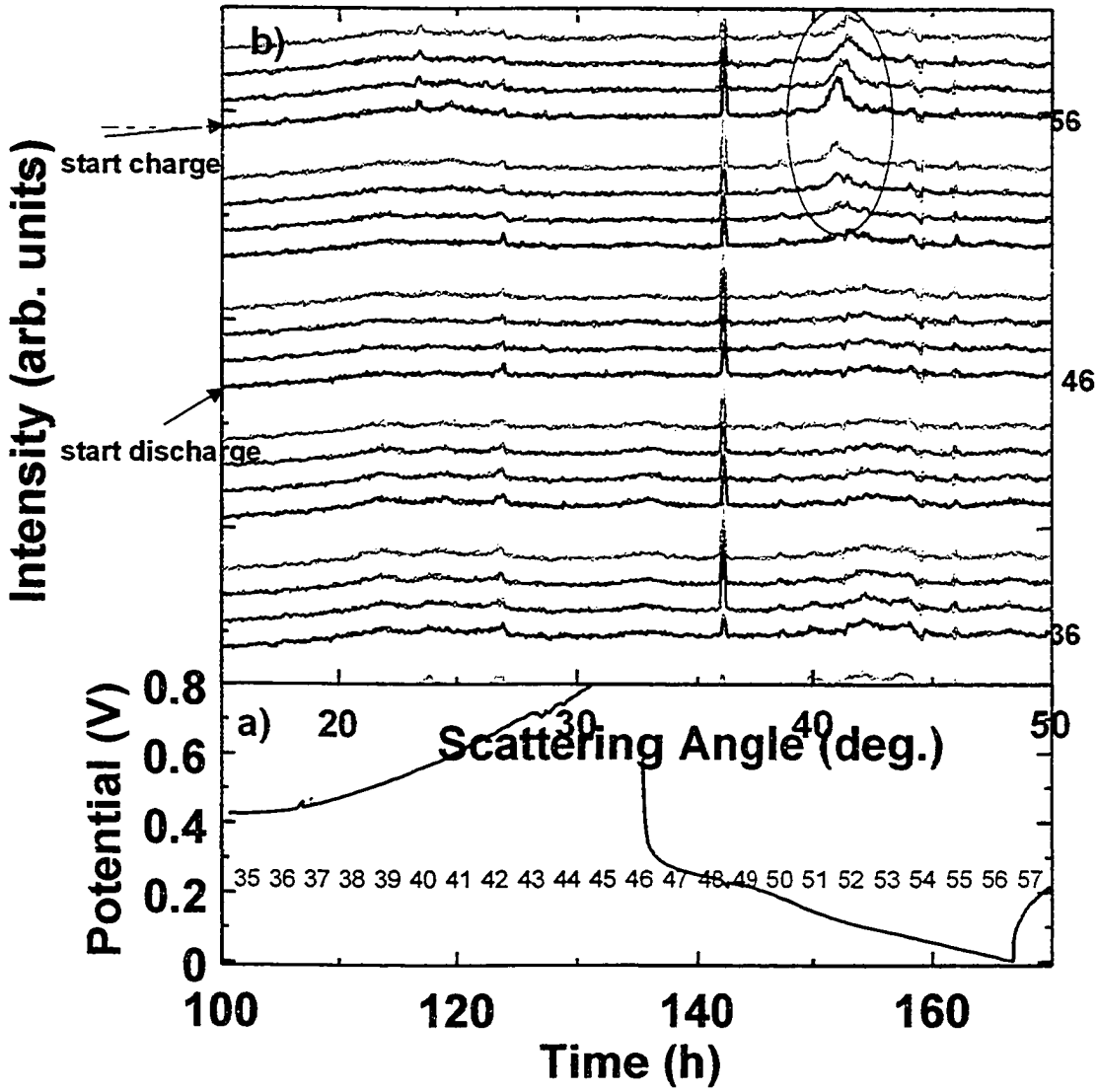

Figure 6.47. Plot of data collected for the end of the first charge, the second discharge and the beginning of the second charge of the $Si_{78}Zn_{22}$ *in-situ* XRD cell showing a) potential *versus* time and b) selected XRD scans. The numbers in 6.47a show the start time of the XRD scans. Some scans are labeled to the right pf 6.47b. The colour code in 6.47b is described in the text.

Figure 6.48 shows an expanded view of scans 49 to 59 of Figure 6.47. There is a broad hump centered at about 25° in addition to the new peak at 41°. It is speculated that these features are from a Li_4Si phase similar to a Li_4Sn phase described by Dahn et al. [99]. In this phase, the Li and Sn atoms are placed on an underlying BCC lattice with the Sn atoms grouped in randomly oriented tetrahedra. The peak at 41° would arise from the BCC lattice and the broad hump at 25° from the random Sn tetrahedra. In this cell, it is thought that the same structure has formed with Si (and probably Zn) in place of the Sn.

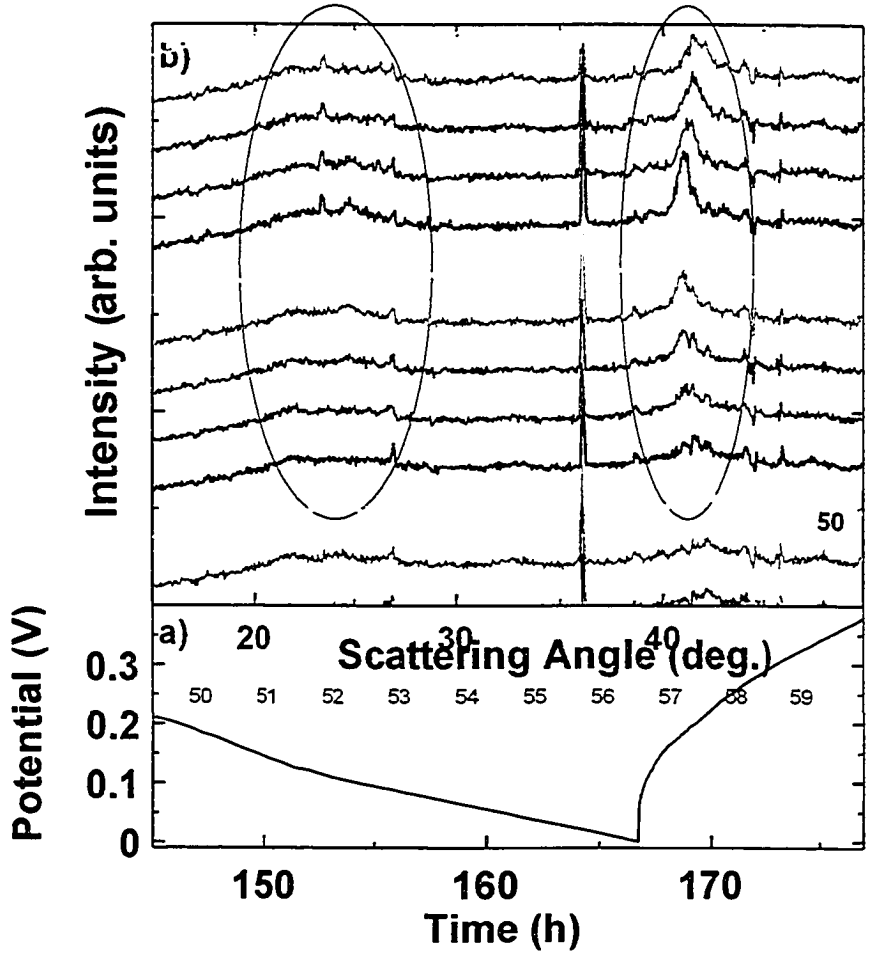

Figure 6.48. Plot of data collected for the end of the second discharge and the beginning of the third charge of the $Si_{78}Zn_{22}$ *in-situ* XRD cell showing a) potential *versus* time and b) selected XRD scans. The numbers in 6.48a show the start time of the XRD scans. Scan 50 is labeled to the right pf 6.48b. The colour code in 6.48b is described in the text.

6.3.3. Conclusions for SiZn

The SiZn system has been studied both with the combinatorial electrochemical cell and with *in-situ* XRD. The electrochemical cycling for SiZn has been found to be superior to that of SiAg, although it is not as good as SiSn. The irreversible capacities for SiZn were approximately 10 % of the first discharge, which is good compared to other alloy systems in the literature but not as good as the SiAg system which was a couple of percent less. Reversible capacities of over 1000 mAh/g were found for compositions of approximately $Si_{0.4}Zn_{0.6}$ that cycled quite well.

The success of the SiZn compositions is likely due to the fact that, as they are electrochemically cycled, the films become amorphous or nanocrystalline. With lower zinc content, Li_2SiZn and $Li_{15}Si_4$ are formed during the first discharge. Zinc does not reform during the charge, and the Li_2SiZn and $Li_{15}Si_4$ phases do not reappear during subsequent discharges. A $Li_4(SiZn_x)$ phase similar to Li_4Sn reported in [99] forms during the second charge. It should be noted that the $Li_{15}Si_4$ phase disappeared much more quickly for the thicker *in-situ* cell than for the corresponding compositions on the combinatorial electrochemical cell. This is not fully understood, but may be due to greater stress and better adhesion to the substrate in the thinner film that does not allow as much mobility of atoms as the thicker film.

For cells with higher zinc content, $LiZn_9$, Li_2SiZn and LiZn form during the first discharge. Zinc does reform during the charge, but the particle size is likely quite small. No $Li_{15}Si_4$ is formed at any time. After a few charge/discharge

cycles the entire film appears to become amorphous or nanocrystalline. Overall, it has been seen that Zn does suppress the formation of the $Li_{15}Si_4$ phase, and other crystalline phases in general. This *in-situ* amorphization is why these films cycle better than the SiAg cells.

The structure of the Li_2SiZn phase is quite interesting. It is a layered structure with the Si and Zn forming layers between which the Li are located. A diagram is shown in Figure 6.49. The space group is P -3 m 1. The Zn atoms are located in the 2c positions at (0, 0, 0.135) and (0, 0, 0.385). The Si are on the 2d positions at (1/3, 2/3, 0.375) and (1/3, 2/3, 0.875). The Li also occupy 2d positions with c coordinates of 0.042, 0.208, 0.542 and 0.708. The lattice constants are a = 0.4247 nm and c = 1.6448 nm. These are the parameters reported for this phase in [102]. The parameters for the phase encountered in this work have not yet been determined. The layered structure may allow the Li to easily move in and out of the structure. This may be why the compositions of SiZn with moderate to high Zn content perform as well as they do, since these compositions form the Li_2SiZn phase during the first discharge. An interesting future experiment would be to prepare Li_2SiZn and make coin type test cells. This would test the performance of non-sputtered (likely larger particle size) material and help indicate if it could successfully be adapted for use in mass produced cells.

The reason why in a given film some phases initially crystallize and others don't may be related to particle size. Figure 6.50 shows the SiLiZn phase diagram with the phases that occur in the cells discussed above indicated. The

paths taken by the two *in-situ* XRD cells as Li is added are marked on the diagram. If the path passes close to a phase, it is more likely to crystallize than if it passes farther away. If the path is closer to a phase it means that there should be more of that phase present, which should lead to larger particles.

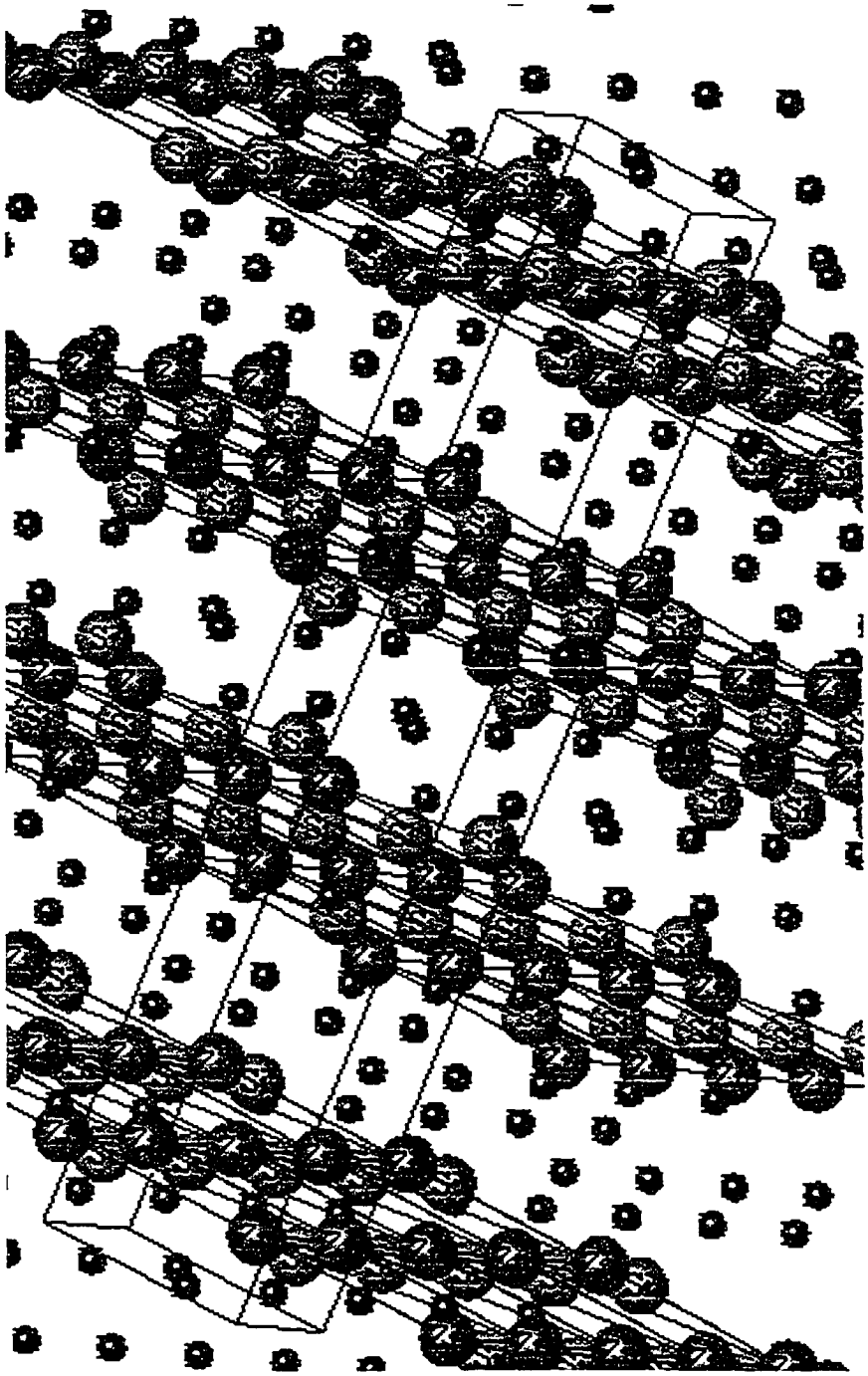

Figure 6.49. Structure of Li_2SiZn. Si atoms are green, Zn are red and Li are blue. The unit cell is drawn in black.

For SiZn films with low Zn, it seems that the Zn may be incorporated in the $Li_{15}Si_4$ phase, much like what was thought for SiAg with low Ag. When the Zn content becomes higher however, the behaviour is much different than for Ag. During discharge, the Si and Zn become incorporated in various phases. Either a $Li_4(SiZn_x)$ phase similar to Li_4Sn reported in [99] or Li_2SiZn. The Li content in these phases is likely variable over a wide range. In the Li_2SiZn phase, extra Li may be able to be accommodated between the SiZn layers. During charge, the Li is removed and the Si and Zn dissociate. However, the Si and Zn cannot completely phase separate and so form only very small particles of nanocrystalline Zn distributed in an a-Si matrix. Li_2CuP has a similar structure to Li_2SiZn. This material has been studied recently by Nazar and co-workers [105]. Their work suggests that extra Li may be inserted between the Cu and P layers for that material as well. The XRD pattern for Li_2CuP was not found in *in-situ* XRD experiments when the Li was removed, suggesting that material may be becoming amorphous. This makes it difficult to tell if the layering is preserved when the Li is removed. More work is needed to clarify the machanisms of Li insertion and removal for these very interesting materials.

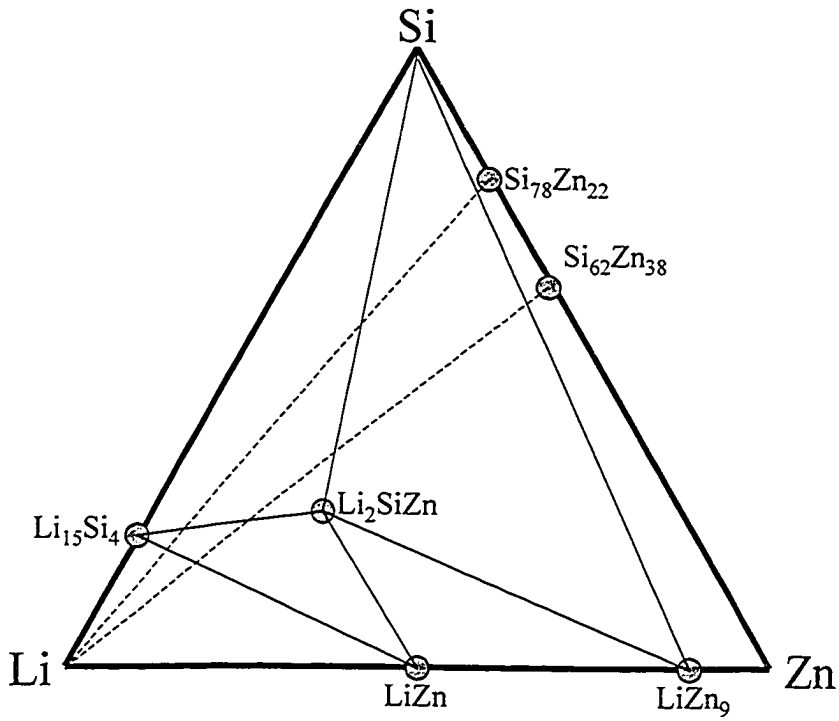

Figure 6.50. The SiLiZn phase diagram showing important phases and the paths taken during lithiation of the two *in-situ* XRD cells.

Figure 6.51 illustrates what is speculated for $Si_{0.5}Zn_{0.5}$. In Figure 6.51a we see the as-sputtered film with fairly large particles of crystalline Zn distributed in an a-Si matrix. This agrees with XRD for films of this composition. During the discharge of this film, Li_2SiZn forms, as would be expected from Figure 6.50. The phase is labeled as $Li_{2+x}SiZn$ in Figure 6.51b because the final Li content is not known. All of the Si and Zn would be incorporated in this phase. After the Li is removed, the a-Si matrix reforms. The Zn cannot diffuse well at room temperature, so only very small particles are formed. This leaves either nanocrystalline Zn distributed in an a-Si matrix or amorphous Si-Zn in Figure 6.51c. Note that the Zn grains in Figure 6.51c are not drawn to scale. They are thought to be very much smaller than the grains in Figure 6.51a (nanometers in

scale). It would be interesting to try this at higher temperatures to see if this would improve the diffusion of the Zn and result in larger Zn particles at the top of charge.

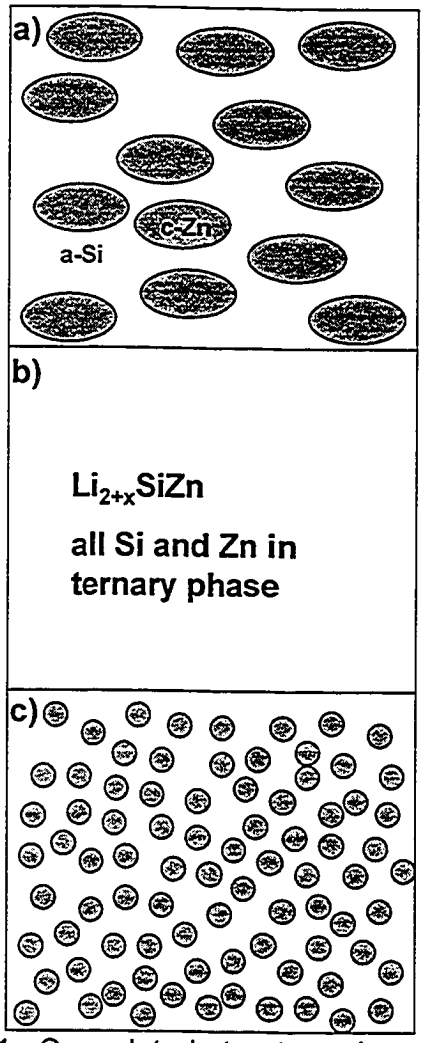

as sputtered $Si_{50}Zn_{50}$. Large c-Zn dispersed in a-Si.

bottom of first discharge. $Li_{2+x}SiZn$

top of charge. Nanocrystalline or amorphous Si-Zn. Atoms unable to phase separate at low temperatures.

Figure 6.51. Speculated structure changes to a $Si_{50}Zn_{50}$ film during insertion and removal of Li.

6.4. Summary of Si-M Binaries

There are significant differences in the way each of the three binary systems studied in this chapter behave when cycled electrochemically in a Li-metal test cell.

In the Si-Sn binary system, it was found that if the film was amorphous as sputtered then it would remain amorphous as Li was inserted and removed. The shape of the dQ/dV *versus* potential graphs was constant with cycle number and had no sharp peaks. It is interesting that there are no SiSn binary phases found in reference [102]. This indicates that Si and Sn do not tend to mix readily or form alloys or compounds. However, it must be noted that the sputtered films are amorphous mixtures with the Si and Sn perfectly mixed in what appears to be the a-Si structure with Sn substituted for some of the Si. The Sn substitutions also cause larger interatomic spacing. There are also no Li-Si-Sn ternary phases reported. The Si and Sn seem to react with the Li while remaining in the amorphous phase as opposed to forming ternary Li-Si-Sn phases. No crystalline Li-Si or Li-Sn phases are formed. This explains the superior performance of this binary system over the other two studied.

In the Si-Zn binary system, there are also no binary phases formed [102]. The film starts as an amorphous mixture of Si and Zn or as a 2-phase system with a-Si and nanocrystalline Zn. In this system however, there is a ternary phase: Li_2SiZn. Depending on the Zn content, this phase or a $Li_4(SiZn_x)$ phase [99] will form as Li is inserted. When the Li is removed the Si and Zn cannot separate, so only nanoparticles of each phase (a-Si and nano-Zn) can form. Perhaps at higher temperatures the Zn could phase separate and form large crystalline grains. At room temperature the entire film becomes nanocrystalline or amorphous. In this case, the films cycle fairly well electrochemically, although not as well as SiSn, because of the very small particle sizes.

In the Si-Ag binary system there are several metastable binary phases reported [102]. There was no evidence of these phases in the sputtered films discussed in this thesis. The behaviour of the SiAg library was very different from the other two binary systems. As the films were electrochemically cycled, the Ag seemed to aggregate into larger particles than in the as sputtered film. This enabled the formation of $Li_{15}Si_4$, unlike the other two systems. There is a ternary phase in this system: $Li_8Si_5Ag_3$. This phase has the same ratio of one Li per Si or metal atom as Li_2SiZn. The Li-Ag-Si phase also has a hexagonal structure, but the space group and atom positions were not reported [102]. It is not clear that this phase forms during the lithiation of Si-Ag films. It is likely that the Ag phase separates from the a-Si during delithiation, forming large Ag grains. The Ag and Si are not mixed well enough to form the ternary phase when Li is again inserted, as was the case with the Si-Zn system. Instead, the Ag alloys with Li independently from the Si and the capacity from the Ag then quickly fade.

It is also of interest that the addition of Sn to a-Si inhibited the formation of the $Li_{15}Si_4$ phase while the addition of Ag and Zn did not. For compositions of $Si_{85}M_{15}$ there was evidence of crystallization for M = Ag and Zn but not for M = Sn. It is not clear why this is the case. More work is needed to find the reason for this behaviour.

Chapter 7. Si-A-B Ternaries

7.1. SiAlSn

7.1.1. Amorphous Range

Ternary films of $SiAl_xSn_y$ ($0 < x,y < 1$) were prepared using the combinatorial sputtering system described in Chapter 3. The sputtering powers used were 200 W net RF for Si, 30 W DC for Al and 13 W DC for Sn. The argon pressure was about 2.5 mTorr during deposition. The deposition proceeded for about 8 hours, after which the film was about 1μm thick in its thickest location. Substrates used were a 75 mm x 75 mm copper foil, a 75 mm x 75 mm cleaved Si wafer (111) and twenty-five 1.3 cm diameter pre-weighed Cu foil discs.

The film deposited on the Cu foil was used for electron microprobe analysis. 100 data points were collected on a 10 x 10 grid with a spacing of 7.5 mm between data points. Figure 7.1 shows a contour map of the Sn:Si and Al:Si atomic ratios measured by electron microprobe plotted *versus* position on the 75 x 75 mm foil. As can be seen, the ratios of Sn and Al to Si vary approximately linearly and orthogonally.

The film deposited on the Si wafer was used for X-ray diffraction. The same 7.5 mm grid spacing employed for electron microprobe measurements was also used for the X-ray diffraction study. Figure 7.2 shows the x-ray map for this film. The angular range displayed is from 20° to 50°. In this figure, the Sn content is increasing from right to left and the Al content is increasing from bottom to top.

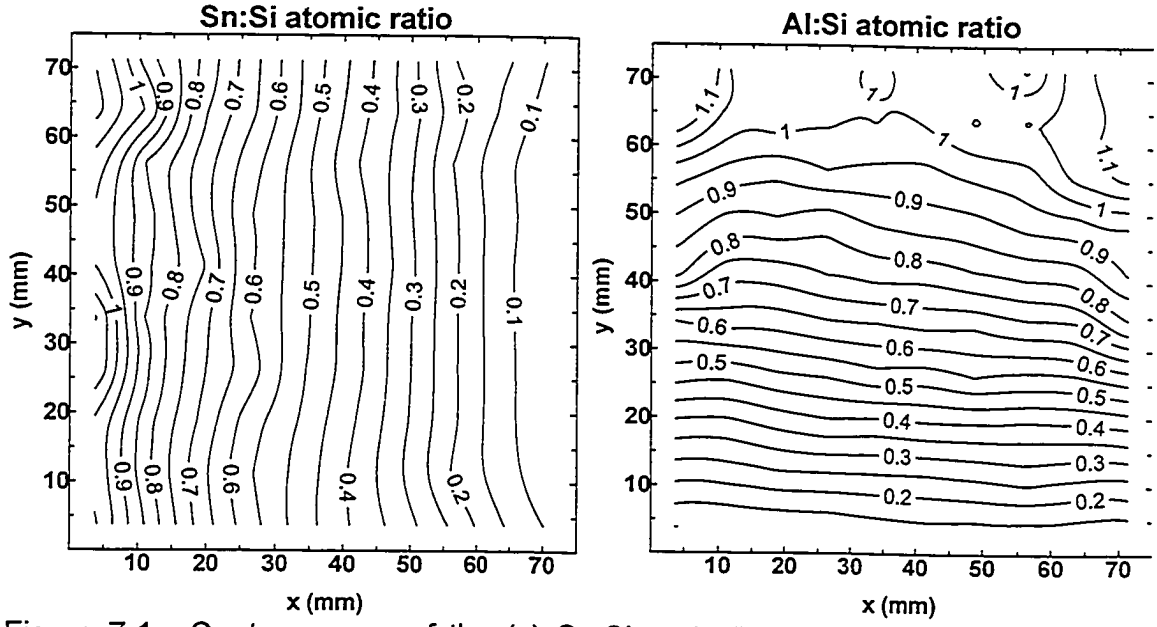

Figure 7.1. Contour maps of the (a) Sn:Si and (b) Al:Si atomic ratios *versus* position on the first 75 mm x 75 mm $SiAl_xSn_y$ ($0 < x,y < 1$) film.

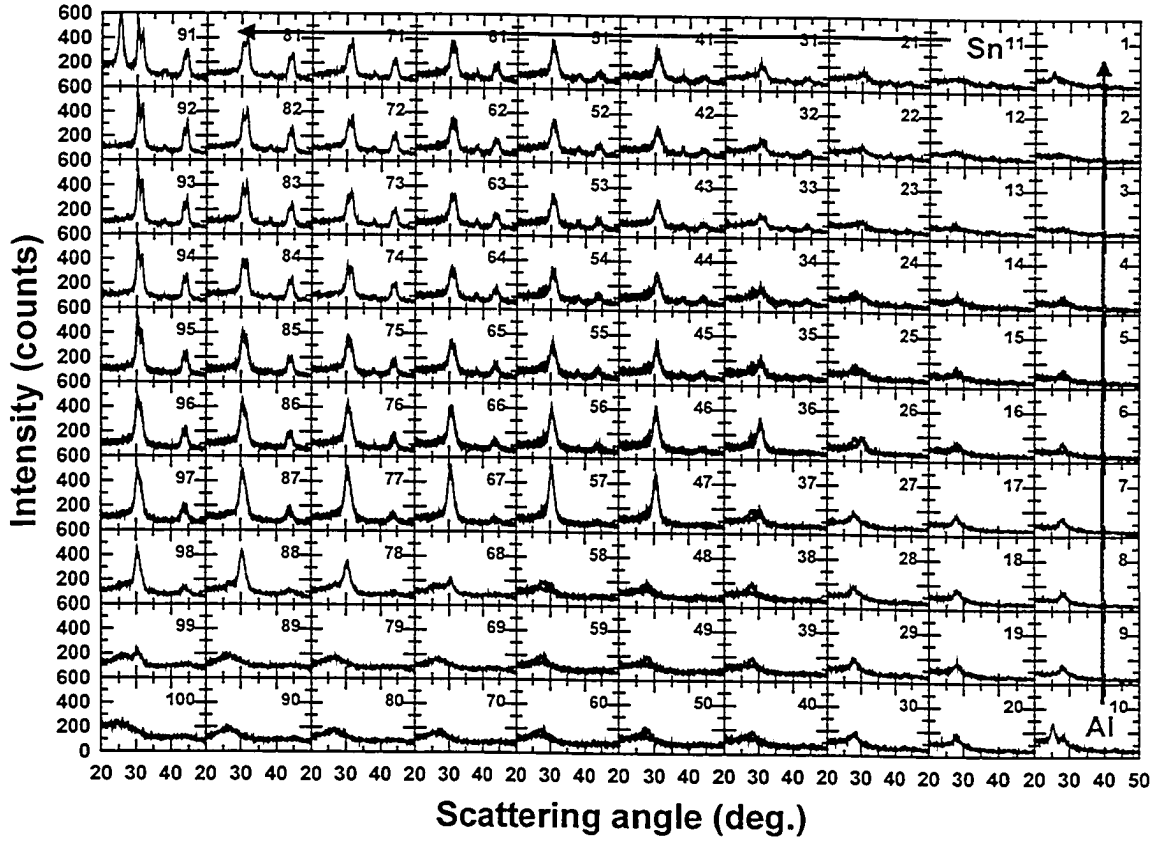

Figure 7.2. X-ray patterns displayed as a function of position on the first 75 mm x 75 mm $SiAl_xSn_y$ ($0 < x,y < 1$) film. The Al content increases from bottom to top and the Sn content increases from right to left. The angular range shown is from 20° to 50°.

Some of the patterns displayed in Figure 7.2 actually contain more than one pattern collected from the same grid point. The x-y stage on our X-ray machine is only capable of moving 50 mm in either direction, while our sample is 75 mm on a side. It was necessary to collect data with the wafer in four different orientations to cover the entire wafer. As a result, some grid points were scanned up to four times. The same collection parameters were used for each of the four runs so each individual scan could be correlated to its proper place on the film. If a grid point had multiple patterns collected, they are all displayed. Figure 7.3 shows the four X-ray patterns collected for one grid point near the centre of the film. As can be seen, they match almost perfectly, as would be expected.

There are minor differences in the x-ray patterns shown in Figure 7.3, but this is because the background reflections from the Si wafer are not identical for each orientation. The background of the wafer was checked before the sputtering run was done. As we knew it would be necessary to X-ray the film in four orientations, the background was checked in these orientations and found to be different. In one orientation in particular, there were some anomalies. The asterisk in Figure 7.3 shows one of these anomalies. It can be seen that one of the patterns differs significantly from the others at the indicated point. This corresponds to a broad, shallow peak at that angle observed in the wafer's background when in the same orientation that the indicated pattern was collected.

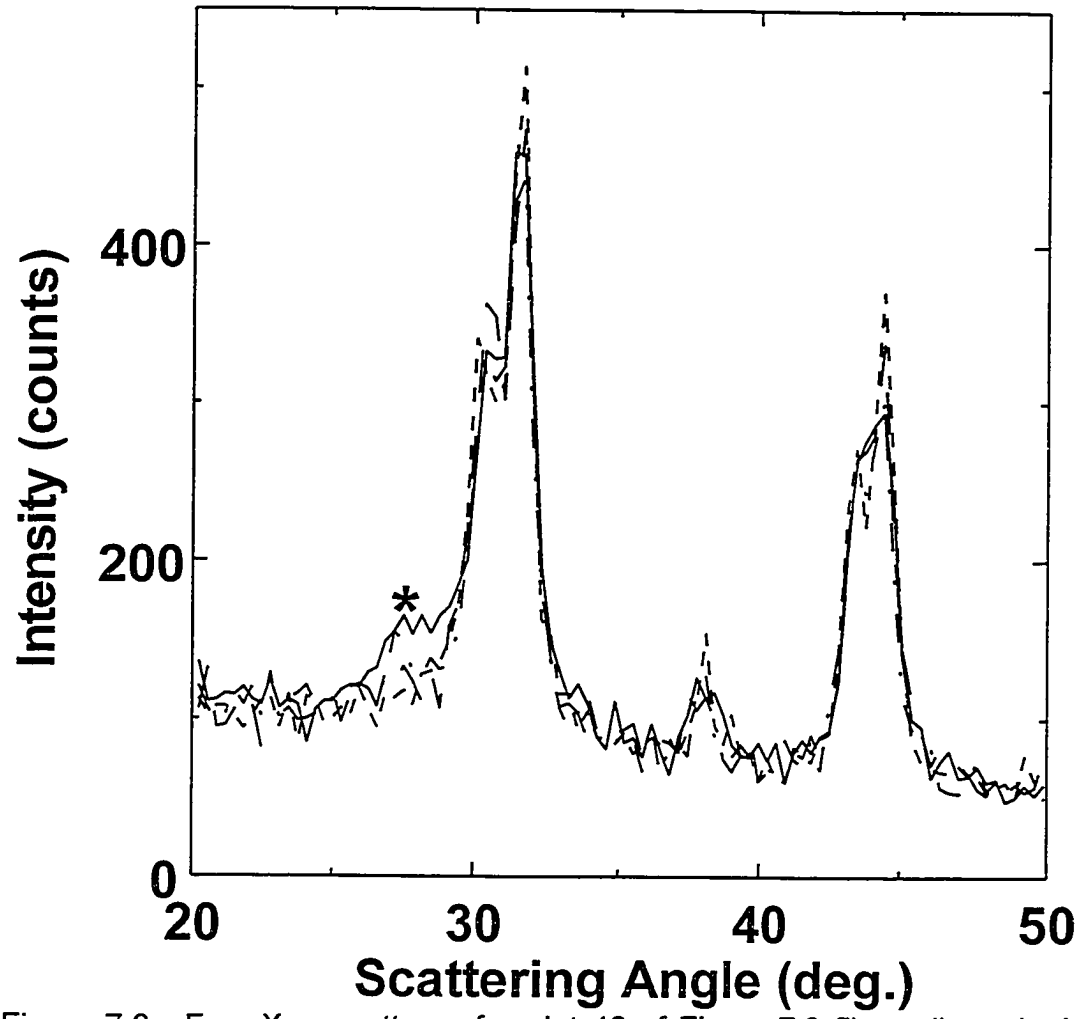

Figure 7.3. Four X-ray patterns for plot 46 of Figure 7.2 film collected with the film in four different orientations. The asterisk marks a difference in the patterns due to differing background reflections of the Si wafer when in different orientations relative to the detector.

Figure 7.2 contains a large amount of information about the structures found in the SiAlSn ternary system. The set of scans along the bottom edge ($Si_{1-x}Sn_x$; $0<x<0.5$) show that the corresponding range of stoichiometries is amorphous. The next row up, which now contains a constant amount of Al, is also amorphous. The three rightmost columns (rightmost column is $Si_{1-x}Al_x$; $0<x<0.5$, with Sn being added to the left) are also amorphous, showing that this system has quite a large amorphous range. As more of the elements Sn and Al

are added, the amorphous structure no longer spans across the entire film. As an example consider the column of scans from 69 at the bottom to 60 at the top. Scan 69 contains a moderate amount of Sn ($SiSn_{0.65}$ at this position from Figure 7.1) but is still amorphous. Proceeding up this column, the amount of Al increases and the amount of Sn is constant. Scan 67 is still amorphous, but in scan 66, there is a well defined peak indicating crystalline Sn, even though the amount of Sn has not changed but the Al content has increased. Not until scan 65 or even 64 can evidence of crystalline aluminum be found in the X-ray patterns, and the peak is quite small. It seems that as the Al content increases, it is dissolved preferentially into the amorphous phase while the Sn is forced to crystallize out.

If columns farther to the left of Figure 7.2 are examined, it can be seen that as the Sn content is increased, less Al is needed to cause Sn crystallization. Finally, the presence of the Sn seems to limit the amount of Al that can be incorporated into the amorphous phase. An examination of the top row of scans in Figure 7.2 shows that with no Sn the structure is amorphous with maximum Al content. By scan 50, however, there is evidence of crystalline Al in the X-ray pattern indicating that the amorphous phase can no longer accommodate all of the Al.

To produce a film composition, $SiAl_xSn_y$ ($0 < x,y < 2$), one only needs to double the power used for Sn and Al (or halve the power for Si). To do this, a second deposition was performed using 200W for Si, 60 W for Al and 26 W for Sn. Figure 7.4 shows the electron microprobe results for this film, collected on a

3.75 mm (20 x 20 points) square grid. Comparing to Figure 7.1, it is clear that the Sn:Si and Al:Si ratios have about doubled, as desired.

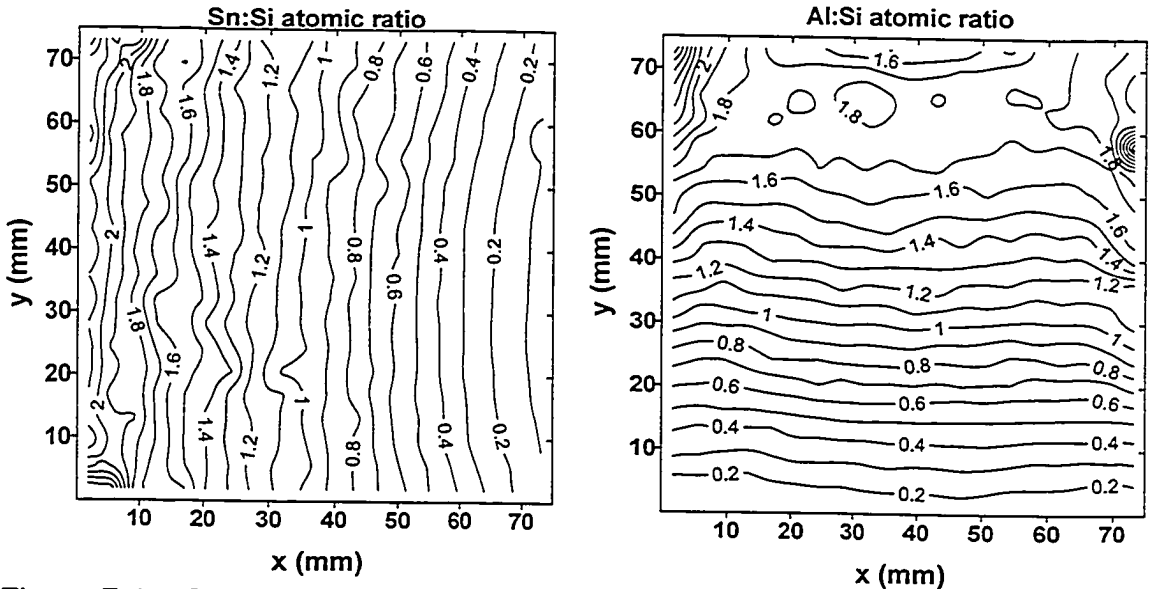

Figure 7.4. Contour maps of the (a) Sn:Si and (b) Al:Si atomic ratios *versus* position on the second 75 mm x 75 mm $SiAl_xSn_y$ ($0 < x,y < 2$) film.

By combining the electron microprobe composition measurements and the X-ray structural data, it is possible to construct a portion of the ternary phase diagram for the SiAlSn system. Of course, due to the method of preparing the films, this is a non-equilibrium phase diagram. Figure 7.5 shows the phase diagram of the SiAlSn system. The dots on the diagram correspond to the 3.75 mm X 3.75 mm grid points on the sample. The amorphous range is denoted by the thick solid lines, with the 2 and 3 phase regions also labelled. It is worth noting that there is very little solid solubility of either Al or Sn in Si according to equilibrium phase diagrams (for example see the Si-Sn phase diagram in Figure 6.1) [100]. The rapid quenching rates achieved by sputtering apparently stabilize

a single-phase amorphous range for samples with over 60 atomic percent of silicon.

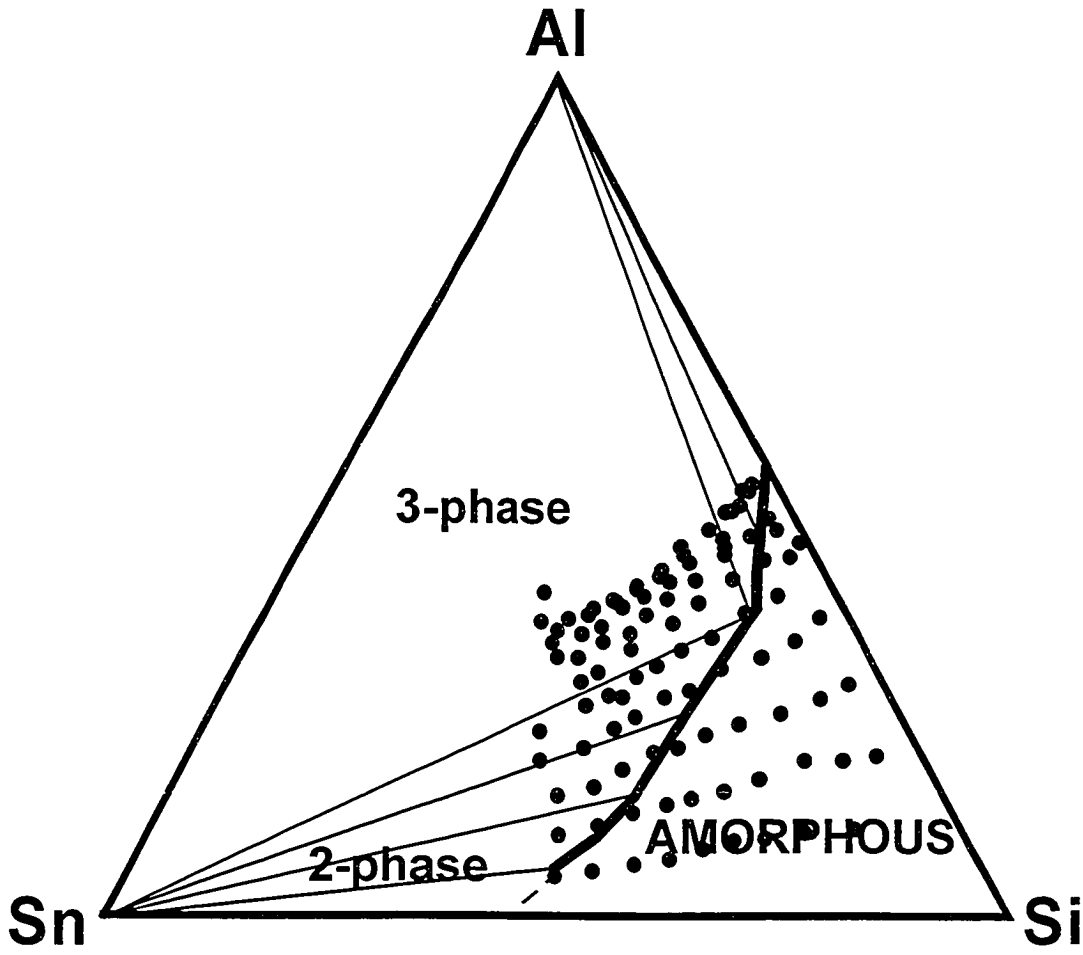

Figure 7.5. Non-equilibrium ternary phase diagram for sputtered SiAlSn films produced from data collected on the 75 mm x 75 mm $SiAl_xSn_y$ films. The thick solid line denotes the boundary pf the amorphous region. Each dot represents one 7.5 mm x 7.5 mm grid point.

For the SiAlSn system, many different films have been produced and characterized. In each case, the amorphous range determined from XRD and electron microprobe data have been consistent. No inter-metallic phases have been found in this system, just the amorphous phase mixed with nano-crystalline Sn and Al. No crystalline Si has appeared in any of the as sputtered films.

7.1.2. Electrochemical Results

Electrochemical measurements were performed on SiAlSn films using both coin type test cells and combinatorial electrochemical cells. The results for coin cells and combinatorial cells were found to be very similar [87] except that the cycle life of combinatorial cells seemed to be somewhat better than for coin cells. This is attributed to the reduced handling and flexing of the substrate for the combinatorial cells, which leads to better adhesion and film quality. One representative set of data from the combinatorial cell will now be discussed for the SiAlSn system.

Figure 7.6 shows a non-equilibrium phase diagram, or Gibb's Triangle, for a sputtered SiAlSn ternary library with the approximate compositions of the individual channels of a combinatorial cell plate indicated. The numbers on the diagram represent the approximate position of the corresponding channels. This library covers about the same range of Al content as the library from Figure 7.2, but has somewhat more Sn. This cell plate was included in a combinatorial cell as described in Chapter 4. This cell was cycled using the Scribner MMA described in Chapter 4. The cell was discharged to 0.005 V at a sweep rate of 0.03 mV/s, held at that potential for two hours, charged to 1.2 V at a sweep rate of 0.03 mV/s and then held for 30 minutes. This process was then repeated.

Figure 7.7 shows plots of dQ/dV *versus* potential for the SiAlSn combinatorial cell. The directions of increasing Al and Sn are marked on the figure with arrows. The left most column of graphs corresponds approximately to the SiSn binary (with a small amount of Al) with Sn increasing from bottom to top.

Sharp peaks begin to appear at higher potentials during charge for high Sn content (plots 57 and 58). This is expected as Figure 7.6 shows that these compositions are outside of the amorphous range. The bottom row corresponds to the SiAl binary (with a small amount of Sn) with Al increasing from left to right. No peaks appear for these channels, indicating no crystalline material, in agreement with Figure 7.6 except that channel 8 should have some crystalline Al. There are a large number of plots in the top right corner of Figure 7.7 that do show peaks in the dQ/dV *versus* potential relationship. These peaks are from the crystalline Sn in the film. There are no peaks that are characteristic of Al.

The electrochemical data in Figure 7.7 shows the same trends as the XRD data shown in Figure 7.2. There is a large amorphous range, where there are no sharp peaks in the dQ/dV *versus* potential graphs. When the Al and/or Sn content gets too high, peaks in dQ/dV *versus* potential begin to appear, indicating crystalline material. As with the XRD data, crystalline Sn is seen first, even if it is the Al content that is being increased. The Al seems to be absorbed preferentially into the a-Si matrix. It should be noted that sharp peaks do not appear in Figure 7.7 until the channels are well in to the crystalline range. This may be because the crystalline grains are very small (nanocrystalline) which also creates smooth dQ/dV *versus* potential relationships.

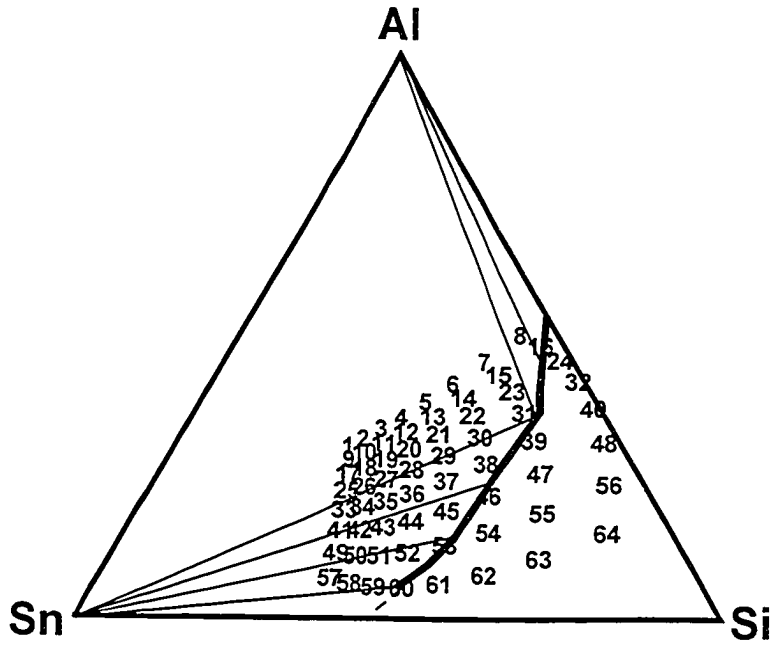

Figure 7.6. Plot of channel locations for a SiAlSn combinatorial electrochemical cell.

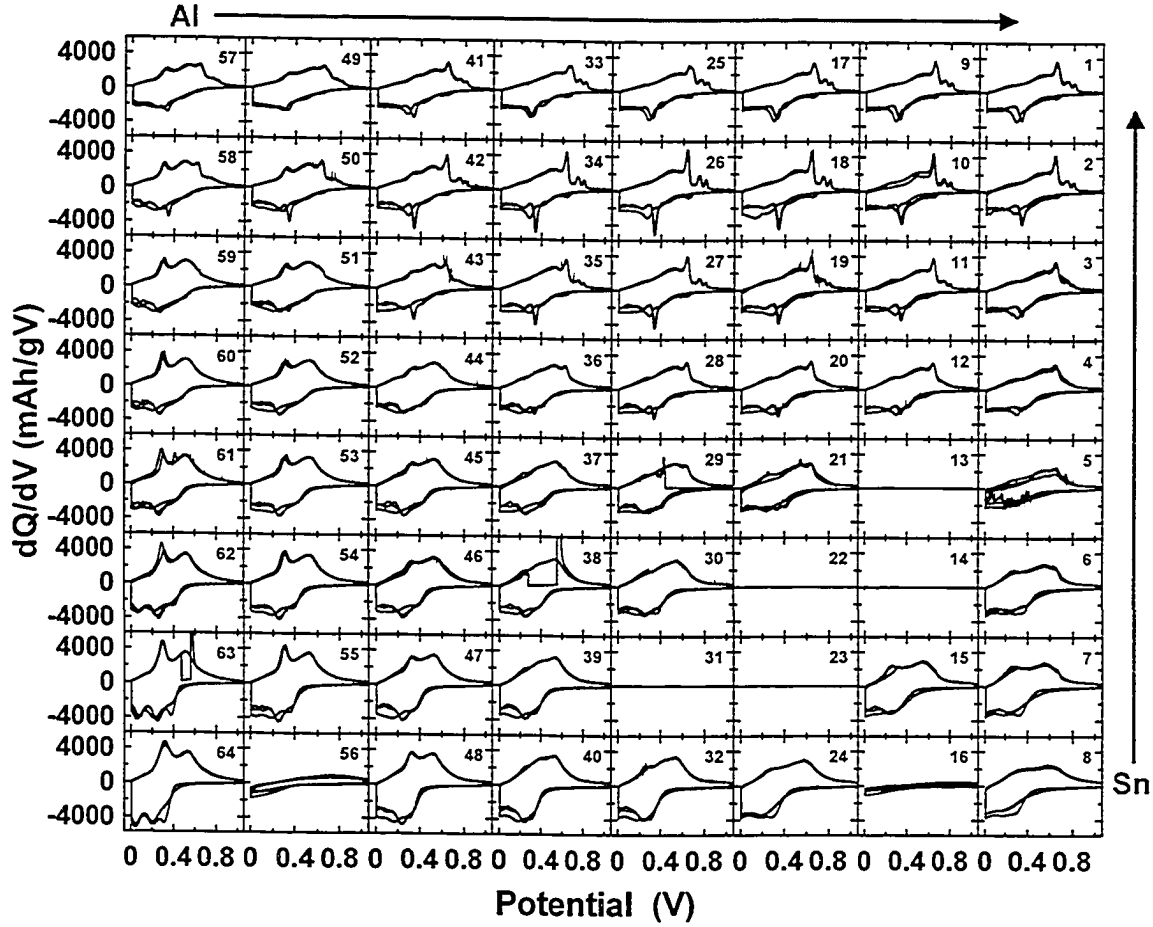

Figure 7.7. Plots of dQ/dV *versus* potential for the first three cycles of all 64 channels of a SiAlSn combinatorial electrochemical cell with compositions as indicated in Figure 7.6.

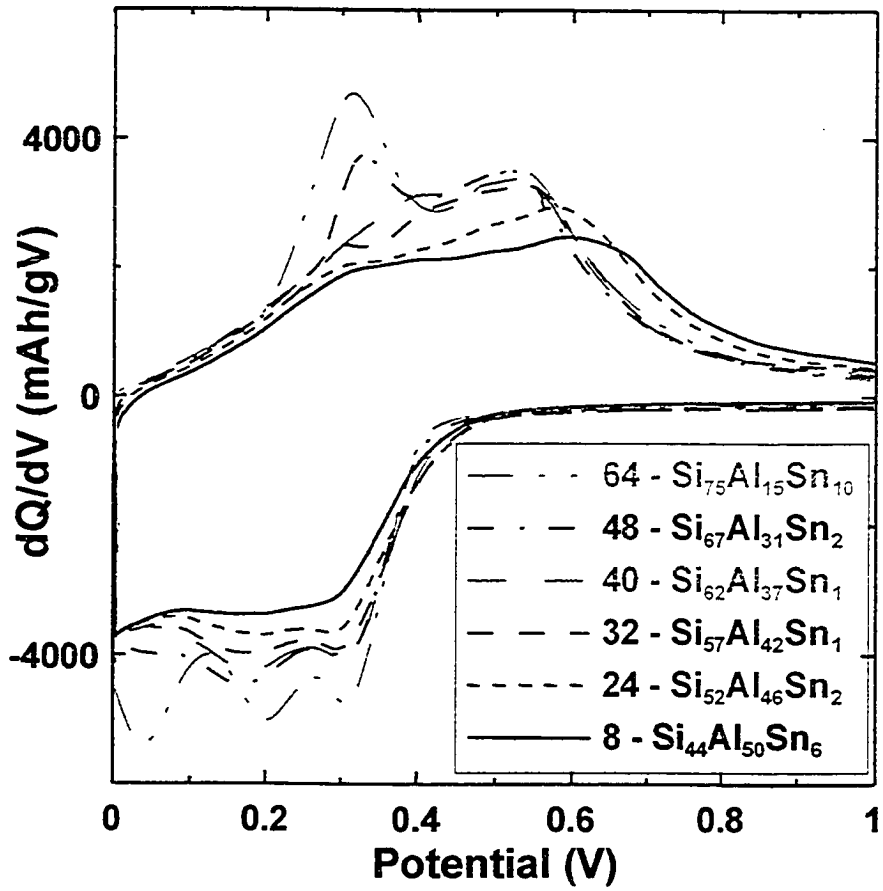

Figure 7.8. Plots of dQ/dV *versus* potential for the first cycle of the bottom row of cells from Figure 7.7. The approximate composition of each cell is indicated.

Figure 7.8 shows dQ/dV *versus* potential graphs for the first cycle of the bottom row of channels of Figure 7.7 plotted on the same axis so the effect of adding Al to a-Si can be seen. The approximate compositions of the channels are indicated. The only effects of adding Al are to diminish the lower potential hump during charge and to shift the higher potential hump to higher potential. Even though Al is added, the dQ/dV *versus* potential relationships seem to become more like an amorphous material with no sharp, well defined features.

The shifting of the high potential hump for channel 8 may be an indication that the Al content is near the amorphous limit and the broad peak from the charge (see Figure 5.12) is starting to form. Alternatively, the lack of a peak

even though Figure 7.6 indicates crystalline Al should be present may indicate *in-situ* amorphization, with the crystalline Al being absorbed into the a-Si matrix. An *in-situ* XRD experiment for this composition should be very interesting.

There is another possibility for the shape of the dQ/dV *versus* potential graph for channel 8. Figure 7.9 shows a plot of known phases in the SiAlLi ternary system. There is a SiAlLi phase. Channel 8 is approximately $Si_{0.5}Al_{0.5}$. It is possible that the SiAlLi phase forms during the first discharge. When Li is removed, the Al may not phase separate, much like the case for Li_2SiZn in the SiZn binary system in Chapter 6. This could also explain the lack of a sharp peak during charge in the dQ/dV *versus* potential relationship for channel 8 of the SiALSn library. This may also be the case for channel 24, which has a shape similar to channel 8, and other channels in the high Al, low Sn area of the library.

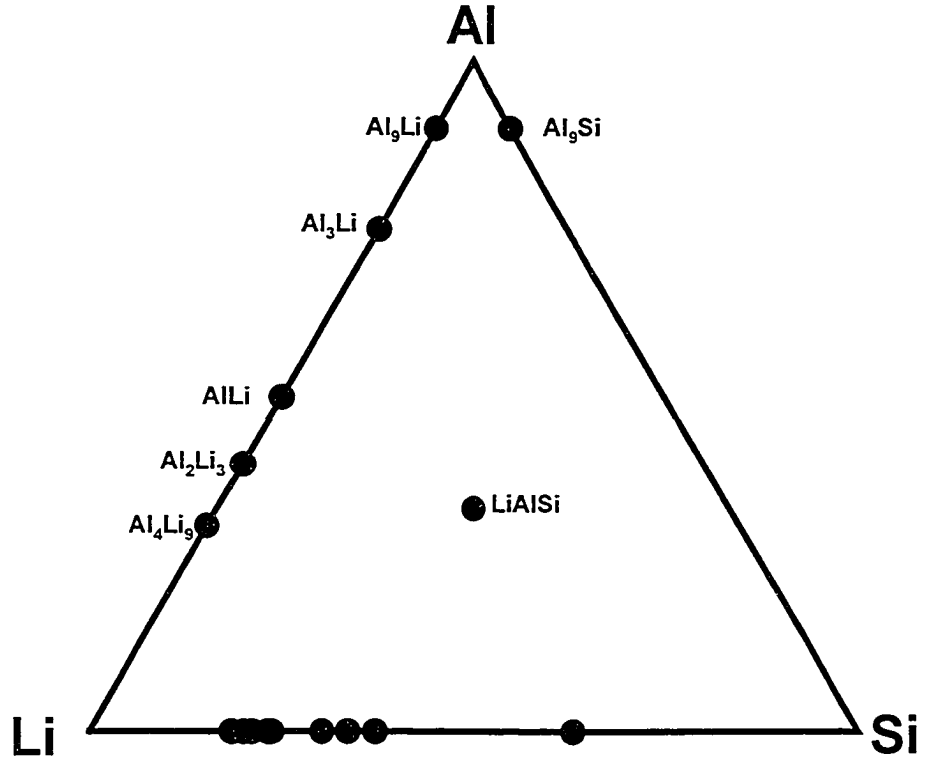

Figure 7.9. Plot of known phases in the SiAlLi ternary system. LiSi phases are not labeled to avoid confusion, but most phases are found in Figure 5.1.

Figure 7.10 shows the dQ/dV *versus* potential graphs for the first cycle of the right most column of channels of Figure 7.7 plotted on the same axis so that the effect of adding Sn to SiAl can be seen. The approximate compositions of each channel are indicated on the graph. As Sn is added to the SiAl mix, the shape of the dQ/dV *versus* potential graph does not change significantly until more than 20 at. % Sn has been added. At this point, the lower potential hump during charge quickly disappears and the peaks associated with crystalline Sn begin to emerge. This is what should be expected based on the XRD data for this system, which shows that the Al is absorbed in the a-Si matrix while the Sn is forced to crystallize. In the $Si_{1-x}Sn_x$ system of Chapter 6, Sn peaks also appeared when there was crystalline Sn present.

In the SiAlSn ternary system, much like the SiSn binary, there are no significant changes to the shape of the dQ/dV *versus* potential relations with cycle number. This indicates that the structure of the film is not changing from one cycle to the next, as is the case for the SiAg and SiZn binary systems. Also, from the dQ/dV *versus* potential plots there is no evidence of the $Li_{15}Si_4$ phase. While this does not show that Al also suppresses the formation of this phase, it does show that it does not hinder the suppression of the phase by Sn.

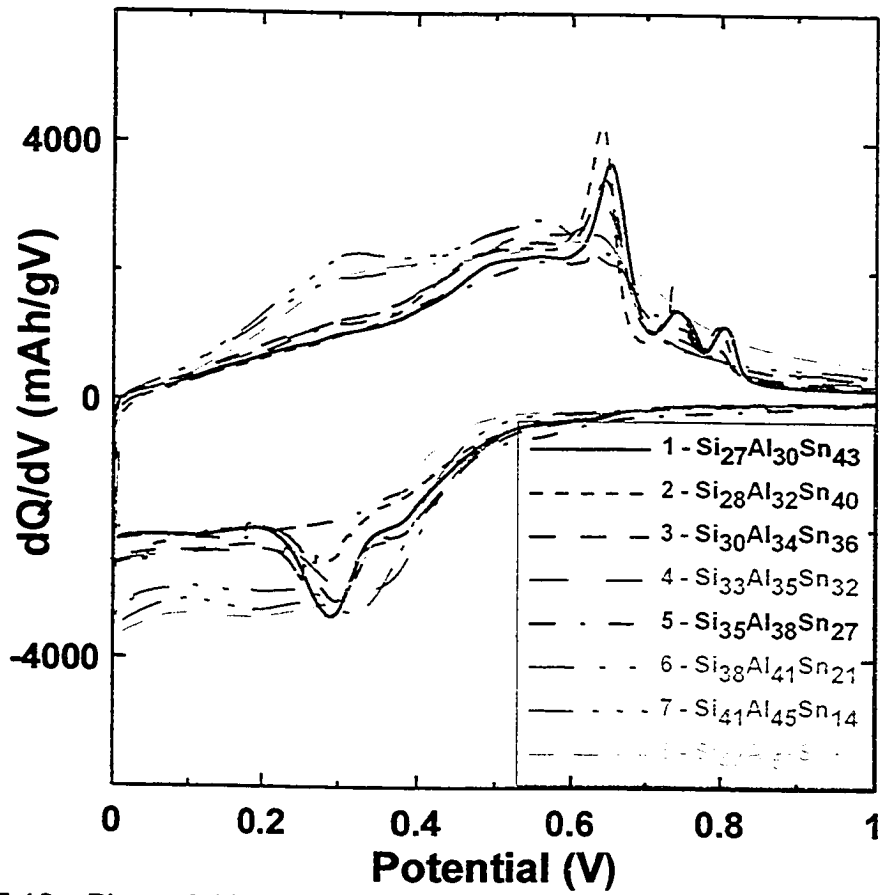

Figure 7.10. Plots of dQ/dV *versus* potential for the first cycle of the right most column of cells from Figure 7.7. The approximate composition of each cell is indicated in the figure.

Figure 7.11 shows a contour plot of the percent of theoretical capacity achieved during the first charge as a function of composition. The theoretical capacities have been calculated using equation 6.1 extended to include three elements. The theoretical capacity of Si used was 4199 mAh/g, with 990 mAh/g used for Sn and 991 mAh/g used for Al. This assumes 4.4 Li per Si and Sn and one Li per Al. Figure 7.11 shows that the percent of theoretical capacity achieved during the first charge increases with Sn content, as was the case for the Si-Sn binary system in Chapter 6. There does not seem to be an influence on percent of theoretical capacity achieved from the Al content except for high

values of both Sn and Al it seems to decrease slightly with Al content. It does not seem that Al allows the $Li_{22}M_5$ phase to be reached but also does not significantly hinder the ability of Sn to allow that phase to be reached.

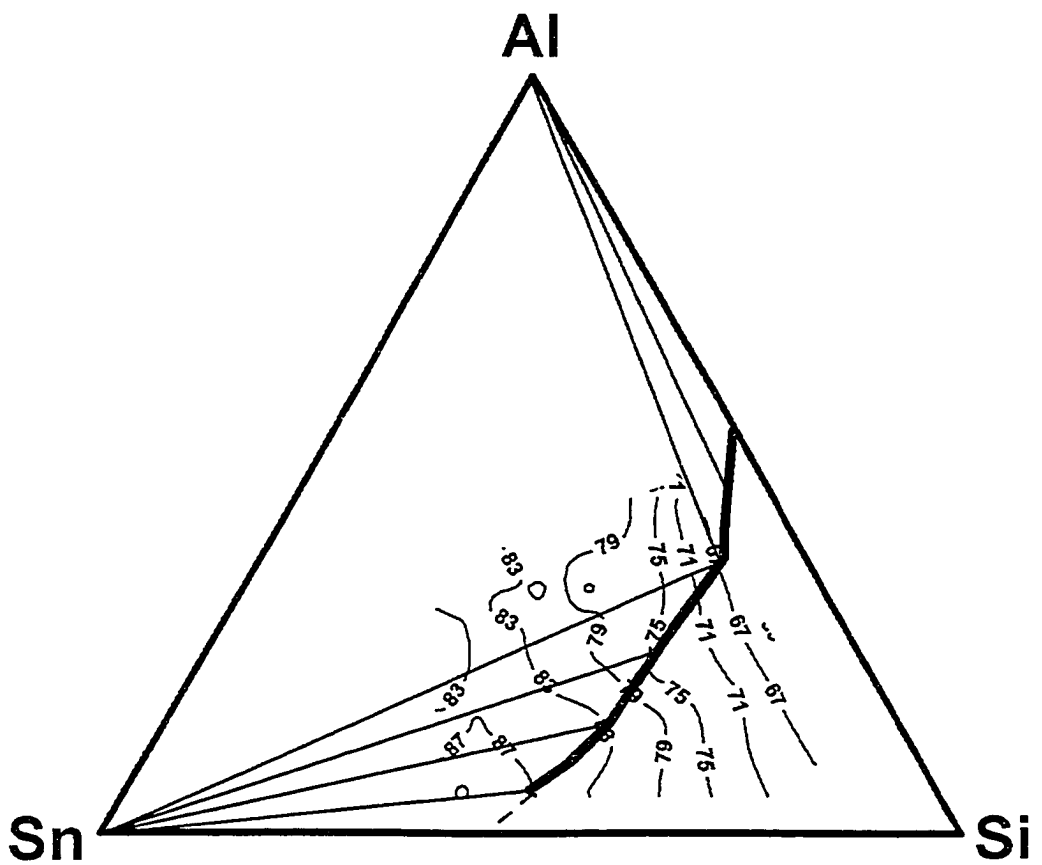

Figure 7.11. Contour plot showing the percent of theoretical capacity achieved on the first charge as a function of composition for the SiAlSn ternary system.

The irreversible capacities for the SiAlSn combinatorial cell are shown in Figure 7.12. Irreversible capacities are generally in the range of 8 – 16 %. The irreversible capacity tends to decrease with increasing Sn content. Irreversible capacity increased with increasing Al content inside the amorphous range and then decrease again. The maximum was along the boundary of the amorphous range with about 30 – 40 at. % Al. Along the SiSn binary axis the irreversible capacities found are comparable to those reported in Chapter 6.

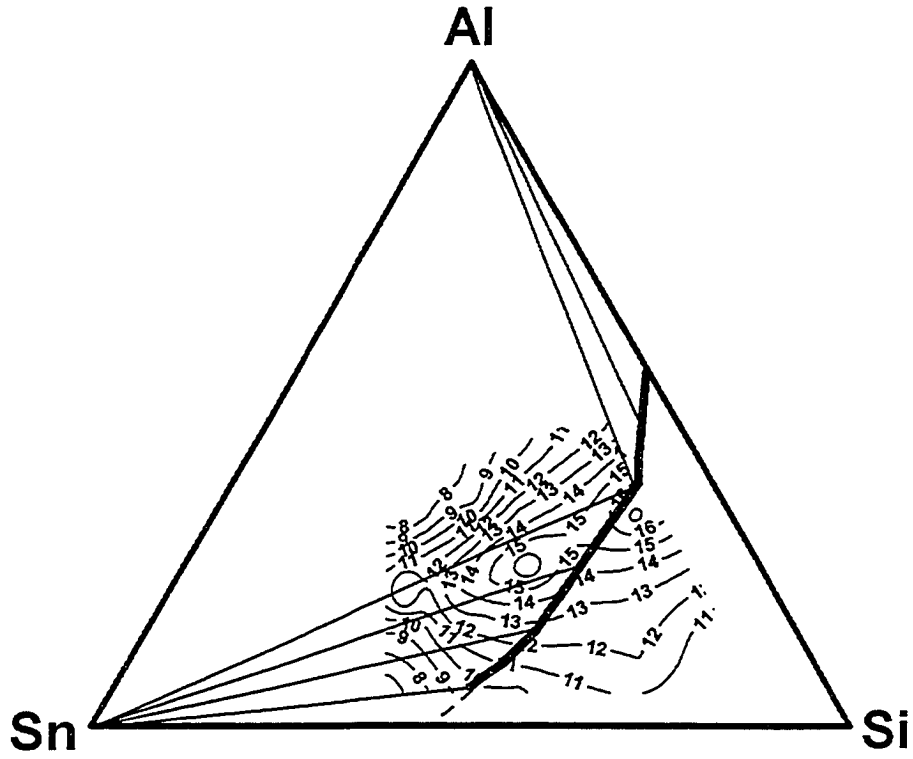

Figure 7.12. Contour plot of irreversible capacity in percent of the first discharge as a function of composition for the SiAlSn combinatorial electrochemical cell.

The combinatorial cell was only cycled three times before a power outage interrupted the experiment. As a result, data on cycle life for this particular cell is not available. From other cells and from coin cells, it has been found that cycling for the SiSn compositions is equivalent to that found in Chapter 6. As Al is added, cycling does not improve and begins to degrade when the Al content gets too high [62].

7.1.3. Conclusions for SiAlSn

The SiAlSn system has been studied over a wide stoichiometry range by means of a combinatorial electrochemical cell. A large amorphous range has been found in the sputtered films that has been mapped using XRD and electron

microprobe. It was found that Al is absorbed preferentially over Sn in the a-Si matrix. Selected electrochemical results have been presented.

Electrochemical performance for this system is comparable to the SiSn binary as long as Al content is low. Too much Al hinders capacity retention of the film and encourages the crystallization of Sn. Irreversible capacities are superior to alloy systems reported in the literature although they are higher than some of the binary systems discussed in Chapter 6. The $Li_{15}Si_4$ phase was not found for any compositions in this ternary system. It was found that Al hinders the tendency for moderate Sn contents to allow the $Li_{22}M_5$ phase to be reached. Overall there does not seem to be any benefit from adding Al to a-SiSn.

7.2. SiAgSn

7.2.1. Non-equilibrium Phase Diagram

A plot of known compositions for the SiAgSn system is presented in Figure 7.13. This diagram marks the phases for this system that appear in references [93, 102]. There are no ternary phases. Also, most of the binary phases are reported to be meta-stable except Ag_3Sn, Ag_4Sn and Ag_9Sn. These are the phases most likely to appear in sputtered films for this ternary system.

Ternary films of $SiAg_xSn_y$ were prepared in the same manner as the $SiAl_xSn_y$ films above. A combination of XRD and electron microprobe data was used to map the phase diagram of the as sputtered films. Figure 7.14 shows contour plots of the Ag:Si and Sn:Si ratios for a SiAgSn film. This film covers the range of $SiAg_xSn_y$ ($0 < x < 1.5$, $0 < y < 2$). Figure 7.15 shows the 10 x 10 grid of x-ray patterns for this film. There is a fairly large amorphous range for this film as

well as regions with crystalline phases. This system is more complicated than the SiAlSn system discussed above. The peaks in the XRD patterns will now be identified in order to construct the phase diagram for SiAgSn sputtered films.

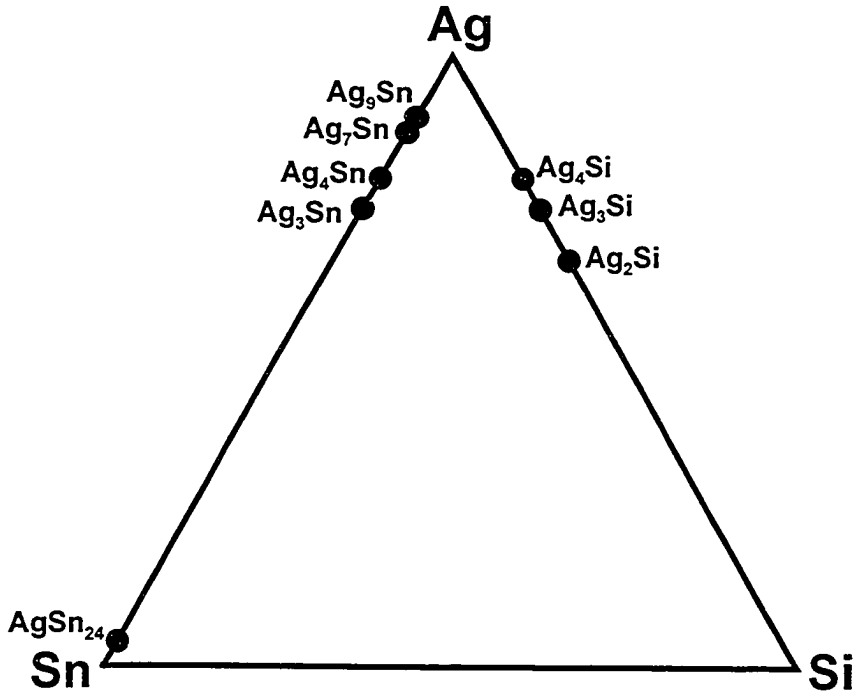

Figure 7.13. Plot of known phases in the SiAgSn ternary system.

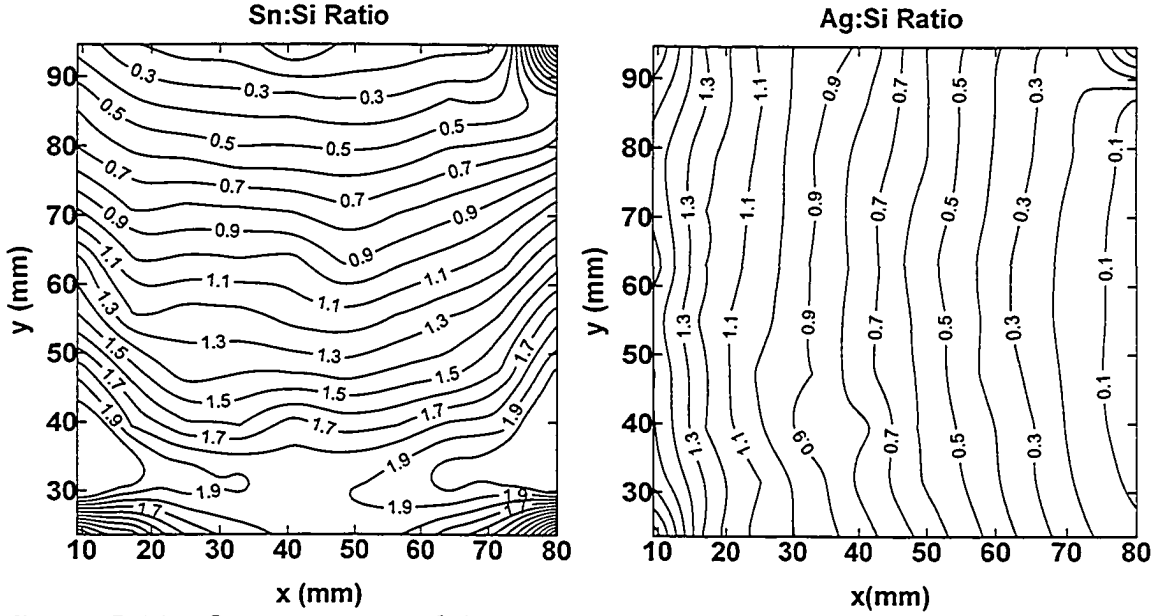

Figure 7.14. Contour maps of the (a) Sn:Si and (b) Ag:Si atomic ratios *versus* position on a 75 mm x 75 mm SiAgSn film.

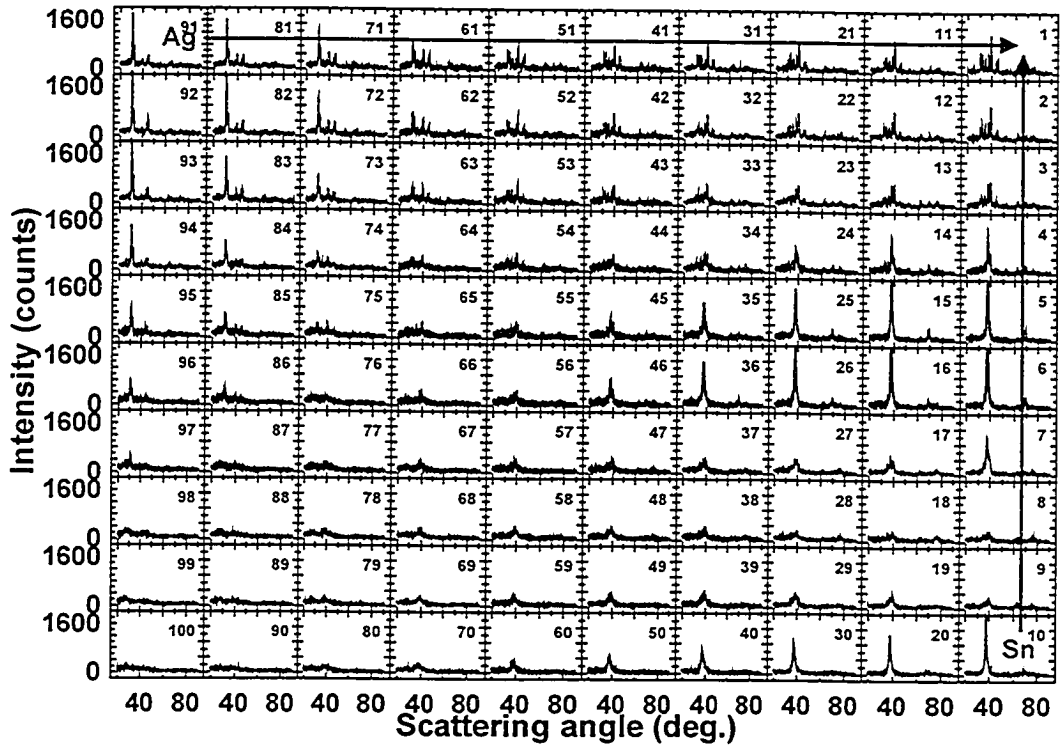

Figure 7.15. X-ray patterns displayed as a function of position on a 75 mm x 75 mm SiAgSn film. The direction of increasing Ag and Sn content is marked.

Figure 7.16 shows an expanded view of the left most column of XRD patterns from Figure 7.15. The scans are numbered from 100 on the bottom to 91 on the top with Sn content increasing from bottom to top. The Ag content is low for these scans. At the bottom (scan 100) with low Sn content the XRD pattern shows no peaks, indicating an amorphous film. As Sn content increases, the XRD pattern begins to show peaks from crystalline Sn by scan 97. As the Sn content becomes even higher, new peaks begin to appear (blown up in scan 95). These peaks match the positions for Ag_4Sn and also for Ag_3Sn.

Figure 7.17 shows an expanded view of the bottom row of scans from Figure 7.15. These scans have low Sn content and Ag increases from left to right. This set of scans also starts out amorphous for low Ag content. As the Ag

content increases, a peak begins to appear at about 37.5° in scan 60. This is the position of the (020) peak of Ag_3Sn or the (002) peak of Ag_4Sn.

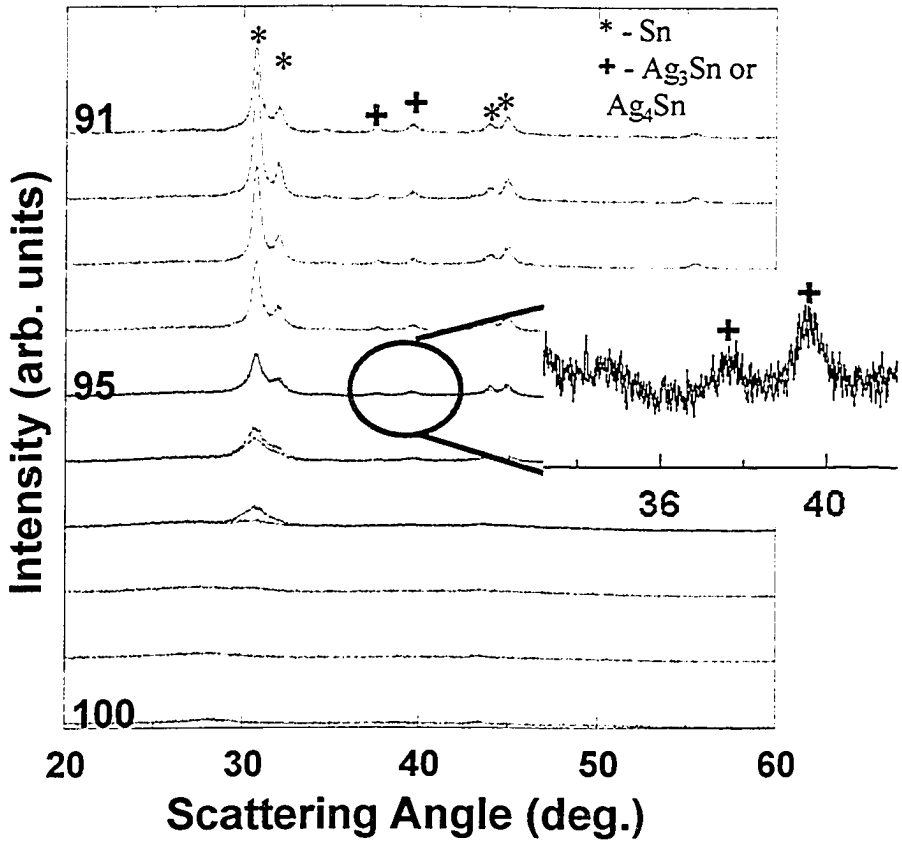

Figure 7.16. Expanded view of scans 91 to 100 of Figure 7.15. Ag content is constant (low) and Sn increases from bottom to top. Some scans are numbered in the figure.

In the previous two figures, it is unclear which Ag-Sn phase is causing some of the peaks in the XRD pattern. The patterns for the two phases (Ag_3Sn and Ag_4Sn) were calculated using Rietica [97] based on the parameters given for these phases in [102]. These two patterns turned out to be nearly identical. The space group of Ag_3Sn is given as Pmmn, which is orthorhombic. The lattice parameters given are a = 0.5968 nm, b = 0.47802 nm and c = 0.51843 nm. Sn are on the 2a sites with Ag occupying 2b and 4f sites. A diagram of this structure

is shown in Figure 7.18 with Ag atoms in green and Sn atoms in red. The unit cell has been drawn in black.

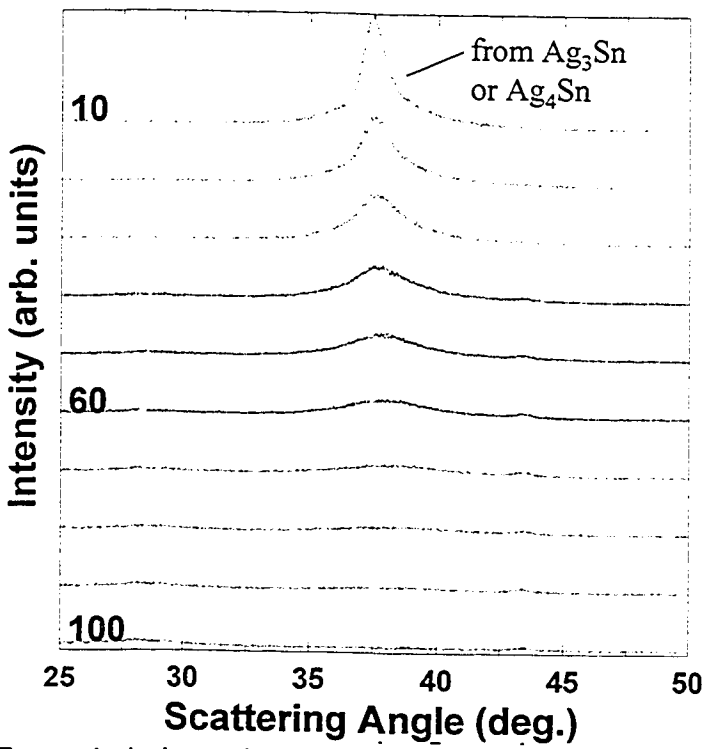

Figure 7.17. Expanded view of the bottom row of scans from Figure 7.15. Sn content is constant (low) and Ag increases from bottom to top. Some of the scans are numbered in the figure.

The space group of Ag_4Sn is $P6_3/mmc$, which is hexagonal. The lattice parameters given are a = 0.29658 nm and c = 0.47842 nm. The Ag and Sn atoms are randomly distributed on the 2c sites. It should be noted that c for Ag_4Sn is approximately equal to b for Ag_3Sn. Also, a for Ag_3Sn is approximately twice that for Ag_4Sn and c for Ag_3Sn is approximately $\sqrt{3}$ times a for Ag_4Sn. The two structures are essentially the same. They are both hexagonal close packed, with the Ag_4Sn phase having Sn atoms randomly located instead of occupying specific sites as they do in the Ag_3Sn phase. To illustrate this more clearly, the unit cell for Ag_4Sn has also been added in blue to Figure 7.18.

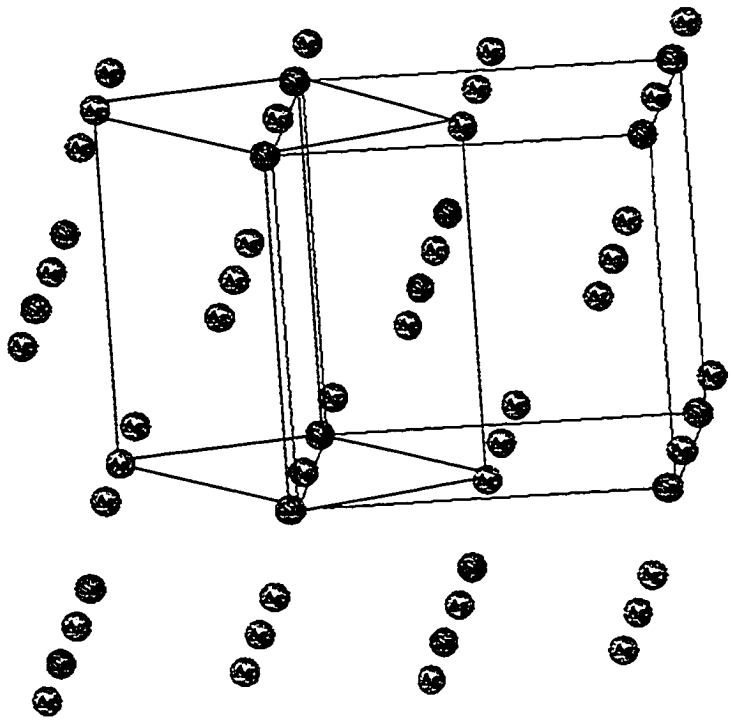

Figure 7.18. Structure for Ag_3Sn (black unit cell) and Ag_4Sn (blue unit cell). Ag atoms are green and Sn atoms are red.

In light of the above discussion, it seems that a Ag_xSn phase is causing the unidentified peaks in Figures 7.16 and 7.17. As the Ag and Sn atoms strike the substrate during sputtering, they assume the hexagonal close packed arrangement common to both Ag_3Sn and Ag_4Sn with the Sn randomly placed in the structure. The value of x then depends on the location on the film and the peaks appearing would be from the hexagonally close packed structure. If there is enough Sn, it forms regions of crystalline Sn as well, as seen in Figure 7.16.

Figure 7.19 shows an expanded view of the column of scans from Figure7.15 made up of scans 21 to 30. This column has moderately high Ag and Sn increases from bottom to top. In plot 30, at the bottom, with low Sn content the only peak is the (002) peak from the Ag_xSn phase just described. There seems to be a preferred orientation in this phase, as the dominant peak in the

pattern should be the (101) peak at 39.8°. As Sn is added, more peaks of Ag_xSn appear during scans 29 to 27. For scans 26 to 24 the Ag_xSn (002) peak centred at 37.6° becomes very large. This is likely from preferred orientation of the Ag_xSn, although it is not clear why the preferred orientation would occur in this region. This could be tested in future work by tilting the substrate through various angles while performing XRD. If the film has grown with a certain plane aligned in a specific way, the peak for that plane would change in intensity with substrate angle (see Figure 4.4). Beyond scan 24, the Ag_xSn peaks assume expected intensity ratios and peaks from crystalline Sn emerge. At maximum Sn content the XRD pattern shows a mix of crystalline Sn and Ag_xSn.

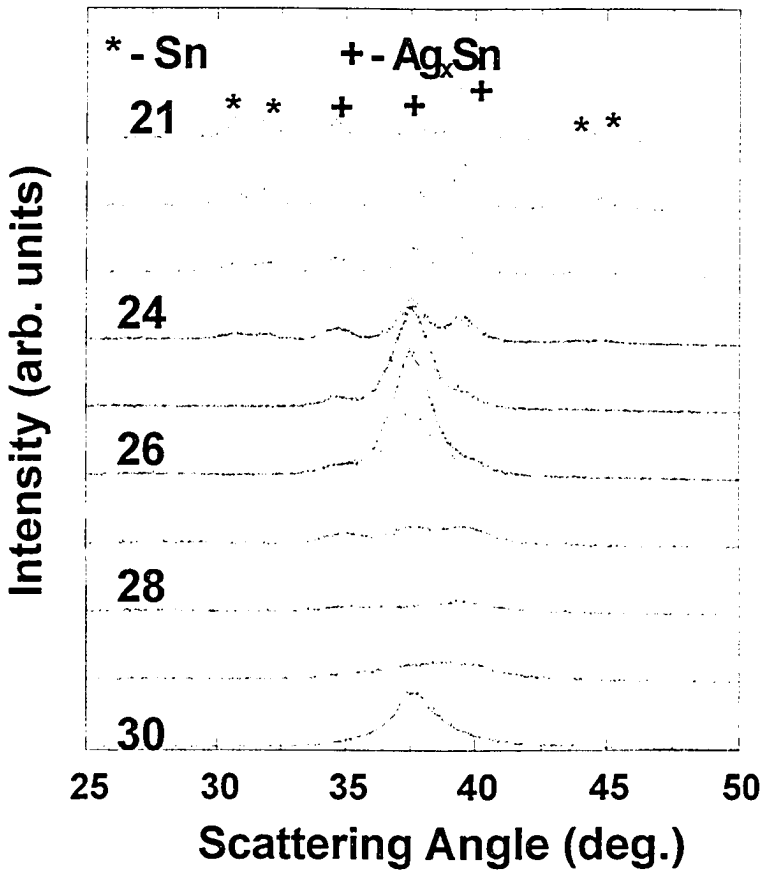

Figure 7.19. Expanded view of scans 21 to 30 from Figure 7.15. Ag content is constant (moderate to high) and Sn increases from bottom to top. Some of the scans are numbered in the figure.

Figure 7.20 shows an expanded view of scan 91 from Figure 7.15, which is the scan from the region of the film with highest Ag and Sn content. In this scan it seems clear that there is a mix of crystalline Sn and Ag_xSn.

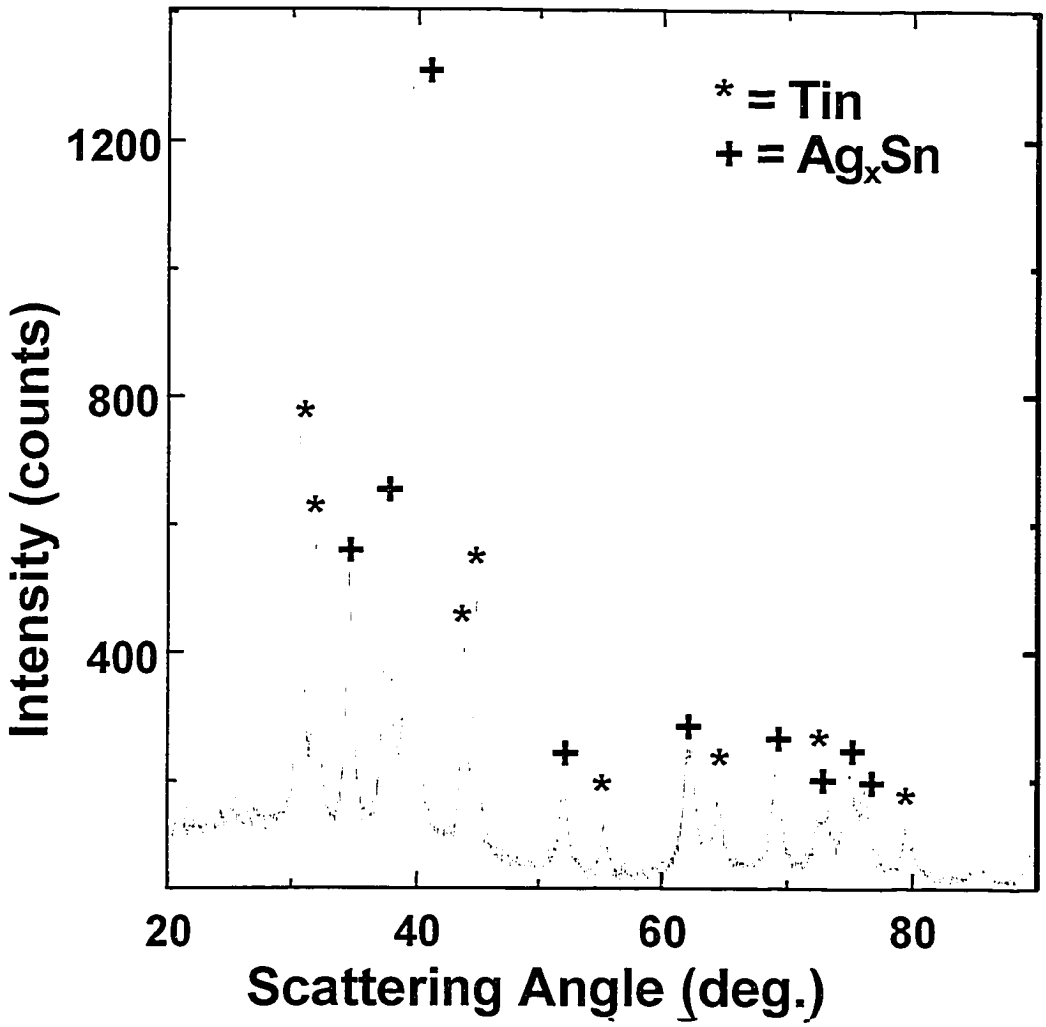

Figure 7.20. XRD scan 91 from the SiAgSn film of Figure 7.15. Peaks of Sn and Ag_xSn are marked in the figure.

The above XRD data was used in conjunction with the electron microprobe data to construct the phase diagram shown in Figure 7.21. It should be noted that this is a non-equilibrium phase diagram. The thick solid line denotes the amorphous region of the film and the dashed lines represent approximate boundaries of different two and three phase coexistence regions.

Ag_3Sn and Ag_4Sn have been removed from the diagram because it cannot be said that either of these phases are present. Instead, there is a Ag_xSn phase with the structure of Ag_3Sn and Ag_4Sn with Sn randomly distributed. The Ag_xSn phase has been placed approximately in the location of Ag_4Sn and Ag_3Sn, although it likely occupies a fairly wide range on the Ag-Sn axis.

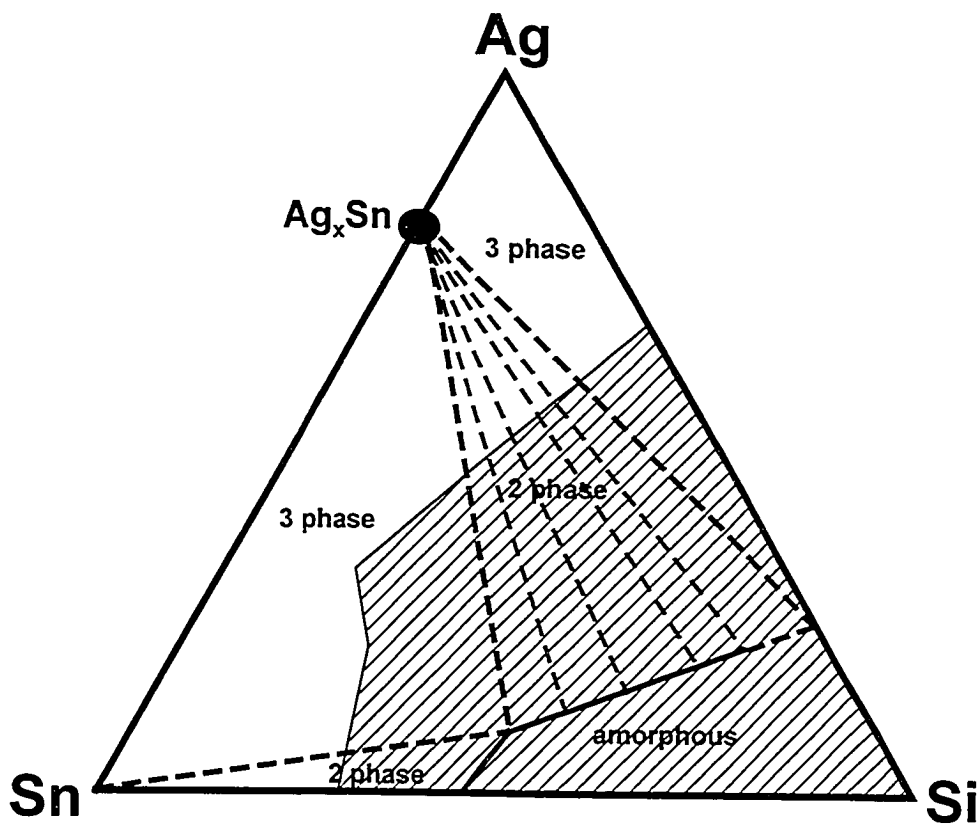

Figure 7.21. Non-equilibrium phase diagram for sputtered SiAgSn films. The amorphous region as well as two and three phase regions are marked. The shaded region represents the total area covered in all libraries.

7.2.2. Electrochemical Results

Electrochemical testing for the SiAgSn system was also performed with both coin type test cells and with the combinatorial electrochemical cell. Much

like the SiAlSn system, the combinatorial cell provides the best results and also better resolution with an 8 X 8 grid on the same sample space as the 5 X 5 grid provided by coin cells. One representative set of data from the combinatorial cell will now be discussed for the SiAgSn system.

Figure 7.22 shows a plot of channel locations for a SiAgSn combinatorial electrochemical cell plate. The numbers on the diagram represent the approximate position of the corresponding channels. This cell plate was included in a combinatorial cell as described in Chapter 4. This cell was cycled using the Scribner MMA described in Chapter 4. The cell was discharged to 0.005 V at a sweep rate of 0.03 mV/s, held at that potential for two hours, charged to 1.2 V at a sweep rate of 0.03 mV/s and then held for 30 minutes. This process was then repeated.

Figure 7.23 shows plots of dQ/dV *versus* potential for the SiAgSn combinatorial cell. The directions of increasing Ag and Sn are marked on the figure with arrows. The top row of graphs in Figure 7.23 corresponds roughly to the SiSn binary system (with a trace of Ag) described in Chapter 6, with Sn increasing from right to left. No sharp peaks appear in these graphs. From Figure 7.22, it might be expected that Sn peaks would appear in channel 57 as it is outside of the amorphous range. It should be noted that channel 57 did not perform well and also its estimated composition is very close to the boundary of the amorphous range so the lack of peaks should not be too surprising. The right-most column corresponds to the SiAg binary (with a small amount of Sn) with Ag increasing from top to bottom. From Figure 7.22, however, the only cell

that should closely resemble one from the SiAg binary of Chapter 6 is channel 8. This channel has an approximate composition of $Si_{63}Ag_{37}$ and should be compared to Figure 6.20, which has similar (not exact) behaviour over the first two cycles. The remaining channels from this column are either in a different two-phase region or the amorphous range and should be expected to differ from the SiAg binary.

Figure 7.24 shows the dQ/dV *versus* potential graphs for the first cycle of the bottom row of channels of Figure 7.23 plotted on the same axis so that the effect of adding Sn to the SiAg mix can be observed. The approximate compositions of each channel are indicated on the graph. Moving from channel 8 to channel 16 on Figure 7.22 crosses the boundary from one two phase region to another. As might be expected this causes a significant change in the shape of the dQ/dV *versus* potential graph. Above 0.2 V during charge there is much more activity for channel 16 than channel 8. There are now broad humps at about 0.4 V, 0.6 V and 0.75 V. This pattern is repeated for channels 24, 32, 40 and 48, although the lower potential hump begins to fade. In moving from channel 48 to 56, another boundary is crossed on Figure 7.22. There is again a change in shape of the dQ/dV *versus* potential graph. The 0.4 V hump is now gone and the other two have shifted up in potential by about 0.1 V. During the discharge of channels 16 to 48, there is one broad hump that moves between 0.1 and 0.2 V and broadens as Sn is added. For channels 56 and 64, the discharge has become relatively constant between 0.3 and 0 V.

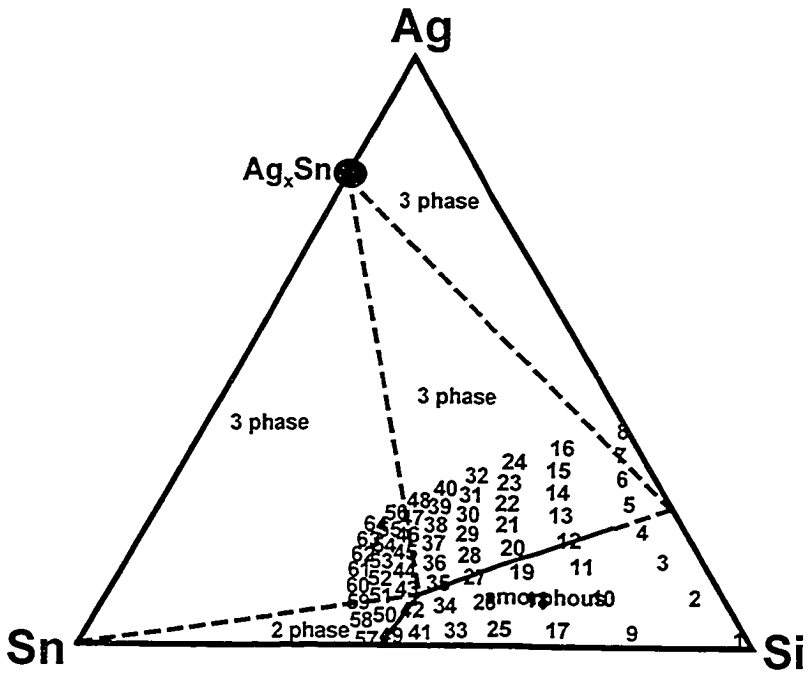

Figure 7.22. Plot of channel locations for a SiAgSn combinatorial cell.

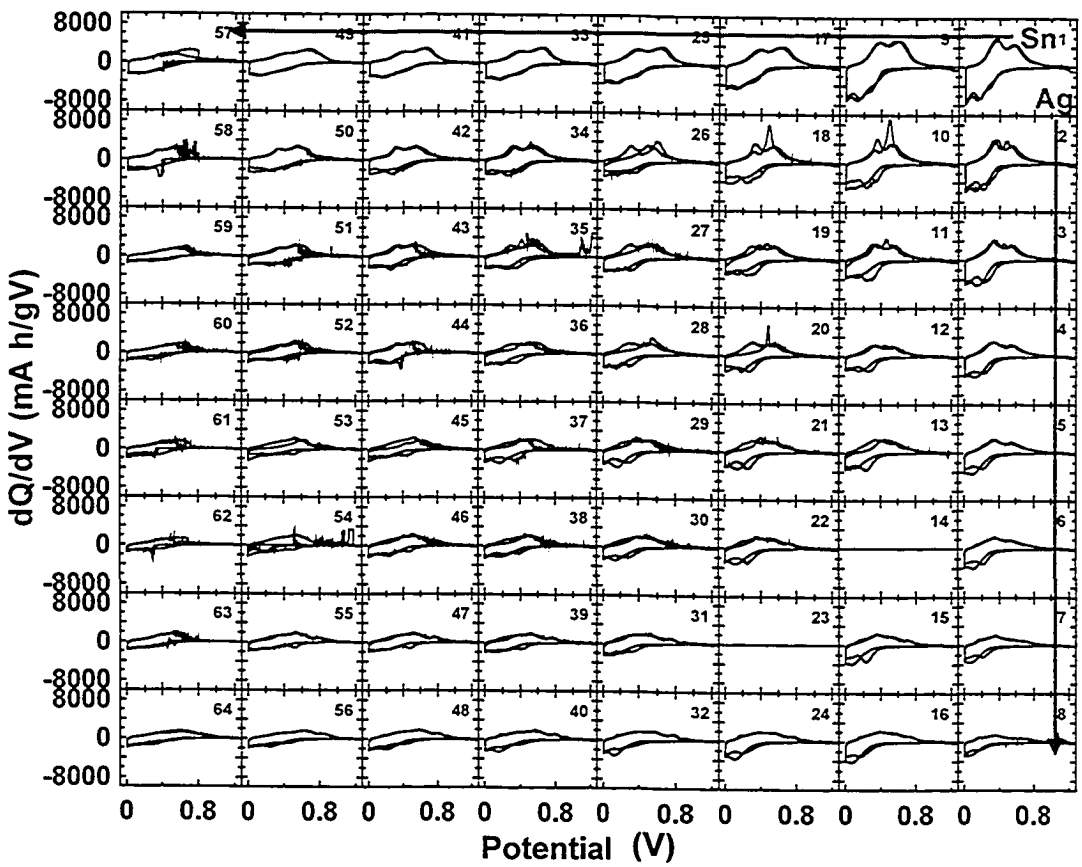

Figure 7.23. Plots of dQ/dV *versus* potential for the first two cycles of all 64 channels of a SiAgSn combinatorial electrochemical cell with compositions as indicated in Figure 7.22.

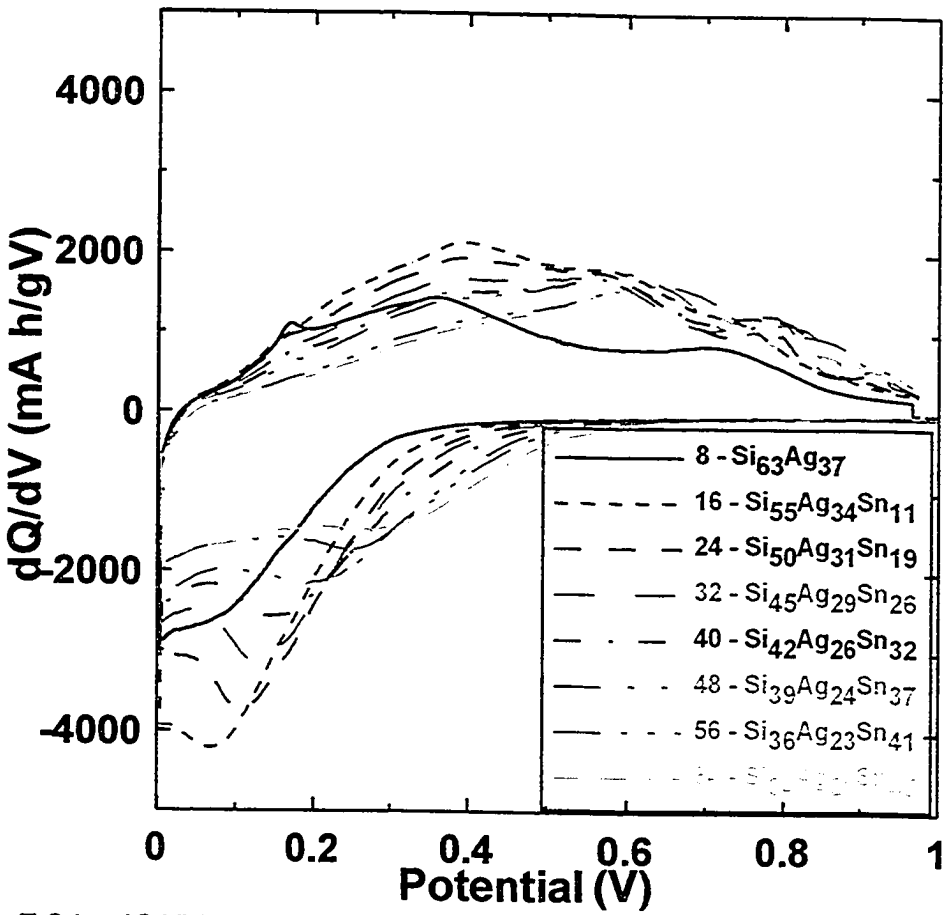

Figure 7.24. dQ/dV *versus* potential for the first cycle of the bottom row of cells from Figure 7.23. The approximate composition of each cell is indicated in the figure.

For the channels plotted in Figure 7.24, there was no significant change in the shape of the graph with cycle number. The Ag content in these channels is nearing the level that was found in Chapter 6 to make the formation of $Li_{15}Si_4$ take many cycles if it occurred at all. The presence of the Sn in the SiAgSn ternary may have prevented the formation of $Li_{15}Si_4$ altogether. This is not the case for all channels however.

Figure 7.25 shows the dQ/dV *versus* potential relationships for channels 2, 10, 18 and 26. These cells have only a moderate Ag content and Sn content increases with channel number. For these channels the second cycle differs

significantly from the first. For channel 2 the two broad humps during charge both sharpen somewhat and shift to lower potential. It is not clear if this is from new phases forming or some other mechanism.

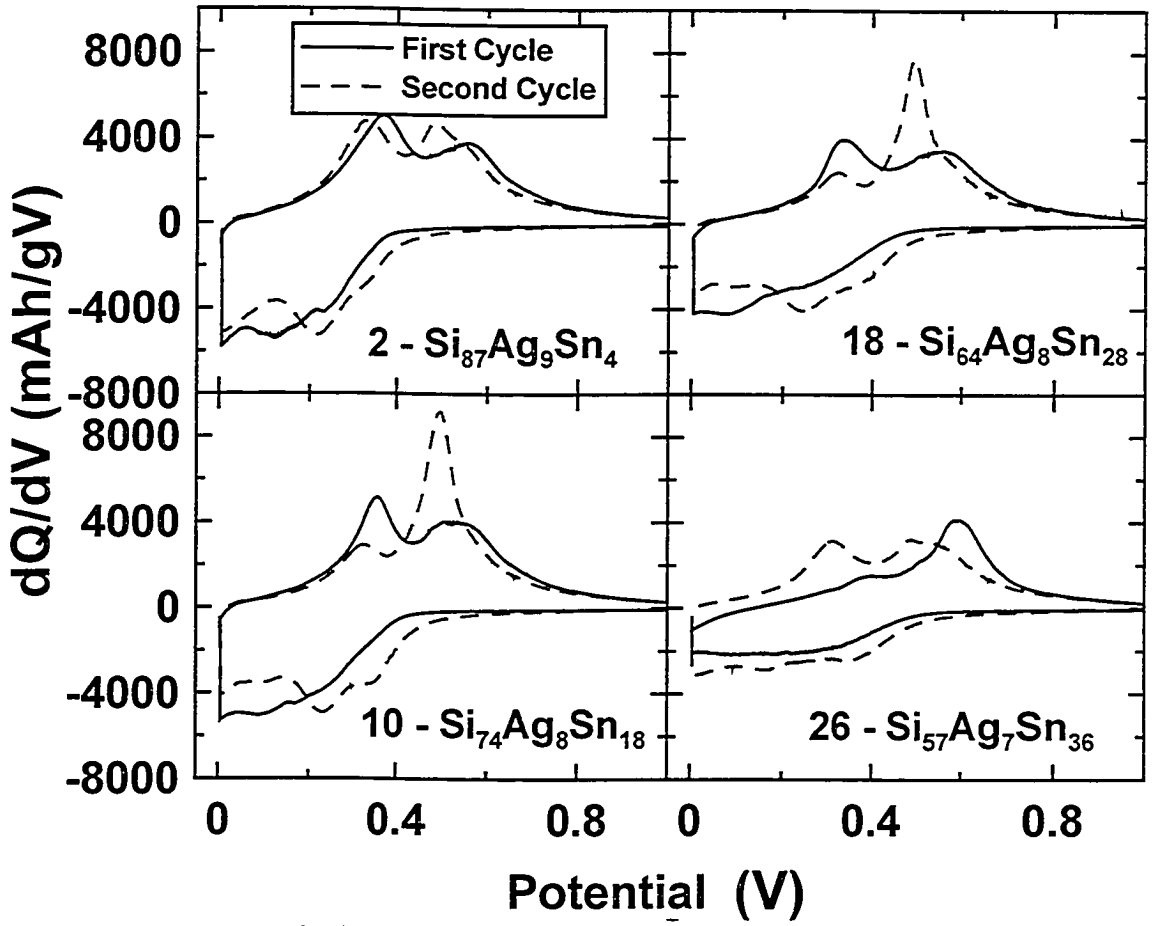

Figure 7.25. Plots of dQ/dV *versus* potential for the first two cycles of channels 2, 10, 18 and 26 from Figure 7.23. The approximate composition of each channel is indicated in the Figure.

Channels 10 and 18 both show a change from a SiSn-like shape with a sharper first hump on the first charge to a more SiAg like shape with only a small hump at 0.3 V but a large, quite sharp peak at about 0.5 V. This could be from the formation of the $Li_{15}Si_4$ phase induced by the Ag without adequate Sn to prevent it.

The first cycle of channel 26 has a new shape, with one peak during charge at 0.6 V. The second cycle looks very much like SiSn. A possible explanation here is that some phase has formed during the first discharge (maybe $Li_{15}Si_4$ or maybe something else), but the Sn suppresses this phase on later cycles. Other channels surrounding channel 26 also have a similar first cycle. The reason for this odd shape is not known, but it could be similar to the 'formation cycle' seen for some of the SiSn binary system in Figure 6.4. More work is needed to clarify this issue.

In Chapter 6 it was found that the SiSn binary system had the best cycling performance of the binary systems tested. The SiAg system showed the lowest overall irreversible capacity. One hope of adding Ag to SiSn would be to reduce the irreversible capacity but retain the cycling performance. Although the combinatorial cell for the SiAgSn system discussed here was only cycled a small number of times due to a power failure, other cells for this system did not cycle as well as SiSn. Figure 7.26 shows a contour plot of the irreversible capacity for the SiAgSn combinatorial cell as a function of composition. This figure shows that the irreversible capacities of SiSn have not been improved. Many values are above 10 %. These values are comparable to the irreversible capacities of SiSn.

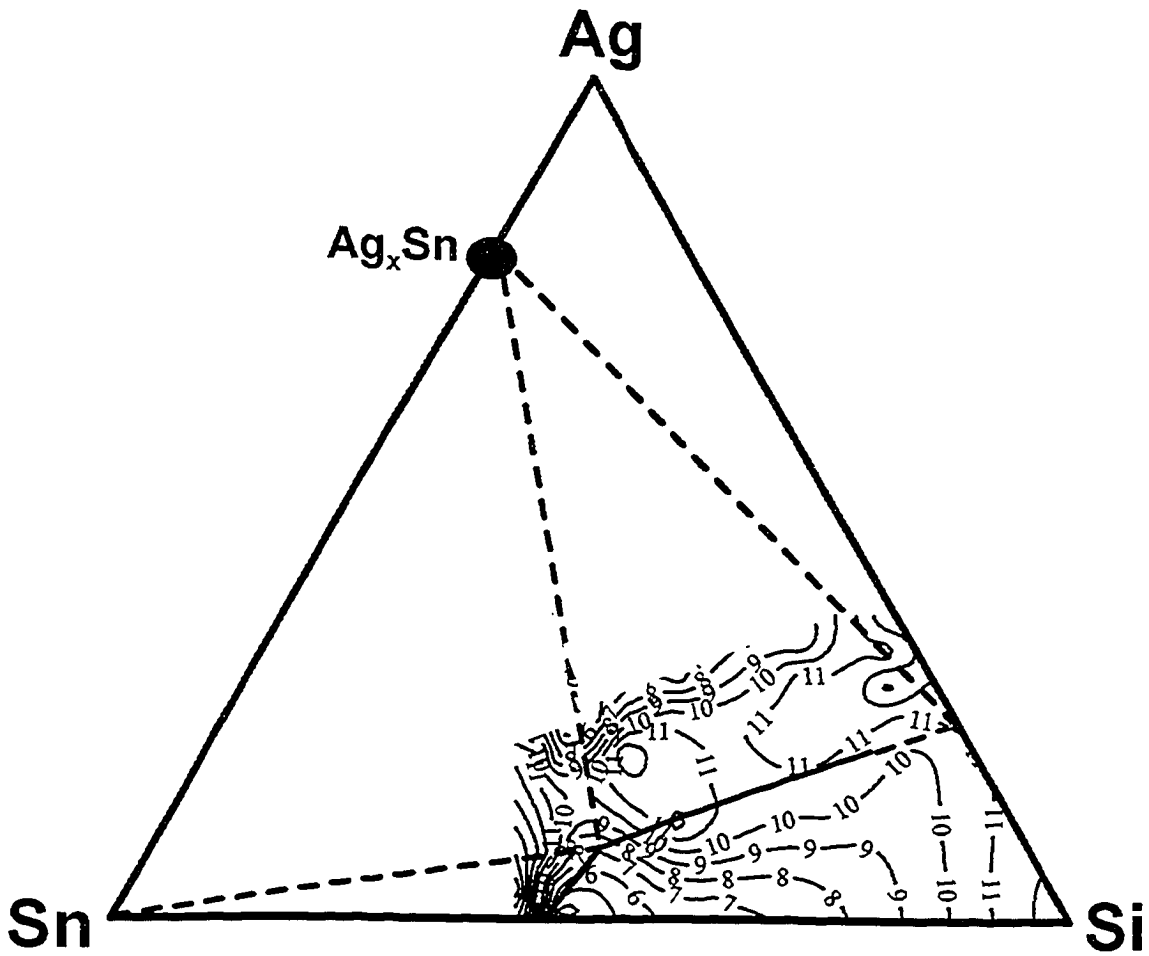

Figure 7.26. Contour plot showing irreversible capacity as a percent of the first discharge *versus* composition for the SiAgSn combinatorial electrochemical cell.

For the SiAgSn system the percent of theoretical capacity achieved on the first charge is shown in Figure 7.27. The theoretical capacities were calculated assuming 4.4 Li per Sn and Si and 3 Li per Ag. Along the SiSn binary, the percent of theoretical capacity achieved increased with Sn content in much the same manner as in Chapter 6. The percent of theoretical capacity achieved during the first charge decreased quite rapidly with Ag content in the amorphous range. Outside of the amorphous range, it levelled off at about 65 to 75 %.

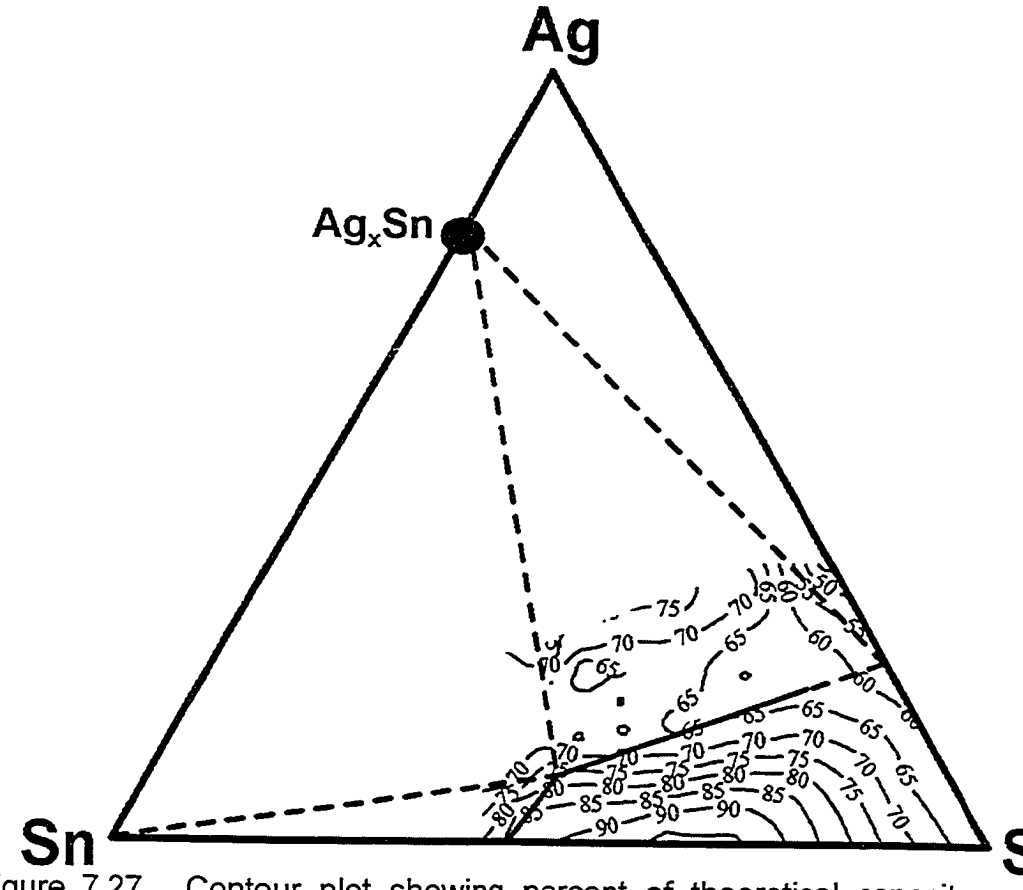

Figure 7.27. Contour plot showing percent of theoretical capacity achieved during the first charge for the SiAgSn ternary system.

7.2.3. Conclusions for SiAgSn

A wide range of the SiAgSn system has been produced by combinatorial sputtering and studied with XRD, electron microprobe and a combinatorial electrochemical cell. The non-equilibrium phase diagram of the sputtered film has been produced. The phase diagram includes a large amorphous range along with several two and three phase coexistence regions. The hcp Ag_xSn is the only inter-metallic phase that was discovered. Selected electrochemical results have been presented.

The electrochemistry of the SiAgSn system was found to be somewhat more complicated than the SiAlSn system. Several compositions in this system

show variation in their dQ/dV *versus* potential relations with cycle number. It is not yet clear what phases are formed during each charge and discharge, but some $Li_{15}Si_4$ may be formed for a limited composition range.

The irreversible capacity of SiSn does not seem to be improved by the addition of Ag. Also, the cycle life becomes worse as Ag is added. Overall, there is no benefit from the addition of Ag to SiSn. The Ag is likely aggregating in this library as it did for the SiAg binary library. This creates two phase regions and non-homogeneity as it did for the binary system and this adversely effects the capacity retention for the SiAgSn library.

7.3. SiSnZn

7.3.1. Amorphous Range

The good electrochemical performance of SiSn and SiZn libraries makes the SiSnZn ternary system an excellent candidate for testing. A plot of known phases for the SiSnZn ternary system is shown in Figure 7.28. In this system there is only one phase is reported and it is metastable. There are no ternary phases and no SiZn or SiSn binary phases. The tendency for these elements to not form alloys or compounds with each other may create a large amorphous range in the sputtered libraries for this system. Also, it may help the electrochemical cycling as crystalline phases may not form.

Libraries of SiSnZn were created using the combinatorial sputtering machine described in Chapter 3. Figure 7.29 shows the 10 X 10 grid of XRD patterns from taken from a $SiSn_xZn_y$ library spanning the range $0 < x < 1.1$ and $0 < y < 2.4$. Sn content is increasing from left to right and Zn content is increasing

from bottom to top. There is a fairly large amorphous range for this ternary system as well as some crystalline material.

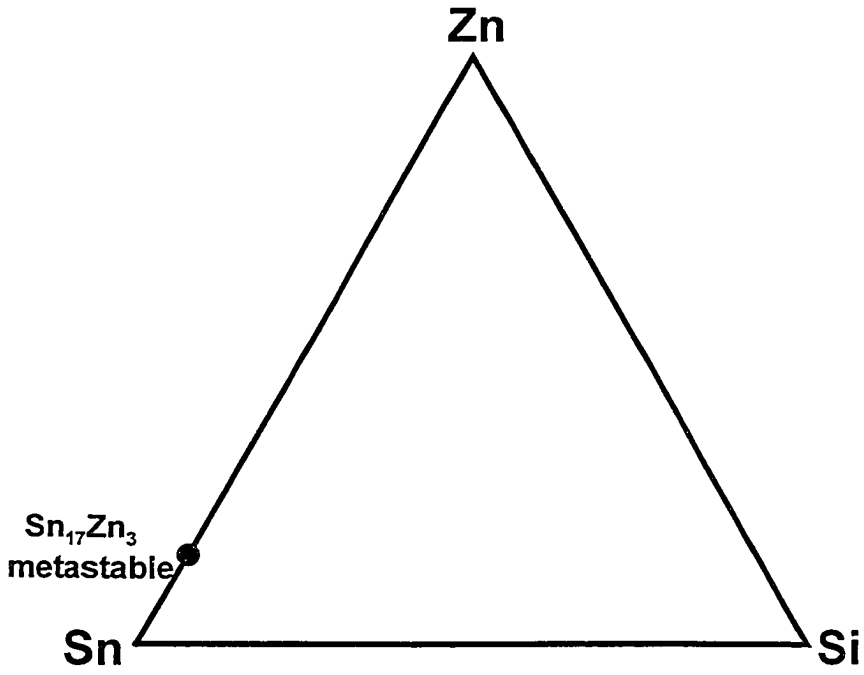

Figure 7.28. Plot of known phases in the SiSnZn ternary system.

No Sn peaks appear in the bottom row of XRD patterns in Figure 7.29, indicating that the edge of the amorphous range has not been reached. From other libraries of SiSnZn it was found that the library of Figure 7.29 was just at the edge of the amorphous range on the SiSn axis. The amorphous limit is comparable to that of the SiSn system.

Figure 7.30 shows an expanded view of the patterns in the top left corner of Figure 7.29. This area has high Zn and low Sn content. All of the peaks in this figure are from Zn. Peaks from crystalline Zn begin to appear in the third pattern up in the left hand column of Figure 7.29. This indicates the edge of the amorphous range on the SiZn binary axis.

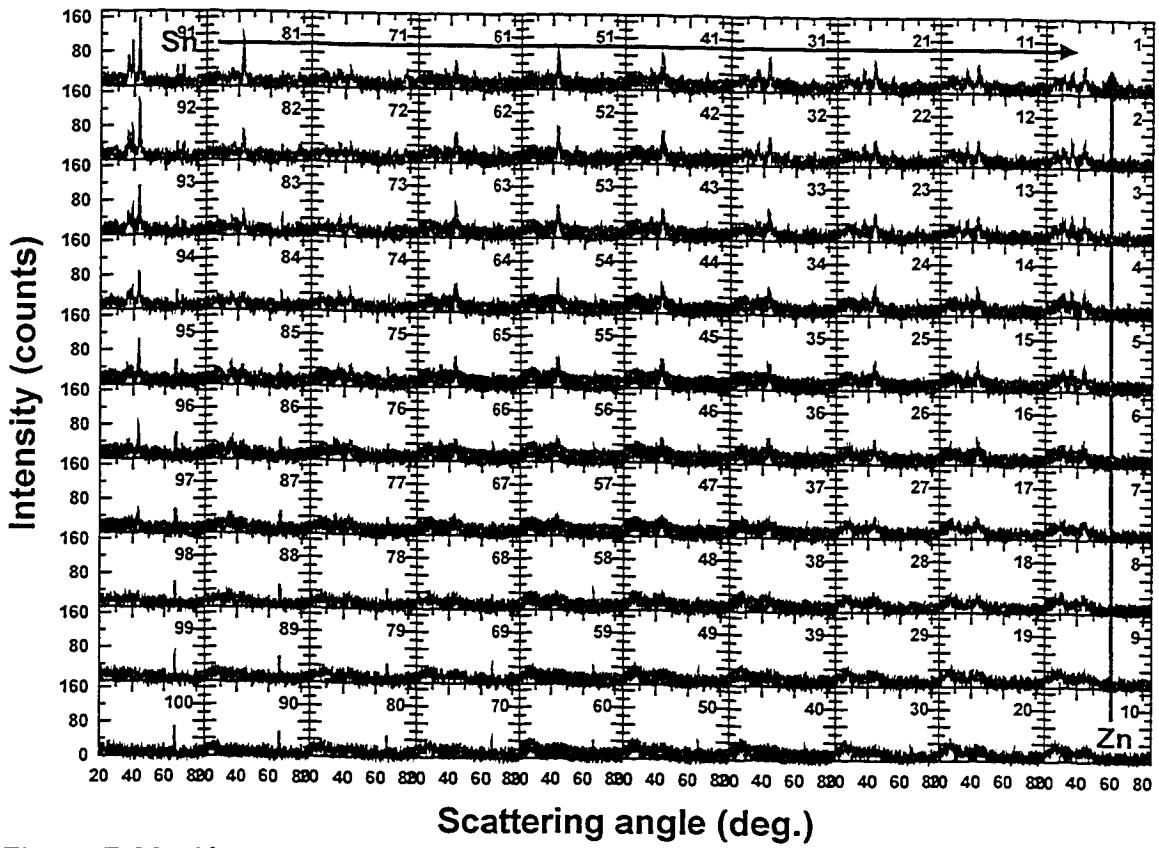

Figure 7.29. X-ray patterns displayed as a function of position on a 75 mm x 75 mm SiSnZn film. The direction of increasing Sn and Zn is marked.

Figure 7.31 shows an expanded view of the nine patterns in the top right corner of Figure 7.29. This area has high Zn and Sn content. Zn is the dominant phase in this figure as well. There may be some evidence for the 30° peak of Sn in plots 1, 2, 3 and 13 indicating that these patterns were taken near the edge of a three phase coexistence region.

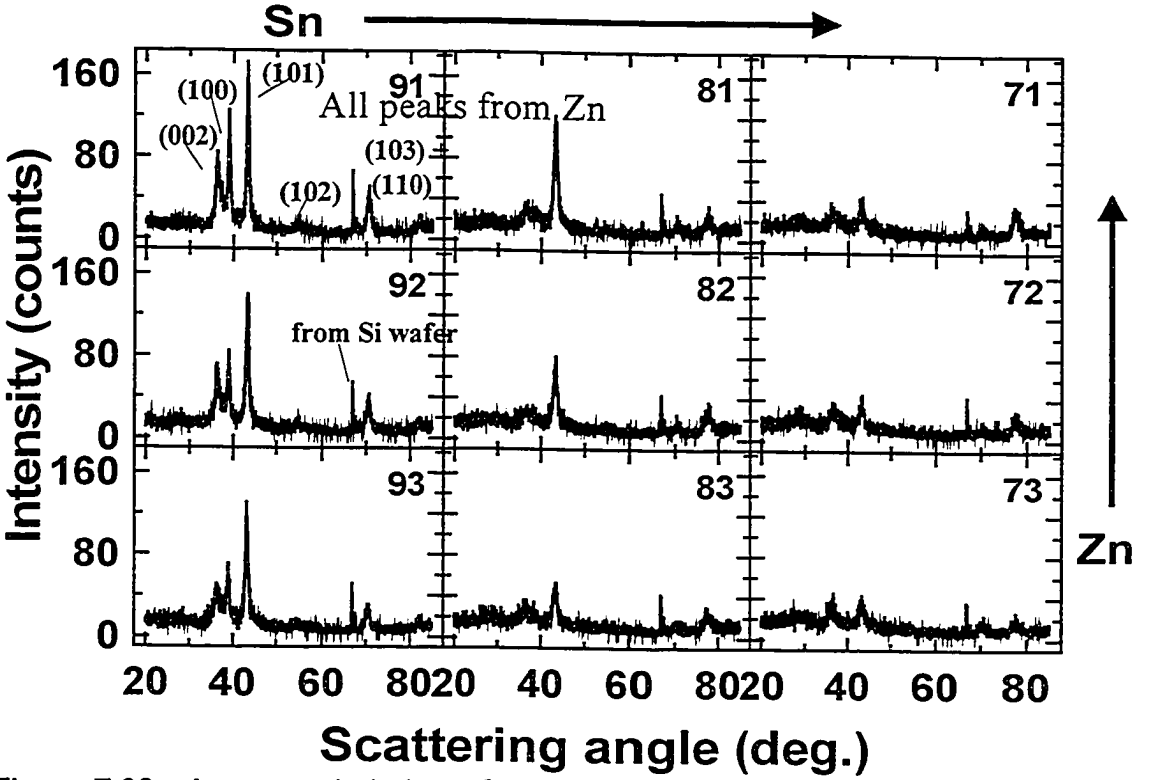

Figure 7.30. An expanded view of the XRD patterns from the top left corner of Figure 7.29. The directions of increasing Sn and Zn are indicated.

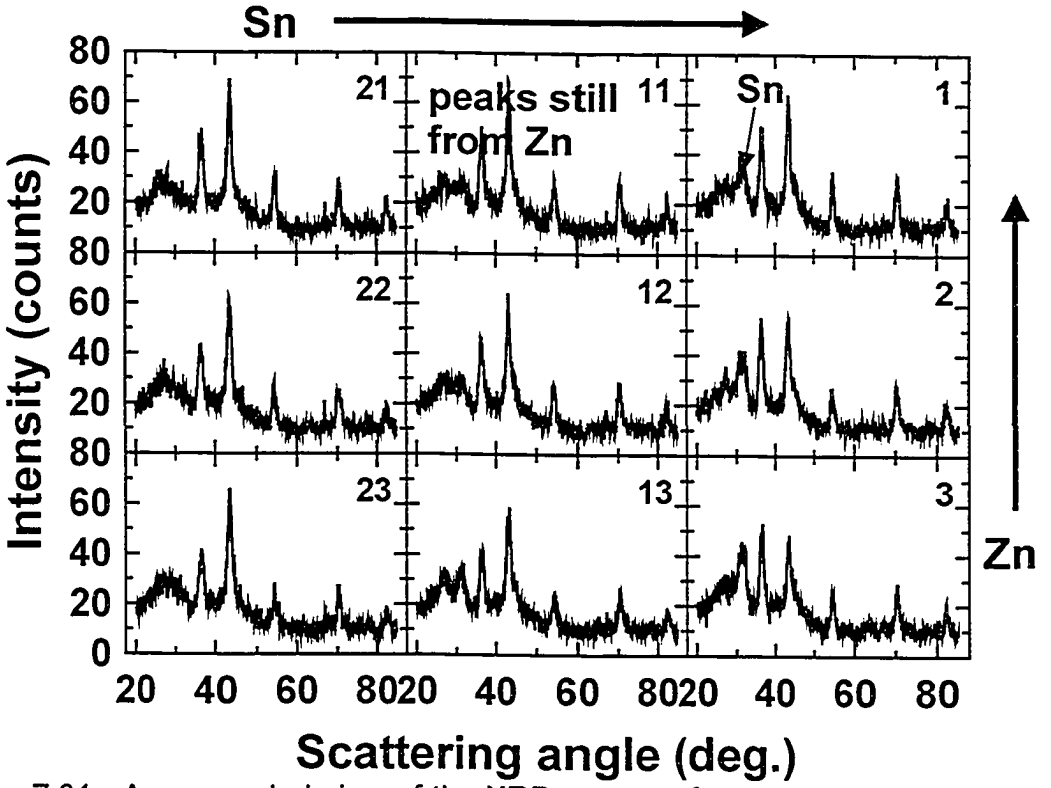

Figure 7.31. An expanded view of the XRD patterns from the top right corner of Figure 7.29. The directions of increasing Sn and Zn are indicated.

The XRD and microprobe data collected were used to produce the non-equilibrium ternary phase diagram for the sputtered SiSnZn system shown in Figure 7.32. The thick dark lines indicate the boundary of the amorphous range. The boundaries of the two and three phase coexistence regions have been drawn in with dashed lines.

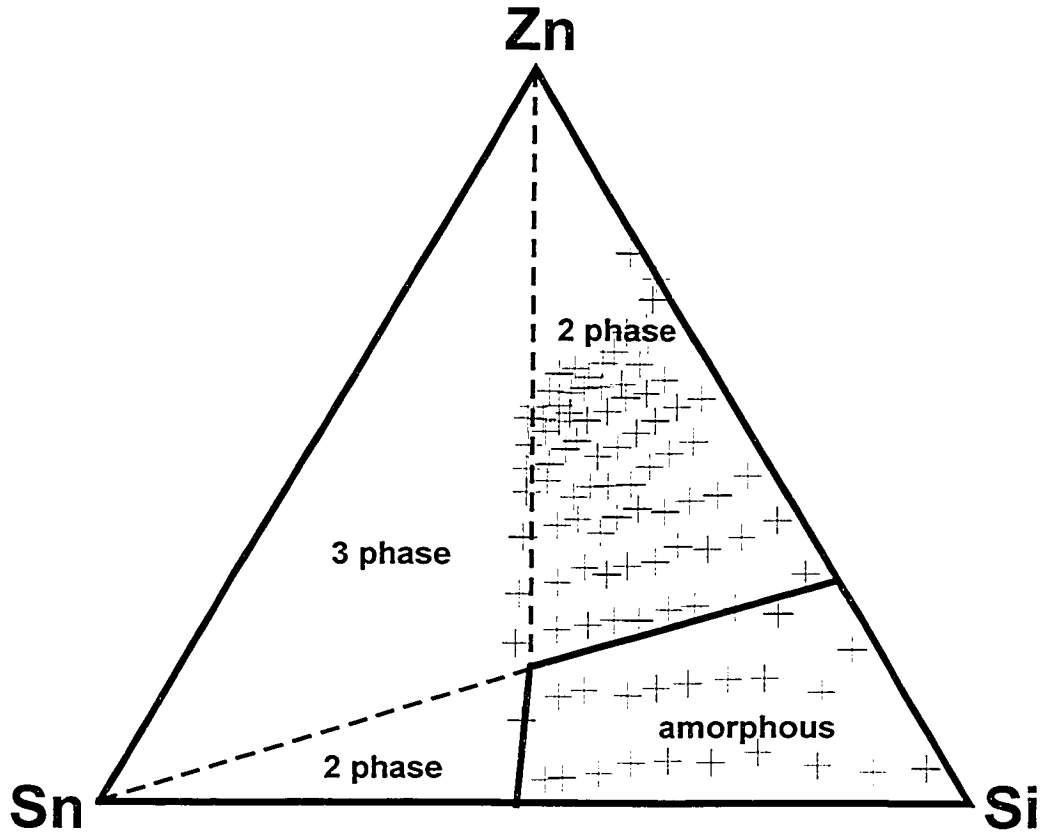

Figure 7.32. Non-equilibrium phase diagram for a sputtered SiSnZn library. The amorphous region and two and three phase regions have been marked.

7.3.2. Electrochemical Results

SiSnZn libraries were tested electrochemically with the combinatorial electrochemical cell. The electrochemical results to be described here are from a $SiSn_xZn_y$ library spanning the range $0 < x < 1.5$ and $0 < y < 0.8$. Figure 7.33 shows a plot of the approximate locations of the 64 channels of a combinatorial

cell. This library has more Sn than the previous one discussed and therefore extends into the region with crystalline Sn. The cell plate was included in a combinatorial cell and cycled using the Scribner MMA described in Chapter 4. The cell was discharged to 0.005 V at a sweep rate of 0.03 mV/s, held at that potential for two hours, charged to 1.2 V at a sweep rate of 0.03 mV/s and then held for 30 minutes. This process was then repeated.

Figure 7.34 shows plots of dQ/dV *versus* potential for the SiSnZn combinatorial cell. Arrows indicate the directions of increasing Sn and Zn.

The left column of graphs in Figure 7.34 corresponds roughly to the SiSn binary system (with a trace of Zn) described in Chapter 6, with Sn increasing from top to bottom. The first cycle of these channels is plotted on the same axis in Figure 7.35. The approximate composition of each channel is marked. In channel 62, a peak is starting to grow during charge at about 0.6 V. This is expected as this channel is on the edge of the amorphous range as shown in Figure 7.33. Channels 63 and 64 have clearly developed peaks from crystalline Sn. This column of channels follows the SiSn binary from Chapter 6 quite closely.

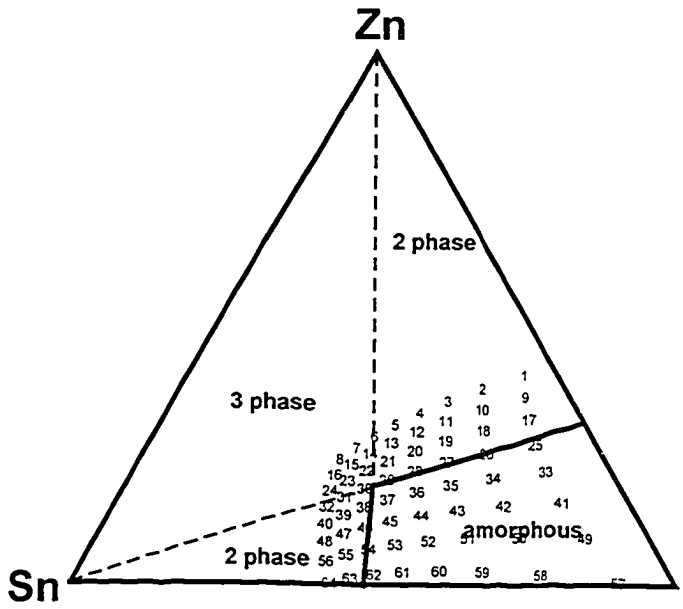

Figure 7.33. Plot of channel locations for a SiSnZn combinatorial cell.

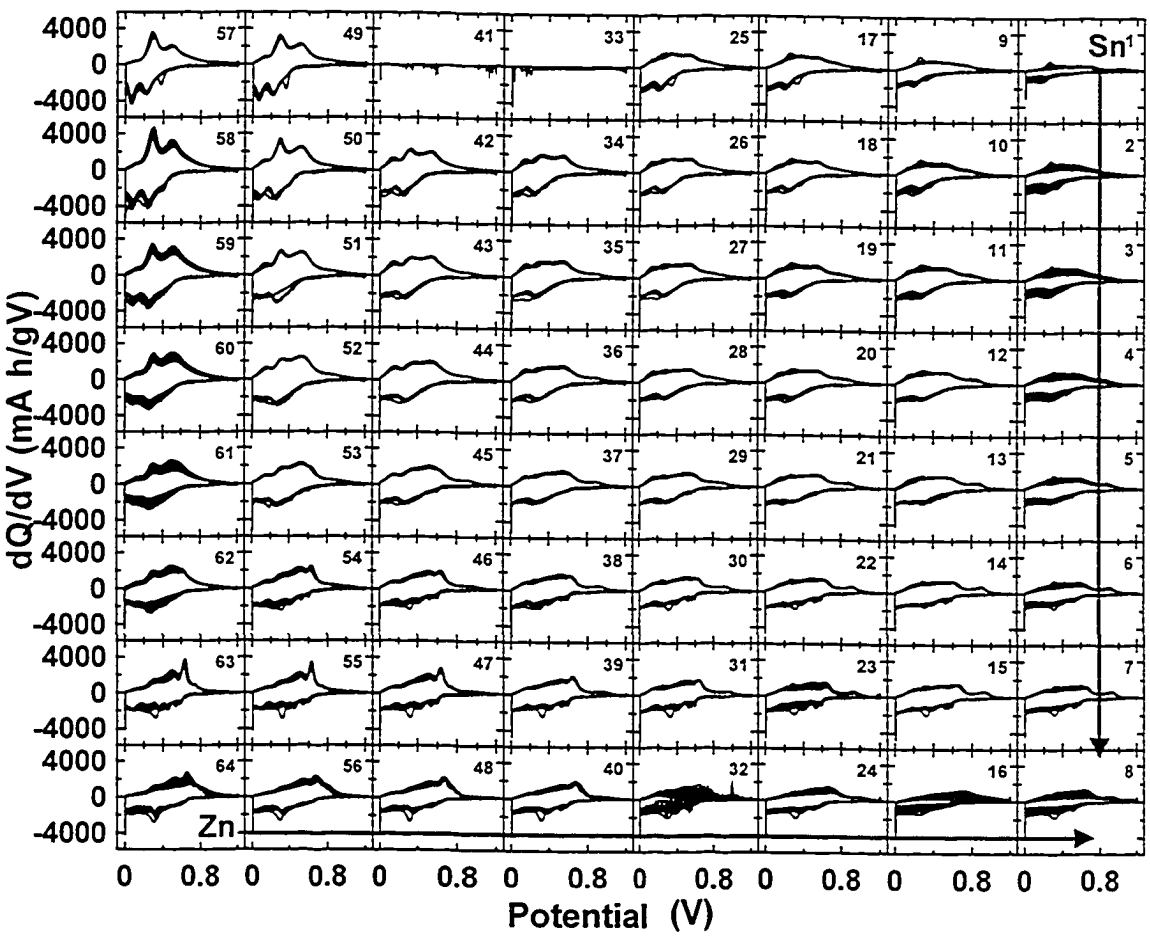

Figure 7.34. Plots of dQ/dV *versus* potential for the first 15 cycles of all 64 channels of a SiSnZn combinatorial electrochemical cell with compositions as indicated in Figure 7.33.

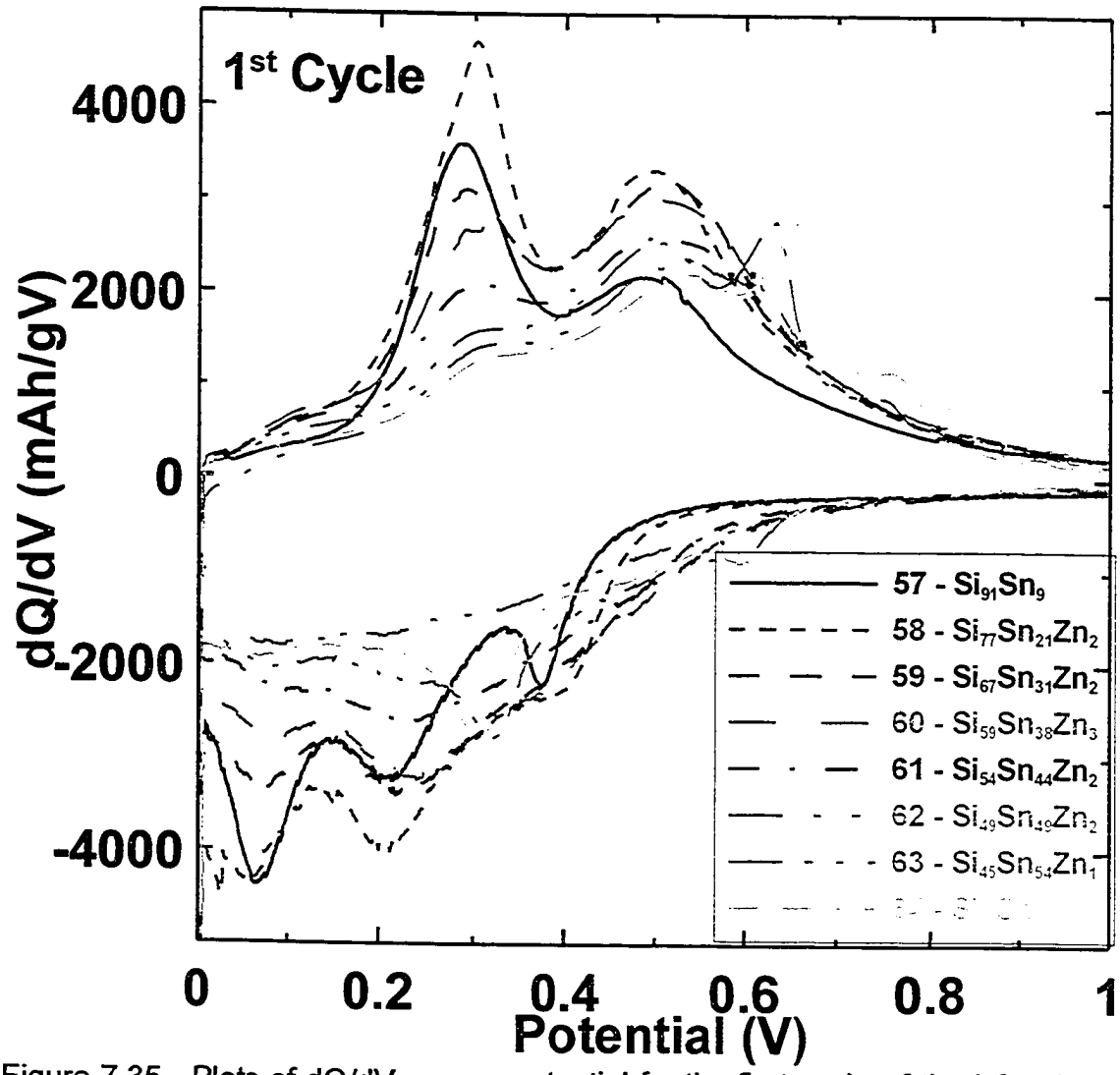

Figure 7.35. Plots of dQ/dV *versus* potential for the first cycle of the left column of cells from Figure 7.34. The approximate composition of each cell is indicated in the figure.

The top row of graphs in Figure 7.34 corresponds roughly to the SiZn binary with Zn increasing from left to right, although there is at least 5 at. % Sn in these channels. While some of these channels are outside of the amorphous range, there are no sharp peaks during charge in the dQ/dV *versus* potential relationships. It could be that the Sn suppresses the formation of $Li_{15}Si_4$ and the Zn is used in making the Li_2SiZn phase found in the *in-situ* XRD cells of Chapter 6. Figure 7.36 shows the plots of dQ/dV *versus* potential for the first cycle of the

third row down in Figure 7.34 (channels 59, 51, 43, 35, 27, 19, 11 and 3). These channels have a constant amount of Sn with Zn increasing as channel number decreases (from left to right in Figure 7.34). As Zn is added, the broad peaks in the dQ/dV *versus* potential relationship smooth out until there is a mostly featureless graph with a small hump near 0.3 V and one near 0.8 V during charge. For channels 35 and 43 there is also a small hump near 0.15 V during charge. It is not certain what phase is causing these humps to appear, as Figure 7.33 shows that these channels are from an area of the library that was amorphous by XRD.

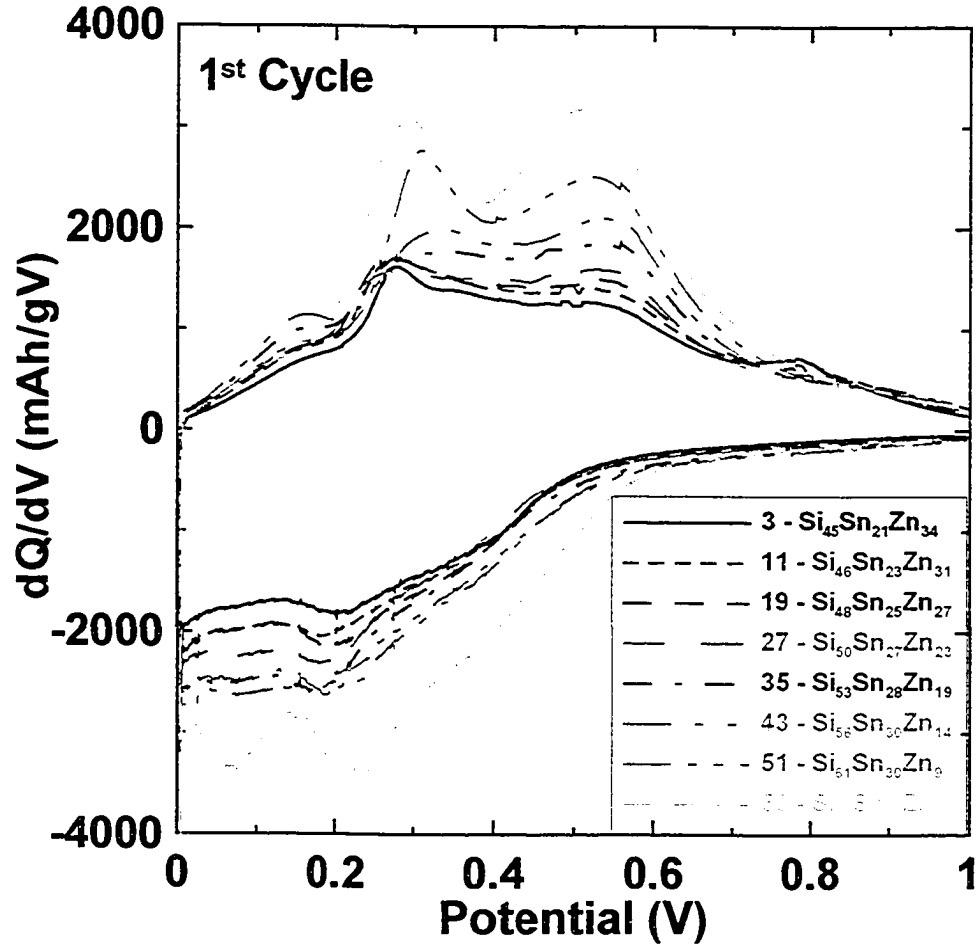

Figure 7.36. Plots of dQ/dV *versus* potential for the first cycle of the third row of cells from Figure 7.34. The approximate composition of each cell is indicated in the figure.

It is also interesting to see what happens to the shape of the dQ/dV *versus* potential graph when Sn is added at a fairly high Zn content. Figure 7.37 shows the plots of dQ/dV *versus* potential for the first cycle of channels 19 to 22 in Figure 7.34. These channels have a constant amount of Zn with Sn increasing with channel number (from top to bottom in Figure 7.34). As Sn is added the lower potential of the two broad humps during charge becomes smaller. Also, when enough Sn is present, the higher potential of the two broad humps begins to shift to slightly higher voltage. More noticeably, a new peak develops above 0.9 V during charge and near 0.6 V during discharge. This peak is small for channel 21, but is quite well developed for channel 22. This peak has not been seen in any previous plots. The 0.9 V peak does develop for many other channels. These channels all have the common characteristic that the Sn content is very close to or larger than the Si content. As one goes down a column of channels in Figure 7.34, the 0.9 V peak appears when the Sn content exceeds the Si content. For the channels shown previously, the only ones that had more Sn than Si (channels 63 and 64) had negligible Zn content and the 0.9 V peak did not appear. It is possible that the Sn excludes Zn from interacting with Si to form Li_2SiZn. When there is enough Sn, the Zn can then react with Li, forming peaks at higher voltages. Recall from Figure 5.18 that Zn has a sharp peak above 0.6 V. If this peak were shifted up in potential in the SiSnZn ternary films it could be responsible for the high potential peak during charge for channels 21 and 22. More work is needed on this issue.

When there is a large amount of Sn and Zn added to the a-Si (channels 8 and 16) the dQ/dV *versus* potential graph becomes mostly shapeless. The reasons for this are not clear.

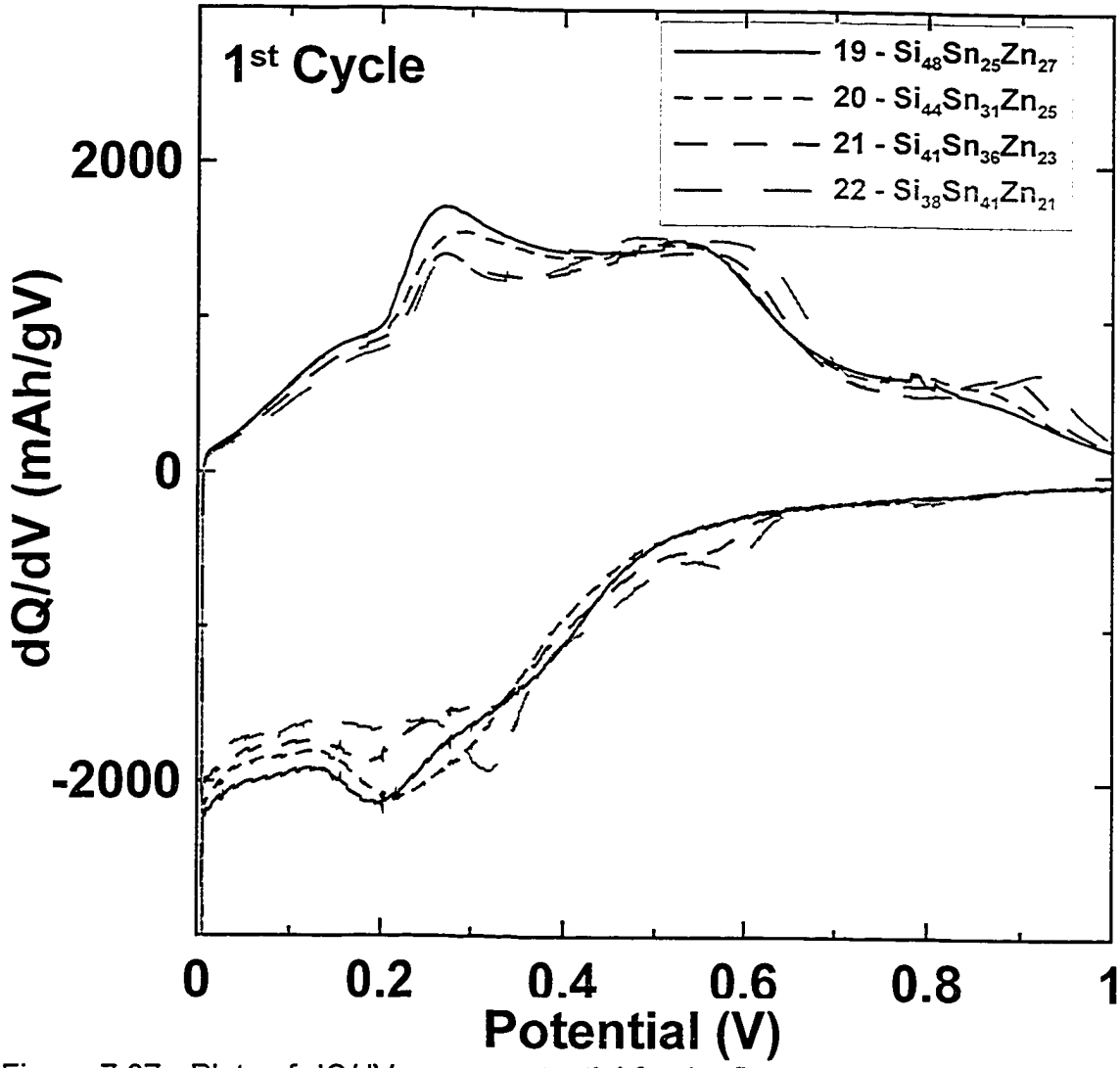

Figure 7.37. Plots of dQ/dV *versus* potential for the first cycle channels 19 to 22 from Figure 7.34. The approximate composition of each cell is indicated in the figure.

Figure 7.38 shows a contour plot of irreversible capacity *versus* composition for the SiSnZn combinatorial cell. The irreversible capacity is moderate, in the range of 6 to 16 % for most channels. There is little dependence on Zn content although there is a slight increase with Zn content

inside the amorphous region and then a decrease outside the amorphous region. The irreversible capacity showed a strong dependence on Sn content, being lowest for the channels with the most Sn.

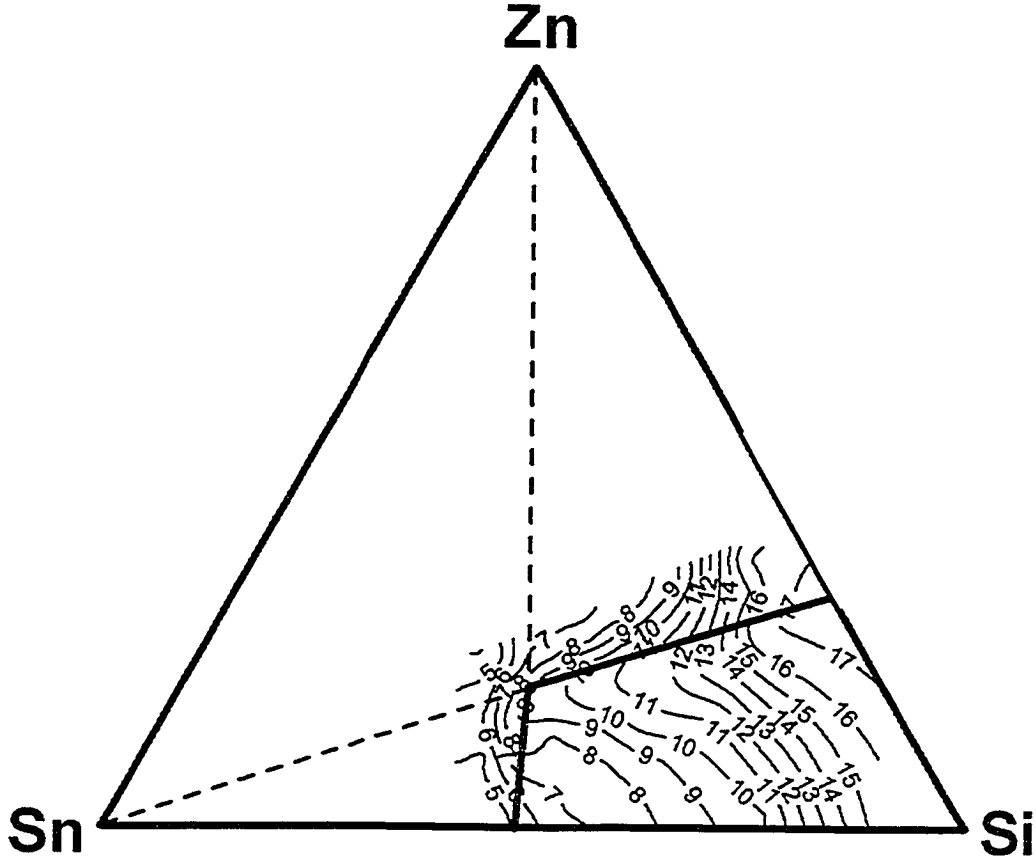

Figure 7.38. Contour plot showing irreversible capacity as a percent of the first discharge *versus* composition for the SiSnZn ternary system.

The capacity fade as a percent of the first discharge is shown in the contour plot of Figure 7.39. The capacity fade is quite low. Most channels have fade rates of less than 2 %/cycle and several have rates of less than 1 %/cycle. These numbers are comparable to the SiSn binary library discussed in Chapter 6. There are no strong relationships between fade rate and composition for the SiSnZn system. This is not surprising as the SiSn and SiZn system both performed quite well, and there are no ternary phases in the SiSnZn system.

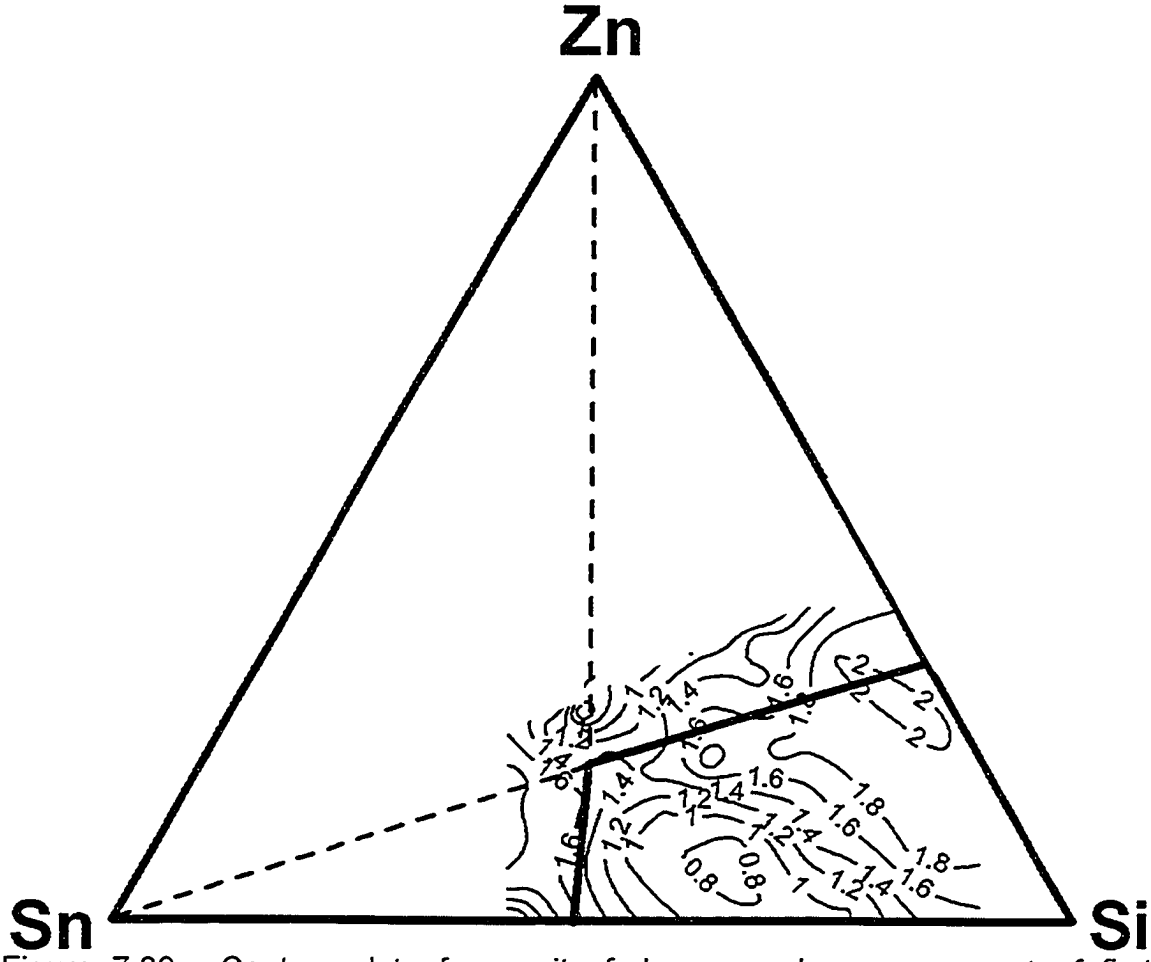

Figure 7.39. Contour plot of capacity fade per cycle as a percent of first discharge capacity plotted *versus* composition for the SiSnZn combinatorial electrochemical cell.

None of the channels in Figure 7.34 showed any significant changes in the shape of the dQ/dV *versus* potential relationship with cycle number. This is very different from the SiZn binary system discussed in Chapter 6. This would indicate that for the SiSnZn ternary system the $Li_{15}Si_4$ and other phases found in the LiZn *in-situ* XRD cells do not form. However, for all of the channels in Figure 7.34 there was a significant amount of Sn (at least 5 at. %). If some channels from other combinatorial cells from this system are checked, then some evidence of crystallization is found.

Figure 7.40 shows plots of dQ/dV *versus* potential for the first four cycles of some channels from a combinatorial cell built with a cell plate produced in the sputtering run in which the library was made that was used to determine the amorphous range in the SiSnZn system. These graphs are from the area of the cell with lowest Sn and Zn content. Some of these cells apparently do form the $Li_{15}Si_4$ phase as there is a sharp peak at about 0.4 V during charge superimposed on the a-Si like broad humps at 0.3 V and 0.5 V. Channel 57 does not have the 0.4 V peak, but the peak at 0.5 V does become sharper with cycle number. In channels 58 and 59 the 0.4 V peak grows with cycle number while the 0.3 V hump is diminished. Channels 49 and 50 both exhibit the 0.4 V peak. For channel 49 the shape is constant and similar to those for the SiZn binary with comparable composition. For channel 50 the peak grows after two cycles. Channel 51 does not have the 0.4 V peak. Channels 41 and 42 both have a tiny peak at 0.4 V during charge that does not change with cycle number. Channel 43 does not have the 0.4 V peak at all. For higher Sn contents than those shown the 0.4 V peak does not appear. For higher Zn it is not expected based on the performance of the SiZn binary from Chapter 6. There are several questions remaining about when $Li_{15}Si_4$ can form for this system. A series of *in-situ* XRD experiments are needed to figure out exactly what is taking place in these cells.

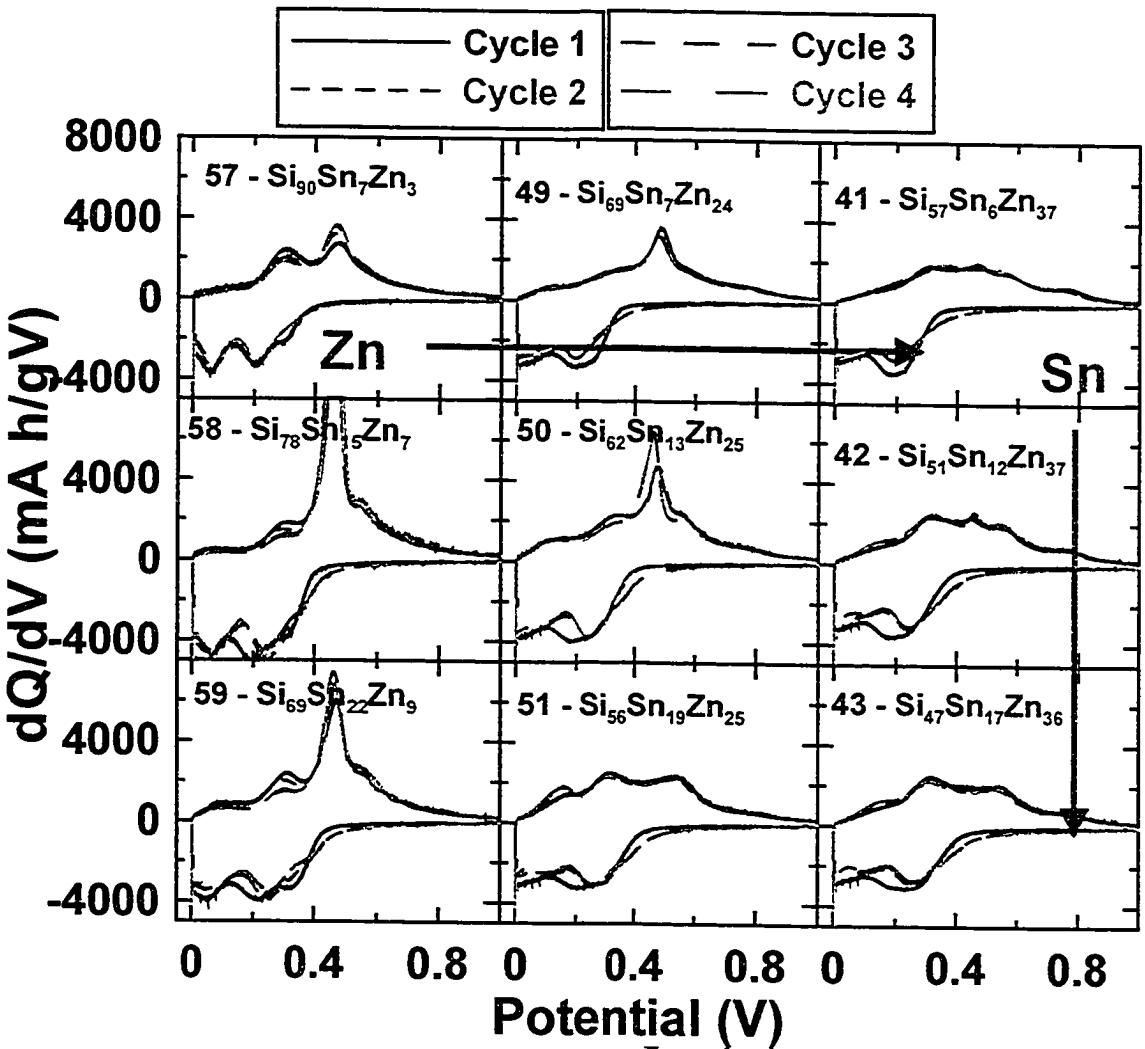

Figure 7.40. Plots of dQ/dV *versus* potential for several channels of a SiSnZn combinatorial cell. The approximate compositions are indicated on the figure.

7.3.3. Conclusions for SiSnZn

A wide range of the SiSnZn ternary system has been produced by combinatorial sputtering. The libraries have been characterized using XRD and electron microprobe experiments in order to determine the amorphous range. The amorphous range is quite large, although it is not as big as that of the SiAlSn system. No intermettalic phases were found in this system.

The electrochemical performance of the SiSnZn was the best of the ternary systems discussed to this point. The irreversible capacities were low with

the best compositions being those high in Sn. Cycle life over the first ten cycles was also found to be quite good, with many channels of one combinatorial electrochemical cell having fade rates of less than 1 % of the first discharge capacity per cycle.

It was found that the $Li_{15}Si_4$ phase that was frequently encountered for the binary systems in Chapter 6 only occurred for a very limited range of stoichiometries in the SiSnZn ternary system, based on features in dQ/dV *versus* potential that have been found to be indicative of that phase. Only compositions that were low in Sn and had more than a trace of Zn would form the $Li_{15}Si_4$ phase (all of the atoms are likely incorporated in the phase, so it would be $Li_{15}(SiSn_xZn_y)_4$). With enough Sn present this phase would not form regardless of Zn content. As with the SiZn binary, if the Zn content was high enough the $Li_{15}Si_4$ was not found.

The electrochemical performance of this ternary system and the apparent lack of crystalline phases over a wide range of compositions make this an interesting system for further study. It would be good to find out the precise mechanisms involved in some of the structure changes seen in these libraries. The phases formed during discharge should also be determined for the various compositions as well. Answering the questions remaining for this ternary system could take several months or even years worth of experiments.

7.4. SiAgZn

7.4.1. Non-equilibrium Phase Diagram

A plot of the known phases for the SiAgZn ternary system is shown in Figure 7.41. The metastable SiAg phases seen previously are indicated along with the known AgZn phases. There are no SiZn binary phases and no ternary phases known for this system.

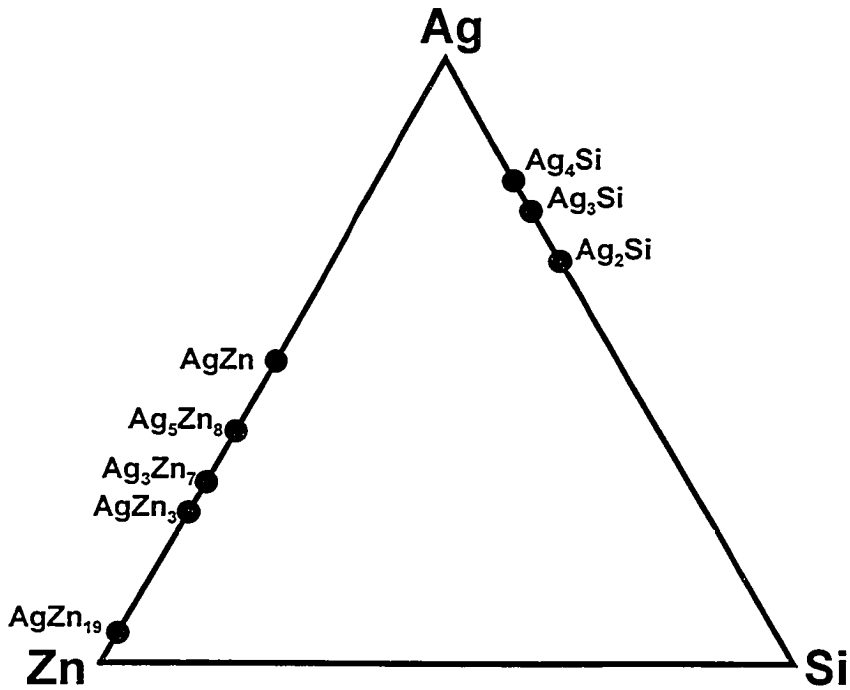

Figure 7.41. Plot of known compositions for the SiAgZn ternary system.

Ternary libraries of SiAgZn were created using the combinatorial sputtering system described in Chapter 3. The libraries were characterized for structure and composition using XRD and electron microprobe. The library used to partially map the non-equilibrium phase diagram covered the range of $0 < x < 1.3$, $0 < y < 1.1$ in $SiAg_xZn_y$. The XRD patterns for this library are shown in Figure 7.42.

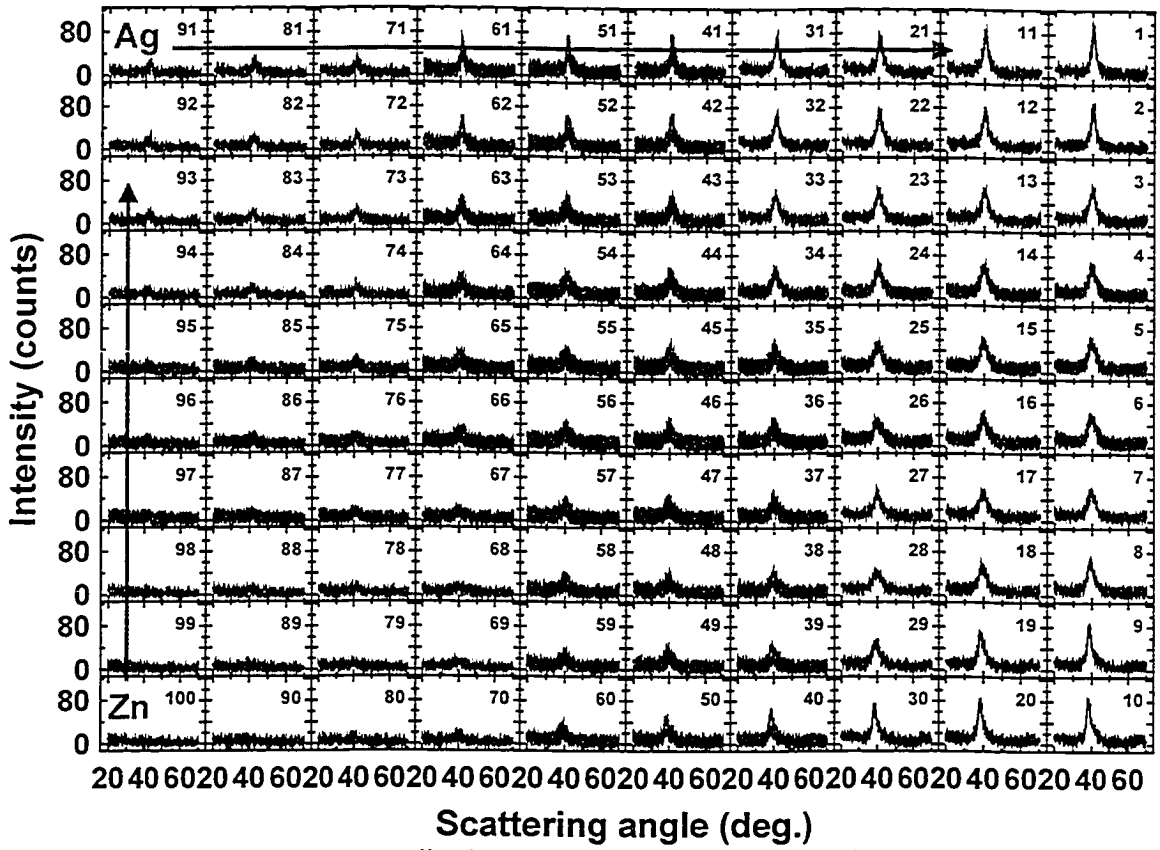

Figure 7.42. X-ray patterns displayed as a function of position on a 75 mm x 75 mm SiAgZn film. The direction of increasing Ag and Zn is marked.

The left column of patterns in Figure 7.42 has low Ag content with Zn increasing from bottom to top. The peak that appears at about 42° corresponds to the (101) peak of $AgZn_3$ or the (101) peak of Zn (see scan 91 in Figure 7.45). These two phases have the same hexagonal structure and similar lattice constants with the atoms on the same sites [102], so the peak in the left column is likely a hexagonal Ag_xZn phase with $0 < x < 0.33$.

The bottom row of patterns in Figure 7.42 has low Zn content with Ag increasing from left to right. These patterns are shown in Figure 7.43. The broad peak that appears in scan 60 is centred near 38° with a shoulder centred at about 40°. These are likely the Ag (111) and AgZn (110) peaks respectively.

The end of the amorphous range on this binary axis is consistent with the SiAg system from Chapter 6. As Ag content increases, the Ag (111) peak grows in intensity.

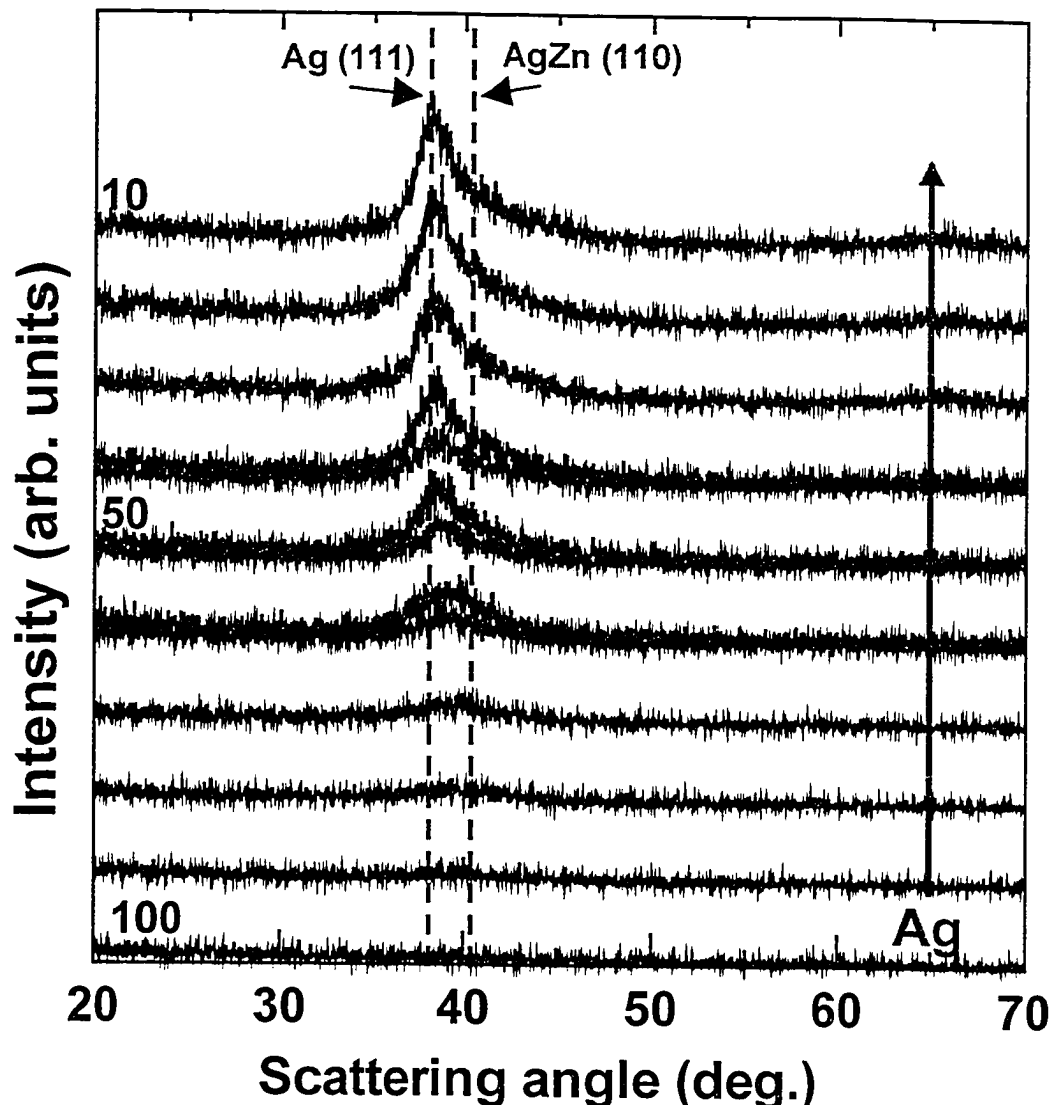

Figure 7.43. Expanded view of the bottom row of XRD patterns from Figure 7.42.

The right column of patterns in Figure 7.42 has high Ag content with Zn increasing from bottom to top. These patterns are shown in Figure 7.44. As Zn is added, the Ag (111) peak fades, leaving only the AgZn (110) peak at about 40° by the time maximum Zn content is reached.

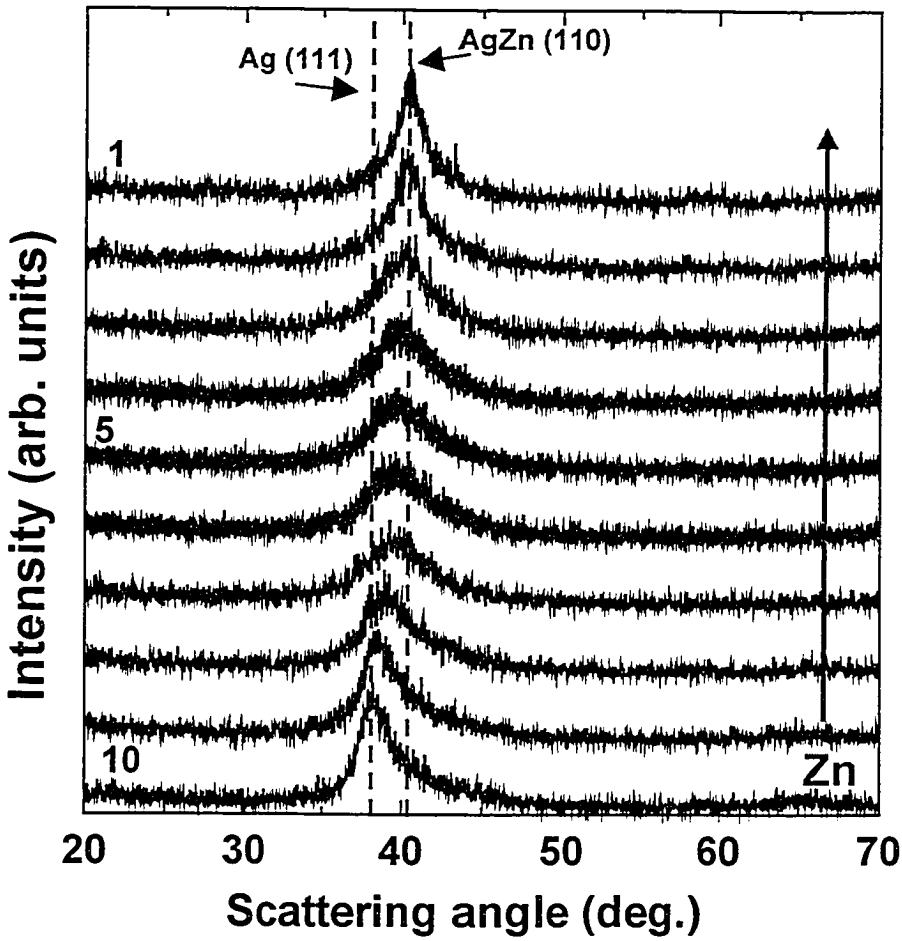

Figure 7.44. Expanded view of the right column of XRD patterns from Figure 7.42.

The top row of patterns in Figure 7.42 has high Zn content with Ag increasing from left to right. These patterns are shown in Figure 7.45. In the figure, the position of the Zn (101), $AgZn_3$ (101), Ag_5Zn_8 (330) and AgZn (110) peaks are marked with dashed lines. These are the most intense peaks for these phases. The (101) peaks of Zn and $AgZn_3$ can be considered as the (101) peak of Ag_xZn, as described above. As Ag is added the (101) peak of Ag_xZn (located between the $AgZn_3$ and Zn peak positions) fades and the (330) peak of Ag_5Zn_8 forms. With more Ag, the (330) peak of Ag_5Zn_8 fades and the (110) of AgZn forms so that it is the only peak left with maximum Ag content in scan 1.

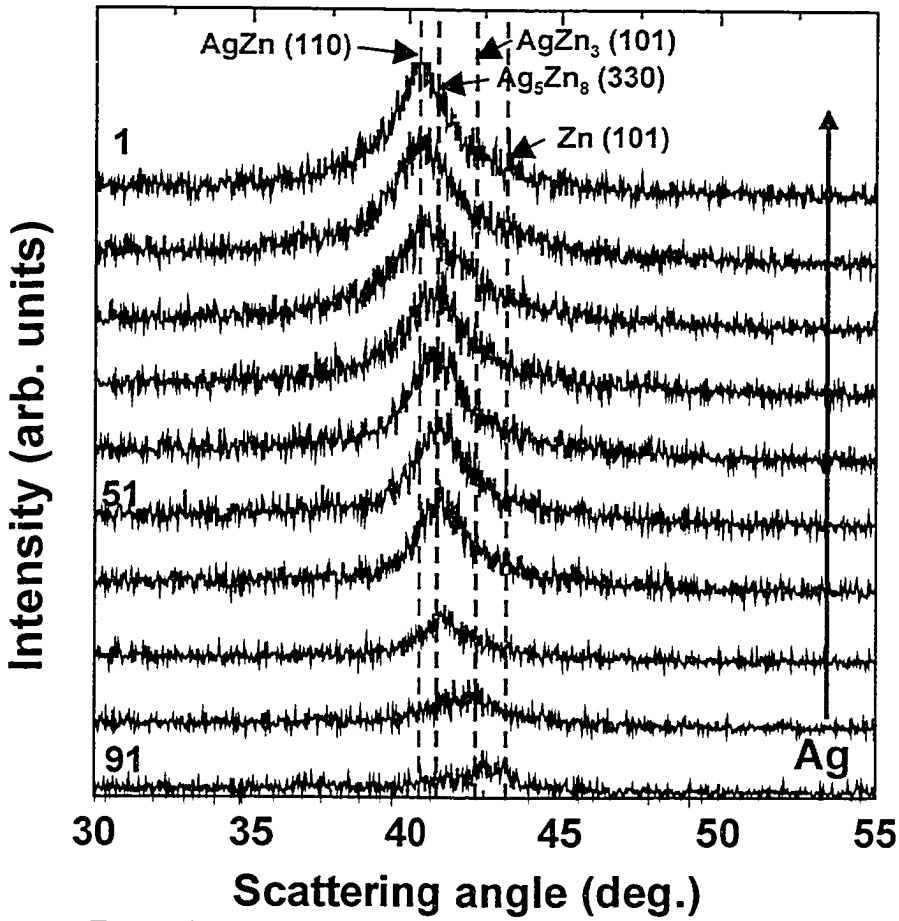

Figure 7.45. Expanded view of the top row of XRD patterns from Figure 7.42.

The XRD and electron microprobe data were used to construct the non-equilibrium phase diagram for the SiAgZn ternary system shown in Figure 7.46. The thick solid line marks the boundary of the amorphous region. The dashed lines mark the boundaries of various two and three-phase coexistence regions. The dashed lines are somewhat uncertain because the limited stoichiometry range of the combinatorial library did not cover the boundaries of all the regions found. Also, for some areas in the XRD map it was difficult to tell if a peak was shifting position as the composition of a phase changed (such as with the Ag_xZn phase on the AgZn binary axis) or if a peak from one phase was fading as a peak from a new phase appeared nearby on the 2theta axis.

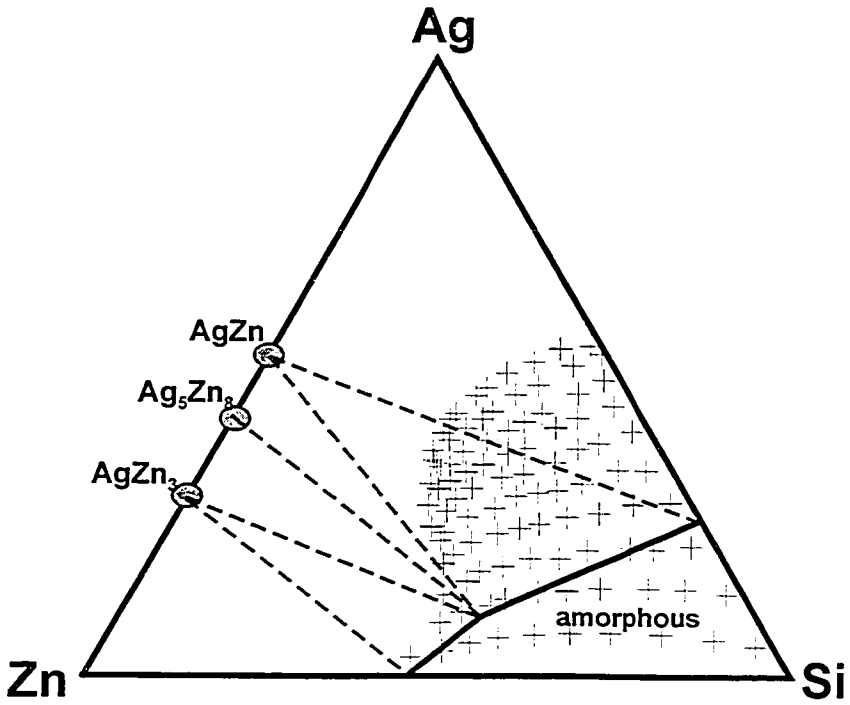

Figure 7.46. Non-equilibrium phase diagram for a sputtered SiAgZn library. The amorphous region has been marked.

7.4.2. Electrochemical Results

SiAgZn libraries were tested electrochemically with the combinatorial electrochemical cell. The results to be described here are from a $SiAg_xZn_y$ library spanning the range $0 < x < 1.1$ and $0 < y < 0.8$. Figure 7.47 shows a plot of the approximate locations of the 64 channels from a SiAgZn combinatorial cell. This cell plate was included in a combinatorial cell as described in Chapter 4. This cell was cycled using the Scribner MMA described in Chapter 4. The cell was discharged to 0.001 V at a sweep rate of 0.03 mV/s, held at that potential for two hours, charged to 1.2 V at a sweep rate of 0.03 mV/s and then held for 30 minutes. This process was then repeated.

Figure 7.48 shows plots of dQ/dV *versus* potential for the SiAgZn combinatorial cell. The directions of increasing Ag and Zn are marked with

arrows. The top row of graphs in Figure 7.47 corresponds roughly to the SiZn binary system from Chapter 6 with Zn increasing from left to right, although there is quite a bit of Ag in these channels. These channels follow the SiZn binary results fairly well with a large peak at 0.4 V during charge for those channels with low to moderate Zn and no sharp peaks for higher Zn contents. However, the presence of the Ag may be interfering with the formation of the Li-Si-Zn ternary phases. It seems that it takes more Zn for the large peak during charge to disappear than it did in the SiZn binary in Chapter 6. Without the Ag, the dQ/dV *versus* potential graph becomes flatter more quickly than it does here.

The left-most column of Figure 7.48 corresponds to the SiAg binary (with some Zn) with Ag increasing from top to bottom. From Figure 7.47 it might be expected that these channels will differ from the SiAg binary, as there are different phases along this axis of the phase diagram. However, these cells perform similarly to those in Figure 6.16 except there are more sharp peaks at lower potential during charge for the channels from Figure 7.48.

Many of the channels for the SiAgZn combinatorial cell in Figure 7.48 do not show sharp peaks during discharge or charge. For cells with high Ag content, there are peaks at low potential during charge, but as Zn content increases, these disappear and the dQ/dV *versus* potential plots become quite featureless.

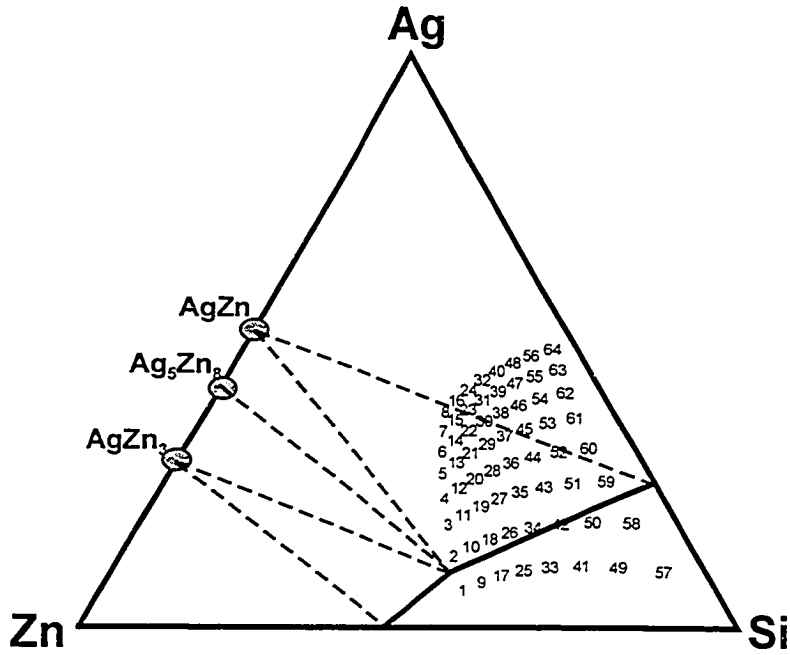

Figure 7.47. Plot of channel locations for a SiAgZn combinatorial cell.

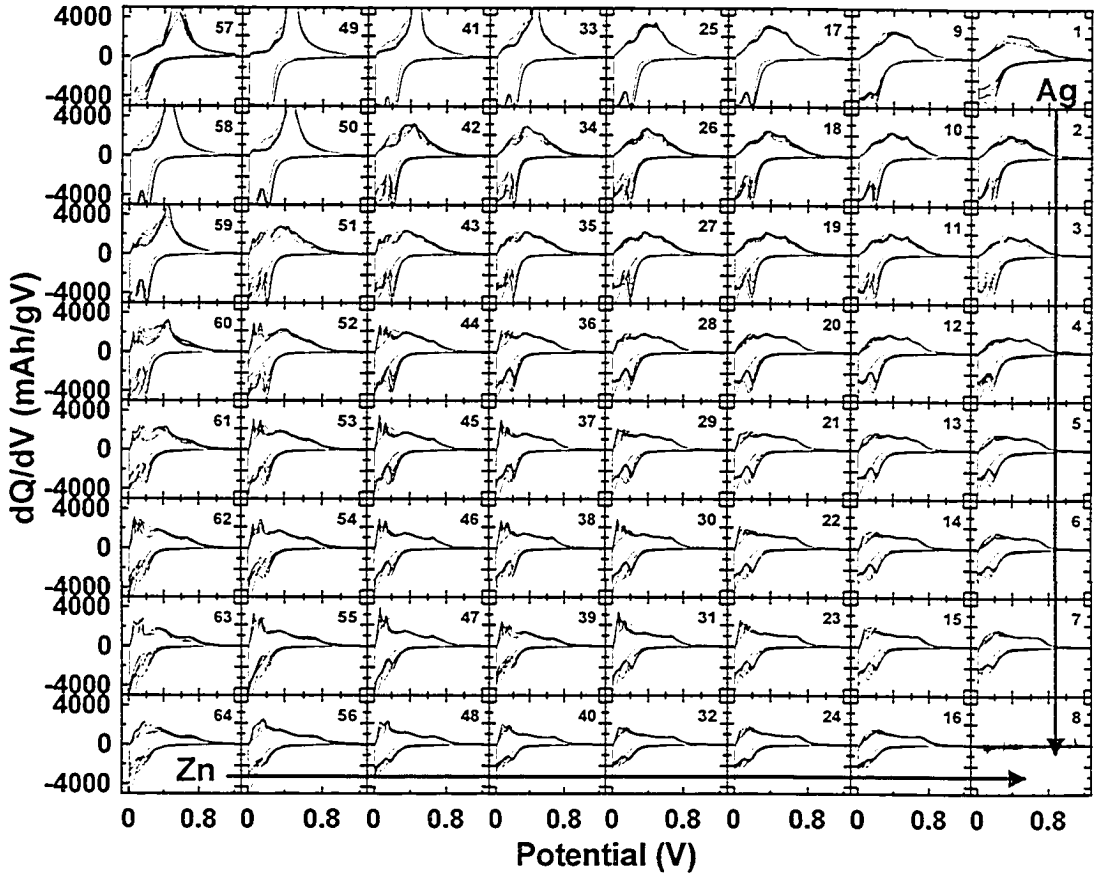

Figure 7.48. Plots of dQ/dV *versus* potential for the first six cycles of all 64 channels of a SiAgZn combinatorial electrochemical cell with compositions as indicated in Figure 7.47.

The lack of sharp peaks in dQ/dV *versus* potential for many channels should be expected after examining the XRD patterns in Figure 7.41. Most of the patterns in this figure have very broad, poorly defined peaks. This indicates very small particle sizes or nanocrystalline material. If the particle sizes are small enough, the material may behave as if it is amorphous. This was a possible explanation for the behaviour of the SiZn binary in Chapter 6 and may also be true here. The areas with the most well defined XRD peaks would correspond to the left side and bottom of Figure 7.48, and this is where the majority of sharp peaks appear in the dQ/dV *versus* potential plots.

Many of the plots in Figure 7.48 degrade quite quickly with cycle number, indicating that the electrochemical performance was not very good for much of this combinatorial cell. An example is the bottom of the left column in Figure 7.48. This area is high in Ag content with low Zn. content The capacity in this area is fading quickly. In contrast, many of the plots along the top row do not degrade very quickly. These have Zn content increasing from left to right with low Ag content. The capacity is not fading quickly in this area. This is what should be expected, given the results in Chapter 6 for SiAg and SiZn binary libraries. The plots for channels 14, 22 and 30 are also quite interesting. These channels have moderate Zn and Ag content. The low voltage peaks during charge from Ag (see Figure 5.17) of the graphs for these channels degrade quickly while the higher voltage portion from Zn (see Figure 5.20) do not degrade.

Figure 7.49 shows contour plots of irreversible capacity and capacity fade *versus* composition for the SiAgZn combinatorial cell of Figure 7.48. Figure 7.49a shows the irreversible capacity as a percent of the first discharge. The irreversible capacity is a little higher for this system than for the SiSnZn system. Most are in the range of 8 to 12 % with a few even higher. There is no strong correlation between irreversible capacity and composition. The capacity fade rate shown in Figure 7.49b has been calculated as a percent of the third discharge per cycle between cycles three and six. The calculation was done in this manner to allow the structure of the electrode to become stable in with respect to Ag aggregation and Zn nanocrystallization as described in Chaptter 6. This also eliminates effects of irreversible capacity if the first charge is used. The fade rate is, as should be expected, best for channels with low Ag content, with some along the SiZn binary axis below 1% per cycle. The fade rate increases rapidly with Ag content, with some channels exceeding 8% per cycle.

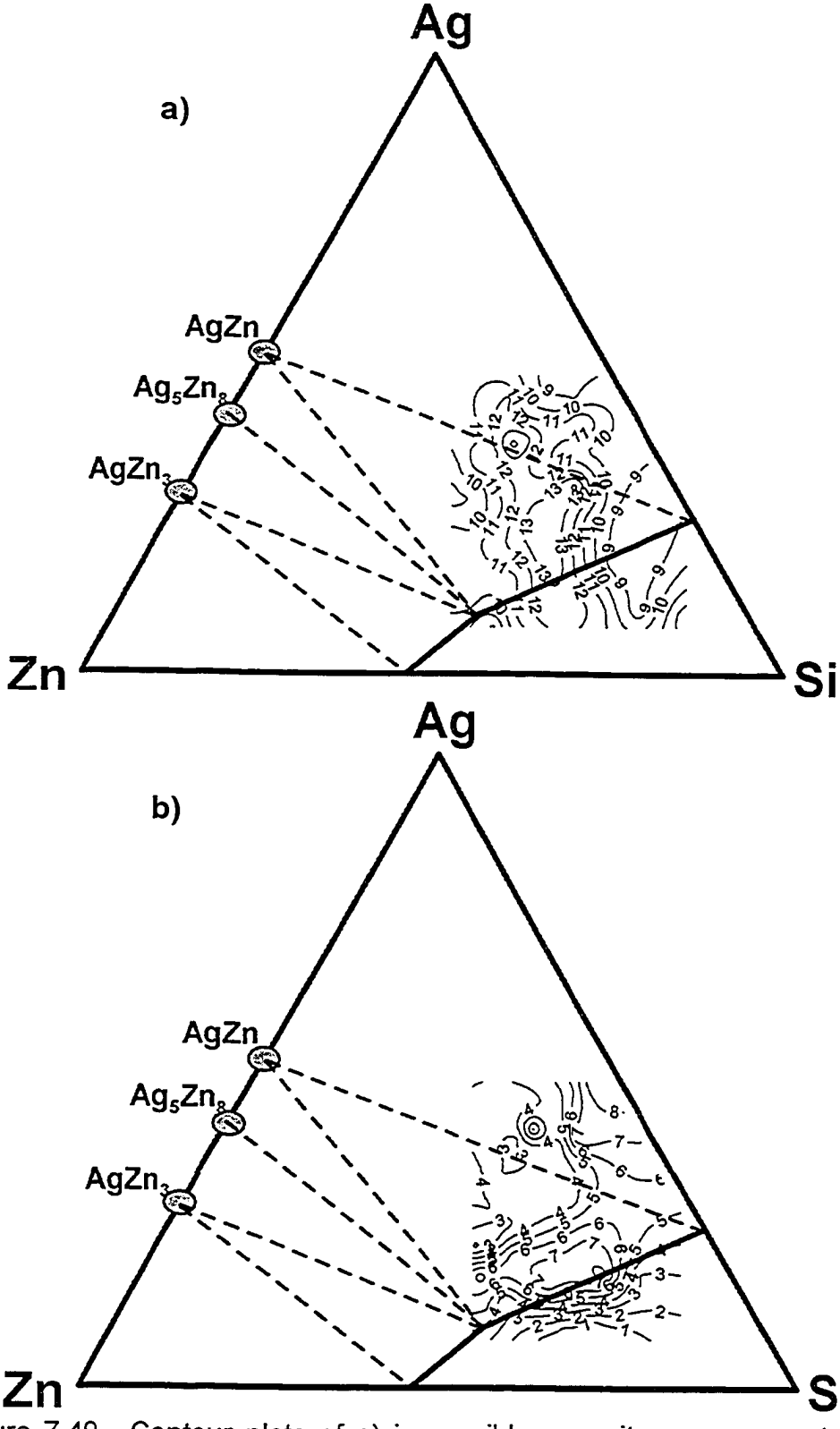

Figure 7.49. Contour plots of a) irreversible capacity as a percent of the first discharge and b) capacity fade per cycle as a percent of the third discharge *versus* composition for the SiAgZn combinatorial electrochemical cell of Figure 7.48.

7.4.3. Conclusions for SiAgZn

A wide range of the SiAgZn ternary system has been produced by combinatorial sputtering. The libraries have been characterized using XRD and electron microprobe experiments in order to determine the amorphous range. The amorphous range is smaller in size than the amorphous range from the SiSnZn ternary system. This is not surprising given the larger amorphous range in the SiZn binary as compared to that in the SiAg binary. Several intermetallic phases were found in this system. One phase was a Ag_xZn phase that has the same structure as that reported for Ag_3Zn (and Zn) [102] with the amount of Ag varying. There was also evidence of Ag_5Zn_8 and AgZn in the XRD data.

The electrochemical performance of SiAgZn was not as good as the SiSnZn system. The irreversible capacities were higher than those for SiSnZn. Also, the cycle life over the first six cycles was found to be much worse than SiSnZn, with many channels of the combinatorial electrochemical cell having fade rates of more than 4 % of the first discharge capacity per cycle.

The $Li_{15}Si_4$ phase was found over only a very limited range of compositions for the SiAgZn system. Only compositions that were low in Ag and Zn would form the $Li_{15}Si_4$ phase. When there was too much metal content the $Li_{15}Si_4$ phase was not present. This is consistent with what was found for the SiZn and SiAg systems.

The electrochemical performance of this ternary system was quite disappointing in light of the lack of evidence of crystalline phases in dQ/dV *versus* potential over a wide range of compositions. Despite the apparently

amorphous structure or small particle size of crystalline materials, the combinatorial cells for this ternary system did not show good cycling performance. The poor performance is likely due to the presence of Ag.

7.5. SiGeSn

7.5.1. Non-equilibrium Phase Diagram

To investigate the effects of combining three Group IV elements the SiGeSn ternary system was sputtered over a range of $SiGe_xSn_y$ with $0 < x < 1.7$ and $0 < y < 1.5$ using the combinatorial sputtering machine described in Chapter 3. The film was characterized using XRD and electron microprobe in order to determine the phase diagram for the sputtered system.

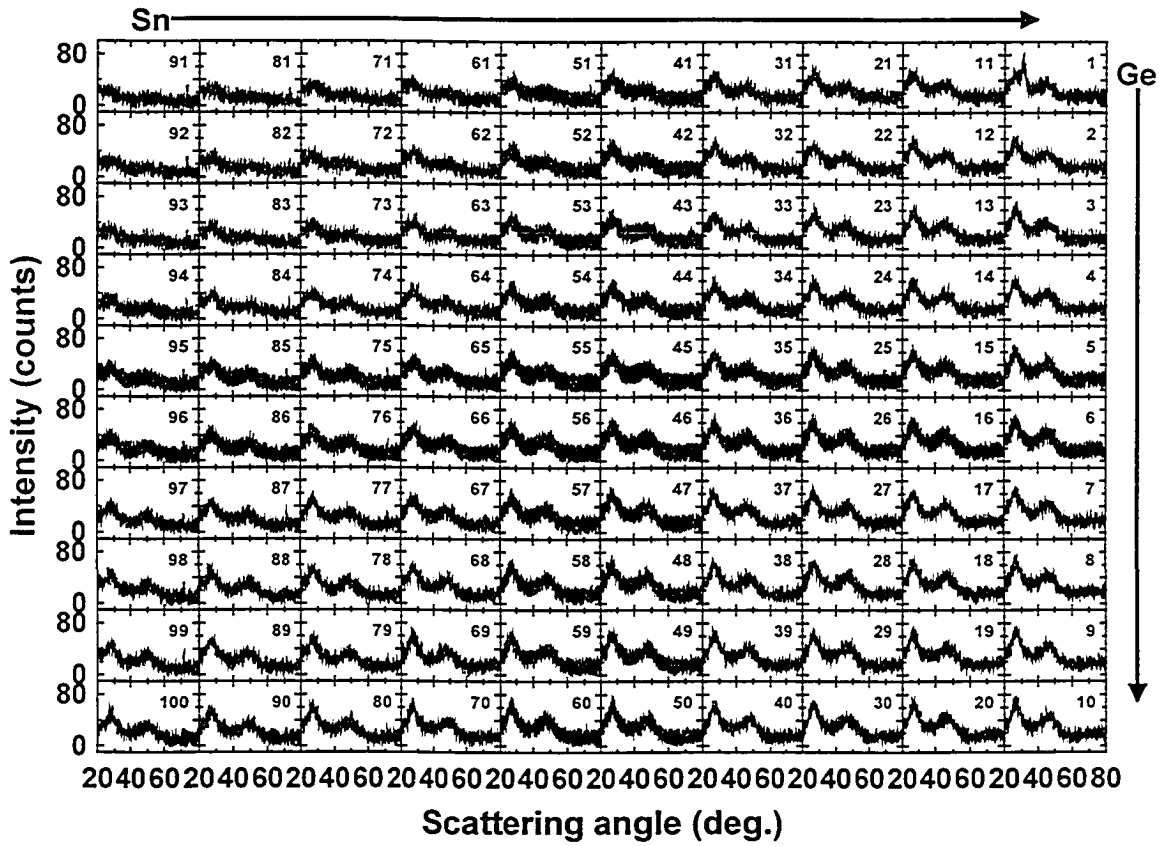

Figure 7.50. X-ray patterns displayed as a function of position on the 75 mm x 75 mm SiGeSn film. The Ge content increases from top to bottom and the Sn content increases from left to right.

The XRD data for the SiGeSn film is shown in Figure 7.50. The directions of increasing Ge and Sn are marked with arrows. All of the XRD patterns with the exception of the top right hand corner (scan 1) show an amorphous pattern like that of a-Si, and no other phases. Scan 1 shows some weak evidence of nano-crystalline Sn. This data was used to draw the non-equilibrium phase diagram shown in Figure 7.51. The +'s mark the positions of the data points measured by electron microprobe. This entire area is amorphous, although the amorphous limit is being approached on the SiSn axis. No boundary lines between phases can be added to this diagram as they have not yet been found. An amorphous to crystalline transition is expected about half way along the SiSn binary axis. The amorphous range in this sputtered system is very large.

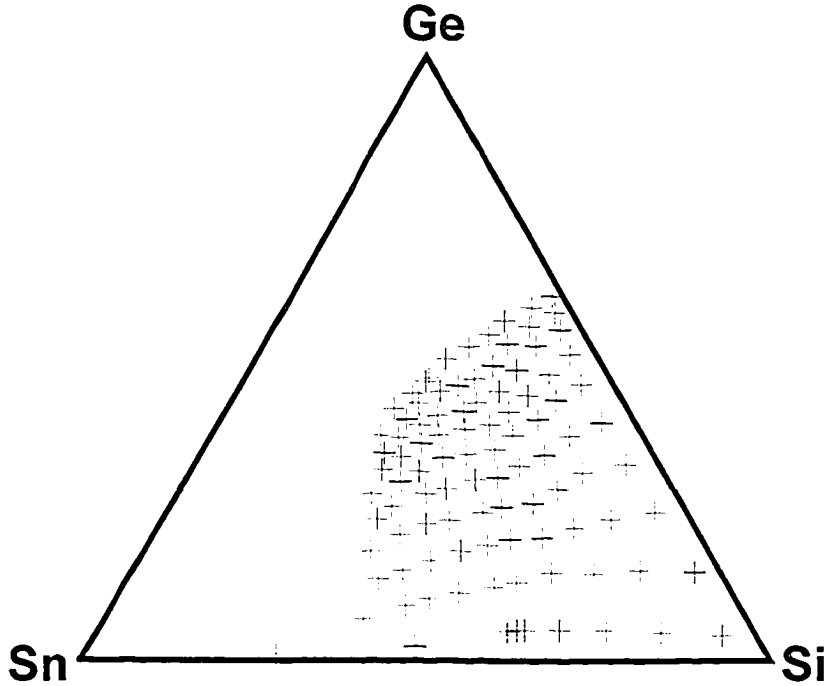

Figure 7.51. Ternary phase diagram for sputtered SiGeSn films produced from data collected on the 75 mm x 75 mm SiGeSn films. The entire area covered is amorphous. Each + represents one 7.5 mm x 7.5 mm grid point.

7.5.2. Electrochemical Results

Figure 7.52 shows a plot of channel locations for SiGeSn combinatorial electrochemical cell plate. The numbers on the diagram represent the approximate position of the corresponding channels. This cell plate was included in a combinatorial cell as described in Chapter 4. This cell was cycled using the Medusa multichannel pseudo-potentiostat described in Chapter 4. The cell was discharged to 0 V over 12 hours, held at that potential for two hours, charged to 1.2 V over 12 hours and then held for 30 minutes. This process was then repeated.

Figure 7.53 shows plots of dQ/dV *versus* potential for the SiGeSn combinatorial cell. The directions of increasing Ge and Sn are marked on the figure with arrows. Only the first cycle is shown for this cell plate. Many of the channels did not function properly for this cell in the second cycle and beyond. This makes the data very noisy and difficult to view. For this cell, however, there was not a lot of change in shape with cycle number, so little information has been lost. Selected channels will be shown with additional cycles below.

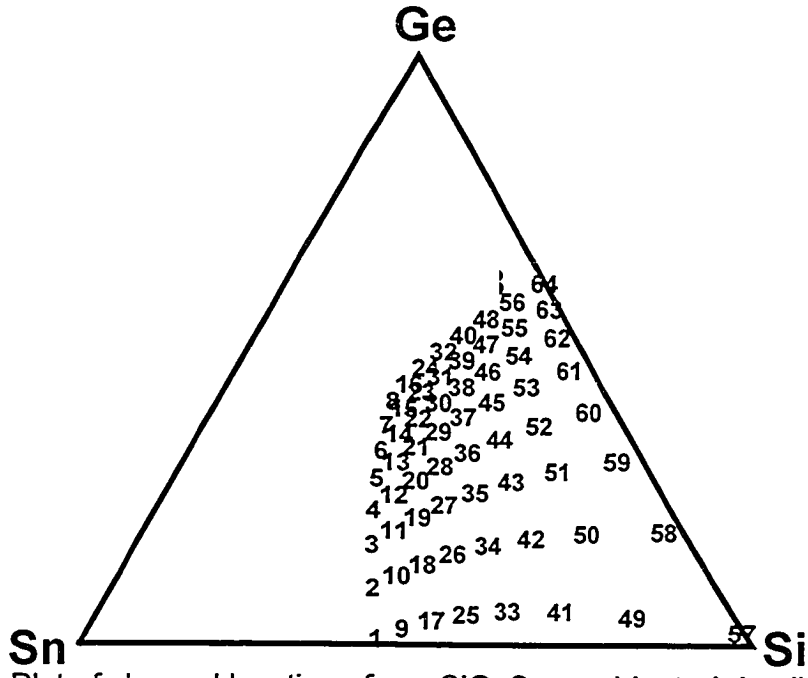

Figure 7.52. Plot of channel locations for a SiGeSn combinatorial cell.

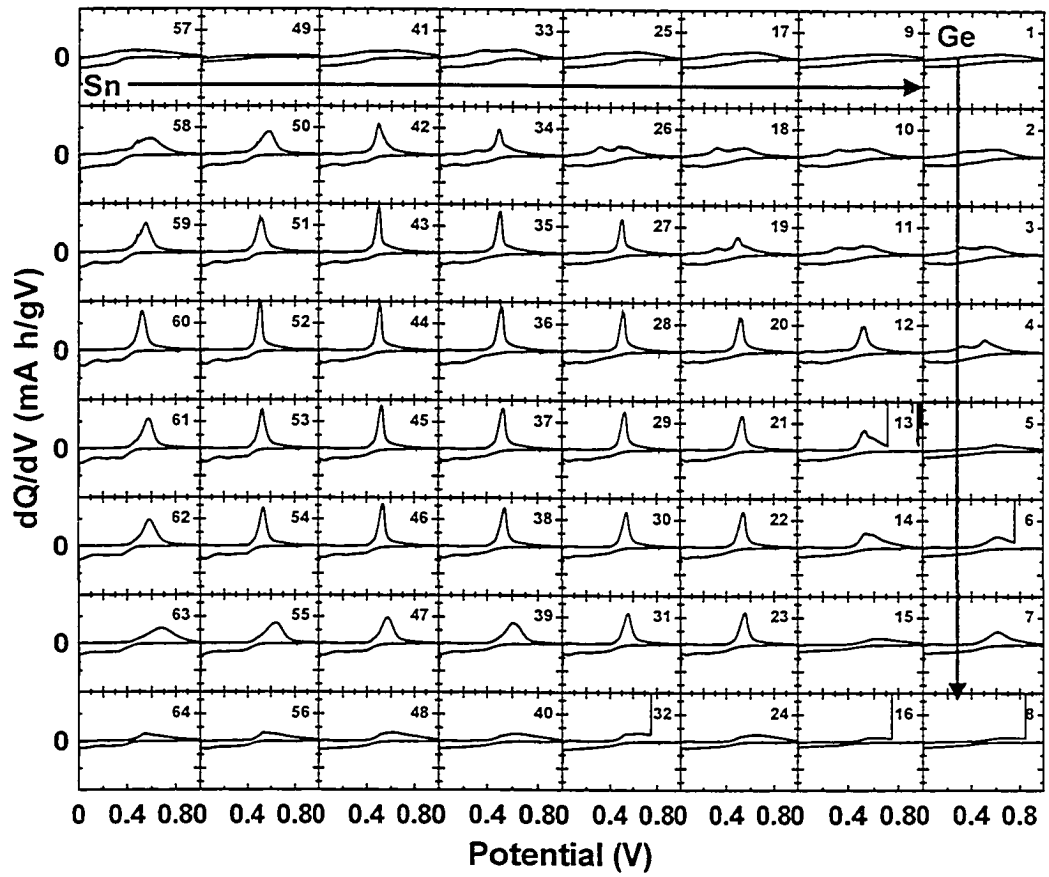

Figure 7.53. Plots of dQ/dV *versus* potential for the first cycle of all 64 channels of a SiGeSn combinatorial electrochemical cell with compositions as indicated in Figure 7.52.

In Figure 7.53, if there is significant Ge content (below the top row of graphs) there seems to be a diagonal line that divides channels that form the $Li_{15}M_4$ phase from those that do not. This is based on the presence of the sharp peak in dQ/dV *versus* potential during charge which has previously been associated with $Li_{15}Si_4$.

Figure 7.54 shows the plots of dQ/dV *versus* potential for the third row of channels in Figure 7.53 (59, 51, 43, 35, 27, 19, 11 and 3). These channels have a moderate Ge content and Sn content increases from left to right on Figure 7.53 or as channel number decreases. Channels 59 to 27 all show evidence of the $Li_{15}M_4$ phase. It is likely that the crystalline phase is $Li_{15}Si_4$ or some variation of $Li_{15}(SiGe_x)_4$. Recall that $Li_{15}Ge_4$ has the structure that $Li_{15}Si_4$ was based on in Chapter 5.

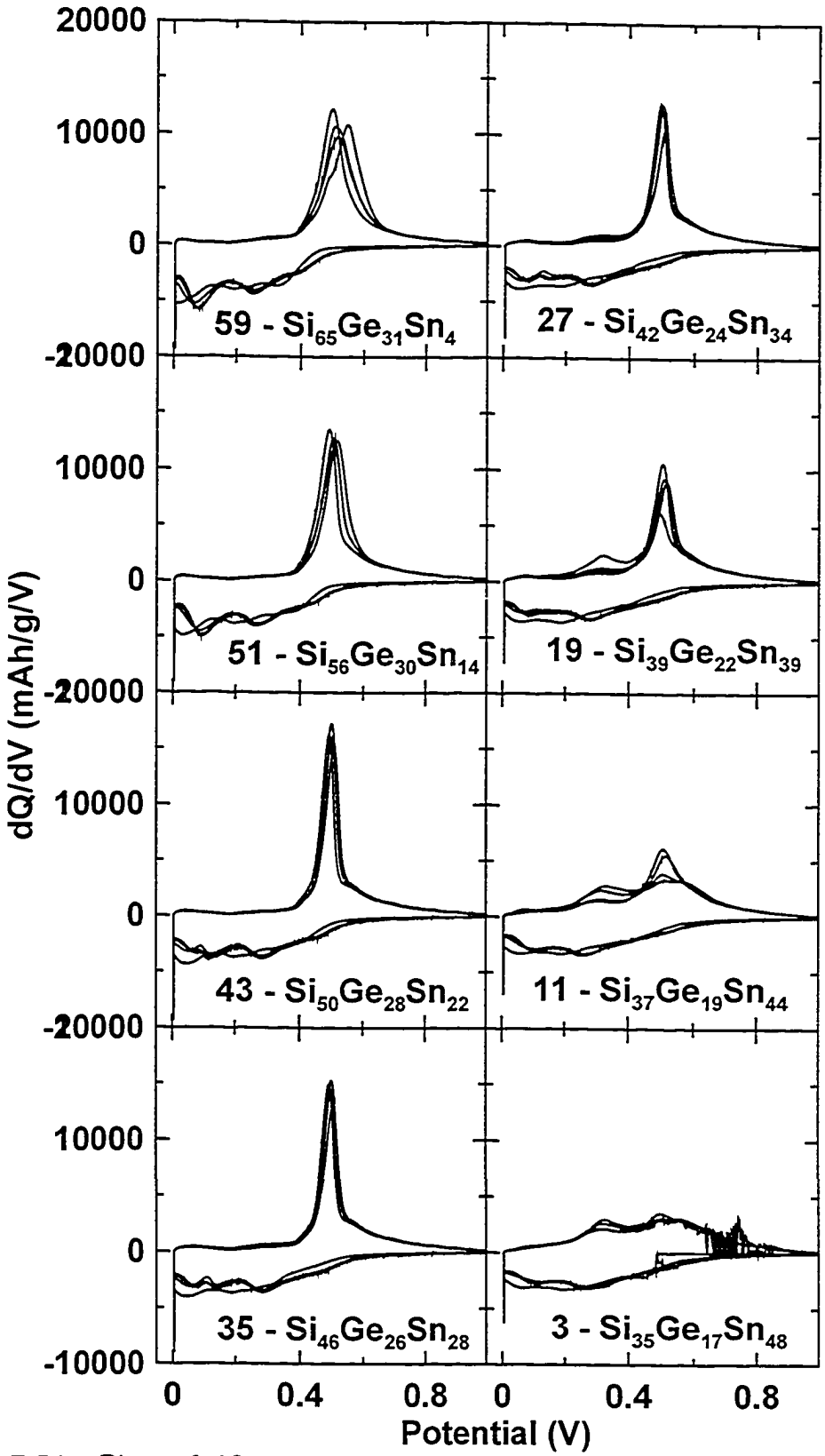

Figure 7.54. Plots of dQ/dV *versus* potential for one row of channels for the SiGeSn combinatorial cell of Figure 7.53. Channel numbers and approximate compositions are shown in the figure.

The channels shown in Figure 7.54 all have the same basic shape for the dQ/dV *versus* potential relation except that in some channels the peak during charge shifts in potential from cycle to cycle. For channel 19, the dQ/dV *versus* potential plot shows the two broad humps characteristic of a-SiSn during the first charge but then switches to the one peak near 0.4 V that is indicative of $Li_{15}Si_4$. Channel 11 does not switch to the $Li_{15}Si_4$ shape until the third charge. Channel 3, with the most Sn, stays amorphous for at least four cycles. It seems that for SiGeSn, if total metal content is not too high adequate Sn suppresses the formation of crystalline phases. For rows with higher Ge content, it takes more Sn to suppress the crystalline phase. Figure 7.53 reveals that if metal content is too high, the dQ/dV *versus* potential plot will not change to the familiar a-SiSn pattern with two humps during charge. However, the peak that does appear tends to be broader and higher in potential than the peak typical for $Li_{15}Si_4$.

Figure 7.55 shows a contour plot of the percent of theoretical capacity achieved for the SiGeSn combinatorial cell *versus* composition. The theoretical capacities were based on fully lithiated phases of $Li_{15}Si_4$, $Li_{15}Ge_4$ and $Li_{22}Sn_5$. The percent of theoretical capacity achieved increases with Sn content as would be expected from the SiSn results described in Chapter 6. The percent of theoretical capacity also increases with Ge content. This figure shows that Sn allows the fully lithiated phase to approach $Li_{22}M_5$. It is not clear if Ge allows $Li_{22}M_5$ to be approached as the capacity achieved along the Si-Ge binary axis is even less than that expected for the $Li_{15}M_4$ phase. It does appear that Ge does not interfere with the ability of Sn to allow the $Li_{22}M_5$ phase to be reached.

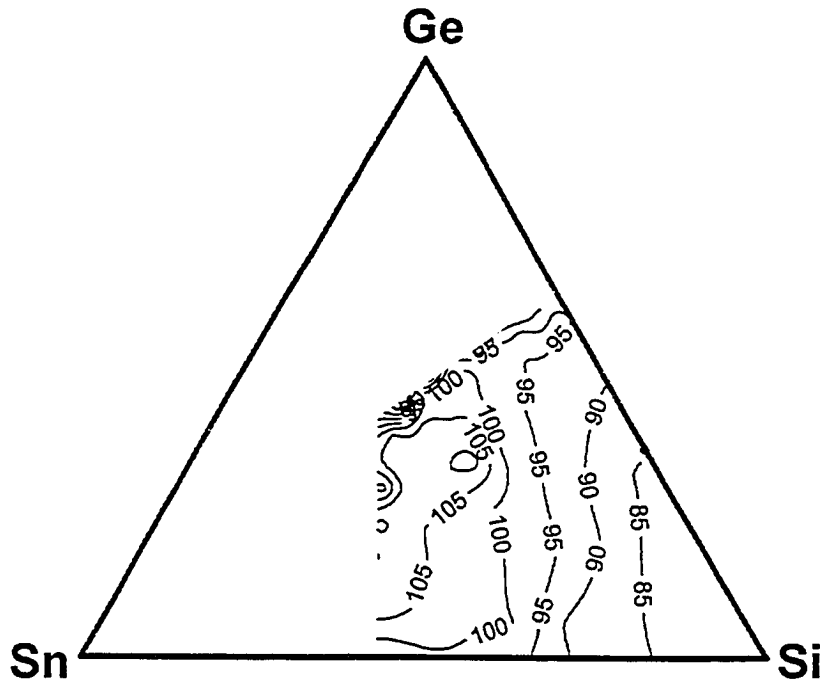

Figure 7.55. Contour plot of percent of theoretical capacity achieved *versus* composition for the SiGeSn combinatorial cell.

Figure 7.56 shows a contour plot of the irreversible capacity of the SiGeSn combinatorial cell plotted against composition. The irreversible capacities are generally quite low with most channels being below 6 %. The irreversible capacity decreases slightly for higher Sn and Ge content for this system.

Figure 7.57 shows a contour plot of the capacity fade rate plotted *versus* composition for the first four cycles of the SiGeSn combinatorial cell. The fade rate is higher for SiGeSn than it is for SiSn, with most channels being over 2 %/cycle. It should be noted that the effect of first cycle irreversible capacity is included in the fade rate and since it is averaged over a small number of cycles this may make the fade rate look higher than it actually is. With irreversible capacity being about four to six percent, when the fade is calculated over only four cycles, this adds at least one percent to the calculated fade rate. The best

rates are found for high Sn and Ge content, although there is a lot of scatter in the data points and no strong dependence is evident.

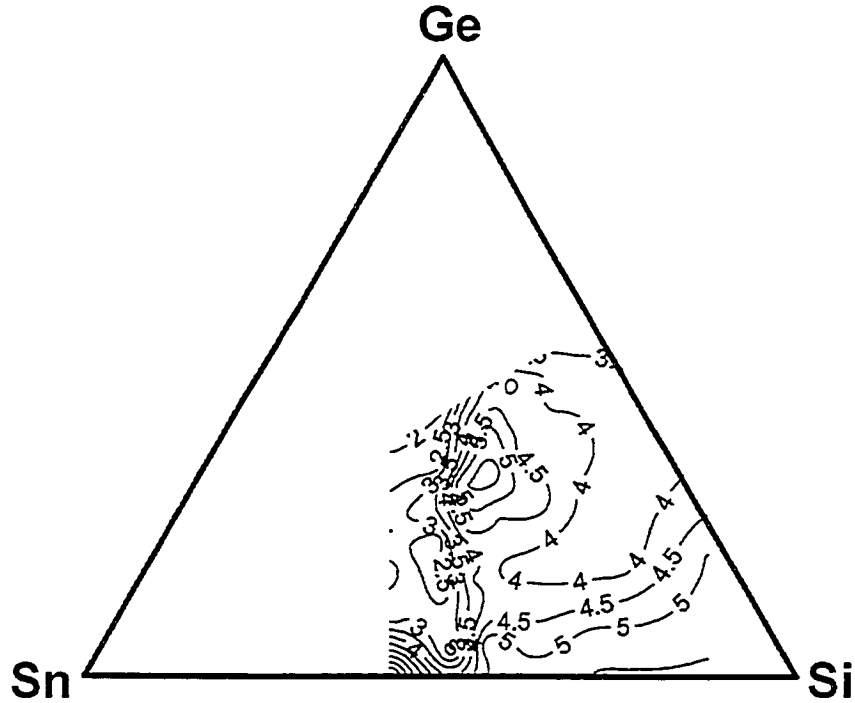

Figure 7.56. Contour plot of irreversible capacity as a percent of the first discharge *versus* composition for a SiGeSn library.

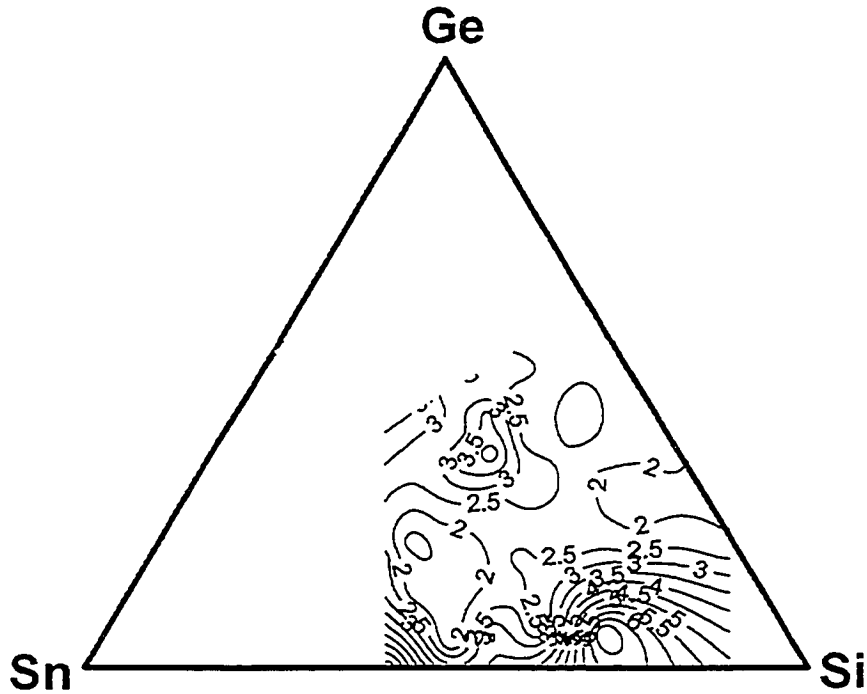

Figure 7.57. Contour plot of capacity fade rate as a percent of the first discharge *versus* composition for the first four cycles of the SiGeSn combinatorial cell.

7.5.3. Conclusions for SiGeSn

A wide stoichiometry range of the SiGeSn ternary system has been produced using the combinatorial sputtering machine described in Chapter 3. No crystalline phases were found by XRD in the films produced, indicating a very large amorphous range for this system.

It was found that compositions low in Sn tended to crystallize during discharge, but if Sn content was large enough crystallization was suppressed. Ge did not suppress the $Li_{15}M_4$ phase although more work is needed in order to confirm the phase(s) that form during the discharge of those channels showing evidence of crystalline material. Sn did allow the $Li_{22}M_5$ phase to be reached.

The electrochemical performance of the SiGeSn system was quite promising. Irreversible capacity was very low for the SiGeSn system and while the capacity fade rate was higher than some other systems, that may be because only a small number of cycles was used to calculate the fade rate. A high fade rate would make this system less attractive for use in Li-ion batteries. However, the high rate is surprising (and may not be accurate) given the large amorphous range for this system. Throughout the thesis, amorphous materials have had better capacity retention than crystalline ones. This has also been found by others [31 - 35, 92]. Only one SiGeSn library has been tested to date. When the very low irreversible capacity of this library is combined with the expectation of high capacity retention for amorphous materials, it is evident that more work is still needed on this system before it is regarded as unsuitable for use as a negative electrode material in Li-ion batteries.

Chapter 8. Concluding Remarks and Future Directions

One of the main objectives of the work described in this thesis was to develop the combinatorial infrastructure described and to show that it could be successfully applied to the development of improved electrode materials for Li-ion batteries. Through the efforts of a large group of people at Dalhousie, this has been accomplished. The combinatorial methods employed can be used to synthesize and test large numbers of samples at once. Entire binary systems and large portions of ternary systems can easily be produced in one sputtering run. Two sets of 64 different electrode compositions can also be produced in the same sputtering run that can then be electrochemically cycled at once. The results obtained with the combinatorial techniques have been found to be at least as good as with conventional one at a time methods, and in many cases they are superior.

The use of combinatorial techniques has greatly increased the speed with which materials research can be performed. While the development work on the sputtering method, characterization techniques, combinatorial electrochemical cell and the Medusa for cycling the combinatorial cells took approximately two years, the majority of the work on the binary and ternary systems described herein has been performed in approximately eight months. Without using combinatorial methods it would be difficult to imagine that one researcher could synthesize, characterize, test and analyze the hundreds of different compositions that have been described in this thesis in the same amount of time.

One criticism that is sometimes levelled at combinatorial techniques and those who employ them is that it is soft science. It might be said that it is all guess work and random chance used to find a better material with no real thought or understanding of why the material is better. I believe this to be a very short-sighted and narrow-minded point of view. The quality of the work is based on the quality of the thought and planning that go into each experiment. It is not sufficient to simply perform combinatorial experiments and look for results. One must carefully plan an experiment and then examine the data produced in a conscientious and systematic manner. The next experiment can then be planned based on the findings of the previous one. In this way, rapid advancement can be made while at the same time a solid understanding of the results is achieved.

Apart from the goal of establishing the combinatorial infrastructure for battery research (much of which is now being applied to fuel catalyst research as well), this thesis has presented a rather broad summary of results of several a-Si-based binary and ternary systems for use as anode materials in Li-ion batteries. The results in general may be seen as an overview or first look at many of these systems with a closer look at a-Si and some of the SiZn binary system.

There are some specific examples of the power of the combinatorial technique throughout the thesis. With the large amounts of data produced it is sometimes very easy to see trends that may not be noticeable from a series of one-at-a-time experiments performed over a long period of time. Specific examples of this are the tendency for Sn to permit Si to alloy with more Li than it would on its own as seen in Chapter 6 and the change in behaviour of SiZn and

SiAg binaries as the Zn and Ag content is changed. With the data from the combinatorial experiments available to be examined at one time, it becomes obvious that the mechanisms involved in the electrochemical cycling of these binary systems is changing with composition.

Another strong point of the combinatorial technique is that multiple samples can easily be produced to demonstrate reproducibility and double check results. The sputtering technique used in this study produces five nominally identical samples so that results can be verified without doing additional sputtering runs. Also, in the case of the SiSn binary, many channels of a certain composition showed poor behaviour (second row from top in Figure 6.4). With traditional techniques a researcher might perform two or three experiments at this composition and find bad results, thus concluding that the composition would always perform poorly. However, with the combinatorial method used, there were eight samples with the particular composition in question. Two of these performed very well, indicating that this composition could perform very well.

The results of the combinatorial experiments can also point out areas where more in-depth study by traditional methods is needed. The best example of this is a-Si. Although the results from the study of the a-Si were presented first, the work was not performed until the results from the SiSn binary were examined. It was clear from the SiSn work that a better understanding of a-Si was needed, so the *in-situ* XRD work was performed. This work provided valuable insights to the reaction of Li with a-Si.

In-situ XRD experiments were also performed on two compositions from the SiZn binary system. These experiments showed that the SiZn films in the library likely do not become amorphous during electrochemical cycling as was first thought based on the dQ/dV *versus* potential relationships from the combinatorial electrochemical cell. Instead, it seems that a LiSiZn ternary phase is formed (either a $Li_4(SiZn_x)$ phase or $Li_{2\pm x}SiZn$ phase depending on starting composition) during discharge. When the Li is removed the Zn forms small grains dispersed in an a-Si matrix. The Zn is unable to phase separate to form larger grains.

Like most scientific studies, there are many questions left to be answered. It was impossible to examine the data from a combinatorial electrochemical cell without finding at least one new question or avenue of research that requires further study. For a-Si more study is needed to determine the thickness limit below which the film will crystallize when lithiated and above which it will not. This could possibly be determined by using a combinatorial cell plate with a wedge of Si sputtered on it through a linear mask. Most important is to understand why the thickness of the film, either through adhesion to the substrate (clamped boundary conditions) or for some other reason, can affect the crystallization of $Li_{15}Si_4$. It would also be interesting to try electrochemical cycling at elevated temperatures to see if the $Li_{22}Si_5$ could be achieved in an electrochemical cell. To the author's knowledge, this has not been attempted with a-Si.

In the SiAg binary system a model was proposed describing the aggregation of Ag during electrochemical cycling. Several *in-situ* XRD experiments could be performed for different SiAg compositions in order to either disprove or support this model. TEM studies could also be useful for measuring any changes in Ag grain size. In the SiZn binary system, some speculation on the behaviour of $Si_{50}Zn_{50}$ was described. An *in-situ* XRD experiment would also be interesting for this composition to test the accuracy of this speculation.

Given the model for SiAg and the findings and speculation for SiZn, it would be interesting to study them at higher temperatures to see how this would effect the ability of the elements to phase separate when Li is removed. Zn may be able to phase separate from the Si at higher temperatures and form larger crystalline grains. If larger grains did form, the impact on capacity retention could be studied.

In the SiAlSn ternary system, no evidence of crystalline Al was found in the dQ/dV *versus* potential relationships even when crystalline Al was found by XRD. Some experiments with either SiAl or SiAlSn with low Sn and perhaps more Al could shed some light on this. Is the LiSiAl ternary phase forming for these films (in a similar manner to the Li_2SiZn in Chapter 6) or is there *in-situ* amorphization of the Al, with the Al being drawn into the a-Si matrix? Some work performed on the SiAlMn system has shown the formation of LiSiAl during the discharge [103]. When the Li was removed, the LiSiAl phase remained. It would be interesting to see if the same thing happens in sputtered SiAl films.

In the other ternary systems a peak appeared at about 0.4 V during charge in the dQ/dV *versus* potential graphs for many compositions. It was assumed that this was from the formation of the $Li_{15}Si_4$ phase (or a variation of this phase with some Si replaced by other elements). Also, many other peaks were also found in the dQ/dV *versus* potential graphs that were unexplained. The study of these systems to verify what these phases are would take enormous amounts of work. They could possibly form the basis for future graduate work by other students.

The SiSnZn system would be especially interesting. The SiSn and SiZn systems showed the best electrochemical performance for the binaries and SiSnZn was the best of the ternaries, although more work is needed on the SiGeSn system. The tendency for SiSn to stay amorphous and SiZn to become nano-structured makes these elements very promising for use as anode materials in Li-ion batteries. The shape of the dQ/dV *versus* potential relationship for the SiSnZn ternary showed a strong dependence on composition with the possibility of several different phases forming. It would be interesting to determine what these phases are. Some effort to optimize this system may also be warranted. The best composition should be found and also the best electrolytes and binders could also be investigated. Polymeric binders like those in [56] could also be beneficial for these materials.

The SiSnZn materials can only be made amorphous by sputtering. The best compositions should also be produced by a more traditional means such as ball milling and cycled electrochemically. As described in Chapter 1, it was found

that c-Si became amorphous when cycled electrochemically [89, 90]. If SiSnZn was made crystalline with small particle size, it may also become amorphous or nanocrystalline in a similar manner. A large amount of Sn can be incorporated in an a-Si matrix, and SiZn tends to become nano-structured when cycled. If a method could be found to achieve this result, then these materials could possibly be mass-produced by physical mixing or melt spinning followed by electrochemical processing. If this could be made to work, then SiZn or SiSnZn anodes could possibly replace graphite in commercial Li-ion cells. SiSn may not work in this manner, as in the SiSn binary, Sn showed no tendency towards *in-situ* amorphization if crystalline Sn was present in the as-sputtered sample However, if a starting material of $Si_{0.8}Sn_{0.2}$ were used, the Sn may be drawn into the amorphous matrix since this amount of Sn can be accomodated ni a-Si without crystallizing.

A combinatorial approach to the testing of mixed systems could be performed with the sputtering equipment described in chapter 3. As an example, consider a series of wedges of Si and Zn. By using the two axis table and linear deposition masks over a Si and Zn target, a series of orthogonal wedges could be created as shown in Figure 8.1. This profile can be created by programming the power supplies to periodically turn off and on so that a wedge of one material is deposited for a set time, and the other material is deposited for a set time. By repeating this sequence, a series of multilayers is built up. The sputter time per wedge could be programmed to give, say, 50 nm at the thick edge. All possible thickness combinations of Si and Zn layers between 0 and 50 nm would be

produced in this way. This would be a simulation of having a variety of Si and Zn particle sizes. A combinatorial cell could then test how many cycles it would take to achieve the Li_2SiZn phase (if this could be achieved at all) as a function of layer thickness. Temperature effects could also be tested in this way by running the combinatorial cell at elevated temperatures.

Similar studies to the one suggested above could also be done that incorporate Sn. For example, wedges of Si and Zn could be sputtered that are at 180° to each other. A thin wedge of Sn could be sputtered between each Si and Zn layer so that the Zn and Si were separated by Sn. If the Sn wedge was at 90° to the Si and Zn, then a large range of layer thicknesses would be found. The combinatorial electrochemical cell could then be used to test if the Si and Zn could still react together as a function of Sn thickness. Could the Sn be drawn into an amorphous or nanocrystalline matrix with the other elements in this manner? Temperature effects would also be important for this experiment.

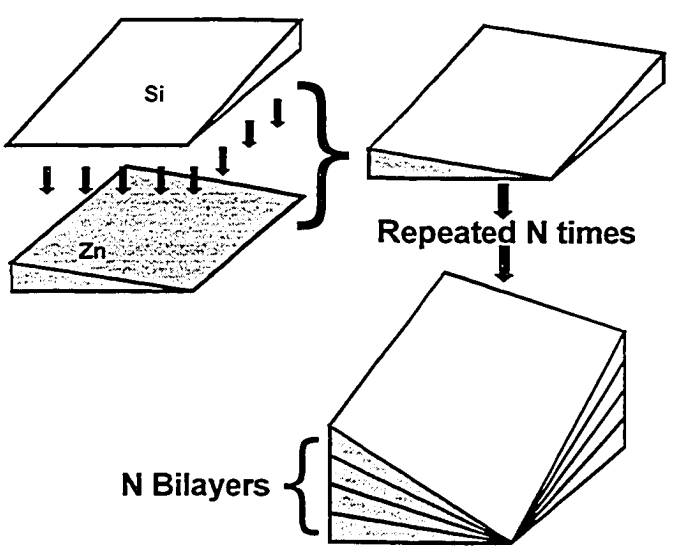

Figure 8.1. Schematic diagram showing the production of a series of Si and Zn wedges at 90° to each other. This method produces all thickness combinations of the two elements between 0 and the maximum wedge thickness.

Another approach could be to use the first wedge experiment for Si and Zn described above and sputter a small amount of Sn throughout all of the layers. This method would avoid the need for Sn to be drawn into a matrix with other elements as it would be there from the beginning. It would be interesting to see if the Sn would stay mixed with the other elements when (or if) they mix and if the formation of Li_2SiZn is helped or hindered by the presence of Sn. High temperature cycling could test to see which element would tend to aggregate first, if at all.

There are virtually a limitless number of experiments that could be performed. The wedge experiments described above could also be performed with Ag, Al or Ge. It might be instructive to include some elements that are inactive towards Li as well. The presence of these elements might buffer the expansion when Li is inserted. Also, they might prevent the aggregation of the active elements, such as Ag, during electrochemical cycling.

Finally, it should be noted that all of the sputtering experiments in this thesis have been performed with the same Ar pressure and with similar powers for each element from one run to the next. In work where powers and pressures were varied, the resulting films had very different characteristics [82]. It might be useful to investigate the effects of things like Ar pressure or substrate temperature on the amorphous range achieved in and the electrochemical performance of the systems described in this thesis.

References

[1] I. Buchmann, *Batteries in a Portable World*, Cadex Electronics, Vancouver, BC, Canada (2001).

[2] M.S. Whittingham, *Science*, **192**(4244), 1126-1127 (1976).

[3] I. Faul and J. Knight, *Chem. Ind.*, **24,** 820-825 (1989).

[4] F.C. Laman and K. Brandt, *J. Power Sources*, **24,** 195 (1988).

[5] K. Brandt, *J. Power Sources*, **18,** 117-125 (1986).

[6] K. Brandt, *J. Power Sources*, **17,** 153-159 (1986).

[7] D.P. Wilkinson, H. Blom, K. Brandt and D. Wainwright, *J. Power Sources*, **36**(4), 517-527 (1991).

[8] D. Fouchard and J.B. Taylor, *J. Power Sources*, **21,** 195 (1987).

[9] J.J. Murray and J.E.A. Alderson, *J. Power Sources*, **26**(3-4), 293-299 (1989).

[10] T.L. Brown, H.E. LeMay and B.E. Bursten, *Chemistry: The Central Science*, Prentice-Hall, New Jersey, eighth edition, 2000.

[11] J.R. Dahn, U. von Sacken, M.W. Juzkow and H. Al-Janaby, *J. Electrochem. Soc.*, **138**(8), 2207 (1991).

[12] D.P. Wilkinson, J.R. Dahn, U. von Sacken and D.J. Fouchard, Paper 53 presented at The Electrochemical Society Meeting, Seattle, WA, Oct. 14-19, 1990.

[13] J.O. Besenhard, editor, *Handbook of Battery Materials*, Wiley-VCH, Weinheim, 1999.

[14] M. Winter. J.O. Besenhard and P. Novak, *Adv. Mater.*, **10,** 725 (1998).

[15] M. Wakihara and O. Yamamoto, editors, *Lithium Ion Batteries*, Kodansha/Wiley-VCH, Tokyo/Weinheim, 1998.

[16] A.N. Dey, *J. Electrochem. Soc.*, **118,** 1547 (1971).

[17] J. Antula and B.F. Becker, *J. Phys. Chem.*, **79,** 2470 (1975).

[18] B.M. Rao, R.W. Francis and H.W. Christopher, *J. Electrochem. Soc.*, **124**(10), 1490-1492 (1977).

[19] J.O. Besenhard, *J. Electroanal. Chem.*, **94,** 77-81 (1978).

[20] E. Peled, A. Lombardi and C.R. Schlaikjer, *J. Electrochem. Soc.*, **130**(6), 1365-1368 (1983).

[21] T. Nohma, S. Yoshimura, K. Nishio, Y. Yamamoto, S. Fukuoka and M. Hara, *J. Power Sources*, **58**(2), 205-207 (1996).

[22] J. Wang, I.D. Raistrick and R.A. Huggins, *J. Electrochem. Soc.*, **133**(3), 457 (1986).

[23] B.A. Boukamp, G.C. Lesh and R.A. Huggins, *J. Electrochem. Soc.*, **128,** 725 (1981).

[24] R.A. Huggins, US Patent # 4,436,796, 1984.

[25] A.A. Anani, S. Crouch-Baker and R.A. Huggins, *J. Electrochem. Soc.*, **135**(8), 2103 (1988).

[26] A.A. Anani, S. Crouch-Baker and R.A. Huggins, *J. Electrochem. Soc.*, **134**(12), 3098 (1987).

[27] R.A. Huggins, *J. Power Sources*, **22,** 341-350 (1988).

[28] J. Yang, M. Winter and J.O. Besenhard, *Solid State Ionics*, **90**(1-4), 281-287 (1996).

[29] J.O. Besenhard, J. Yang and M. Winter, *J. Power Sources*, **68**(1), 87-90 (1997).

[30] M. Winter and J.O. Besenhard, *Electrochim. Acta*, **45,** 31-50 (1999).

[31] L.Y. Beaulieu, K.W. Eberman, L.J. Krause and J.R. Dahn, *Electrochem. Solid-State Lett.*, **4**, A137 (2001).

[32] L.Y. Beaulieu. K.C. Hewitt, R.L. Turner, A. Bonakdarpour, A.A. Abdo, K.W. Eberman, L.J. Krause and J.R. Dahn, *J. Electrochem. Soc.*, **150**, A149 (2003).

[33] L.Y. Beaulieu, T.D. Hatchard and J.R. Dahn, Abstract 251, poster presented at the 11th International Meeting on Lithium Ion Batteries, Monterey, CA, 2002.

[34] L.Y. Beaulieu, T.D. Hatchard, A. Bonakdarpour, M.D. Fleischauer and J.R. Dahn, *J. Electrochem. Soc.*, **150**, A1457 (2003).

[35] K. Sayama, H. Yagi, Y. Kato, S. Matsuta, H. Tarui and S. Fujitani, Abstract 52, poster presented at the 11th International Meeting on Lithium Ion Batteries, Monterey, CA, 2002.

[36] J.P. Maranchi, A.F. Hepp and P.N. Kumta, *Electrochem. Solid-State Lett.*, **6**, A198 (2003).

[37] H. Jung, M. Park, Y.G. Yoon, G.B. Kim and S.K. Joo, *J. Power Sources*, **115**, 346 (2003).

[38] Y. Idota, A. Matsufuji, Y. Maekawa and T. Miyasaka, *Science*, **276**(5317), 1395-1397 (1997).

[39] I.A. Courtney and J.R. Dahn, *J. Electrochem. Soc.*, **144**(6), 2045-2052 (1997).

[40] I.A. Courtney and J.R. Dahn, *J. Electrochem. Soc.*, **144**(9), 2943-2948 (1997).

[41] I.A. Courtney, R.A. Dunlap and J.R. Dahn, *Electrochim. Acta.*, **54**(1-2), 51-58 (1997).

[42] I.A. Courtney, W.R. McKinnon and J.R. Dahn, *J. Electrochem. Soc.*, **146**(1), 59-68 (1999).

[43] I.A. Courtney, J.S. Tse, O. Mao, J. Hafner and J.R. Dahn, *Phys. Rev. B*, **58**(23), 15583-15588 (1998).

[44] O. Mao, R.A. Dunlap and J.R. Dahn, *J. Electrochem. Soc.*, **146**(2), 405-413 (1999).

[45] O. Mao and J.R. Dahn, *J. Electrochem. Soc.*, **146**(2), 414-422 (1999).

[46] O. Mao and J.R. Dahn, *J. Electrochem. Soc.*, **146**(2), 423-427 (1999).

[47] O. Mao, R.L. Turner, I.A. Courtney, B.D. Fredericksen, M.I. Buckett, L.J. Krause and J.R. Dahn, *Electrochem. Solid-State Lett.*, **2**(1), 3-5 (1999).

[48] O. Mao, R.A. Dunlap, I.A. Courtney and J.R. Dahn, *Electrochem. Solid-State Lett.*, **145**(12), 4195-4202 (1998).

[49] M. Green, E. Fielder, B. Scrosati, M. Wachtler and J. Serra Moreno, *Electrochem. Solid-State Lett.*, **6**(5), A75 (2003).

[50] M. Yoshio, N. Dimov, T. Iwao, K. Fukuda and T. Umeno, Abstract 248, oral presentation at the 200th Meeting of the Electrochemical Society, San Francisco, CA, 2001.

[51] N. Dimov, S. Kugino, M. Yoshio, T. Umeno and K. Fukuda, Abstract 315, oral presentation at the 204th Meeting of the Electrochemical Society, Orlando, FL, 2003.

[52] Z. Shi and M Alamgir, Abstract 319, oral presentation at the 204th Meeting of the Electrochemical Society, Orlando, FL, 2003.

[53] K. Inoue, H. Yoshizawa, H. Koshina, H. Shimamura and Y. Nitta, US Patent # 6,506,520 B1, 2003.

[54] J. Cho, Y. J. Kim, J. T. Kim, and B. Park, *Angew. Chem. Int. Ed.*, **40**(18), 3367 (2001).

[55] Z. Chen and J.R. Dahn, *Electrochim. Acta*, **49(7)**, 1079-1090 (2004).

[56] Z. Chen, L. Christensen and J. R. Dahn, *Electrochemistry Communications,* **5**(11), 919 (2003).

[57] A. Netz, R.A. Huggins and W. Weppner, *J. Power Sources*, **119-121**, 95 (2003).

[58] M. Wachtler, M. Winter and J.O. Besenhard, *J. Power Sources*, **105**, 151 (2002).

[59] M.M. Thackeray, J.T. Vaughey, C.S. Johnson, A.J. Kropf, R. Benedek, L.M.L. Fransson and K. Edstrom, *J. Power Sources*, **113**, 124 (2003).

[60] I. Rom, M. Wachtler, I. Papst, M. Schied, J.O. Besenhard, F. Hofer and M. Winter, *Solid State Ionics*, **143**, 329 (2001).

[61] J.T. Vaughey, L. Fransson, H.A. Swinger, K. Edstrom and M.M. Thackeray, *J. Power Sources*, **113-121**, 64 (2003).

[62] T.D. Hatchard, J.M. Topple, M.D. Fleischauer and J.R. Dahn, *Electrochem. Solid-State Lett.*, **6** A129 (2003).

[63] S.W. Song, K.A. Striebel, X. Song and E.J. Cairns, *J. Power Sources*, **119-121**, 110 (2003).

[64] H.M. Geyson, R.H. Meloen and S.J. Barteling, *Proc. Natl. Acad. Sci. U.S.A.*, **91**, 3998-4005 (1984).

[65] K. Kennedy, T. Stefansky, G. Davy, V.F. Zackay and E.R. Parker, *J. App. Phys.*, **36**, 3808 (1965).

[66] J.J. Hanak, *J. Materials Science,* **5**, 964 (1970).

[67] J.J. Hanak, H.W. Lehmann and R.K. Wehner, *J. Appl. Phys.*, **43**, 1666 (1972).

[68] J.J. Hanak and B.F.T. Bolker, *J. Appl. Phys.*, **44**, 5142 (1973).

[69] J.J. Hanak, J.I. Gittleman, J.P. Pellicane and S. Bozowski, *Physics Letters*, **30**(3) 201-202 (1969).

[70] J.J. Hanak and J.I. Gittleman, *Physica*, **55**, 555 (1971).

[71] X.D. Xiang, X. Sun, G. Briceno, Y. Lou, K.A. Wang, H. Chang, W.G. Wallace-Freedman, S.W. Chen and P.G. Schultz, *Science*, **268**, 1738 (1995).

[72] E. Danielson, J.H. Golden, E.W. McFarland, C.M. Reaves, W.H. Weinberg and X.D. Wu, *Nature,* **389**, 944-948 (1997).

[73] E. Danielson, M. Devenney, D.M. Giaquinta, J.H. Golden, R.C. Haushalter, E.W. McFarland, D.M. Poojary, C.M. Reaves, W.H. Weinberg and X.D. Wu, *Science,* **279**, 837-839 (1998).

[74] R.B. van Dover, L.F. Schneemeyer and R.M. Fleming, *Nature,* **392**, 162 (1998).

[75] H. Chang, I. Takeuchi and X.D. Xiang, *Appl. Phys. Lett.*, **74**, 1165 (1999).

[76] X.D. Xiang, *Annu. Rev. Mater. Sci.*, **29**, 149 (1999).

[77] K. Fujimoto, I. Yanase, T. Ohtaki, A. Kajiyama, K. Takada, T. Sasaki and M. Watanabe, Abstract 268, poster presented at the 11th International Meeting on Lithium Ion Batteries, Monterey, CA, 2002.

[78] J.E. Mahan, *Physical Vapor Deposition of Thin Films,* John Wiley & Sons Inc. (2000).

[79] J.L. Vossen and W. Kern (eds), *Thin Film Processes*, Academic Press Inc., New York, USA (1978).

[80] D.M. Mattox, *Handbook of Physical Vapor Deposition (PVD) Processing*, Noyes Publications, NJ, USA (1998).

[81] D.L. Smith, *Thin-Film Deposition, Principles and Practice*, McGraw-Hill (1995).

[82] A. Bonakdarpour, M.Sc. Thesis, Dalhousie University, Halifax, NS, Canada (2002).

[83] R. Jenkins and R.L. Snyder, *Introduction to X-ray Powder Diffractometery*, John Wiley & Sons, Inc. (1996).

[84] R. Woldsseth, *X-ray Energy Spectroscopy*, Kevex Corporation, Burlingame, California (1973).

[85] J.I. Goldstein, D.E. Newbury, P. Echlin, D.C. Joy Jr., A.D. Romig, C.E. Lyman, C. Fiori and E. Lifshin, *Scanning Electron Microscopy and X-Ray Microanalysis*, (1992).

[86] A. Brown, *Nature*, **206**, 502 (1965).

[87] M.D. Fleischauer, T.D. Hatchard, G.P. Rockwell, J.M. Topple, S. Trussler and J.R. Dahn, *J. Electrochem. Soc.,* **150**(11), A1465 (2003).

[88] Vivien K. Cumyn, M.D. Fleischauer, T.D. Hatchard and J.R. Dahn, *Electrochem. Solid State Lett.*, **6,** E15 (2003).

[89] P. Limthongkul, Y.I. Jang, N.J. Dudney and Y.M. Chiang, *J. Power Sources*, **119-121**, 604 (2003).

[90] P. Limthongkul, Y.I. Jang, N.J. Dudney, Y.M. Chiang, *Acta Materialia*, **51**, 1103 (2003).

[91] S. Ohara, J. Suzuki, K. Sekine and T. Takamura, *J. Power Sources*, **119-121**, 591 (2003).

[92] J. Graetz, C.C. Ahn, R. Yazami and B. Fultz, *Electrochem. And Solid State Lett.*, **6**(9), A194 (2003).

[93] Binary Alloy Phase Diagrams, Second Edition Plus Updates, Windows version, ASM International, Materials Park, OH, USA, 1996.

[94] M.N. Richard, I. Koetschau and J.R. Dahn, *J. Electrochem. Soc.*, **144**(2), 554 (1997).

[95] M. Doyle, J. Newman and J. Reimers, *J. Power Sources*, **52**(2), 211 (1994).

[96] M.N. Obrovac and L. Christensen, *Electrochem. And Solid State Lett.*, **7**, A93 (2004).

[97] Rietica v1.7.7, Microsoft Windows version of LHPM, R.J. Hill, C.J. Howard, *J. Appl. Crystallogr.* **18**, 173 (1985); D.B. Wiles, R.A. Young, *J. Appl. Crystallogr.* **14**, 149 (1981).

[98] T.D. Hatchard, J. R. Dahn, S. Trussler, M. Fleischauer, A. Bonakdarpour, J.R. Mueller-Neuhaus, and K.C. Hewitt, *Thin Solid Films*, **443**(1-2), 144-150 (2003).

[99] J.R. Dahn, I.A. Courtney and O. Mao, *Solid State Ionics*, **111**(3-4), 289-294 (1998).

[100] W.G. Moffat, *The Handbook of Binary Phase Diagrams*, Genium Publishing Co., Schenectady, New York (1990).

[101] R.B. Schwarz and W.L. Johnson, *Phys. Rev. Lett.*, **51**, 415 (1983).

[102] P. Villars and L.D. Calvert, Pearson's Handbook of Crystallographic Data for Intermetallic Phases, 2nd ed., Vol. 4, ASM International, 1991.

[103] M.N. Obrovac, unpublished results.

[104] Tridus International Inc. website: http://www.tridus.com/

[105] O. Crosnier, C. Mounsey, P. Subramanya Herle, N. Taylor and L.F. Nazar, *Chem. Mater.*, **15**, 4890-4892 (2003).